NNT: 2017SACLS587

THÈSE DE DOCTORAT DE L'UNIVERSITÉ PARIS-SACLAY
PRÉPARÉE A L'UNIVERSIT'É PARIS–SUD
au sein du Laboratoire Leprince Ringuet,
ÉCOLE POLYTECHNIQUE

ECOLE DOCTORALE : PHENIICS N° 576

DISCIPLINE : Astroparticules et Cosmologie

par

Floriana Zefi

Gamma-ray flux variation studies from the blazar B2 1215+30 with the Fermi-LAT and the Crab Nebula with the H. E. S. S. experiment

Etude de la variabilité temporelle de l'émission gamma
du blazar B2 1215+30 avec Fermi-LAT
et de la Nèbuleuse du Crabe avec le réseau de télescopes H. E. S. S.

Soutenue le 18 Octobre 2017 à l'École Polytechnique, Palaiseau

Composition du jury :

Directeur de thèse :	Mathieu DE NAUROIS	Professeur (LLR-Ecole Polytechnique)
Co-directeur de thèse :	Stephen FEGAN	Chargé de recherche (LLR-Ecole Polytechnique)
Rapporteur	Oscar BLANCH	Professeur (IFAE, Barcelona, Spain)
Rapporteur (President du jury)	Christopher VAN ELDIK	Professeur (ECAP, Erlangen, Germany)
Examinateur	Stefan KLEPSER	Directeur de recherche (DESY, Zeuthen, Germany)
Examinateur	Mathieu LANGER	Professeur (IAS, Orsay, France)
Examinateur	Jean-Philippe LENAIN	Directeur de recherche (LPNHE, Paris, France)
Examinateur	Reshmi MUKHERJEE	Professeur (Columbia University, New York)

LABORATOIRE LEPRINCE RINGUET

To my parents and my brothers

Abstract

The current state-of-the-art experiments in gamma-ray astronomy are the Fermi-LAT in space and the ground-based H. E. S. S., VERITAS and MAGIC experiments. The monitoring of the very-high-energy gamma-ray emitting sources indicates the diverse physics taking place in astrophysical environments. To study the most energetic form of radiation and the most violent phenomena taking place in the Universe, individual source analyses are important. BL Lac objects, a subcategory of active galaxies, are the most abundant source class detected both in the GeV and TeV energies, while pulsar wind nebulae represent the most numerous identified source class in the galactic plane. Both source classes exhibit gamma-ray flux variations.

In this thesis, the gamma-ray variability of the BL Lac object B2 1215+30 is presented with Fermi-LAT data. A bright flare, with 16 times the average quiescent flux, was detected in February 2014. In collaboration with the VERITAS experiment, the gamma-ray variability was investigated over five decades in energy. This work resulted in the detection of a luminous flare, seen simultaneously in GeV and TeV energies by both instruments. These results were used to set constraints on the size of the emission region and on the Doppler factor of the relativistic jet. Additionally, the long-term variability was studied using nine years of Fermi-LAT data. This brought out new flux enhancements, which characterize the long-term lightcurve from 100 MeV up to 500 GeV. Other striking characteristics are a steady linear increase of the yearly average flux, together with a hardening of the spectral index. The investigation of the lightcurve indicates a hint of quasi-periodic behavior with a period of around 1083 ± 32 days.

This work includes spectrum and flux variability studies for the well-studied but ever-surprising Crab Nebula at TeV energies with more than a decade of H. E. S. S. observations. The spectrum measured in this work goes from 280 GeV to 62 TeV, making this the first measurement that extends to such very-high-energies. Considered as a standard candle for ground-based gamma-ray astronomy, the Crab Nebula is also used for calibration and instrument studies. The detection of GeV flares by the Fermi-LAT were unexpected and motivated the search of flux variations at TeV energies with the H. E. S. S. experiment. The position of the Crab Nebula in the northern hemisphere makes this investigation challenging due to the large systematic uncertainties introduced by the non-optimal observation conditions. This work showed that the systematic uncertainties can be reduced by taking into account the atmospheric transparency. No flux variations were found at energies above 1 TeV from the H. E. S. S. I data. A flare reported by the Fermi-LAT in October 2016 was also investigated. This analysis showed the GeV flare lasting for one month, while the flux with H. E. S. S. II had an excess variance of 15%. This should be compared to the commonly quoted 20% systematic uncertainty by H. E. S. S. experiment.

Résumé

Les rayons gamma astrophysiques de haute énergie sont les messagers de l'Univers non thermique. Ils sont le produits de l'accélération de particules chargées, un phénomène qui se déroule dans de très nombreux endroits de l'Univers (voir par exemple le centre galactique en Figure 0.1). En particulier, ils portent des informations importantes sur les plus puissants mécanismes d'accélération de particules dans les environnements extrêmes de l'Univers. Les processus qui accélèrent ces particules énergétiques dans l'Univers peuvent être étudiées indirectement par la détection de rayons gamma, produits par les interactions avec le milieu interstellaire (ISM) ou avec le champs de rayonnement. Une introduction à l'astronomie gamma est présentée au Chapitre 1 de ce manuscrit. Cela couvre une introduction aux rayons gamma cosmiques, aux mécanismes possibles responsables de la production de rayons gamma de haute énergie et un résumé des sources astrophysiques émettant aux très hautes énergies.

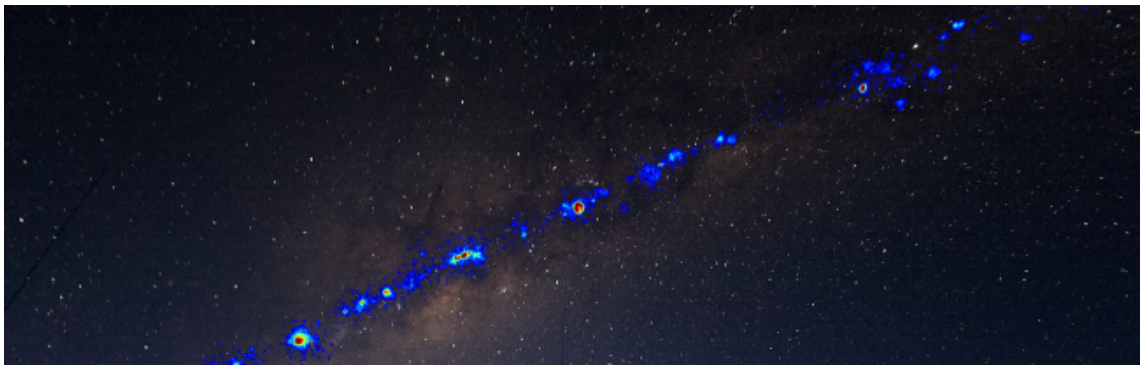

Figure 0.1: Images superposées du plan galactique en lumière optique et rayons gamma de très haute énergie. Les images à très haute énergie sont prises avec les télescopes H.E.S.S. en Namibie. Photographie et montage de F. Acero.

Les rayons gamma de très haute énergie émis par différents processus dans l'Univers sont étudiés par des détecteurs spatiaux et des détecteurs au sol. Comme l'atmosphère est opaque aux rayons gamma, empêchant une mesure directe des propriétés de ce rayonnement à partir du sol, le rayonnement gamma de haute énergie provenant de l'Univers peut donc seulement être étudié directement par de satellites envoyés au-dessus de l'atmosphère. Ces instruments sont conçus pour détecter et localiser des sites d'émission de rayons gamma de haute énergie en utilisant les propriétés d'interaction des rayons gamma avec des matériaux denses. C'est une technique robuste pour reconstruire l'énergie, la direction et le temps d'arrivée des rayons gamma avec des énergies allant du MeV au GeV. Aux énergies supérieures au Ter-

aelectronvolt (TeV), les flux de rayons gamma sont faibles et des détecteurs avec de grandes surfaces de collections sont nécessaires. A ces énergies, seules les expériences au sol offrent cette possibilité. Lorsque les rayons gamma et les rayons cosmiques de très haute énergie atteignent la Terre et interagissent avec les molécules de l'atmosphère, ils déclenchent une cascade de particules secondaires. L'atmosphère servant de calorimètre pour le dépôt d'énergie d'une particule de très haute énergie, les détecteurs au sol peuvent détecter les particules secondaires produites au cours de ce processus. La lumière Cherenkov produite pendant les cascades atmophériques peut être détectée avec la technique d'imagerie Cherenkov atmosphérique (IACT). Les principes de base de la détection des rayons gamma dans l'espace et au sol sont décrits au Chapitre 2.

Figure 0.2: *En haut*: l'expérience H.E.S.S. située dans l'hémisphère sud en Namibie est composée de cinq télescopes Cherenkov. *En bas à gauche*: l'expérience MAGIC installé à La Palma. *En bas à droite*: l'expérience VERITAS, composée de quatre télescopes Cherenkov, est située dans l'hémisphère Nord, en Arizona.

Les expériences principales actuellement en service en astronomie gamma sont le satellite Fermi-Large Area Telescope (LAT) et les expériences au sol tel que H.E.S.S., VERITAS et MAGIC (voir Figure 0.2). La génération actuelle des détecteurs a ouvert une nouvelle fenêtre pour étudier l'émission gamma dans l'Univers. En particulier, la génération actuelle des télescopes Cherenkov a amélioré la compréhension du ciel à haute énergie. Pour le travail présenté dans ce manuscrit de thèse, les données de Fermi-LAT et de l'expérience H.E.S.S. sont utilisées. Le satellite Fermi-LAT observe le ciel entier toutes les trois heures dans la gamme d'énergie allant de 30 MeV à plus de 500 GeV depuis juin 2008 et est décrit dans la première partie du Chapitre 2. L'expérience H.E.S.S., située dans l'hémisphère sud en Namibie, détecte quant à elle les rayons gamma de très haute énergie de quelques dizaines de GeV à

des centaines de TeV depuis 2003. L'expérience H.E.S.S. est décrite plus en détails dans le Chapitre 3 de ce manuscrit. La combinaison des données des deux expériences couvre plus de cinq ordres de grandeur en énergie et aide à étudier l'émission des différentes sources astrophysique.

La surveillance des sources de très haute énergie indique une physique diversifiée se déroulant dans différentes parties du ciel. Afin d'étudier la forme la plus énergétique de radiation et les phénomènes les plus violents qui se déroulent dans l'Univers, l'analyse des sources individuelles est importante. Les BL Lacs, un type de galaxies actives, constituent la classe de sources extragalactiques la plus abondante détectée dans les énergies du GeV au TeV, tandis que le nébuleuses de vents de Pulsar constituent la classe la plus peuplée dans le plan galactique. Ces deux types de sources ont des émissions variables de rayons gamma.

Les Blazars constituent la grande majorité des sources détectées en rayons gamma. Les observations multi-longueurs d'onde des blazars montrent qu'ils sont variables dans toute le spectre électromagnétique. Les observations révèlent que leur émission est caractérisée par des événements de haute luminosité avec une variation rapide de flux qui ont lieu dans de petites régions d'émission. Les variations de flux qu'ils subissent ont un comportement différent à haute énergie, offrant une nouvelle opportunité d'étudier et de caractériser l'émission gamma de ces sources. Une partie du travail présenté dans ce manuscript est consacrée à l'étude de l'émission d'une source de cette classe; le blazar B2 1215 + 30 qui représente un cas intéressant pour l'étude de l'émission de haute énergie. Cette étude tire partie des données publiques obtenues avec le satellite Fermi-LAT. Une grande variation de flux, détectée par Fermi-LAT en février 2014, est simultanément accompagnée par une éruption très lumineuse observée au TeV et observée par l'expérience VERITAS (Very Energetic Radiation Imaging Telescope Array System). VERITAS est un réseau de quatre télescopes Cherenkov situé à l'observatoire Fred Lawrence Whipple dans le sud de l'Arizona, sensible aux rayons gamma entre 0,1 et 30 TeV. En collaboration avec l'expérience VERITAS, la variabilité du flux en rayons gamma a été utilisée pour établir des contraintes sur la taille de la région d'émission et sur le facteur Doppler des jets relativistes. Les observations multi-longueurs d'onde prises quasi simultanément au cours de l'épisode d'observation 2014 ont été utilisées pour modéliser et comprendre l'émission de haute énergie. Deux scénarios ont été considérés pour expliquer l'émission du B2 1215 + 30: la partie la plus élevée de la distribution d'énergie spectrale peut être expliquée par les modèles Compton synchrotron ou Compton externe. Dans le scénario "Synchrotron Self Compton", le rapport entre les luminosités synchrotron et inverse-Compton a été utilisé pour estimer le champ magnétique.

Les observations à long terme avec le Fermi-LAT ont ouvert une nouvelle fenêtre pour étudier et surveiller l'émission gamma des objets du ciel à long terme. La variabilité du blazar B2 1215+30, en utilisant près de neuf ans de données de Fermi-LAT de 100 MeV jusqu'à 500 GeV, a permis de détecter plusieurs éruption. Cette analyse a montré d'autres éruptions de flux au GeV au cours desquelles le flux a atteint des valeurs similaires à celles du sursaut spectaculaire de février 2014. Trois éruptions majeures, où le flux moyen a été multiplié par 16, ont été mises

en évidence. Les études de la variabilité à long terme montrent que le flux moyen annuel augmente linéairement avec le temps, de façon corrélée avec un durcissement de l'indice spectral. L'étude de la variabilité du flux indique un comportement quasi périodique avec une période de 1083 ± 32 jours. Les interprétations possibles peuvent être liées à un processus quasipériodique au sein du jet relativiste. Ce comportement peut également être lié à des effets géométriques. C'est une direction intéressante pour les observations futures, et beaucoup plus longues, de galaxies actives. Le travail sur B2 1215+30 est présenté au Chapitre 4.

Dans une dernière partie, la variabilité du flux au TeV et le spectre de l'un des objets les plus étudiés, la Nébuleuse du Crabe (Figure 0.3), est étudiée avec dix ans d'observation de l'expérience H.E.S.S. Cette source, la première détectée à très haute énergie dès 1989, est une nébuleuse à vent de pulsar dans le plan galactique, à une distance de presque 2 kpc de la Terre.

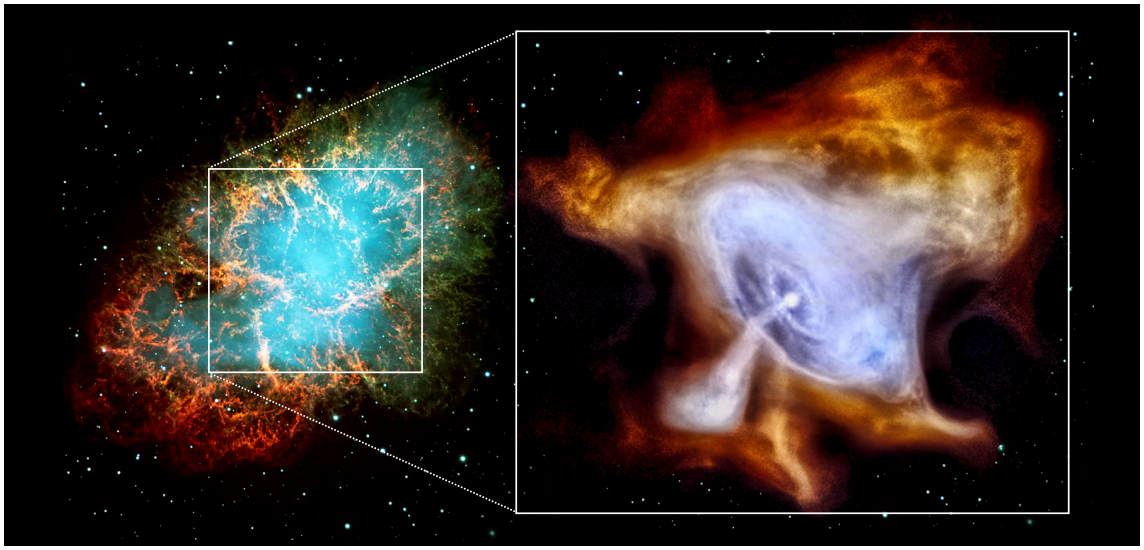

Figure 0.3: Le système de nébuleuse du crabe et le Crabe pulsar zoomé.

Aux très hautes énergies, la nébuleuse du crabe sert comme source d'étalonnage pour de nombreuses expériences d'imagerie Cherenkov atmosphérique car elle est très brillante et aucune variation de son flux n'est jusqu'à présent prédite par de simples modèles de "Synchrotron Self Compton", traditionnellement utilisés pour expliquer l'émission aux très hautes énergies. De plus aucune variation de flux n'a été observée par les IACT jusqu'à présent. A contrario, les expériences spatiales, telles que AGILE et Fermi-LAT ont rapporté la détection de variations de flux de la composante synchrotron aux énergies du GeV. L'expérience H.E.S.S. fournit les meilleures opportunités pour des études à des énergies supérieures à 10 TeV en raison de la grande surface d'observation. De plus, avec la mise en service de H.E.S.S. II, s'ouvre une nouvelle possibilité d'exploiter d'une part, la partie basse de l'énergie de l'émission gamma et d'autre part l'augmentation de la statistique de H.E.S.S. permettant d'étendre le spectre à des énergies encore plus élevées.

Le spectre de la Nébuleuse du Crabe est mesuré par H.E.S.S. pour des énergies comprises entre 280 GeV et 62 TeV. Ceci est la première mesure qui s'étend jusqu'à

des énergies aussi élevées. Lesx variations de flux au GeV ont motivé la recherche de variations de flux au TeV en utilisant les données de l'expérience H.E.S.S. La position de la nébuleuse de crabe dans l'hémisphère nord et la localisation de H.E.S.S. en Namibie rendent cette approche complexe en raison des importantes erreurs systématiques introduites par des conditions d'observation non optimales. Le travail sur la nébuleuse du crabe a montré que la prise en compte de la transparence de l'atmosphère pour l'étude de l'évolution du flux avec le temps résulte en une réduction des effets systématiques. En prenant compte de cet effet, aucune variation de flux supérieure à 20 % n'a été observée à des énergies supérieures au TeV dans toutes les données de H.E.S.S. I. Une autre éruption au GeV signalée par le Fermi-LAT en octobre 2016 par télégramme astronomique, a été étudiée avec H.E.S.S. II. Cette analyse a montré que l'éruption au GeV a duré pendant un mois, L'impact sur le flux mesuré par H.E.S.S. a un excès de variance de 15 %. Cela peut être comparé à l'incertitude systématique de 20 % considérée en général par H.E.S.S. Les résultats de l'étude avec H.E.S.S. I sont présentés au Chapitre 5, et ceux de H.E.S.S. II au Chapitre 6 dans ce manuscrit de thèse.

Acknowledgements

This thesis was financially supported by the University of Paris-Sud and PHENIICS doctoral school. Without their support this work would not have been possible.

I would like to start by expressing my gratitude to the dissertation committee members: C. Van Eldik, O. Blanch, S. Klepser, M. Langer, R. Mukherjee, J-P. Lenain for the comments and suggestions. I would like to particularly thank the two rapporteurs, Christopher and Oscar who went deeply through the thesis and provided useful comments to improve the manuscript. And thanks Christopher for the good humor before starting the presentation, that helped me to keep calm.

Most of all, I am thankful to Professor Mathieu de Naurois for the very fruitful discussions, scientific advices and the support during the PhD. Considering his busy schedule, I would like to express my gratitude for finding the time to read the thesis and provide very helpful comments and suggestions.

Being part of the H.E.S.S. collaboration was a great opportunity. My sincere gratitude goes to the Crab Nebula task members, the "Crabbers", as Joachim referred to us, and I thank them all for the comments, suggestions and discussions. Are to be mentioned the traditional H. E. S. S. collaboration meetings and I would like to thank my colleagues: Daniel, Matteo, Jill, Sabrina, Rachel, Eva, Carlo, Monica, Mathieu, Raphael et al. for the times spent together and the fun. I mention also the shift in Namibia and in particular I would like to thank Frikie for the hospitality.

Thanks to the members of the group who were very helpful with comments and advices during presentations for conferences and meetings. Thanks to Denis, Philippe (B & G), Prof. B. Degrange and Prof. G. Fontaine for the scientific discussions and the good moments during the traditional lunches all together. A big thanks goes to my colleagues Sami and Christian for the very helpful scientific discussions, coffee breaks and also for the funny jokes in the office.

I would like to extend my sincere thanks to Prof. L. Dobrzynski for his unconditional help and support. He was my second family, always supporting and advising me in difficult and stressful situations during the PhD.

Thanks also to Prof. Mimoza Hafizi for her support since I was a student in Tirana.

To my colleagues from the laboratory: Chiara, Marina, Luca, Philipp, Kostia, Toni, André, Iurii and Simon for the nice times spent together in the lab and outside. I especially thank Marie-Thérèse and Sylvaine for the help with French paperwork.

To my close friends during my studies in France: Lara, Julia, Jeta and Bianka. In particular I would like to thank Jonas for reading, redacting and providing useful comments to improve the manuscript and for the support while writing the thesis.

During this journey a very big support come from my family. To my mom, who was always supporting me during my studies: -*"Thanks for all the patience mom!"*. To my brothers, Joti, Olti, Luciano and Donaldi. They are a blessing in my life!

To my dad and my brother Besi, my two angels who were physically missing during the PhD journey but they are always in my heart. I hope they are proud up there.

Jam shumë mirënjohëse për mbështetjen e pakushtëzuar që kam marrë gjithmonë nga ju. Faleminderit ty mami që bashkë me babin keni sakrifikuar shumë për shkollimin tim edhe të vëllezërve. Faleminderit edhe ju vellezerit e mi të dashur.
Ju dua shumë!

Paris, 16th of November 2017

Contents

1 High-Energy Gamma-Ray Astronomy **1**
1.1 Introduction to Cosmic Gamma Rays . . . 2
1.1.1 One Century of Cosmic Rays . . . 2
1.1.2 The Birth of Gamma-Ray Astronomy . . . 3
1.2 Acceleration Mechanisms . . . 6
1.2.1 Diffusive Shock Acceleration . . . 6
1.2.2 Sites of Gamma-Ray Emission . . . 8
1.3 Origin of Cosmic Gamma Rays . . . 8
1.3.1 Hadronic Origin of Gamma-Rays . . . 8
1.3.2 Leptonic Origin of Gamma-Rays . . . 10
1.3.2.1 Bremsstrahlung . . . 10
1.3.2.2 Synchrotron Radiation . . . 10
1.3.2.3 Inverse Compton Scattering . . . 11
1.4 High Energy Gamma-Ray Sources . . . 13
1.4.1 Supernova Remnants . . . 14
1.4.2 Pulsars and Pulsar Wind Nebulae . . . 15
1.4.3 Active Galactic Nuclei . . . 16
1.4.4 Other Sources . . . 18
1.5 Summary . . . 19

2 Detectors for High-Energy Gamma-Ray Astronomy **21**
2.1 Space Detectors . . . 22
2.2 The Fermi Large Area Telescope . . . 23
2.2.1 Principles of the Large Area Telescope . . . 24
2.2.2 The Anticoincidence Detector . . . 25
2.2.3 The Tracker . . . 26
2.2.4 The calorimeter . . . 26
2.2.5 Data-Processing Pipeline . . . 26
2.2.6 Analysis Method . . . 27
2.3 Ground-based Detectors . . . 30
2.4 Extensive Air Showers . . . 31
2.4.1 Electromagnetic Showers . . . 31
2.4.2 Hadronic Showers . . . 33
2.4.3 Cherenkov radiation . . . 33
2.5 Imaging Atmospheric Cherenkov Telescopes . . . 35
2.5.1 Currently Operating IACTs . . . 37
2.5.1.1 MAGIC experiment . . . 37
2.5.1.2 VERITAS experiment . . . 38
2.5.1.3 H. E. S. S. experiment . . . 38

2.5.2 Future Telescope Arrays . . . 38
2.6 Summary and Conclusions . . . 39

3 The H.E.S.S. Experiment 41
3.1 H.E.S.S. Phase-I . . . 42
3.2 H.E.S.S. Phase-II . . . 43
3.3 Data Acquisition . . . 44
3.4 Calibration . . . 44
3.4.1 Camera calibration . . . 45
3.4.2 Gain Calibration . . . 45
3.4.3 Flat-Field Coefficients . . . 45
3.4.4 Pedestal Calibration . . . 46
3.4.5 Pointing Correction . . . 46
3.4.6 Optical efficiency . . . 46
3.4.7 Atmospheric Monitoring . . . 47
3.5 Reconstruction Techniques . . . 47
3.5.1 Hillas Reconstruction . . . 48
3.5.2 Model Reconstruction . . . 48
3.5.3 Shower Image Model . . . 49
3.5.4 Model Variables . . . 52
3.6 Model Analysis . . . 52
3.6.1 H. E. S. S. I . . . 53
3.6.2 H. E. S. S. II . . . 54
3.6.3 Source detection and background estimation . . . 55
3.6.4 Spectrum . . . 56
3.6.5 Lightcurve . . . 58
3.7 Multivariate Analysis . . . 59
3.7.1 Boosted Decision Trees . . . 59
3.7.1.1 BDT Settings . . . 60
3.7.2 Monoscopic reconstruction . . . 61
3.7.3 Discussion . . . 64
3.8 Summary . . . 65

4 Characterizing the Gamma-Ray Variability of B2 1215+30 67
4.1 Introduction . . . 68
4.2 VERITAS Observations . . . 69
4.3 *Fermi*-LAT Observations . . . 70
4.3.1 Event Selection . . . 70
4.3.2 Background Modeling and Source Detection . . . 71
4.3.3 Spectrum . . . 72
4.3.4 Lightcurve . . . 73
4.4 Multiwavelength observations . . . 74
4.4.1 X-ray Observations . . . 74
4.4.2 UV and Optical Observations . . . 76
4.4.3 Spectral Energy Distribution . . . 76
4.4.4 Size of the Emission Region . . . 76

4.5 Long-Term Variability with *Fermi*-LAT . . . 79
4.5.1 Recent flaring activities . . . 83
4.5.2 Fractional variability . . . 83
4.6 Periodic Behaviour . . . 84
4.7 Summary and Discussion . . . 87

5 Crab Nebula with a decade of H. E. S. S. I observations 91
5.1 Introduction . . . 93
5.2 Data Set . . . 95
5.2.1 Data Quality Selection . . . 96
5.3 Analysis Results . . . 98
5.4 Differential Energy Spectrum . . . 99
5.5 Long-Term Variability Studies . . . 103
5.6 Atmospheric Transparency Effect . . . 106
5.6.1 Correcting the Flux for Atmospheric Transparency . . . 107
5.6.2 Systematic Flux Uncertainty . . . 111
5.6.3 Season Dependence on Flux Measurements . . . 112
5.7 Discussion and Conclusions . . . 113

6 Crab Nebula with H. E. S. S. Phase-II Observations 115
6.1 Introduction . . . 116
6.2 Data Set . . . 116
6.3 Data Analysis . . . 117
6.4 Energy Spectrum with H. E. S. S. II . . . 119
6.5 Spectral Energy Distribution . . . 122
6.6 Variability Studies . . . 123
6.7 The Crab Nebula 2016 GeV Flare . . . 125
6.7.1 H. E. S. S. II Observations . . . 125
6.7.2 Fermi-LAT Analysis . . . 126
6.7.2.1 Background Model File . . . 127
6.7.2.2 Spectral Analysis . . . 127
6.7.2.3 Temporal flux variations . . . 128
6.7.3 H. E. S. S.-*Fermi* lightcurves . . . 128
6.8 Summary and Discussion . . . 130

7 Conclusions and Outlook 133

List of Tables 140

List of Figures 149

Acronyms List 151

Bibliography 153

Appendix A 165

Appendix B 167

Chapter 1

High-Energy Gamma-Ray Astronomy

Astrophysical high-energy gamma rays are the messengers of the non-thermal Universe. They are secondary products of charged particle acceleration, a phenomenon taking place all-over the Universe. Particularly, they carry important information on the most powerful particle acceleration mechanisms in extreme environments.

High-energy particles from outer space hit the Earth's atmosphere continuously. The up-to-date cosmic-ray energy spectrum is measured from below 10^9 eV up to 10^{20} eV. Measurements of cosmic rays over twelve orders of magnitude in energy reveal that the majority of cosmic rays are high-energy protons and nuclei. Their emission sites are difficult to locate as they are deflected by turbulent magnetic fields in the Galaxy and arrive isotropically upon the atmosphere.

Presently, hunting for cosmic ray sites and their acceleration mechanisms relies on gamma rays, which preserve their direction information. High-energy gamma rays are produced in the most extreme environments of the Universe from the interaction of energetic charged particles with radiation and magnetic fields and/or from hadronic interactions. The creation of gamma rays is taking place by either leptonic or hadronic processes, while the full acceleration scenario of the charged particles is still a matter of debate. Identifying the high-energy sources which accelerate cosmic rays up to PeV range is important if we wish to solve the cosmic ray origin problem. Hence, high-energy gamma rays offer a unique possibility to understand and complete the "puzzle" of the origin and acceleration mechanisms of cosmic rays.

This chapter gives an introduction on the field of gamma-ray astronomy. A short historical overview on cosmic rays and on the early days of gamma-ray astronomy is given in Section 1.1. The possible mechanisms responsible for the production of high-energy gamma rays and acceleration of charged particles in astrophysical environments are described in Section 1.2 and in Section 1.3. A brief introduction on the astrophysical sources established as gamma-ray emitters is given in Section 1.4 and a short summary is given in Section 1.5.

1.1 Introduction to Cosmic Gamma Rays

1.1.1 One Century of Cosmic Rays

In the early years of the 20th century, Victor Hess used a sequence of ten balloon ascents to measure the level of ionizing radiation at different altitudes (Figure 1.1a). He finalized his study in 1912, using the measurements of three electrometers in a free balloon flight to an altitude of 5300 meters. About the results of his measurements, Hess wrote (from a translation by [3]):

"Immediately above ground the total radiation decreases a little...at altitudes of 1000 to 2000 m there occur again a noticeable growth of penetrating radiation. The increase reaches, at altitudes of 3000 to 4000 m, already 50 % of the total radiation observed on the ground. At 4000 to 5200 m the radiation is stronger by (producing) 15 to 18 (more) ions than on the ground."

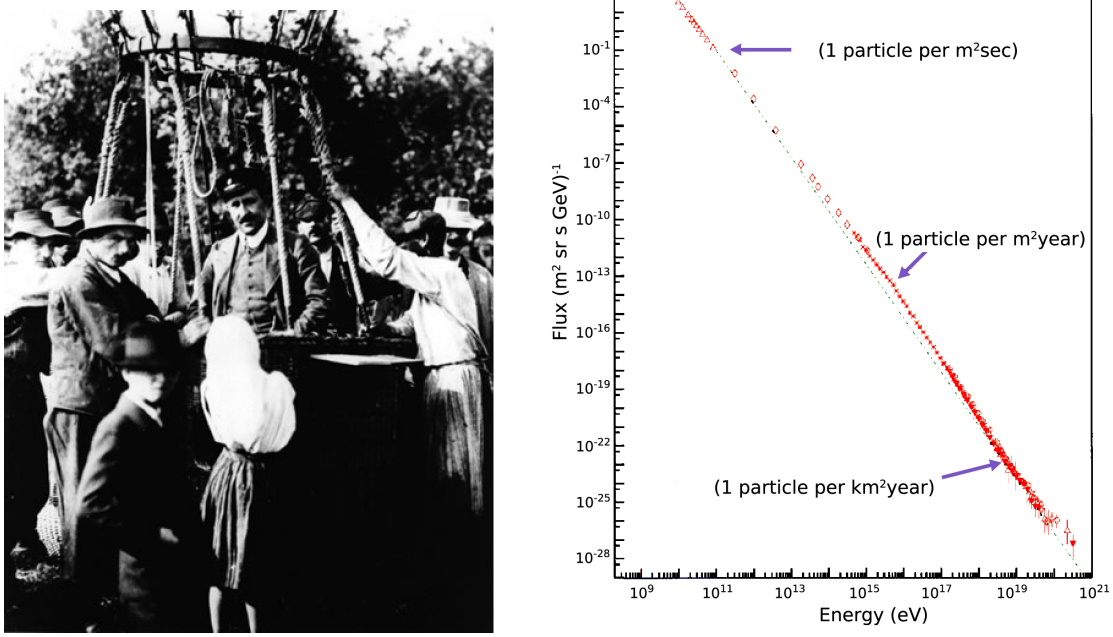

(a) (b)

Figure 1.1: (a) Victor Hess in one of his balloon accents. Picture taken before take-off of one of his famous flights that took place between 1911 and 1913. Image courtesy [1]. (b) Present-day spectrum of cosmic rays spanning over twelve orders of magnitude in energy as measured from several independent experiments. The majority of the spectrum follows a power-law over twelve orders of magnitude in energy with a spectral index of 2.7. The two features of the cosmic ray spectrum, known as the "knee" and "ankle" are seen around 10^{15} eV and 10^{17} eV respectively. Image courtesy [2].

In the conclusions of the study, Hess wrote:

"The results of my observation are best explained by the assumption that a ***radiation of very great penetrating power enters our atmosphere from above****."*

These results were confirmed later and honored with the Nobel Prize of Physics in 1936 for the discovery of cosmic rays [4]. The cosmic radiation, or as Hess referred to it, the *"radiation of very great penetrating power"* has become a very powerful research tool leading to important new results, as well as new problems to understand and solve about matter composition in the Universe.

Ever since its discovery, physicists have been trying to understand the origin of this radiation. In the 105 years since, many experimental and theoretical contributions have broadened the knowledge on the cosmic-ray spectrum and its composition. Observations from numerous successive experiments reveal that cosmic rays are mainly high energy protons or nuclei whose flux follows a power-law over more than ten orders of magnitude in energy (Figure 1.1b). The overall measured cosmic ray spectrum exhibits some features, connected to a spectral change or "break" of the spectrum. The first feature, commonly referred as the "knee" is seen around energies of 10^{15} eV, whereas a second break occurs around 10^{17} eV, which is known as the "ankle" [5]. There is growing evidence for another spectral change, a "second knee" between the knee and the ankle which is still under investigation [6].

In the present picture, various sources are considered as possible candidates for powering different ranges of the measured cosmic ray spectrum. The acceleration of cosmic rays from the lowest energies up to the knee is attributed to solar flares and to galactic sources. Beyond the knee, extragalactic sources are potential candidates for cosmic ray acceleration. Changes in the spectral index of the cosmic ray spectrum are commonly explained by a change of the acceleration mechanism. The spectral index changes around the knee and the ankle are believed to correspond to the transition from galactic to extragalactic origin. The exact explanation of how and where this transition takes place is still not fully understood. The measured spectrum of the cosmic rays has reached levels that were unexpected in the beginning of the field: the Universe is a TeVatron accelerator. It is remarkable that up to date, state-of-the-art experiments have not found yet a natural end of the cosmic ray spectrum. An ultimate theoretical limit on the propagation of proton cosmic rays is expected by Greisen-Zatsepin-Kuzmin at around 5×10^{19} eV [7].

Beside all the efforts and progress, the fundamental question of the origin of cosmic rays remains not fully solved and is still matter of debate. Gamma-ray astronomy offers an opportunity to study the high-energy sky using observations of gamma rays from space and ground. The early days of the field and some remarkable years are given in the following.

1.1.2 The Birth of Gamma-Ray Astronomy

In 1912, cosmic rays introduced for the first time the non-thermal processes taking place in the Universe and raised a series of questions about their origin and prop-

agation. Right after their discovery, supernova remnants were proposed as possible candidates of galactic cosmic ray emission [8]. The discovery of the π-meson in 1947, and the π^0 decay into two photons indicated that charged cosmic rays can produce gamma rays. During these years, particle cascades and high-energy nuclear reactions were seen in nuclear emulsions (as seen for example in extensive air showers) [9]. Therefore, possible sources of cosmic rays, like supernova remnants and regions of cosmic ray confinement were expected to be visible and detectable at gamma-ray energies [10]. Additionally, it was expected that the sites of nucleosynthesis would reveal themselves in the gamma-ray energy range [11]. It was soon understood that detecting gamma rays can help to trace sources of cosmic rays. Accelerated particles, undergo interactions and energy losses via different mechanisms producing gamma rays as they travel through the astrophysical source and beyond. Therefore, gamma rays are expected from different environments containing populations of charged particles. Unlike the charged cosmic rays, gamma rays that arise indirectly from nuclear or very-high-energy processes preserve source information as they move in straight lines. On the other hand, charged particles lose this information on their way to the Earth, as they are deflected by the Universe's turbulent magnetic fields, except possibly at the highest energies [12].

In September 1952 a simple experiment carried out by Galbraith and Jelley gave hope to start a new field of astronomy: gamma-ray astronomy from ground [13]. Their experiment allowed the first observation of the Cherenkov light emitted from cosmic rays air showers in the atmosphere. They measured the counts from the oscilloscope using a 25 cm mirror and a 5 cm phototube arranged in a rubbish bin painted black. It took decades to establish this technique and the first source emitting in gamma rays was detected in 1989 [14]. In this remarkable year, the Whipple air-Cherenkov telescope in the US detected the Crab Nebula at TeV gamma rays, as it was originally suggested by C. Giuseppe at the 1959 ICRC in Moscow [15].

In the meantime, the detection of gamma rays from space satellites had already made quite some progress. As Earth's atmosphere is opaque to gamma rays, satellites above the atmosphere are needed to directly detect gamma rays, e.g. via Compton scattering or electron[1] pair creation in the detector. Gamma-ray astronomy from space was presented by Morrison in 1957, predicting gamma-ray fluxes from various sources [16]. A first milestone in gamma-ray astronomy from space was reached in 1961 with the Explorer 11, the first gamma-ray satellite on orbit that picked up a few more than 100 cosmic gamma-ray photons [17, 18]. Another remarkable year was 2008 with the launch of the *Fermi*-**L**arge **A**rea **T**elescope (LAT), which scans the entire sky every three hours and has brought new, unexpected discoveries.

The gamma rays cover a large dynamic range of the electromagnetic spectrum and the study of the sky in this energy range requires more than one type of detection technique (see Chapter 2). Nowadays, the study of the sky in gamma rays is covered by space and ground based instruments. Space detectors played an important role in the beginning of the field and they are suitable for observations in the energy range from 100 MeV to 100 GeV. As the flux at higher energies is low and launching large collection area detectors to space is challenging, Cherenkov telescopes on the ground

[1] hereafter the electron notation is used for electron/positron

are more suitable for high-energies due to their large collection areas associated with the large size of the Cherenkov light pool on the ground.

The field of gamma-ray astronomy relies strongly on observations and detectors with good sensitivity, angular resolution, and a large field of view. The highlights of each decade since the early days of the field are given in the following:

- **1950s** - Also referred as the decade of predictions of gamma-ray astronomy. The main goals of gamma-ray astronomy were defined: to establish the sources of cosmic rays and the seats of nucleosynthesis.
- **1960s** - The detectors of this decade were background dominated and poor in sensitivity e.g. **O**rbiting **S**olar **O**bservatory OSO-3 [19].
- **1970s** - The space detector OSO-3 produced for the first time a Milky Way map in gamma rays [19]. Other successful observations were done during this decade by SAS 2 [20], Cos-B [21], SMM and others [22].
- **1980s** - Preparation decade of an all-sky view satellite named Compton Gamma-Ray Observatory. The Whipple Observatory detected for the first time the Crab Nebula from the ground [23].
- **1990s** - The **E**nergetic **G**amma **R**ay **E**xperiment **T**elescope (EGRET) on board of the Compton Gamma-Ray Observatory produced the first all-sky map in gamma rays, with energies of 20 MeV to 30 GeV [24].
- **2000s** - Design and operation of other space and ground-based instruments e.g. the *Fermi*-LAT satellite as well as the MAGIC and H. E. S. S. experiments.
- **2010s** - The current decade counts the largest operating ground gamma-ray instruments ever. The presently operating imaging atmospheric Cherenkov telescopes are H. E. S. S., MAGIC, VERITAS and FACT.

Decade	1970s	1980s	1990s	2000s	2010s
Space-based	OSO-3	SAS II	EGRET	*Fermi*-LAT	
Ground-based		Whipple	CAT CELESTE	STACEE MAGIC VERITAS H. E. S. S.	FACT HAWC

Table 1.1: Main historical instruments used in high-energy gamma-ray astronomy. Details about these instruments can be found in the reference list given here and references therein [19, 20, 25, 26, 27, 28, 29, 30, 31, 32, 33, 34].

The field of gamma-ray astronomy is rapidly progressing. The pioneering efforts and data from space and ground-based detectors have expanded the knowledge on the high-energy sky. No matter the efforts and improvements in the field, the full scenario of particle acceleration mechanisms taking place in the Universe is however still incomplete. Possible acceleration mechanisms responsible for accelerating particles to such very-high-energies and the possible cosmic-ray acceleration sites are given next.

1.2 Acceleration Mechanisms

The number of detected astrophysical sources emitting at very-high-energies has increased significantly in the last decade from the observations carried out by the gamma-ray experiments. These sources provide non-thermal spectra of very-high-energy gamma-rays, which often can be approximated by a power-law:

$$\frac{\mathrm{d}N}{\mathrm{d}E} \propto \mathrm{E}^{-\Gamma}, \tag{1.1}$$

with a spectral index Γ typically between 2 and 3. The cosmic ray spectrum, measured over twelve orders of magnitude in energy, has a spectral index of the same order. Therefore, the Universe's most extreme particle acceleration scenarios must account for both a gamma-ray and cosmic ray spectrum of the form given in Equation 1.1 and for the extension of cosmic ray spectrum up to energies 10^{20} eV.

1.2.1 Diffusive Shock Acceleration

The first particle acceleration mechanism was proposed by E. Fermi in 1949 [35]. The first order Fermi acceleration or *diffusive shock acceleration* describes the acceleration of charged particles in the vicinity of strong shock waves. In his model, Fermi used stochastic means to explain how particles colliding with clouds in the interstellar medium could be accelerated to high energies. Supernova remnants were considered as cosmic ray acceleration candidates right after their discovery in the 1930s. In the late 1970s, many authors, such as Bell (1978), adapted the Fermi acceleration to the supernova shocks (for a review see [36] [37]).

Suppose a strong (supersonic) shock wave of relativistic particles propagating through a diffuse plasma medium at velocity U. Non-thermal particles are moving at relativistic velocities, and the shock is moving non-relativistically [38]. The plasma in front of the shock is referred to as the unshocked plasma (or upstream medium) and the plasma behind the shock as the shocked plasma (or downstream medium).

Let us first consider the flow of the interstellar gas in the vicinity of the shock front. The upstream gas enters the shock front at a velocity $v_1 = U$ and leaves it at a velocity v_2. Applying the continuity equation and asking for mass conservation, the densities and velocities of the gas are related by $\rho_1 v_1 = \rho_2 v_2$. In the case of strong shocks in a fully ionized or monoatomic gas, $\rho_2/\rho_1 = (\gamma+1)/(\gamma-1)$, where $\gamma = 5/3$ is ratio of the specific heat capacities of the gas. Hence, the gas leaves the downstream at a velocity $v_2 = 1/4U$ (as shown in Figure 1.2 left).

Secondly, let us consider high energy particles in the rest frame of the upstream medium (Figure 1.2 middle). The shock advances through the medium at velocity U whereas the gas behind it travels at $3/4U$. Particles crossing the shock will get scattered by the turbulences behind the shock, become isotropic with the downstream and gain an increase of ΔE in energy.

Now, let us consider the process in the rest frame of the downstream medium. The particles are diffusing from downstream to uptream medium, encounter again gas

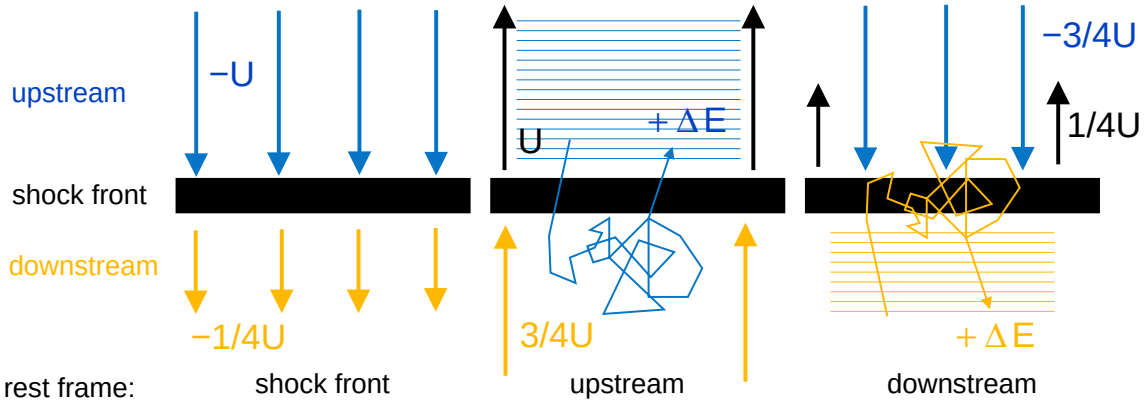

Figure 1.2: Schematic of Fermi acceleration in a strong shock wave. The dynamics of high-energy particles in the rest frames of the shock front, the upstream and downstream medium. *(Left)*: Rest frame of the shock front; the upstream gas is moving with velocity $v_1 = U$ and the shocked plasma with velocity $v_2 = 3/4U$. *(Middle)*: Rest frame of the upstream medium; particles from downstream are moving with velocity of $3/4U$. *(Right)*: Rest frame of the downstream medium; particles from the upstream are advancing with velocity $3/4U$. Everytime particles cross the shock, there is a gain of energy by ΔE (shown in blue and orange lines). Image courtesy [39].

moving towards the shock front with velocity $3/4U$. Hence, the particles crossing the shock from downstream to upstream will undergo the same increase of ΔE in energy, as when they cross in the opposite way. Regardless of the way the particles enter the shock front, there will be always an increase of ΔE in energy. In the case of a *shock front*, the energy is transferred to the particles via head-on collisions.

It can be shown that the average energy gain after crossing the shock is $2V/3c$. Hence, the total energy after a round trip across the shock and back again is:

$$\left\langle \frac{\Delta E}{E} \right\rangle = \frac{4}{3}\frac{V}{c} \tag{1.2}$$

with $V = 2/3U$, the relative velocity of the upstream and downstream medium. If the particle energy increases by a factor of β after a crossing, the new energy of the particle is $E = \beta E_0$ and the probability that the particle remains in the shock after one collision is P. After k collisions in the acceleration region, there are $N = N_0 P^k$ particles with energies $E = E_0 \beta^k$ (for more details see [40]).

From this, the number of particles is $N(\geq E) = N_0 (E/E_0)^{\ln P/\ln \beta}$. Since $\beta = 1/P$, this implies $\beta > 1$ (energy gain). The spectral index depends on the compression index in the strong shock since $\ln P/\ln \beta = -1$. The energy spectrum of the high energy particles is found to be of the following form:

$$\frac{\mathrm{d}N}{\mathrm{d}E} \propto E^{-2}. \tag{1.3}$$

What is necessary to obtain a spectral index of ~ 2, is that the acceleration happens in the vicinity of a strong shock. There is evidence of strong shocks in astrophysical sources such as supernova remnants, active galaxies and the extended components of extragalactic radio sources.

1.2.2 Sites of Gamma-Ray Emission

Several sources are considered as possible sites of cosmic ray particle accelerators in the Universe. A limit on the maximum energy a particle accelerator can achieve can be set from its size and typical magnetic field values [41]. The gyroradius r_g is the radius of the motion of a particle in a uniform magnetic field B. The condition to contain the particles in a source of size R so that they can be accelerated is that the gyroradius r_g must be smaller than R. Thus, the maximum energy that an accelerator can achieve is estimated to be:

$$E_{\max} = Ze\beta cBR, \tag{1.4}$$

where Ze is the electric charge of the particle and βc its velocity. Accordingly, the maximum energy is proportional to the magnetic field and size of the source and to the charge of the cosmic ray particle. The possible cosmic ray emission sites as function of the magnetic field and of the average size are shown in Figure 1.3. The diagonal lines correspond to the minimum B and L required for the acceleration of protons of 100 EeV (10^{20} eV) and 1 ZeV (10^{21} eV).

It is remarkable that cosmic ray acceleration can take place in different astrophysical sources at very different sizes, from neutron stars up to galaxy clusters.

1.3 Origin of Cosmic Gamma Rays

Very-high-energy gamma-rays are product of the interaction of charged particles with ambient matter or electromagnetic fields, e.g. synchrotron radiation or inverse Compton scattering. The charged particles themselves have firstly been accelerated to ultra-relativistic energies by the electromagnetic fields of the very-high-energy emitting sources or via diffusive shock acceleration processes. The emission processes responsible for producing energetic gamma rays are classified as leptonic and hadronic origin, based on the type of charged particles involved. Gamma rays from hadronic interactions are of great interest since they can be used as a bridge to discover the origin of cosmic rays. A brief description of the hadronic and leptonic processes resulting in the production of very-high-energy gamma-rays is given in the following.

1.3.1 Hadronic Origin of Gamma-Rays

Inelastic proton-proton (pp) and proton-nuclei (pN) collisions are the two main processes responsible for producing gamma rays from hadronic interactions. For

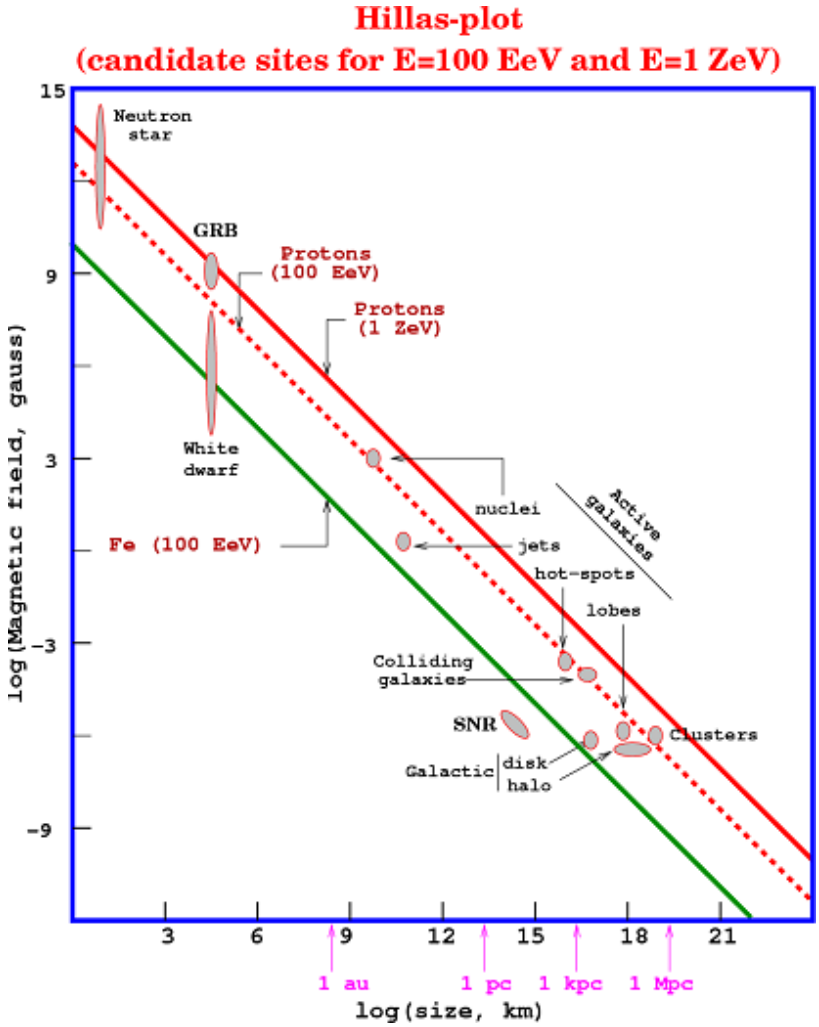

Figure 1.3: Hillas plot showing possible sources of proton acceleration for E = 100 EeV and E=1 ZeV. The linear size R of different sources is plotted versus the magnetic field B in order to accelerate particles up to $E \sim 10^{20}\,eV$. The diagonal line correspond to the maximum reachable energy by a population of sources. Image courtesy [41].

inelastic pp interactions:

$$\mathrm{p} + \mathrm{p} \rightarrow \begin{cases} \mathrm{p} + \mathrm{p} + \pi^0 \\ \mathrm{p} + \mathrm{n} + \pi^+ \\ \mathrm{p} + \mathrm{p} + \pi^+ + \pi^- \end{cases} \tag{1.5}$$

and for pN interactions:

$$\mathrm{N} + \mathrm{p} \rightarrow \mathrm{X} + \pi^0. \tag{1.6}$$

The pN interactions can also produce charged muons.

The neutral pions with a short lifetime of 8.4×10^{-17} s [42], decay predominantly into two photons:

$$\pi^0 \rightarrow \gamma + \gamma. \tag{1.7}$$

Charged pions decay into muons and neutrinos:

$$\pi^+ \rightarrow \mu^+ + \nu_\mu \rightarrow e^+ + \bar{\nu}_\mu + \nu_e + \bar{\nu}_\mu, \tag{1.8}$$

$$\pi^- \rightarrow \mu^- + \bar{\nu}_\mu \rightarrow e^- + \nu_\mu + \bar{\nu}_e + \nu_\mu. \tag{1.9}$$

The last equations show the connection between neutrino physics and gamma-ray astronomy [43]. The energy threshold for the production of pions π^0 from pp collisions is ≈ 280 MeV (for $m_\pi = 135\,\mathrm{MeV}$).

Regions of space filled with dense gas and ambient material with relativistic protons can produce highly energetic pions, which in turn produce very-high-energy gamma rays. Observations indicate that gamma rays from the Milky Way disk and supernova remnants are most likely produced in hadronic interactions. An interesting way to trace the acceleration of cosmic ray protons is the study of high-energy emission from young supernova remnants (see Section 1.4.1), as hadronic interactions are most probable to take place in their environment.

1.3.2 Leptonic Origin of Gamma-Rays

Electrons accelerated to high-energies radiate high-energy photons via synchrotron radiation or upscatter ambibient photons via inverse Compton scattering. These two, together with bremsstrahlung (to a lesser extent) are the main radiation processes at very-high-energy astrophysics. A brief description of them is given next.

1.3.2.1 Bremsstrahlung

Electrons traversing the electric field of a nucleus produce electromagnetic radiation. During this process, the electron transfers energy to the nucleus, is decelerated and emits radiation which is called "braking radiation", or bremsstrahlung. The electrons have an average energy loss rate $dE_e/dt \propto E_e$. The characteristic time for energy loss by bremsstrahlung for electrons with energy E_e, in an ambient with gas density n is:

$$t_{br} = \frac{E_e}{-\mathrm{d}E/\mathrm{d}t} \approx 4 \times 10^7 \left(\frac{n}{1\,\mathrm{cm}^{-3}}\right)^{-1} \mathrm{yr}. \tag{1.10}$$

Thus, bremsstrahlung losses do not modify the shape of the electron spectrum. The emission of the astrophysical sources at very-high-energies is dominated by the synchrotron or inverse Compton radiation.

1.3.2.2 Synchrotron Radiation

Synchrotron radiation is emitted when a charged relativistic particle spirals around strong magnetic fields. This synchrotron radiation of ultra-relativistic electrons is

responsible for the emission observed in many astrophysical sources. The average radiation rate loss of an electron by synchrotron radiation is given by:

$$-\left(\frac{\mathrm{d}E}{\mathrm{d}t}\right) = \frac{4}{3}\sigma_T c U_{\mathrm{mag}} \left(\frac{v}{c}\right)^2 \gamma_e^2, \tag{1.11}$$

where γ_e is the Lorentz factor of an electron moving at a speed v, $\sigma_T = \frac{8\pi}{3} r_e^{22}$ is the Thomson scattering cross-section and $U_{\mathrm{mag}} = B^2/2\mu_0{}^3$ is the energy density of the magnetic field. The lifetime of electrons losing their energy due to synchrotron emission is:

$$t_s = \frac{E_e}{-\mathrm{d}E/\mathrm{d}t} \approx 1.3 \times 10^{10} \left(\frac{E_e}{1\,\mathrm{GeV}}\right)^{-1} \left(\frac{B}{1 \cdot G}\right)^{-2} \mathrm{yr}. \tag{1.12}$$

Synchrotron radiation is likely the source of X-rays and low-energy gamma rays in the *Fermi*-LAT regime, but to explain very-high-energy radiation with it requires unrealistic energies and strong magnetic fields.

1.3.2.3 Inverse Compton Scattering

Inverse Compton scattering happens when high-energy electrons upscatter photons of the ambient radiation fields to very-high energies: $e + \gamma_{target} \rightarrow e + \gamma$, where γ_{target} are the target low-energy background photons and γ is the upscattered photon. Relativistic electrons can collide with target photons from the cosmic microwave background, infrared or optical stellar radiation, or even synchrotron photons and upscatter these photons up to GeV energies or even higher. The high-energy gamma rays created by inverse Compton scattering are the only purely leptonic processes of very-high-energy gamma rays. This can help to understand the emission from active galaxies, gamma-ray bursts and some supernovae. The unpolarized Klein-Nishina differential cross-section, obtained from quantum electrodynamics:

$$\frac{\mathrm{d}\sigma}{\mathrm{d}\Omega} = \frac{3}{16\pi}\sigma_T \left(\frac{\epsilon_f}{\epsilon_i}\right)^2 \left(\frac{\epsilon_f}{\epsilon_i} + \frac{\epsilon_i}{\epsilon_f} - \sin^2\theta\right) \tag{1.13}$$

The final photon energy in the electron rest frame is:

$$\epsilon_f = \frac{\epsilon_i}{1 + \frac{\epsilon_i}{m_e c^2}(1 - \cos\theta)} \tag{1.14}$$

After integrating over all angles in Equation 1.13, the total Klein-Nishina cross-section is:

$$\sigma_{IC} = \frac{3\sigma_T}{4x}\left[\frac{1+x}{x^3}\left(\frac{2x(1+x)}{1+2x} - \ln(1+2x)\right) + \frac{1}{2x} - \frac{1+3x}{(1+2x)^2}\right], \tag{1.15}$$

with $x = \epsilon_i / m_e c^2$.

[2] r_e is the electron radius

[3] magnetic constant in the MKS system

If this energy is small compared to the electron rest mass, the photon is scattered at a different angles but the energy remains unchanged ($\epsilon_i \simeq \epsilon_f$). This is known as the *Thomson regime* and the differential cross-section is reduced to:

$$\frac{\mathrm{d}\sigma}{\mathrm{d}\Omega} = \frac{3}{16\pi}\sigma_T(1+\cos^2\theta) \tag{1.16}$$

For low energy photons ($\epsilon_i << m_e c^2$), the total cross-section is reduced to the Thomson cross-section:

$$\sigma_{IC} \approx \sigma_T(1-2x) \approx \sigma_T \tag{1.17}$$

In the so-called Klein-Nishina regime, when photons are of low energy but the electrons move at relativistic energies with $x >> 1$, the process is no longer treated as continuous but as discrete. The total inverse Compton cross-section becomes:

$$\sigma_{IC} \approx \frac{3}{8}\sigma_T\frac{1}{x}\left(\ln 2x + \frac{1}{2}\right) \tag{1.18}$$

When photons have much larger energies than m_e, the cross section falls quite rapidly (the "Klein-Nishina regime"). Even though the inverse Compton scattering also happens with nuclei, this can be neglected since rate of proton interactions is suppressed by a factor of $(m_e/m_p)^2$ with respect to electrons. In each case, it is important to estimate the energy loss of electrons by the inverse Compton scattering. In the Thomson regime, the electrons lose energy by inverse Compton:

$$-\left(\frac{\mathrm{d}E}{\mathrm{d}t}\right) = \frac{4}{3}\sigma_T c\gamma^2 U_{ph}. \tag{1.19}$$

From this equation together with Equation 1.11 for the synchrotron radiation, the following relation can be found:

$$\frac{P_{IC}}{P_{synch}} = \frac{U_{ph}}{U_B}. \tag{1.20}$$

The ratio of the inverse Compton and synchrotron emission is equal to the ratio of the radiation field over magnetic field energy density.

In the so-called **S**ynchrotron **S**elf-**C**ompton (SSC) scenario high energy electrons upscatter the synchrotron background photons that they emit themselves and produce inverse Compton radiation. This is the most common model used for modeling the emission of the relativistic jets in active galactic nuclei.

Multi-wavelength observations of very-high-energy emitting sources show the presence of double-hump in the **S**pectral **E**nergy **D**istribution (SED). Leptonic scenarios are commonly used to explain the double-hump structure of the SED since the synchrotron and inverse Compton trace the same electron population emitted by a source. The first peak is attributed to the synchrotron emission, whereas the high-energy peak is due to the inverse Compton.

The observations of the current generation of gamma-ray instruments reveal a large number of sources emitting very-high-energy gamma rays. In the following the

main sources emitting very-high-energy gamma rays, their main characteristics and possible acceleration mechanisms are covered.

1.4 High Energy Gamma-Ray Sources

The third *Fermi*-LAT catalog (3FGL), produced with four years of data, lists 3033 gamma-ray sources detected in the energy range from 100 MeV to 300 GeV [44]. This survey show that blazars, a type of active galactic nuclei, are the dominant source class among all other sources (Figure 1.4a) and pulsars the most abundant sources in our Galaxy.

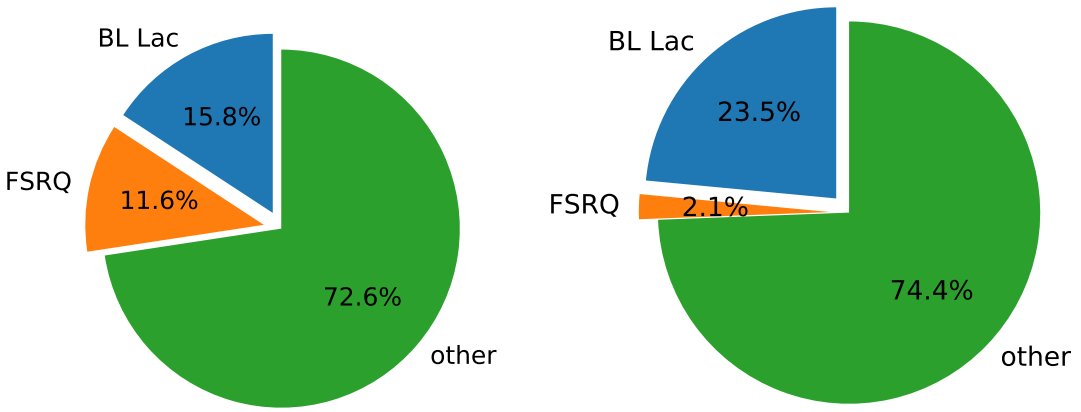

(a) (b)

Figure 1.4: (a) The total sources detected by *Fermi*-LAT instrument in percentage, plotted together with the BL Lac and FSRQ type sources which belong to blazar source class. (b) Total sources detected in TeV show the majority belong to the BL Lac source class, a subclass of active galactic nuclei. The GeV and TeV sky is populated mainly by BL Lac type objects. Plotted with data from [45].

Blazars are subdivided as BL Lacs and Flat Spectrum Radio Quasars (FSRQ). Recent observations with the current generation of imaging atmospheric Cherenkov telescopes reveal that blazars represent the majority of the TeV sources (see Figure 1.4b) and pulsar wind nebulae are the most abundant TeV source class in the galactic plane (refer to [45] for the latest updates). In the following the main gamma-ray sources are introduced. Two main source classes, used for the work presented here are active galaxies nuclei and pulsar wind nebulae, which are described in more detail.

1.4.1 Supernova Remnants

Supernova **R**emnant (SNR) is a common name for sources created either from the collapse of a massive star or from the explosion of a white dwarf. The first type of SNRs is the outcome of the collapse of a massive star at the end its lifetime, when the star cannot withstand its own gravitational force. The second type is created from the explosion of a carbon-oxygen white dwarf in a binary system that has accumulated enough matter from its companion star to exceed the Chandrasekhar limit [46].

The term "super-novae" was first introduced in 1934 in the historical papers of Baade and Zwicky, published a few years after the discovery of cosmic rays. They also proposed supernovae as candidates of cosmic rays and linked supernova explosions with the formation of neutron stars [8, 47]. Ever since, SNRs are of great interest as they are considered as the prime candidates for galactic cosmic ray acceleration up to at least 10^{15} eV (see [48] for a review). This paradigm is supported by the observed energy density of cosmic rays with the one of thermal gas or magnetic fields in our Galaxy. However these connections are not fully understood.

The study of SNRs across the electromagnetic spectrum has helped to better understand the acceleration scenario picture. SNRs exhibit shock fronts (shells), that can accelerate charged particles up to high-energies, hence they offer a unique laboratory to study the hadronic origin of gamma rays from pp collisions (introduced in Section 1.3.1).

Recent observations carried out by the state-of-art experiments in gamma rays have increased the sample of gamma-ray detected SNRs. They reveal that gamma-ray emission is associated with a large variety of SNRs, from young shell-type SNRs up to evolved SNRs interacting with molecular clouds and historical SNRs.

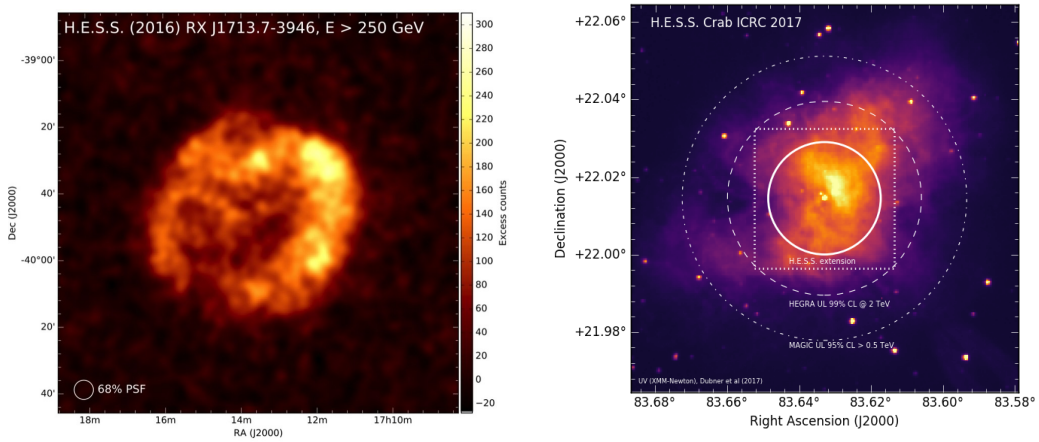

(a) (b)

Figure 1.5: (a) The gamma-ray excess map of the known shell-type SNR RX J1713.7-3946 as measured by H. E. S. S. Image courtesy [49]. (b) First extension measurement of the Crab Nebula at very-high-energies by H. E. S. S. Image courtesy [50].

Young SNRs are the best candidates to study the acceleration of cosmic ray protons through their interaction with the surrounding molecular gas. This may help to establish the possible proton acceleration to very-high-energies. The young SNR RX J1713.7-3946 was resolved in gamma-ray at TeV energies by the H. E. S. S. experiment for the first time ever. It has the largest surface brightness among other SNRs, which allows to study the morphology and spatially resolved spectra of such very-high-energygamma-ray sources (Figure 1.5a). The measured spectrum up to 100 TeV demonstrates that the particle acceleration goes beyond these energies in the shell of the source.

However, the origin of the gamma-ray emission is still under debate and it could be hadronic, leptonic or a mixture of them. For instance, a pion-decay feature signature was reported in the gamma-ray spectra of two known SNRs, IC 443 and W44 [51]. On the other hand, correlation studies between the X-ray and gamma rays are in favour of leptonic models [52]. In order to better understand and complete the acceleration scenario, better angular resolution instruments are required to resolve the emission at very-high-energies.

1.4.2 Pulsars and Pulsar Wind Nebulae

A **P**ulsar **W**ind **N**ebula (PWN) consists of a pulsar and the wind nebula, a flow of relativistic particles in the vicinity of the pulsar. The center of engine is the pulsar, a fast rotating neutron star created in supernova events. The particles are accelerated up to very-high-energies in the electromagnetic fields in the proximity of the pulsar. The neutron star rotational axis is misaligned with respect to the magnetic axis. As the neutron star rotates, co-rotating cones of light are emitted and a pulsed beam of radiation is seen when crossing the observer's line-of-sight on Earth. After being accelerated, the particles move freely within the cylinder cone along the ordered magnetic field and are advected downstream from the shock. These particles create an ultra-relativistic cold wind. Due to the rotation of the pulsar, the magnetic field lines also move and expand in a toroidal pattern.

The equilibrium point is reached when the ram particle wind is balanced by the pressure of the particles in the surrounding nebula. After the shock termination, the magnetic field lines are opened and the particles are accelerated in the presence of the magnetic field and emit synchrotron radiation.

Several models of pulsar magnetospheres are proposed [53]. The full scenario of the PWN particle acceleration is still under debate and the exact place of particle acceleration unresolved (for a review see [54, 55]).

It is commonly assumed that the non-thermal emission of PWNe is of leptonic origin. The hadronic induced emission is unlikely, as it would require dense target material nearby, e.g. a molecular cloud. The leptonic scenario is favoured because the material is swept away from the pulsar since the supernova explosion.

The prototype of the entire PWNe class is the Crab Nebula, one of the best studied object in the sky. The detection of pulsed emission from the Crab Nebula at TeV energies has challenged the current theoretical emission models of pulsars [56].

Furthermore, the detection of flux variations at GeV energies by the *Fermi*-LAT experiment was unexpected and asks for more complex models to explain these observations. H. E. S. S. has measured for the first time the extension at the very-high-energies [50]. Chapter 5 covers the Crab Nebula in more detail.

1.4.3 Active Galactic Nuclei

Active **G**alactic **N**uclei (AGN) are active core galaxies with a central supermassive black hole[4]. The accretion of matter into the black hole powers ultra-relativistic jets in form of collimated outflows. The presence of relativistic jets is an important feature of AGNs since they transport energy and momentum from the black hole up to Mpc[5] scales or even further away. Emission from active galaxies is detected all wavelengths, from radio up to gamma rays for the most energetic objects.

Contrary to normal galaxies, active galaxies exhibit flux variability detected at all energy bands. Their flux can vary on time scales of years down to minutes, as variability studies of PKS 2155-304 from the H. E. S. S. collaboration show [57]. From causality arguments, the emission from a region of size R cannot vary on time scales shorter than the time needed to cross this region at the speed of light i.e R/c. This is used to sets limits on the size and on the relativistic boost of the emitting region (Doppler factor). Observations in gamma rays show that in the jet, particles are accelerated to ultrarelativistic energies reaching Doppler factors greater than 100.

High luminosity stands as another distinctive characteristic of AGNs. Even though active galaxies are distant extragalactic sources, they can sometimes outshine other stars and galaxies. For example, the quasar 3C 273 at a distance of $z = 0.158$ (2.4 Gly) is a bright source in the sky. Back in 1960's, it was surprising to discover that 3C 273 is an extragalactic source with such brightness.

AGNs are known to produce very high luminosities in very compact volumes. Their luminosity can range from $10^{40}\,\mathrm{erg\,s^{-1}}$ for some nearby galaxies up to $10^{48}\,\mathrm{erg\,s^{-1}}$ for some distant quasars. Figure 1.7a illustrates the Centaurus A galaxy including its prominent jet and Figure 1.7b shows the jet of the famous quasar 3C 273.

In the AGN unification model proposed in 1995 by Urry and Padovani, the different active galaxies are classified based on inclination of the jet towards the observer on the Earth [58]. Based on this classification scheme, when looking down-jet, we see a so-called blazar as shown in Figure 1.6. Blazars are classified based on the presence of emission lines as BL Lacertae (BL Lac) and Flat Spectrum Radio Quasars (FSRQ). Most blazars, detected at TeV energies are of BL Lac type. Recent observations reveal thet from all AGN types, blazars are the most abundant sources detected at GeV and TeV energies (see Figure 1.4).

Very-high-energy gamma rays emitted from extragalactic sources are subject to absorption by the **E**xtragalactic **B**ackground **L**ight (EBL) when propagating over cosmological distances. High energy photons are destroyed from pair-production with

[4]SMBH; $M_{SMBH} > 10^6\ M_\odot$
[5]1 Mpc = $3.09 \cdot 10^{19}$ km

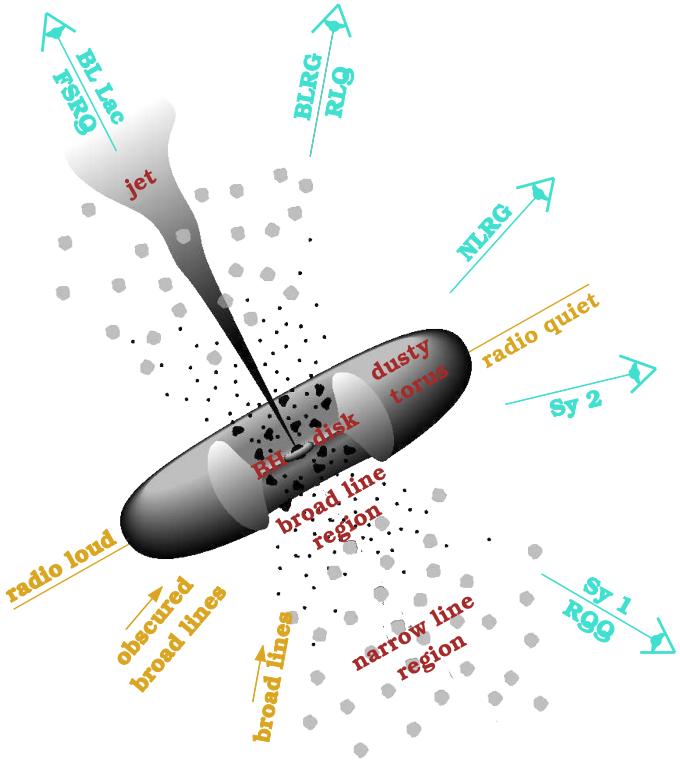

Figure 1.6: Active Galactic Nuclei unification model as described by Urry and Padovani [58]. The classification is based on the orientation of the jet with respect to the observer line-of-sight. If the observer is looking down the jet, it sees a blazar (BL Lac or FSRQ).

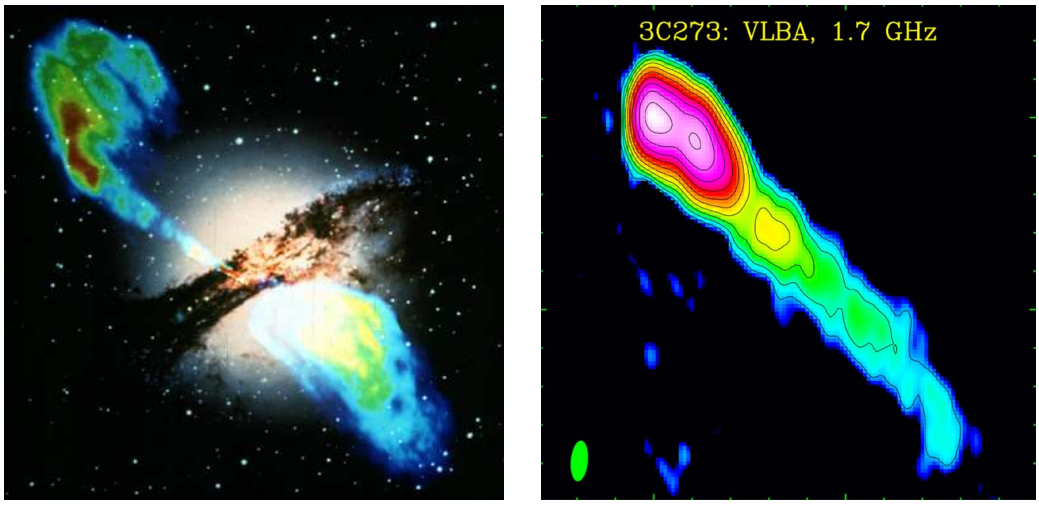

(a) (b)

Figure 1.7: (a) Overlay of the Centaurus A galaxy with the prominent dust lanes and the emerging jet. Image courtesy: optical and radio image (VLA 6 cm), STScI/NASA. (b) The jet of the blazar 3C 279. Image courtesy: VLBA, 1.7 GHz.

the low-energy photons of the EBL, resulting in energy attenuation of the photon density. The mean free path is used to quantify the free length of a photon without any interaction. The free path of the very-high-energy photon before interacting depends on the primary energy of the very-high-energy photon coming from the source. Higher energy photons have a shorter free path length than lower energy ones. The opaqueness of the Universe to the very-high-energy gamma rays leaves an imprint in the spectra of these sources which is used to set limits on EBL from measurements. Blazars detected by H. E. S. S. have been used to determine the EBL level [59].

A particular case of rapid flux variations and luminous flares is found when studying the gamma-ray variability of the BL Lac object B2 1215+30 over five decades in energy which is presented in Chapter 4.

1.4.4 Other Sources

The list of gamma-ray emitters also includes other types of source classes and unidentified sources. More sources are found interesting for the studies at the very-high-energy regime. The one presented here are a pickup of the author.

Binary Systems

A majority of 70% of the stars found in our Galaxy form either a binary system with one companion or live in more complex systems (see Figure 1.8 as illustration) [60]. These systems include gamma-ray binaries and microquasars (MQs).

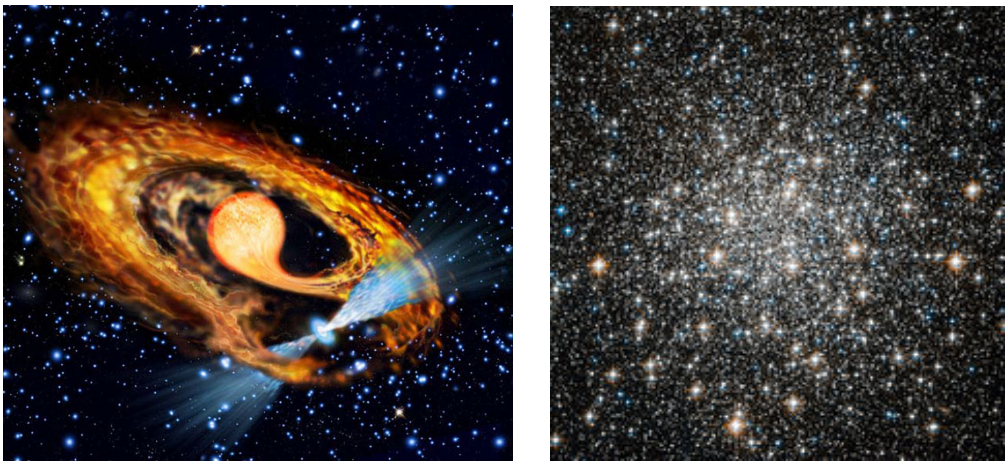

(a) (b)

Figure 1.8: (a) Artistic illustration of a millisecond pulsar and its companion. The pulsar is accreting material from its companion star and increasing its rotation rate. (b) Globular cluster. Images courtesy: ESA.

Both are found to be variable at gamma rays and in some cases periodic. Binary systems consist of a compact object, either a neutron star or a stellar-mass black

hole, and a massive O or B-type star. MQs are binary systems emitting in X-rays and with extended radio emission [61].

Globular Clusters

Globular clusters are regions with extremely high star densities (Figure 1.8). They host the most evolved and oldest stellar populations of our Galaxy. Their gamma-ray emission can originate from the numerous millisecond pulsars or from inverse Compton scattering of relativistic electrons accelerated in the globular cluster. From the analysis performed with the H. E. S. S. data, no point-like or extended emission was detected [62]. These regions are also considered as potential targets for dark matter searches [63].

Molecular Clouds

Although Molecular Clouds are not gamma-ray sources, they are interesting for gamma-ray astronomy as interaction targets for cosmic rays accelerated at SNRs and important to study the gamma-ray diffuse emission [64].

Gamma-Ray Bursts

Gamma-**R**ay **B**ursts (GRBs) are the most energetic events in the gamma-ray regime. They are the most luminous, highly-relativistic events, lasting from few milliseconds up to hundreds of seconds. They are divided in short and long GRBs and can be result of the merging of compact objects or the gravitational collapse of a massive star. No GRB has been detected by the H. E. S. S. experiment so far [65].

1.5 Summary

In this chapter, the gamma-ray astronomy above 100 MeV was introduced. The basic radiative processes responsible for producing energetic gamma rays were described briefly. Possible sites of cosmic ray acceleration can be neutron stars up to galaxy clusters. The exact picture for cosmic ray acceleration is not known but some scenarios, such as the Fermi acceleration are considered as possible mechanisms for powering the non-thermal emission. The main gamma-ray sources and their characteristics were covered. Observations show that blazars are the most abundant source classes at GeV and TeV energy range and PWNe the most abundant source type in the Galaxy. In the past decade, the understanding of the high-energy sky has changed from breakthrough discoveries of the state-of-the-art experiments. Beside all the achievements, the cosmic ray picture is not complete and fully understood.

Chapter 2

Detectors for High-Energy Gamma-Ray Astronomy

The high-energy processes accelerating particles the in Universe can be studied indirectly through the detection of gamma rays produced by interactions with interstellar medium or radiation fields. High-energy gamma rays interact with matter via well-understood quantum electrodynamics processes. Thus, the properties of gamma rays, like energy and direction can be reconstructed by detectors that "see" the secondary products. By reconstructing the directions of the incoming gamma rays, one can locate the emission sites and perform morphology studies. The reconstructed energy gives information on the emission power of astrophysical sources. The observed flux provides important information to study and understand the particle acceleration mechanisms powering particles to such high energies. Sophisticated detection techniques along with continuously advancing reconstruction methods are essential to study the most extreme form of radiation coming from the non-thermal Universe.

In gamma-ray astronomy, space satellites detect and locate high-energy emission sites by directly exploiting the interactions of gamma rays with dense materials, e.g. in *Fermi*-LAT or AGILE. At energies $E > 30\,\mathrm{MeV}$, pair production is the dominant photon interaction process in most materials. A pair conversion instrument typically uses a thin foil of dense metal to convert incoming gamma rays, and a calorimeter with a tracker to measure the energy of the resulting electrons. This is a robust technique for reconstructing energy, direction and arrival time of gamma rays with energies from MeV to GeV. At energies above 1 TeV, the gamma-ray fluxes are low and large collection areas are required. Building and sending large collection area detectors to space is complicated and challenging due to the launch vehicles required. Hence, ground-based experiments are better suited at those energies.

When energetic gamma and cosmic rays reach the Earth's atmosphere and interact with its molecules, they initiate an extended air shower of secondary particles. With the atmosphere acting as a calorimeter for the energy deposition of a very-high-energy particle, ground-based detectors can detect secondary particles produced during this process. The Cherenkov light produced during the extensive air showers can be detected with **I**maging **A**tmospheric **C**herenkov **T**elescopes (IACT). The Whipple telescope, the first successful IACT, was a leap in the development of the technique, which is currently employed by the MAGIC, VERITAS and H. E. S. S. experiments.

In this Chapter, the basic principles of high-energy gamma-ray detectors are described. After describing briefly the photon interaction processes in matter in Section 2.1, the main principles of the *Fermi*-LAT detector are given in Section 2.2. The basic concepts of gamma-ray detection from ground are described in Section 2.3 and the properties of extensive air showers are described in Section 2.4. A historical review on the Cherenkov technique, its application in high-energy gamma-ray astronomy and present and future ground-based gamma-ray experiments are discussed in Section 2.5. A short summary of the chapter is given in Section 2.6.

2.1 Space Detectors

The Earth is opaque to gamma rays, preventing a direct measurement from the ground. The properties of high-energy radiation coming from the Universe can therefore only be studied directly from satellites sent above the atmosphere. These instruments are designed to detect and locate sites of high-energy gamma rays emission using the interaction properties of gamma rays with dense materials. The gamma rays with energies $E \geq 1.022$ MeV can be converted to massive particles near an atomic nucleus via the electron pair production process in accordance with Einstein's mass-energy equivalence principle ($\gamma + \mathrm{N} \rightarrow e^+ + e^- + \mathrm{N}$). Pair production is the dominant photon interaction process at high-energies ($E > 100$ MeV) for most materials [66] [6]. A space-borne pair creation telescope is therefore the instrument of choice for detecting gamma rays above approximately 100 MeV. Using a high Z material, a large fraction of high-energy photons can be converted. Figure 2.1a shows the photon interaction probability for pair production and Compton scattering in lead.

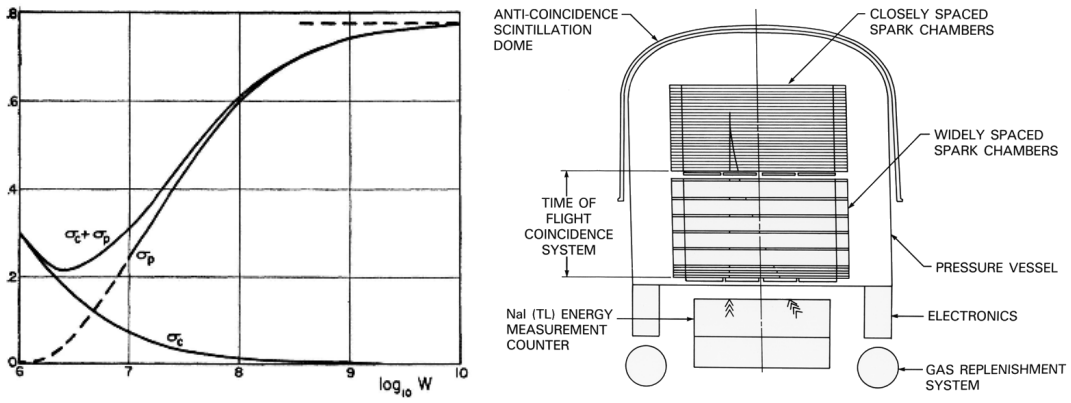

(a) (b)

Figure 2.1: (a) Interaction probability in radiation length of photons as function of energy W in eV in lead material, with σ_p and σ_c the probability of pair creation and Compton scattering. Image courtesy [67]. (b) Schematic construction of EGRET, the predecessor of the *Fermi*-LAT satellite. The main parts of the detector are given to be compared to the *Fermi*-LAT. Image courtesy [68].

The detector on board the satellite has to identify gamma-rays against a large rate of background charged particles (cosmic rays) coming from all directions. To reject the cosmic ray background, a plastic scintillator anti-coincidence detector serving as "veto" (SAS-2[20], COS-B [69], EGRET/CGRO [68] and *Fermi*-LAT [70]) is placed in the outer part of the satellites. It detects the passage of charged particles. Once the gamma ray has converted in the detector, its arrival time, energy and direction is extracted from the electron pair properties. Figure 2.1b shows the schematic construction of the EGRET satellite, which provided a comprehensive view of the gamma-ray sky, by producing also the first all-sky map in gamma rays. The successor of EGRET, the *Fermi*-LAT satellite is based on similar technologies but uses silicone tracker instead of spark chamber.

Measuring the polarization of the gamma ray could give important information about the astrophysical sources, but this is not realized by space detectors so far. Future space satellites, using time projection chambers, are being designed in a way that provides also this information (see [71]).

The current gamma-ray state-of-the-art instruments from space are *Fermi*-LAT and AGILE. The former is used for performing part of the work presented in this thesis and is described next.

2.2 The Fermi Large Area Telescope

The *Fermi Gamma Ray Space Telescope* (*Fermi*) mission was launched on 2008 June 11, with two instruments on board; the Large Area Telescope and the **G**amma-Ray **B**urst **M**onitor (GBM). The *Fermi* spacecraft is shown in Figure 2.2. The GBM instrument is used to monitor and study transient phenomena in the Universe e.g. Gamma-Ray Bursts [72]. The LAT is a pair-conversion telescope detecting gamma rays with energies from 20 MeV up to more than 500 GeV, an energy band that had only partially been explored by previous space satellites.

Figure 2.2: *Fermi* spacecraft with two instruments on board: the Large Area Telescope and the Gamma-Ray Burst Monitor. Image courtesy: NASA.

The LAT has a large field of view of 2.5 sr, corresponding to 20% of the sky at every instant. The *Fermi*-LAT is mainly observing in survey mode where it can scan the

entire sky every three hours making two orbits in a zenith-pointing mode, rocking at 35° north and south of zenith on alternating orbits. The LAT can also observe in pointing mode when required e.g. for **T**arget **o**f **O**pportunity (ToOs) events.

The *Fermi*-LAT, originally planned for five years of operation is now close to its 10th successful operation year. Its main science goals are listed below:

- Monitoring fast transients events from GRBs and variable sources.
- Complete coverage of the high energy sky.
- Measure spectra with extended energy range, from $\sim$ 20 MeV to 500 GeV.
- Localization of point sources i.e pulsars, blazars, new source types.
- Extension studies in sources like SNRs, molecular clouds or nearby galaxies.
- Dark matter searches.
- Diffuse isotropic gamma-ray emission studies.

The *Fermi*-LAT is the successor of the EGRET telescope, with better sensitivity and performance compared to previous missions [25]. The reason for this is a combination of a better detector and reconstruction techniques. The LAT detector is based on principles of high-energy particle detectors as described below.

2.2.1 Principles of the Large Area Telescope

A high-energy gamma-ray hitting a high Z material is converted into an electron-positron pair, which in turn create a cascade of secondary particles, called particle shower, until the energy is completely absorbed by the material. The energy of the primary particle is transferred to the new particles created during the shower development with minimum losses until ionization starts to be dominant. Measuring all the energy deposited during the shower development is equivalent to measuring the energy of the primary particle which initiates the shower, in this case the gamma-ray. The determination of the gamma-ray direction is done by reconstructing the trajectories of the electron/positron pair created in the first step of the shower development. These two important parameters are reconstructed using a tracker, which can reveal the path of electrically charged particles, and a calorimeter which measures the energy deposited during the shower development. The electromagnetic calorimeter is typically segmented transversely and consists of layers of high density material. The aim of the calorimeter is to measure the energy deposition and the development profile of the electromagnetic shower. In order to have a precise reconstruction of the shower, the electromagnetic calorimeter is in conjunction with a tracker.

The *Fermi*-LAT instrument detects the gamma rays by converting them into an electron pair in tungsten foils and following their trajectories using a silicon tracker. When a high energy gamma-ray hits the detector, it traverses the silicon tracker until it interacts with one atom from the thin tungsten foils. After this, the gamma-ray generates a particle shower by firstly converting into an electron pair, and the energy of each electron is deposited and can be measured in the electromagnetic calorimeter.

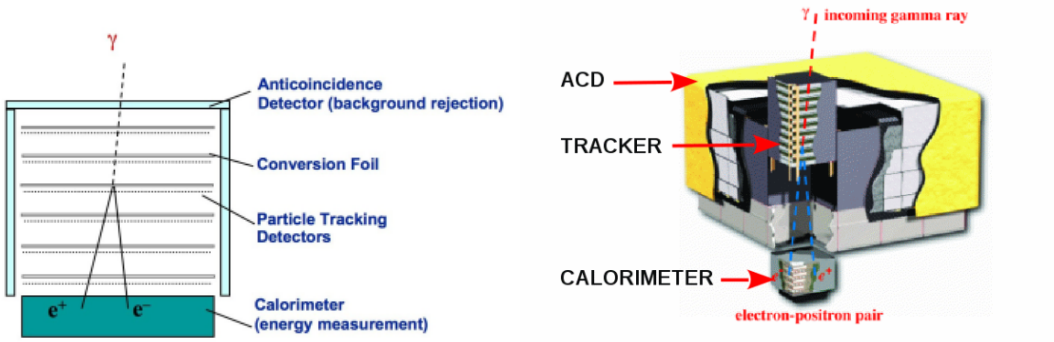

(a) (b)

Figure 2.3: (a) Schematic view of the *Fermi*-LAT cutaway where the three main parts of the detector are shown. (b) Cosmic gamma rays after hitting the silicon tracker get converted into an electron/positron pair. The energy released is measured in the calorimeter. Image courtesy: NASA.

The development of the electromagnetic shower in the electromagnetic calorimeter depends on the direction and energy of the gamma-ray hitting the detector. The segmented calorimeter is designed to allow the profile of this energy deposition to be measured, for a better discrimination and for a long duration.

In the energy range of the *Fermi*-LAT, the charged cosmic ray flux is about 10^5 times higher than that of the gamma rays. To maximize the charged cosmic ray background rejection, the *Fermi*-LAT detector is composed by three main systems: the silicon tracker, the calorimeter and the **A**nti**C**oincidence **D**etector (ACD) (see Figure 2.3). All these parts are combined in the optimal way to reject the largest part of the background. To shield the detector from charged cosmic rays, the ACD is placed in the outer part. In the next sections, the basic principles of each sub-detector part are described, starting from the outermost one.

2.2.2 The Anticoincidence Detector

The main source of background for the *Fermi*-LAT satellite are the charged cosmic rays that hit the detector at much higher rates than the gamma rays. The ACD is made of plastic scintillator tiles and veto responses to the passage of charged particles. It was designed under two main requirements; to have high (0.9997) detection efficiency for charged cosmic rays and to suppress self-vetos caused by the backsplash effects. The later effect is encountered in instruments with massive calorimeters, from where a small fraction of secondary particles from the electromagnetic shower go backwards through the tracker and cross the ACD. False vetos are created from the recoil electrons, resulted from Compton scattering of these particles with the ACD material. This effect limited the performance of the EGRET instrument when it caused false vetos yielding low detection efficiencies for $E > 1$ GeV [25]. In order to suppress the backsplash effect, the LAT team segmented the ACD in 89 tiles of

different sizes and only the segment on the trajectory of incident particle is considered. With only one segment of the ACD contributing in the backsplash, this effect is dramatically suppressed (for more details on the LAT ACD see [70]).

2.2.3 The Tracker

The tracker system of *Fermi*-LAT is the central part of the detector, located between the ACD and the calorimeter. The tracker is made of 16 planes, each with a high Z tungsten converter foil and two layers of silicon strips oriented at 90 degree to each other. The tracker can measure the path of the electron pair into which the gamma-ray converts. More details about the LAT are found here [73].

2.2.4 The calorimeter

The role of the calorimeter is to measure the energy deposited by the electron pair resulting from the converted gamma-ray. The LAT calorimeter is made out of 96 CsI(Tl) crystals arranged in 12 columns and 8 layers with a depth of 8.3 radiation lengths. PIN diodes are attached to each side of the crystal to read out the scintillation light at both ends. The location and the energy deposit along the crystals are given respectively from the ratio and the sum of these light signals at the edges [74].

2.2.5 Data-Processing Pipeline

The *Fermi*-LAT was set on all-sky survey mode after the on-orbit in September 2009, after the check-out and calibration period was completed [75]. In this observation strategy, the normal to the front of the instrument is "rocked" to ± 50 degree, above and below the orbital plane on alternate orbits. The orbital period is about 96 minutes and the full sky is observed with an almost uniform exposure after two orbits. The "all-sky" survey is the primary observation strategy but also the pointing observation mode is supported by the *Fermi*-LAT.

The data-processing pipeline of *Fermi*-LAT detector is designed to be prompt. The data is reduced firstly onboard the *Fermi*-LAT. The online trigger and the LAT software monitor the performance during nominal science data-taking. After the trigger decision, on-board software filters are applied to classify events likely to be used for calibration or scientific purposes [73] [26]. The events passing the filters are then included in LAT data stream and transmitted to the Solid State Recorder for transmission on the ground. The LAT data is downloaded every three hours and the processing of the downlinked satellite is performed in a data time critical manner. This procedure is done on a computer cluster for a fast and effective processing of the data [76]. The events are reconstructed, filtered and classified into categories which are characterized by their own set of instrument response functions. The LAT data, together with the **I**nstrument **R**esponse **F**unctions (IRF) and point-spread functions

are publicly released since August 2009. For this study the publicly available data was used.

The LAT instrument is taking data continuously except during South Atlantic Anomaly passages where the scientific data taking is disabled. Apart this, other gaps on the data taking caused by other factors i.e. technical details, calibration runs, instrument dead time are present. The live time i.e. the effective time to the overall LAT exposure, is important to derive reliable results on spectra and lightcurves for astrophysical sources.

2.2.6 Analysis Method

The standard analysis of the *Fermi*-LAT data is based on a likelihood framework. The application of the likelihood method to photon-counting experiments in astronomy was introduced in 1979 [77]. This method was successfully adapted and implemented to analyze the data from the EGRET satellite [78]. The *Fermi*-LAT standard analysis framework is similar to the one used for the EGRET data. In the field of gamma-ray astronomy, the challenge is to detect the signal on top of the background. Given the observations, a proper model that describes the data is mandatory. A good background model is essential since it affects the accuracy of the scientific results.

The LAT analysis technique uses a three-dimensional counts "map", which contains energy and position information for each event. Figure 2.4a shows an illustration of a 3D map with squared pixels. The emission for a **R**egion **o**f **I**nterest (RoI), is parametrized by the superimposition of models describing different sources. Within the RoI, each gamma-ray source is modeled by a spatial and spectral component.

The likelihood for a set of models describing the data is composed by the likelihoods of the n individual bins in the map as follows:

$$\log \mathcal{L} = \sum_{i=0}^{n} \log p_i, \tag{2.1}$$

where $p_i = \frac{\lambda_i^{n_i} \, \mathrm{e}^{-\lambda_i}}{n_i \, !}$ is the Poisson probability of observing n_i counts in pixel i when are predicted λ_i. The logarithm is taken for computational time reasons.

Given the instrument limitations and imperfections, the source parameters like energy, position and morphology are convoluted with the **I**nstrument **R**esponse **F**unctions (IRFs). Thus, each model $\mathcal{M}$ within RoI has to account for the IRFs, i.e. the probability to reconstruct an event with p_i' for a photon with a true momentum p_i. The IRFs are usually derived from Monte Carlo simulations and split into effective area, point spread function (PSF) and energy response. The effective area (A_{eff}) is the detection probability of a given photon p_i in units of cm^2. The energy response is the probability to reconstruct the energy E_i' of an event with true energy E_i, and the PSF is the probability to reconstruct the direction (x_i', y_i') of a photon with true direction (x_i, y_i).

Suppose a source i located in the center of the map (see Figure 2.4a) and three other sources around. These sources contribute as well in the observed counts from the central source square. The probability to detect an event p_i' originating from a source parametrized by $\mathcal{M}_j$ is defined by convoluting the model components with the IRFs and integrated over true photon attributes as follows:

$$\mathcal{M}_j(p_i') = \int \mathrm{d}x \int \mathrm{d}y \int \mathrm{d}E\, \mathcal{S}(E,x,y) \times \mathrm{IRF}(p_i, p_i'), \tag{2.2}$$

with $\mathcal{S}(E,x,y)$ being the source model as function of energy and direction. To minimize the likelihood function of the form given in Equation 2.1, different minimization packages are available but for this work the `MINUIT` package was used.

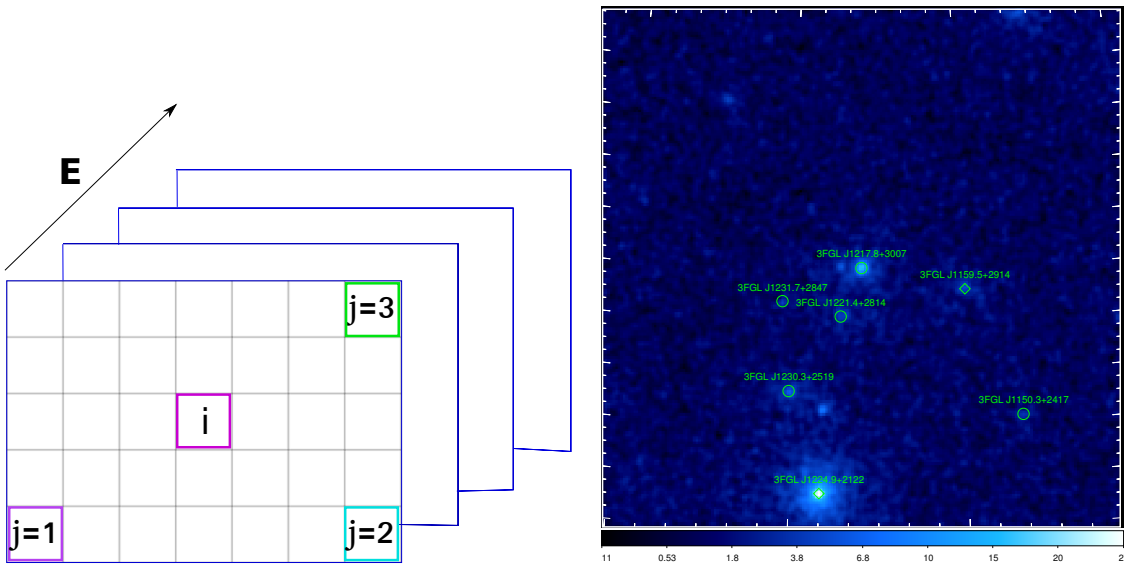

(a) (b)

Figure 2.4: (a) Sketch of 3D maps used to perform data analysis with the *Fermi*-LAT. The source i and other sources are marked with $j = 1, 2, 3$. (b) The counts map of B2 1215+30 for a 15° radius RoI. The known gamma-ray sources from the *Fermi* catalog are marked in green.

For the *Fermi*-LAT analysis, the latest software release, named Pass 8 was used. This reconstruction technique is described here [79] and gives a better gamma-ray acceptance compared to the previous one [80]. This allows to make analysis with energy which up to 500 GeV. The gamma-ray acceptance for these software releases is shown in Figure 2.5.

When point like sources are analyzed, a RoI with a typically radius of 15-20 degrees is used (as shown in Figure 2.4b). In order to have the best parameter estimation for a specific analysis, a proper background model is crucial. The background model has to account for the emission of all the known gamma-ray sources located within RoI, the diffuse and galactic emission. At *Fermi*-LAT energies, the diffuse emission dominates the entire high energy gamma-ray sky, with the highest level of emission

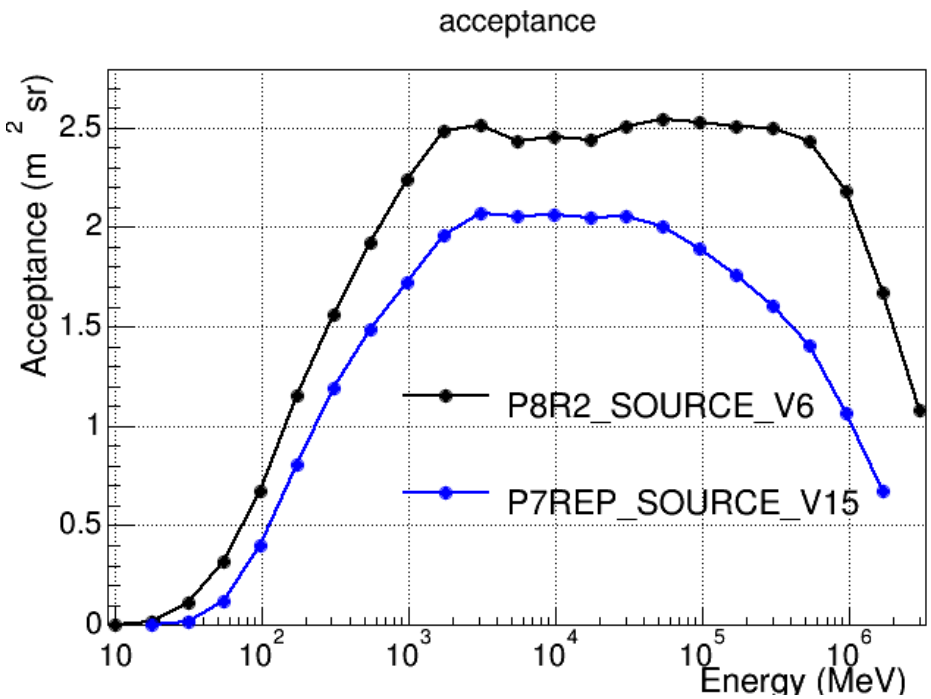

Figure 2.5: Comparison of the gamma-ray acceptance map for Pass 7 and Pass 8, as indicated by the legend in the plot. Image courtesy [81].

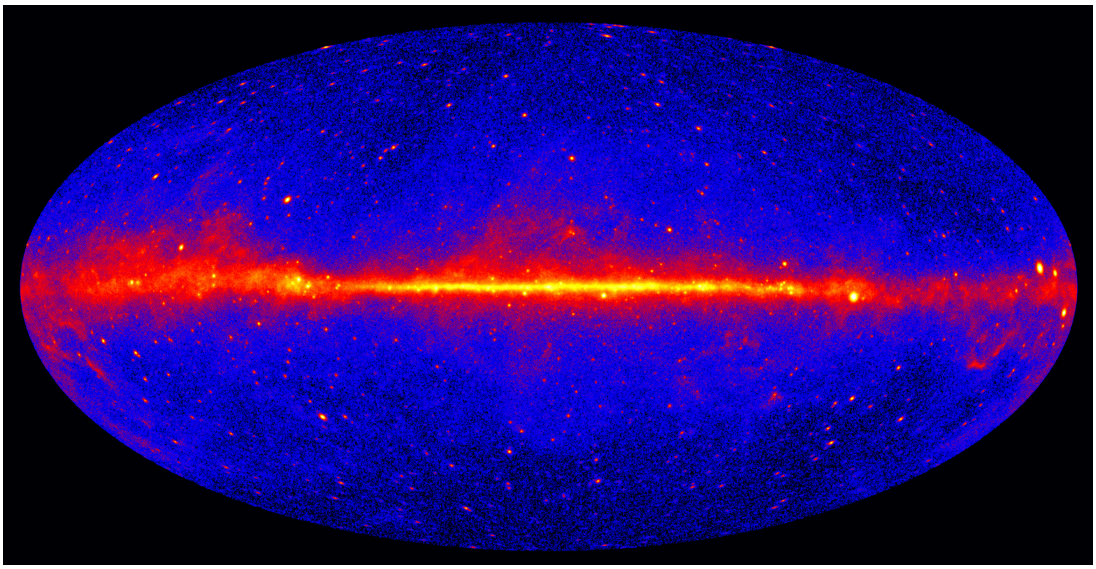

Figure 2.6: The *Fermi*-LAT full sky map in aitoff projection in Galactic coordinates. It shows the gamma-ray intensity for energies $E > 300\,\text{MeV}$ produced from 48 months of observations. Image courtesy [82].

coming from the galactic centre. In Figure 2.6 and Figure 2.7, the full sky map at energies $E > 300\,\text{MeV}$ and all the sources from the *Fermi*-LAT observations are shown. On the first map one can see the Galactic diffuse emission along the galactic plane. Further away from the galactic plane, the background is dominated by a more isotropic emission. More details on this measurement can be found here [83, 84].

The Galactic diffuse emission is represented by energy dependent sky maps whereas the isotropic diffuse model depends only on the energy.

The `FermiScienceTools` is a likelihood analysis framework developed by the LAT team and provided the publicly data analysis. The latest galactic and isotropic diffuse models and the corresponding IRFs can be retrieved from the public *Fermi*-LAT server, and used to define the background.

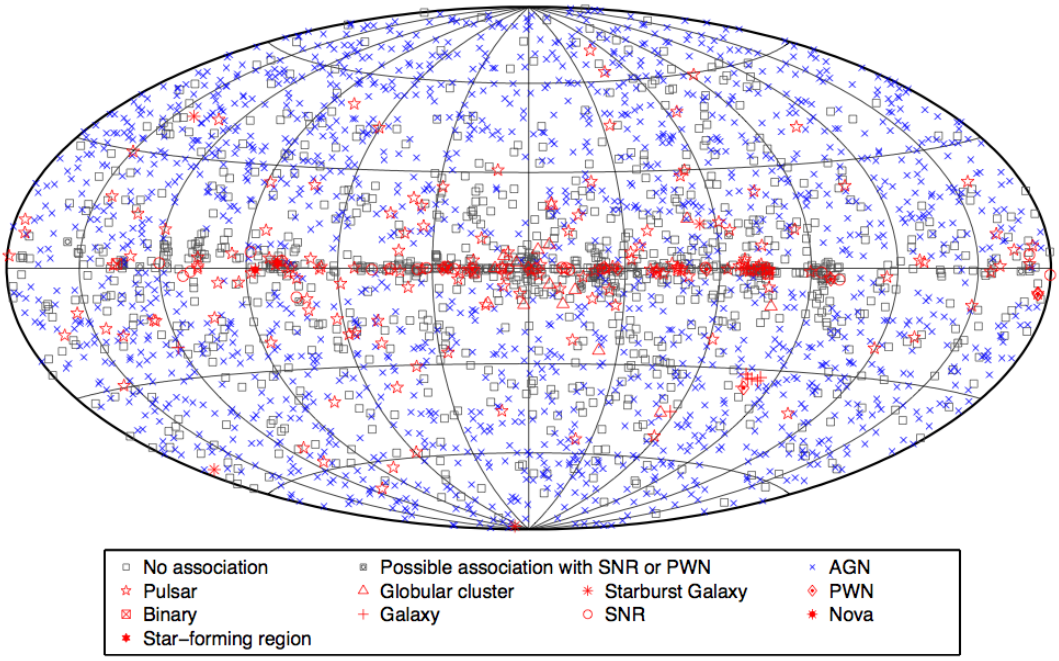

Figure 2.7: All sources detected from the *Fermi*-LAT using 4 years of data. The majority of the sources detected are AGNs, whereas the PWN are the most abundant source class in the Galactic plane. Image courtesy [44].

2.3 Ground-based Detectors

At energies above 100 GeV the photon fluxes of astrophysical sources decrease rapidly with the energy. In this energy range the detection of gamma rays from space becomes challenging since large collection area detectors are required. To study the very-high-energy sky, ground-based detectors with large collection areas are used. When high energy gamma rays arrive upon the Earth's atmosphere, they interact with the atmospheric nuclei, create the cascade of particles and emit Cherenkov radiation (described in Section 2.4.3). Using the properties of the atmosphere as a calorimeter for the energy deposition of a very-high-energy gamma-ray, detectors on the ground detect the Cherenkov light produced during these process. Imaging atmospheric Cherenkov telescopes reconstructing the direction and energy of gamma rays rely on telescopes large reflective areas, fine-pixelized camera and fast read-out electronics. The flux of charged cosmic rays is higher than that of gamma rays,

making the background suppression challenging. Using stereoscopic measurements with more than one telescope offers an efficient method to distinguish gamma rays from cosmic rays.

There are also ground-based experiments in gamma-ray astronomy that detect air-shower particles by recording the Cherenkov light emitted when they pass through water tanks. An example is the **H**igh **A**ltitude **W**ater **C**herenkov (HAWC) experiment, which consists of an array of 300 water tanks (7.3 m diameter and 4.5 m height). The energy range covered by HAWC is from 100 GeV up to 100 TeV [85]. This detector is not restricted to night observations and is operating during all the time. Describing the principle of these detectors is out of this thesis scope.

The current generation of Cherenkov telescopes in gamma-ray astronomy field includes the H. E. S. S., VERITAS and MAGIC experiments. The properties of air showers created when high-energy particles interact in the atmosphere are important to establish methods and variables to discriminate gamma-ray from cosmic-ray induced showers. The basic properties of extensive air showers are given next.

2.4 Extensive Air Showers

High energy particles interact with atmospheric nuclei and initiate **E**xtensive **A**ir **S**howers (EAS). An EAS is a cascade of particles created from collisions and decays occurring during the shower development. Depending on the type of the particle initiating the process, we distinguish EAS of electromagnetic and hadronic origin. Given the rate of cosmic rays (mostly protons, arriving isotropically from outer space) with respect to gamma rays, the majority of the EAS are of hadronic origin. The study of EAS development and their intrinsic differences is important for the discrimination between the two different EAS types.

2.4.1 Electromagnetic Showers

Electromagnetic showers are primarily initiated by energetic gamma rays or by electrons. The main processes in the development of the electromagnetic showers are pair production and the bremsstrahlung. Ionization loss of electrons becomes dominant at lower energies. The majority of secondary charged particles are produced via electron pair-production in the electric field of a nucleus. The bremsstrahlung emission from electrons in the nucleus electric field is responsible for the creation of further high-energy photons. Therefore, the energy of the primary particle initiating an EAS is redistributed over many particles during the shower development in the atmosphere. The amount of matter traversed by electrons and photons to undergo one interaction is characteristic of the material. The material dependent radiation length X_0 is defined as the length scale over which the energy of a particle is reduced to a factor $1/e$ during the shower development.

The energy E of a particle after traveling a given distance x is given by:

$$E(x) = E_0 e^{-x/X_0} \tag{2.3}$$

The radiation length for electrons emitting bremsstrahlung and for photons undergoing pair production in the air are respectively $X_0 \simeq 37-38\,\mathrm{g\,cm^{-2}}$ and $X_{\gamma,0} = 9/7X_0$. A simple model describing the shower development is the Heitler model, developed in 1930s [86]. This model is simplified under these assumptions:

- pair-production and bremsstrahlung are the only dominant processes contributing in the development of the electromagnetic cascade
- the radiation length X_0 to undergo pair-production and bremsstrahlung are equal
- the energy of each particle is distributed evenly at each step among the particles created from these processes

Figure 2.8 shows a schematic view of this model. Each particle splits into two new particles after having traveled a thickness $d = X_0 \ln 2$.

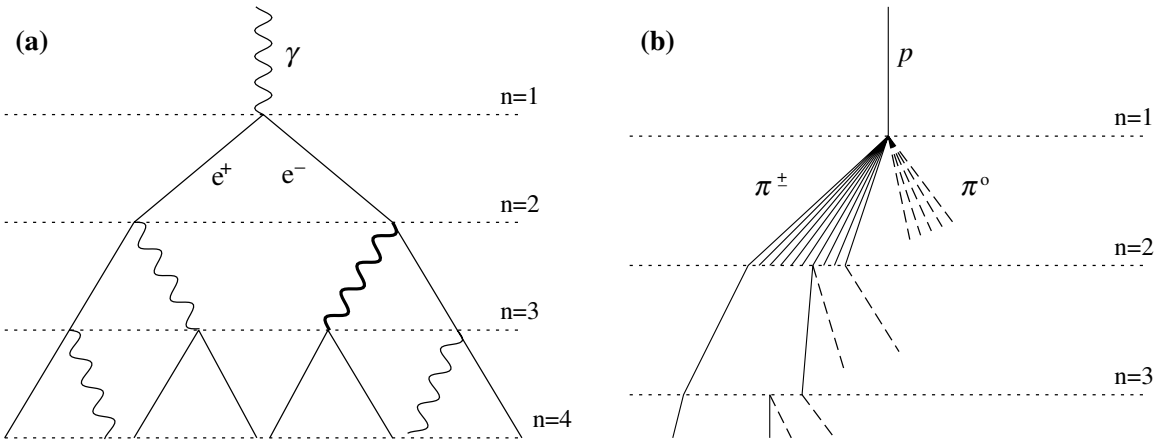

Figure 2.8: In (a) and (b) are shown the schematic view of an electromagnetic and hadronic cascade, respectively. Image courtesy [86].

After n splitting lengths, at the thickness $x = nX_0 \ln 2$, the total of particles is $N = 2^n = e^{x/X_0}$. The radiation becomes less important than collisional energy loss when the particle energy is lower than the energy threshold for pair-production or bremsstrahlung. This energy, where the bremsstrahlung and ionisation losses are equal, referred to as the critical energy is equal to $\mathrm{E_c} = 85\,\mathrm{MeV}$ in air. The depth at which the shower reaches its maximum size is:

$$X_{max} = X_0 \ln\left(\frac{E_0}{E_c}\right) \tag{2.4}$$

Additionally to the pair-production, bremsstrahlung and ionization loss there are other processes like multiple scattering or the Earth's magnetic field that play a role in the shower development, mainly at lower energies.

The shower development is centered around the axis of the incoming gamma-ray initiating the EAS, keeping the directional information down to ground level.

2.4.2 Hadronic Showers

Hadronic interactions in the atmosphere are more complex to describe as many more processes take place during the shower development each with a different characteristic length of interaction. A simple model for hadronic showers based on the Heitler model is given here [86]. In this approach, the atmosphere is assumed to be equally divided into n layers of fixed thickness. In the upper part of the atmosphere, arriving protons interact with air molecules via strong force and create a cascade comprising most importantly nucleons and charged and neutral pions ($\pi^{\pm}$, π^0). The neutral pions π^0 have a mean lifetime of 0.8×10^{-16} s, hence they decay almost immediately into photons:

$$\pi^0 \rightarrow \gamma + \gamma$$

The charged pions continue interacting in the atmosphere until their energy falls below the critical energy $E_\pi < E_c^\pi$. Below this energy, the charged pions ($\pi^{\pm}$) with a mean lifetime of 2.6×10^{-8} s decay predominantly into muons:

$$\pi^+ \rightarrow \mu^+ + \nu_\mu, \qquad \pi^- \rightarrow \mu^- + \bar{\nu}_\mu$$

The typical energies above which the charged pions interact is about 30 GeV.

If the photons resulting from the π^0 decay have enough energy, they can initiate an electromagnetic shower. Electromagnetic showers produced in the early phase of the hadronic shower development might cause confusion with the pure electromagnetic showers. However, the lateral and longitudinal development of the hadronic and electromagnetic showers is different (see Figure 2.8 and Figure **??**). Hadronic showers are typically larger and more irregular than electromagnetic showers. Thus, the lateral distribution and the irregularities of the EAS are used as the basic discriminants to separate gamma rays from cosmic rays showers.

2.4.3 Cherenkov radiation

First investigated by Pavel Cherenkov, the Cherenkov light is the radiation emitted when charged particles move in a dielectric medium at speeds faster than the local phase velocity of light in the same medium [87]. Fast moving charged particles ($v > c/n$) cause polarization by exciting the surrounding molecules and atoms while traversing a medium with refractive index n. Once the particle has passed, the molecules and atoms relax into their normal state emitting electromagnetic radiation. According to Huygen's construction, the wavelets from all points of the particle track will be in phase with one another under a particular emission angle. During this process, a coherent wave front is generated at an angle θ with respect to the particle direction. This coherent radiation, is the so-called Cherenkov radiation. The basic principle is shown in Figure 2.9.

By applying simple geometrical rules as in Figure 2.9, the cosine of the Cherenkov

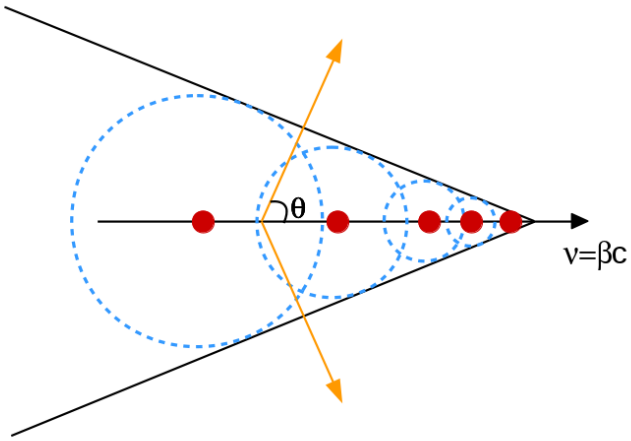

Figure 2.9: Schematic view of the Cherenkov light production when a charged particle moves at speeds $v > c/n$ through a medium of refractive index n. The Cherenkov light is produced at an emission angle θ.

light cone is given by:

$$\theta_c = \arccos\frac{c}{nc} \Rightarrow \theta_c = \arccos\frac{1}{n}, \tag{2.5}$$

where n is the refractive index of the medium. The Cherenkov light is emitted at an opening angle of $2\theta_c$ that depends on the energy of the particle and on the refractive index of the medium.

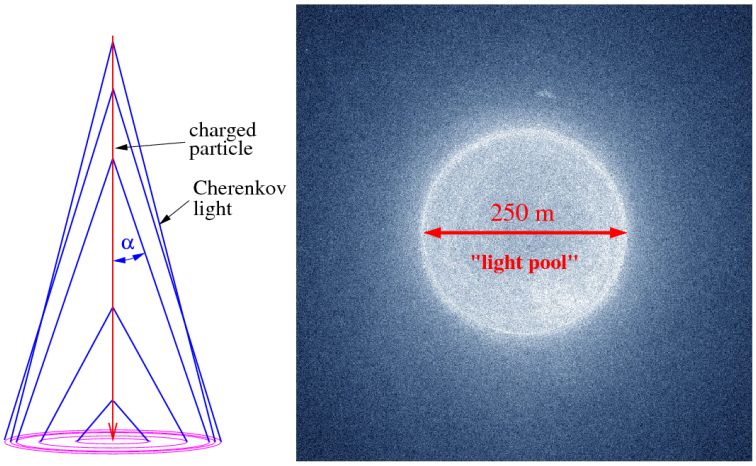

Figure 2.10: The Cherenkov light emitted from a gamma-ray with initial energy of 1 TeV. The emission angle marked as α here changes with altitude and the superimposition of the Cherenkov light illuminates a light poll of 250 m diameter in the ground. This is seen at an observation level at 1800 m above sea level. Image courtesy [88].

As described in section 2.4, very-high-energy particles initiate an EAS by interact-

ing with the nuclei of the atmosphere. The highly energetic electrons, produced during the EAS development, travel faster than light in the atmosphere and emit Cherenkov light. Since the number of particles generated is amplified during the EAS development, this makes the Cherenkov light emitted possible to detect. The Cherenkov radiation creates a "light pool" on the ground with a duration of few nanoseconds. The refractive index depends on the density of the medium hence the radius of the Cherenkov light pool depends on the height at which the emission was originally produced, and on the detection altitude. Figure 2.11 shows different Cherenkov light pools on the ground for different EAS. The Cherenkov light distribution is approximately flat within the pool and rising at the edges (Figure 2.10 left), due to the varying refractive index:

$$n(h) = 1 + n_0 \exp\left(\frac{-h}{h_0}\right). \tag{2.6}$$

where $n_0 = 0.00029$ and $h_0 = 7250\,\mathrm{m}$ (for a hydrostatic, isothermal atmosphere). The superimposition of the Cherenkov light emitted during the shower electromagnetic development illuminates the ground on a light pool with radius of 80-150 m. The number of photons produced per unit wavelength and per unit distance is given by the Frank-Tamm formula:

$$\frac{\mathrm{d}N}{\mathrm{d}x\mathrm{d}\lambda} = 2\pi\alpha Z^2 \lambda^{-2}\left(1 - \frac{1}{\beta^2 n^2(\lambda)}\right) \tag{2.7}$$

where $\alpha = \frac{2\pi e^2}{hc}$ is the fine structure constant. Named after Ilya Frank and Igor Tamm, this was awarded with Nobel Prize in Physics in 1958 [89].

The peak of the Cherenkov emission from the EAS is in the blue to ultraviolet (UV), region at the edge of the optical band (the UV part is mostly absorbed by the atmosphere) [90]. The Cherenkov light emitted during EAS is detected by photomultipliers (PMTs) sensitive to wavelengths between 400-700 nm.

In the following the basic principles of the detection of Cherenkov light from ground are given.

2.5 Imaging Atmospheric Cherenkov Telescopes

The detection of gamma rays from ground is possible by detecting the Cherenkov radiation emitted during an EAS. The main challenge and difficulty is the discrimination of gamma rays and hadronic induced showers. Milestones in the development of IACTs were the Whipple experiment, which demonstrated the power of large mirror areas and imaging cameras [23], and the HEGRA (High Energy Gamma-Ray Astronomy) experiment, which demonstrated the power of telescope arrays to improve angular and energy resolution [92].

In an IACT, the Cherenkov radiation is focused by large reflective areas onto an imaging camera in the focal plane, which is accompanied by fast electronics for

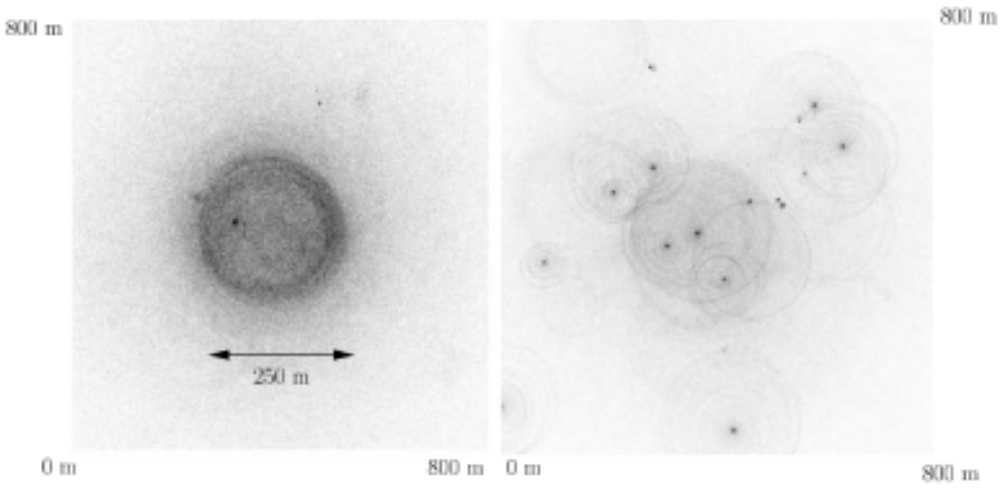

Figure 2.11: Cherenkov light pool of an extensive air shower induced by a photon with energy of 300 GeV (left) and by a proton with an energy of 1 TeV (right). Image courtesy [91].

readout and signal processing (principle shown in Figure 2.12). The reflective area is made of mirror facets supported by a solid frame on an azimuth or equatorial mount to track the sources during their diurnal motion. A finely pixelized camera is important to achieve a high sensitivity, as the number of pixels and in particular the field of view of each pixel determines the angular resolution of the telescope. Traditionally, the camera of an IACT uses photomultiplier tubes as pixels. Lately, SiPM are employed as well, for example in the FACT experiment [33].

The Cherenkov light emitted during a typical 1 TeV shower illuminates an area of $10^5\,\mathrm{m}^2$ on the ground. A Cherenkov telescope placed anywhere in the light pool can see the shower. Multiple factors have to be considered to determine properties of the emitted light. First, the Cherenkov light emitted during an air shower depends on the energy of the primary particle. High energy particles have sufficient energy to generate more secondary particles. Second, the number of particles generated during air showers depends on the altitude of the shower. The refractive index of the atmosphere at high altitudes is smaller but in the early stage of the shower development are not many particles above the energy threshold for Cherenkov light production, resulting in a low amount of light emitted. Other factors that affect the detectability of the Cherenkov light are related to the light pollution from the ground and night sky background i.e. the light from stars.

The gamma-ray energy and direction reconstruction becomes more robust when stereoscopy is employed. The shower direction is reconstructed more precisely when more than one telescope triggers on the same event and the Cherenkov light emitted from the same shower is seen from different angles. The use of the stereoscopy results in a larger collection area on the ground, and a large fraction of the background caused by photon fluctuations is suppressed. The currently operating IACTs make use of the stereoscopy for the event reconstruction.

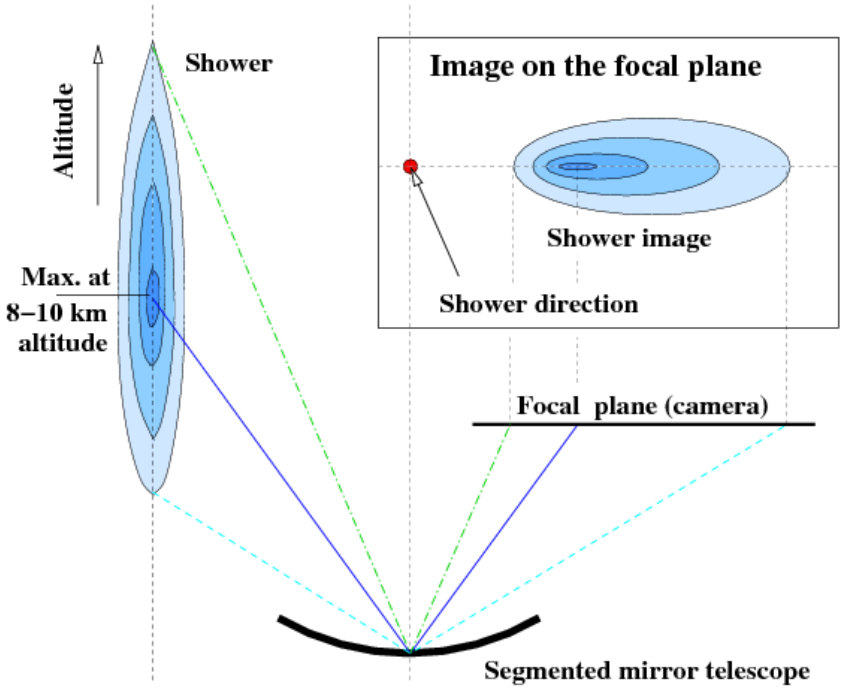

Figure 2.12: Illustration of the shower imaging principle in a telescope. The image shape of the shower in the telescope camera is almost elliptic and the corresponding reflection of different points of the shower into the focal plane of a camera are shown. The two main properties of gamma rays, the energy and direction are derived from the shower image on the camera. For gamma-ray induced showers, the image intensity gives information about its primary energy. Image courtesy [88].

2.5.1 Currently Operating IACTs

The currently major operating IACTs are MAGIC, VERITAS and H. E. S. S. The study at very-high-energy presented in this thesis is done with the H. E. S. S. instrument, which will be covered in detail in Chapter 3. Observation with the IACTs are limited to the night (low duty cycle of $\sim$ 10 % corresponding to moonless and no clouds).

2.5.1.1 MAGIC experiment

The MAGIC (**M**ajor **A**tmospheric **G**amma **I**maging **C**herenkov) experiment is a system of two 17 m diameter telescopes on the Canary Island of La Palma [31]. This experiment started operating in 2003 with one single 17 m diameter telescope. The reflective area is arranged in a parabolic shape reflector design. This is known as MAGIC I and had a 3.5° field of view camera composed of 397 small PMT pixels. In 2009, a second telescope was added 85 m away from the first one (MAGIC II), with a camera of 1039 pixels and a field of view of 3.5°. The camera of the first telescope was upgraded in 2012. The energy covered by MAGIC goes from 30 GeV up to 100 TeV. Figure 2.13a shows the MAGIC telescopes.

(a) (b)

Figure 2.13: (a) The MAGIC telescopes located in La Palma. Image courtesy: Daniel Lopez/IAC. (b) An artistic image of VERITAS telescopes located in Arizona. Image courtesy UCLA [93].

2.5.1.2 VERITAS experiment

The VERITAS (**V**ery **E**nergetic **R**adiation **I**maging **T**elescope **A**rray **S**ystem) is an array of four telescopes in southern Arizona, USA [94]. The telescopes are installed on the site of the Whipple telescope. Each of the telescopes has a 3.5° field of view, a 499-pixel camera and a 12 m reflective area. The VERITAS telescopes follow a Davies-Cotton optical design. The VERITAS observatory is studying the high-energy sky since 2007, by detecting gamma rays with energies from 50 GeV up to 50 TeV. Figure 2.13b shows the VERITAS telescopes. Chapter 4 describes observations of B2 1215+30 with VERITAS and *Fermi*-LAT experiments.

2.5.1.3 H. E. S. S. experiment

The H. E. S. S. in Namibia is an array of five IACTs observing the high-energy sky from the southern hemisphere. The array is comprised of four 12 m telescopes arranged in a square configuration and a bigger size telescope of 28 m placed in the middle. The H. E. S. S. II telescope, installed on the site in 2012 is the biggest IACT telescope to date. The energy range covered by the H. E. S. S. experiment goes from tens of GeV up to a few hundreds of TeV. The H. E. S. S. experiment is covered in more detail in Chapter 3.

2.5.2 Future Telescope Arrays

At the present time, a new ground based gamma-ray observatory is under development [95]. The **C**herenkov **T**elescope **A**rray (CTA) aims to reach a sensitivity improved by a factor of ten compared to the current experiments. The expected CTA differential sensitivity with that of the currently running experiments is shown in Figure 2.14 (taken from the CTA homepage[1]). CTA is planned to cover the en-

[1] https://www.cta-observatory.org

ergy range from a few tens of GeV to some hundreds of TeV using telescopes of three different sizes. CTA is designed to cover the full sky from two observation sites: La Palma in the northern hemisphere and Chile in the southern hemisphere and have a better angular resolution.

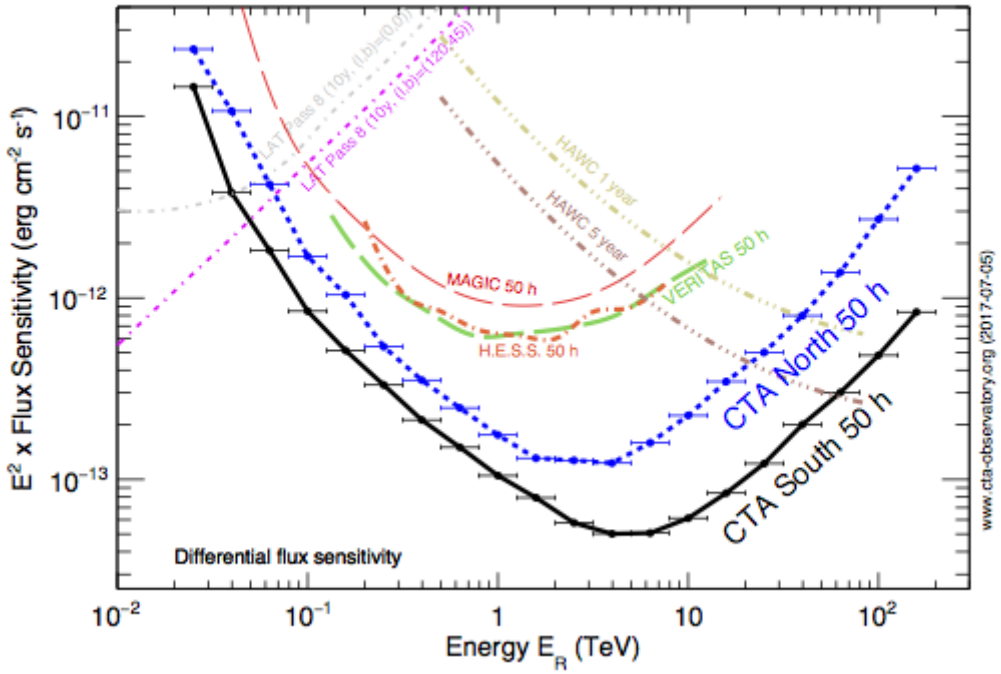

Figure 2.14: The differential sensitivity of CTA South and North compared to H. E. S. S., MAGIC, VERITAS and HAWC experiments. The CTA South and North, for 50 h of observations are expected to have a higher sensitivity with respect to other experiments and extend up to 100 TeV. Image courtesy [96].

2.6 Summary and Conclusions

In this chapter the basic principles for the detection of gamma rays from space and ground are given. For a direct detection of gamma-ray s from space, pair-conversion telescopes are sent above the atmosphere. The current gamma-ray space observatory based on this technique is the *Fermi*-LAT and observes the sky from 20 MeV up to more than 500 GeV. Energetic gamma rays interact with the atmospheric nuclei and generate extensive air showers, which produce Cherenkov light. The MAGIC, VERITAS and H. E. S. S. experiments are detecting very-high energy gamma rays from ground using arrays of imaging atmospheric Cherenkov telescopes. Given their different locations, the science covered by the current IACTs is diverse and brought unexpected results to the scientific community. The next generation of Cherenkov telescopes, the Cherenkov Telescope Array (CTA) is under development for a better sensitivity compared to the other experiments.

Chapter 3

The H.E.S.S. Experiment

The **H**igh **E**nergy **S**tereoscopic **S**ystem (H.E.S.S.) is located in the Khomas Highland of Namibia, at an altitude of 1800 m above sea level. The H. E. S. S. site was chosen, among other reasons, for the quality of the atmosphere and for its proximity to the Southern Tropic which provides optimal conditions for the observations of the Galactic center. Designed to study the very-high-energy sky, the H.E.S.S. experiment detects gamma rays of energies from a few tens of GeV up to hundreds of TeV using five imaging atmospheric Cherenkov telescopes.

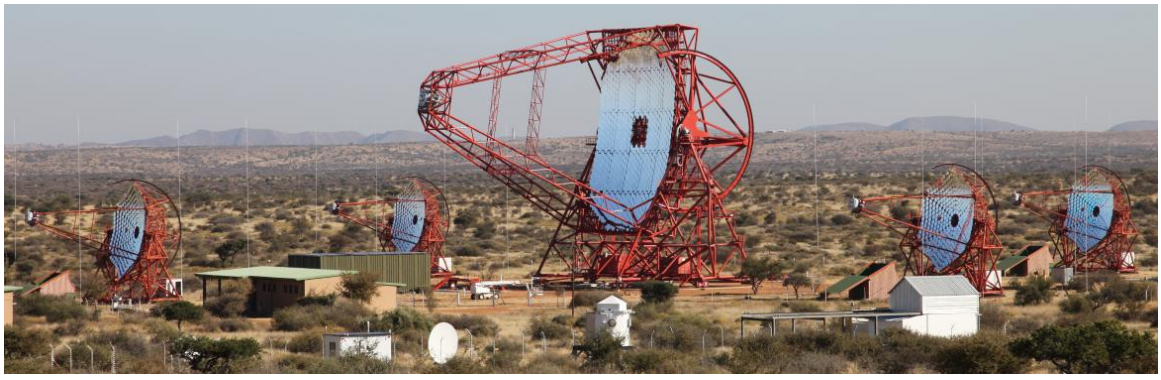

Figure 3.1: Picture of the H.E.S.S. telescopes in Namibia. Different trigger modes are supported by the current telescope configuration.

The experiment started operating in stereoscopic mode in 2003 with four telescopes of 107 m^2 reflective area and with energy range from few hundreds of GeV up to tens of TeV. This is referred to as H. E. S. S. Phase-I, and it consists of four identical telescopes arranged in a square configuration of side 120 m in order to maximize the effective collection area at a few hundred GeV. Since 2012, a big telescope with 614 m^2 reflective area, referred as H.E.S.S. Phase-II, was added to the array in order to lower the energy threshold down to few tens of GeV.

The main characteristics of the H. E. S. S. telescopes are given in Sections 3.1 and 3.2. The data acquisition and calibration procedure are described in Sections 3.3 and 3.4. A gamma-hadron separation method based on the Hillas Paramters and an alternative relying on template fits with simulated shower shapes are described in Sections 3.5 and 3.5.2 respectively. A possible monoscopic discrimination relying on boosted decision trees is elaborated in Section 3.7.

3.1 H.E.S.S. Phase-I

The first H. E. S. S. telescope was installed in Namibia in 2002 and the array become fully operational with the four identical IACTs in 2004. The H. E. S. S. I telescopes are comprised of a reflector area and a fast camera mounted on an steel alt-azimuth space-frame. This mount allows rotation speeds up to 100 degrees per minute, supporting fast slewing observations of transient events e.g. Gamma Ray Bursts. The reflector area is composed of 380 round mirror facets of 60 cm diameter, made of quartz-coated aluminized glass material and arranged in a Davies-Cotton design. Each telescope has a 107 m^2 mirror area in total. All mirror facets have the same focal length f, which is equal to the focal length of the whole telescope. The mirror facets are equipped by an automated alignment system, allowing their remote alignment by a CCD camera for optimum imaging qualities [97].

(a) (b)

Figure 3.2: (a) A picture of CT1 camera taken during the H. E. S. S. I camera upgrade in 2015. (b) One of the camera *drawers*, a unit of 16 photo-multiplier tubes. The drawers are fitted in the hexagonal structure of the camera. Image courtesy of H. E. S. S.

The steel structure supports a 900 kg finely pixelized camera, positioned at a focal distance $f = 15$ m from the center of the reflector area. Given the characteristic dish size d of 13 m, the telescopes have a $f/d \approx 1.2$. The camera consists of 960 Photomultiplier Tubes (PMT) with 0.16 degree field of view each, arranged in 60 drawers of 16 channels containing all the complete electronics needed for triggering, signal processing and digitization. The drawers are fitted in a cylinder structure of 2 m in length and 1.6 m in diameter, making a 5 degree field of view for each camera. Light concentrator "Winston" cones are installed in front of each PMT to guide the Cherenkov light onto the central region of the photo-cathode, where the quantum efficiency of the PMTs is maximal and to eliminate dead space between PMTs [98]. They also shield the albedo light from the ground. More details are given in [99].

Following more than ten years of successful operation of H. E. S. S., a major camera upgrade for H. E. S. S. I telescopes started in 2015 with the aim to improve the performance and reduce the failure rate of the ageing systems. During this upgrade, all the components inside the camera except for the PMTs were replaced. The design is motivated by studies performed for the NECTAR Cam [100].

3.2 H.E.S.S. Phase-II

The H. E. S. S. II telescope was added in the middle of the existing array in 2012, approximately 85 m from each of the H. E. S. S. I telescopes. The dish has a total reflective area of 614 m^2, almost six times larger than the one a H. E. S. S. I telescope. The H. E. S. S. II reflective area with a 28 m circular diameter makes it the biggest IACT up to date. It consists of an alt-azimuth steel mount, similar to that of the H. E. S. S. I telescopes. The H. E. S. S. II telescope is equipped with a fast drive system which allows speeds up to 200 degrees per minute, very favorable for transient observations [101]. The reflective area is composed of 875 hexagonal facets made of quartz-coated aluminized glass, arranged in parabolic design. The Cherenkov light is focused into the camera, at a focal distance of 36 m from the reflective area. The f/d ratio allows to better resolve extensive air shower images. The H. E. S. S. II camera comprises 2048 PMTs, where the signal processing, digitization and trigger are done in 128 drawers structures. The pixel size of each PMT (0.067 degree) gives a total field of view of 3.2 degree on the sky. The total weight of the telescope is 580 tons, where the camera alone has a weight of 3.0 tons.

(a) (b)

Figure 3.3: (a) The H. E. S. S. I telescopes with reflective area made of facet mirrors arranged in Davies-Cotton fashion. (b) The H. E. S. S. II telescope with refractive area made of facets arranged in parabolic fashion. Image courtesy of H. E. S. S.

After the installation of the H. E. S. S. II telescope, different trigger levels are supported by the full array. H. E. S. S. II supports monoscopic, or stereoscopic trigger modes with the H.E.S.S. I telescopes.

3.3 Data Acquisition

The PMT signal is read out in three channels where one is for the analog trigger and two for the high and low gain digitization. The sampling of the signal with different gains is done to increase the dynamical range of the instrument. The amplified signal from the PMTs is sent to an analogue memory which samples the signal at the frequency of 1 GHz. The third channel that sends the PMT signal to the trigger system, which has two levels. The idea of such system is to account for the presence of accidental events caused by night sky background events in the camera of the telescopes. To properly account for this effect the correlation between the neighbor pixels is considered. After the trigger decision at camera level, the coincidences between the other telescopes are considered. For a more detailed description of the H.E.S.S. data acquisition see [102].

3.4 Calibration

In the calibration process, the coefficients required to convert the electronic signals registered during the trigger into physical units are determined. Important information needed for event reconstruction and data analysis are determined and stored during this process. A set of calibration runs is taken during each observation period to ensure that the system is working properly. The list of calibration runs taken regularly with the H. E. S. S. telescopes includes *FlatField*, *SinglePE* and *Pointing* runs.

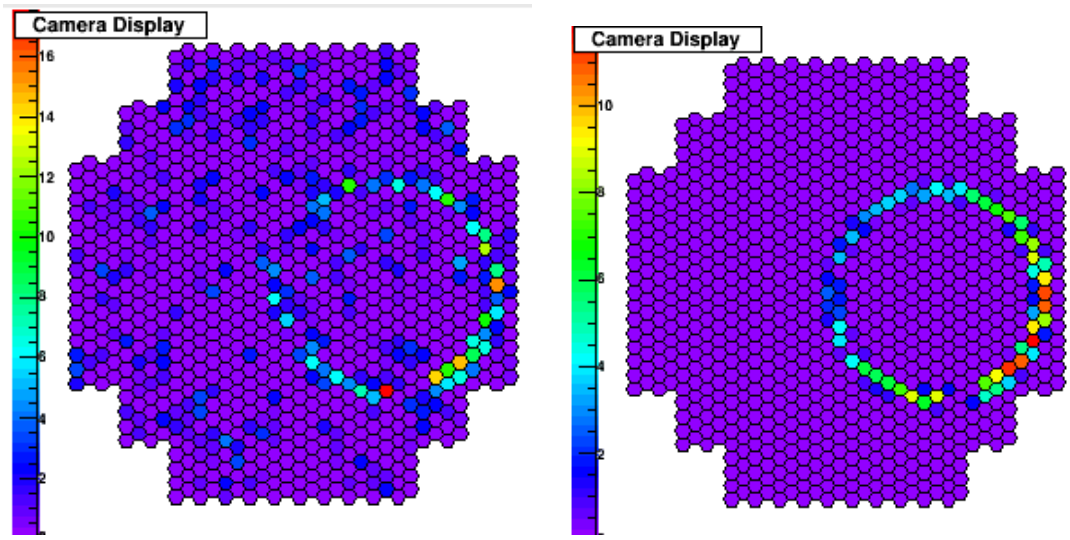

(a) (b)

Figure 3.4: (a) Example of a muon event on the H. E. S. S. camera. (b) The same image after cleaning and fitted by the model used for the calculation of the optical efficiency.

3.4.1 Camera calibration

In the following the camera calibration procedure is given. The detailed description of the H. E. S. S. camera calibration is covered here [103]. The coefficients required to complete the calibration process, the amplitude of pixels in high and low gain are calculated using the following formulas:

$$\begin{aligned} S^{HG} &= \frac{\mathrm{ADC_{HG}} - \mathrm{P_{HG}}}{\gamma_{HG}} \times FF \\ S^{LG} &= \frac{\mathrm{ADC_{LG}} - \mathrm{P_{LG}}}{\gamma_{HG}} \times \left(\frac{\mathrm{HG}}{\mathrm{LG}}\right) \times FF \end{aligned} \tag{3.1}$$

The coefficients presented in Equation 3.1 are described below.

- $\mathrm{ADC_{HG}}$ and $\mathrm{ADC_{LG}}$ are the measured number of *ADC* (Analogue to Digital Converter) counts in high and low gains respectively.
- $\mathrm{P_{HG}}$ and $\mathrm{P_{LG}}$ are the noise pedestals of the electronics in *HG* and *LG*.
- γ_{HG} is the *gain*, the conversion coefficient from *ADC* counts to photo-electrons.
- FF is the flat fielding coefficient. It characterizes the measured pixel efficiency of one specific PMT with respect to the total mean over the camera.
- HG/LG is the amplification ratio between the high to the low gain channels.

In order to complete the full calibration process, the calibration coefficients presented below are estimated separately in some steps.

3.4.2 Gain Calibration

A flashing LED, a stable and controlled light source, is placed in front of the camera to measure the single photo-electron peak of the PMTs. In order to avoid the NSB contamination, the LED is placed within the camera shelter, at a distance of 2 meters from the camera. Only the high gain has the resolution required to make this measurement. These dedicated *SinglePE* runs are taken every two nights and they serve to measure γ_{HG} in Equation 3.1.

3.4.3 Flat-Field Coefficients

The collection and quantum efficiency of individual PMTs is an important information to be measured and stored. This information is needed to convert photo-electrons into incident photons. The procedure is done by taking dedicated *FlatField* runs. A flashing LED (or a laser for H. E. S. S. II) uniformly illuminates the camera and the signal of each PMT is recorded. Then, the *FlatField* coefficients FF are estimated for each individual pixel by comparing the individual PMT responses to the average across the camera.

3.4.4 Pedestal Calibration

The baseline of the electronics is referred to as the noise pedestal. This must be subtracted from the measured ADC values to calculate the Cherenkov signal and therefore requires a precise measurement in order to not bias the determination of the Cherenkov signal. The pedestal is the response of the camera in absence of light. The electronic pedestal mean and width is determined by taking dedicated runs with camera lid closed to avoid noise from the NSB. Since the level of NSB, the atmospheric temperature or other instrumental effects change from one night to another, this process is done for each observation run.

3.4.5 Pointing Correction

The direction reconstruction of single gamma rays is directly affected by the orientation of the telescopes. Dedicated pointing runs are taken in order to calibrate the camera orientations by mapping the position of known stars from catalogs onto the camera of the telescope. A correct pointing model is of fundamental importance, since it affects the whole reconstruction and as a consequence the analysis results.

The mirror planes of the H. E. S. S. I telescopes are equipped with two CCD cameras: LidCCD (centre) and SkyCCD (at an offset of three meters, parallel to the optical axis). During the process of pointing calibration the camera lid is kept closed and only the caps of the camera LEDs are opened as they serve as reference points of the camera position. Bright stars images are taken simultaneously with the LidCCD and SkyCCD, which are compared with respect to the LEDs. This is done to determine the discrepancies between the expected and measured star positions of the LEDs to the known positions. This helps to measure the distortions of star images on the camera lid and to have a properly corrected pointing model, which is of fundamental use in the analysis. Another less robust method is to make a pointing correction while taking observations, which is described here [104].

3.4.6 Optical efficiency

The quality of data taken on a specific source depends on several criteria which can be instrument related or/and from other external factors. The reconstructed energy is calculated from the intensity of the shower on the camera, which depends on the optical efficiency of reflective area. The data accumulated is often spread over several months or even years, showing the importance of the long term stability of the optical system. The optical efficiencies of each telescope are measured using the known properties of muons. As muons interact minimally with the atmosphere, they have roughly constant speed and therefore the Cherenkov angle is constant. This results in a ring-like image on the camera. The velocity of the muon defines the radius of the ring and this along with its impact point on the ground give the number of photons in the muon ring. Hence, using muons to determine the optical efficiency of the telescopes is a very robust method. By definition, the muon efficiency is the ratio of detected to predicted photons. The number of detected photons is affected

by a set of factors such as mirror reflectivity, Winston cones and PMT efficiencies. Figure 3.5 shows the evolution of the H.E.S.S. Phase-I optical efficiency as a function of the run number [105]. A continuous drop is seen until 2011 (run number 60913), related of degradation of the mirror reflectivity and Winston cones. The optical efficiency increased after the re-aluminization of the mirrors.

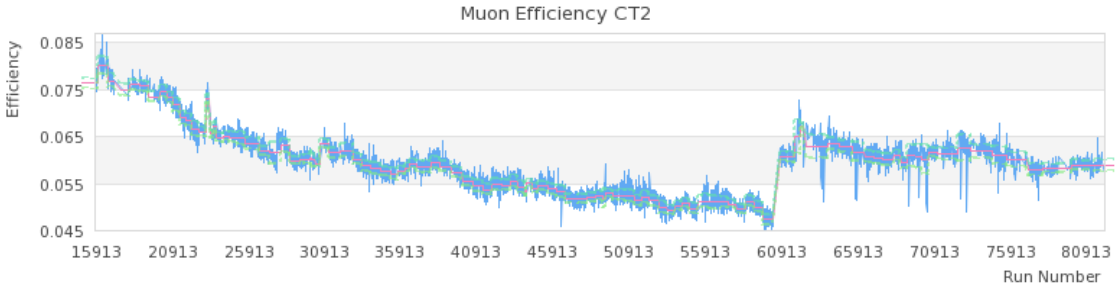

Figure 3.5: Efficiency evolution for one (CT2) of the H. E. S. S. I telescopes (blue). For each period, the calculated muon efficiency is plotted together with the mean (red) and one σ error (green). Figure courtesy [105].

3.4.7 Atmospheric Monitoring

The H. E. S. S. site is far from the city lights (100 km from the closest city), but weather conditions can affect the observations. The quality of the atmosphere affects the density of Cherenkov photons through absorption. In order to take data under optimal conditions and reduce the systematic effects at analysis level, additional facilities are provided on the site. Each telescope is equipped with a radiometer which points at the same direction as the telescope to monitor the sky temperature, humidity level and the clouds crossing the telescope field of view, but not the altitude of the clouds. Other full sky weather information is provided by the weather station and the scanning radiometer installed on the site. The radiometer gives detailed information about the weather and cloud coverage. The shift crew has the necessary weather monitoring information in the control room, helping to decide if the atmospheric conditions are good to start the observations and take good quality data.

3.5 Reconstruction Techniques

The main challenge of the reconstruction in gamma-ray astronomy is the high background rate. To solve this problem, several reconstruction techniques have been introduced by the community. The oldest successful technique for the signal and background separation is based on the Hillas reconstruction. Since its introduction, the robust Hillas reconstruction is widely used. Another powerful technique, called *Model* reconstruction is based on a semi-analytical model, which has been used to perform the analysis during this work. The most sensitive analysis techniques of

the H. E. S. S. data are provided by *Model* and Multivariate analysis methods [106]. The basics of these reconstruction techniques are given in the following.

3.5.1 Hillas Reconstruction

The shape of the images on the camera can be used to separate gamma-ray from hadron initiated showers. Given the main properties of extensive air showers (discussed in Section 2.4), gamma-ray induced showers have a more regular shape in the camera compared to hadron showers. Figure 3.6 shows two camera images, one with a gamma-ray and one with a proton induced shower [107]. Based on Monte Carlo studies a shower parameterization model, using the second moments of the pixel amplitudes in the camera, was proposed by Hillas in 1985. The width, length, center of gravity, angular orientation and position of the parametrized ellipses on the camera are used to reconstruct the shower properties. The camera images are then compared with simulated gamma-ray images to extract the shower parameters and reject hadrons. The robustness of this technique increases with the use of stereoscopy.

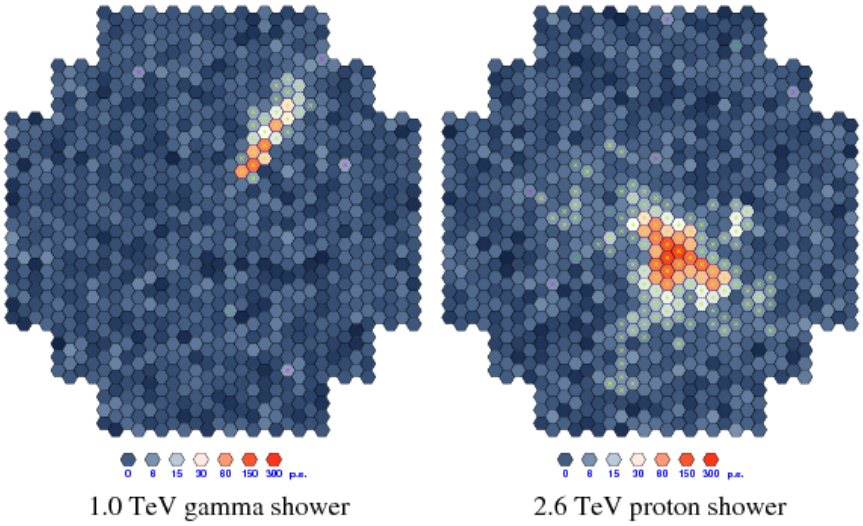

Figure 3.6: Two example images of the light intensity distribution in the camera of the telescope. Left: a 1.0 TeV gamma-ray shower image, with an regular ellipse-like shape. Right: the image of a 2.6 TeV proton in the camera, with an irregular and more wide shape. Image couresy [88].

3.5.2 Model Reconstruction

An alternative method, called the *Model* reconstruction, was adapted for the sterescopic reconstruction of the H. E. S. S. data by de Naurois & Rolland [108] based on the work of Le Bohec for the CAT experiment [109]. Based on image fitting with a semi-analatical model template, it is a powerful separation technique and yields improved sensitivity. With the installation of H. E. S. S. II, this method has been

successfully adapted for monoscopic reconstruction with H. E. S. S. II. The finely pixelized cameras of IACTs enable the use of a likelihood reconstruction, where the recorded shower images are compared to shower images predicted by a semi-analytical model for the Cherenkov light distributions induced by electromagnetic showers. The shower images are parametrized as a function of energy, primary interaction depth, impact distance and direction which results in a better reconstruction and gamma-hadron separation compared to other methods. The work performed here with H. E. S. S. uses the *Model Analysis* pipeline. In the following, the basic principles of the method are presented.

3.5.3 Shower Image Model

A proper and precise *shower model* to predict the Cherenkov photon density emitted during the electromagnetic showers is highly important. A semi-analytical shower model can be constructed by fitting a template function to simulated showers. The longitudinal and the lateral distributions of the charged particles in an air shower depend on the gamma-ray energy and the primary interaction altitude. For a given energy and altitude, the longitudinal, lateral and angular air shower profile under different conditions are modeled using Monte Carlo simulations from KASKADE [110]. The average number of charged particles produced during an electromagnetic air shower as a function of the distance from the primary interaction point for different gamma-ray energies is shown in Figure 3.7.

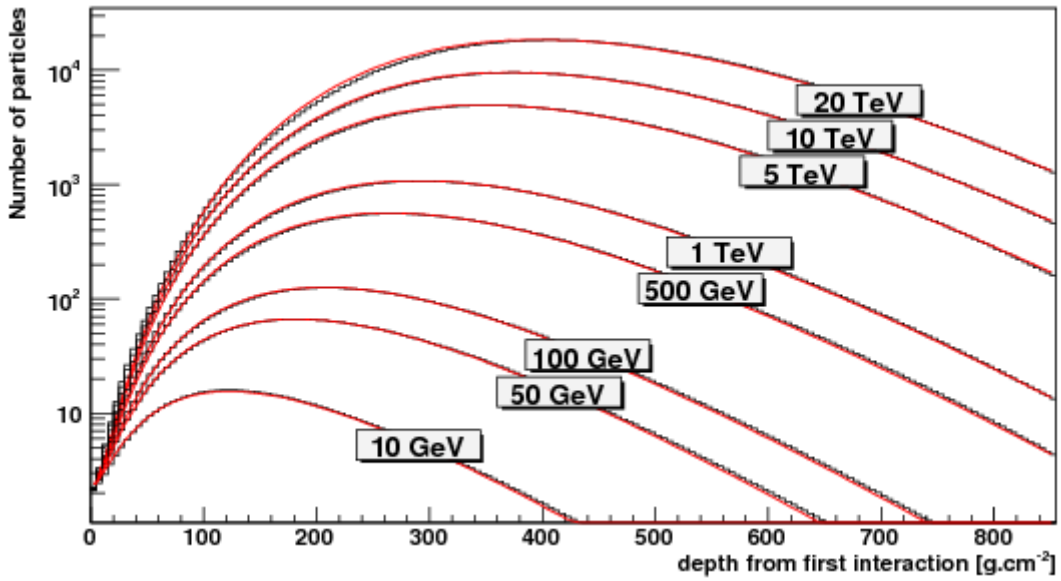

Figure 3.7: Longitudinal shower development as a function of energy, measured from the first interaction point. The black and red histograms correspond to the simulated and analytical (from Equation 3.2) results respectively. Image courtesy [108].

Following Greisens formula, the longitudinal distribution of charged particles is mod-

eled as follows:

$$\mathcal{N}_e\,(y,t) = \frac{a}{\sqrt{y}} \times \exp\left[t \times \left(1 - \frac{b}{b-1} \times \ln(s)\right)\right] + \left(2 - \frac{a}{\sqrt{y}}\right) \times \exp(-t), \quad (3.2)$$

where t is the distance from the first interaction point in units of radiation lengths X_0, y is the primary photon energy in terms of the critical energy $y = \ln(\mathrm{E}_{prim}/\mathrm{E}_{crit}$, and s represents the shower age, which is given by:

$$s = \frac{b}{1 + c \times (b-1)/t} \quad (3.3)$$

By definition, the shower age starts at the first interaction, which correspond to $s = 0$ and lasts until at the shower maximum at $s = 1$. The parameters c and b are the depth of the shower maximum measured from the first interaction and the scaling factor of the shower development, respectively. The best fit values obtained from the simulations are given below:

$$a = 1.05 + 0.033 \times y, b = 2.66, c = 0.97 \times y - 1.32 \quad (3.4)$$

The fit is represented by the solid red color in Figure 3.7 along with the simulations. Similarly, the lateral air shower profiles are considered in the semi-analytical model as well.

The Cherenkov light density, recorded by the telescope camera is calculated from the following integral:

$$\begin{aligned} I(x_T, y_T) \;=\; & \int \mathrm{d}z \int \mathrm{d}E \times \frac{\mathrm{d}\mathcal{N}_e}{\mathrm{d}E}(t,E) \times \frac{\mathrm{d}t}{\mathrm{d}z}(y) \\ & \int \mathrm{d}u \times F_u(u(E,s)) \int \frac{\mathrm{d}\phi}{2\pi} \\ & \int \mathrm{d}X_r \int \mathrm{d}Y_r F_{XY}(X_r, Y_r, E, s, u) \\ & \int \mathrm{d}\phi_{ph} \int \frac{\mathrm{d}\lambda}{\lambda^2} \frac{\mathrm{d}^2 n_\gamma}{\cos\theta \; \mathrm{d}z \; \mathrm{d}\lambda} \times \exp(-\tau(z,\lambda)) \times Q_{eff}(\lambda) \\ & \times Col(z, X_r, Y_r, u, \phi, \phi_{ph}) \; . \end{aligned} \quad (3.5)$$

Each line in the integral represent the electromagnetic shower development are longitudinal development and position of the electrons, the direction of the electrons, lateral position of the electrons, Cherenkov photons angles and distributions and the camera. The terms in Equation 3.5 are:

- $\mathrm{d}\mathcal{N}_e/\,\mathrm{d}E(t,E)$ the longitudinal distributions of charged particles in the shower
- $\mathrm{F}_u(u(E,s))$ the normalized angular distribution of particles as function of the energy and shower age
- $\mathrm{F}_{XY}(E,s,u)$ the normalized lateral distribution of particles as function of energy, age and rescaled angular direction of particles
- $1/\lambda^2 \times \mathrm{d}^2 n_\gamma/(\cos\theta\,\mathrm{d}z\,\mathrm{d}\lambda)$ the Cherenkov photon production rate
- $\exp(-\tau(z,\lambda))$ the atmospheric absorption

- $Q_{eff}(\lambda)$ the detector quantum efficiency
- $Col(z, X_r, Y_r, u, \phi, \phi_{ph}, x_T, y_T)$ is the average geometrical collection efficiency, which depends also on the incident parameters of the gamma-ray

The terms on the integral correspond to the:

- integral over atmospheric altitude z or depth t to account for the longitudinal development of the shower
- integral over the energy E of the electron/positron in the shower
- integral over the electron direction in the coordinate system of the camera
- integral over electron/position with respect to their directions in X_r and Y_r, the lateral coordinates in the shower frame in units of radiation lengths
- integral over the wavelengths of the Cherenkov emission
- integral over Cherenkov photon azimuthal angle around the electron, for a given fixed electron energy

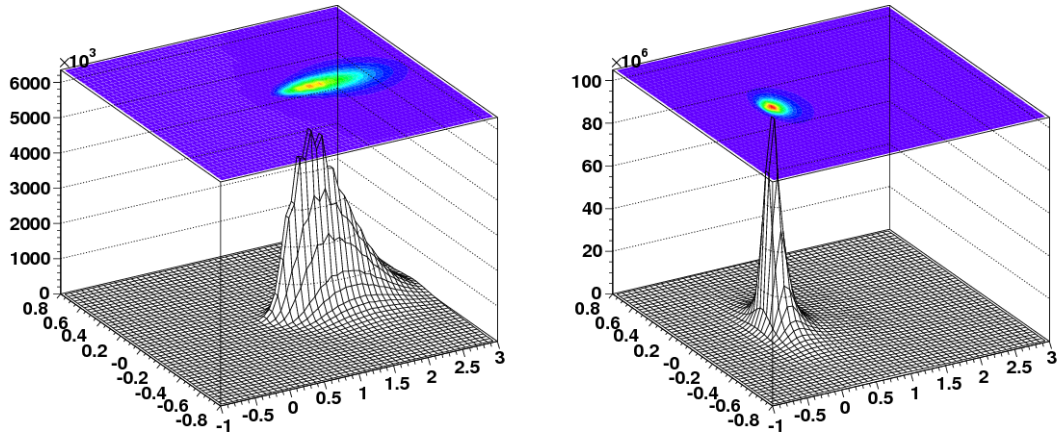

Figure 3.8: (a) Model of a 1 TeV shower started at one radiation length and falling 250 m away from the telescope. (b) Shower falling 20 m away from the telescope. Image courtesy [108].

Additional instrument and electronic related effects as the instrument point spread function, the trigger response and the integral computing time are taken into account. These effects together with the geometric light collection efficiency are simulated and stored in look-up tables over a wide range of different parameters i.e. zenith angles, impact distances, energies and interaction depths. For analysis uses, they are scanned over these parameters.

Two-dimensional shower images in the camera frame are produced from this procedure. Figure 3.8 shows two examples of *Model* showers falling at different distances to the telescope. The raw shower images are then compared with the shower model template from the semi-analytical model on a pixel-by-pixel basis. A likelihood

minimization procedure gives the best parameters from a log-likelihood fit, which determine the properties of the incoming gamma rays.

3.5.4 Model Variables

To quantify the deviation of the gamma-ray shower from the template shower, i.e. the quality of the fit, a parameter called *Goodness* is determined. This quantity is calculated from the log-likelihood values in the pixels i as follows:

$$G = \sum_i \frac{\ln L(s_i|\mu_i) - < \ln L > |_{\mu_i}}{\sqrt{2 \times \mathrm{NdF}}}, \tag{3.6}$$

where $\ln L(s_i|\mu_i)$ represents the log-likelihood to observe a signal s_i in photo-electrons under the hypothesis of a signal μ_i, $< \ln L >$ is the expected value of $\ln L$ if there are μ_i hypothesized photo-electrons and NdF is the number of degrees of freedom. Unlike the *Goodness* which is calculated for the whole camera, the *Shower Goodness (SG)* is calculated for the pixels attributed to the shower. For each telescope, the *Shower Goodness* is determined from the pixels of the shower core, using Equation 3.6. The *Mean Scaled Shower Goodness* is averaged over all-telescopes t:

$$MSSG = \sum_t \frac{SG_t - < SG >}{\sigma_{SG}\sqrt{N_t}}, \tag{3.7}$$

where N_t is the number of telescopes and σ_{SG} is the width of the SG distribution determined from the Monte Carlo simulations. The *Background Goodness* is another parameter for event selection, calculated from Equation 3.6 for only pixels outside the shower. The fluctuations caused due to NSB are also taken into account by a *NSB Likelihood* variable when μ_i is 0.

Another parameter with significant separation power, the *DirectionError*, is calculated from the uncertainty of the fit. Cutting on the direction uncertainty distribution helps to keep the events with the best angular resolution. The *PrimaryDepth*, the first interaction point is another parameter used to discriminate between the gamma and hadron-induced showers, as electromagnetic showers interact later on the atmosphere compared to the hadron induced showers. Cuts based on these parameters are used in the analysis of H. E. S. S. data. Their cut values depend on the analysis method, which are presented next.

3.6 Model Analysis

After defining variables with powerful separation power, they are optimized for the analysis of different astrophysical sources. Since the trigger system of H. E. S. S. supports monoscopic and stereoscopic triggers, different event reconstructions are developed within *Model Analysis*. Figure 3.9 shows different reconstruction techniques supported by H. E. S. S.

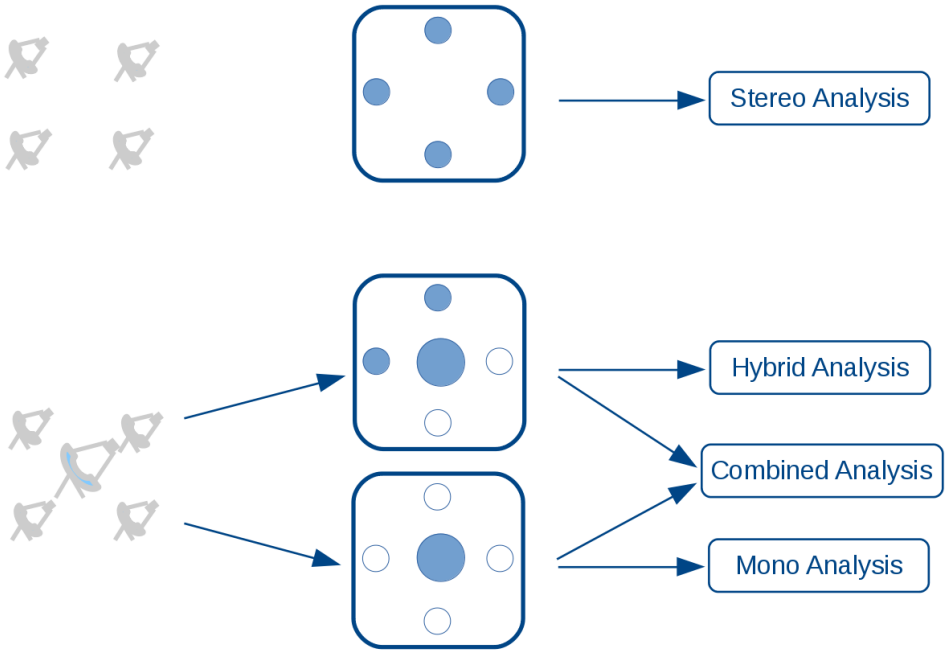

Figure 3.9: Schematic illustration of different event trigger and reconstruction types of the H. E. S. S. experiment. The top part of the figure correspond to the trigger of H. E. S. S. Phase-I which are reconstructed with Stereo. In the bottom are shown the H. E. S. S. Phase-II trigger modes. The array can trigger CT5 and CT1-4 and only CT5 and reconstruct events by using the Combined, Hybrid and Mono.

For the H. E. S. S. I Phase-I, a trigger was required with at least two of the small telescopes participating, named CT1, CT2, CT3 and CT4. After the experiment entered its Phase-II, different observation strategies are supported by the array. The array is split and H. E. S. S. II (CT5) and CT1-4 can take data independently, or CT1-5 observe in Hybrid mode. The monoscopic (hereafter Mono) trigger uses only events from CT5. The stereoscopic (hereafter Stereo) consist of CT1-4 observations with, and without CT5 telescope. Observations including CT5 require it in trigger with at least two from the CT1-4 telescopes (hereafter Hybrid). In the following the different analyses for the H. E. S. S. I- and H. E. S. S. II-era are described.

3.6.1 H. E. S. S. I

Only events with at least two participating telescopes, hereafter *telescope multiplicity*, are accepted for reconstruction. A threshold on the number of photo-electrons for each event in the camera is set to remove faint events caused by noise or NSB. Additional cuts are applied to reject events falling on the camera edge. This is done by cutting on the nominal distance, i.e. the distance between the camera center and center of gravity of the shower, at 2 degrees. Another cut applied on the primary interaction depth i.e. the amount of atmosphere traversed before a particle initiates an electromagnetic EAS, removes showers produced by electrons. Motivated by the diversity of astrophysical sources and their emission spectra, different cut

parameters have been developed for H. E. S. S. I data. Table 3.1 summarizes the *Standard* (Std) and *Loose* cut parameters, as they are used for this work. Other cut configurations for faint or extended sources are available but are not covered here.

Parameter	min p.e.	max MSSG	min NSB	max direction error	min primary depth
Std	60	0.3	20	0.1	-1.1
Loose	40	0.9	10	0.2	-1.1

Table 3.1: Cut parameters for the H. E. S. S. I Stereo analysis and their corresponding cut parameters for *Std* and *Loose* configurations in *Model Analysis*.

3.6.2 H. E. S. S. II

The diverse trigger modes supported by the array allow to perform different event reconstruction with the H. E. S. S. Phase-II data (Figure 3.9 bottom). The Mono reconstruction allows to lower the energy threshold of the analysis, but in absence of the stereoscopy the background substraction is more challenging. The high event rates at lower energies, require precise background estimation methods. The triggered events, where CT5 was part of the observations provide better results if they are reconstructed using the stereoscopy. The Combined reconstruction makes use of the Mono and Stereo events. The H. E. S. S. II telescope allows to exploit the lower energy range and in combination with the H. E. S. S. I they cover a widen energy range. The cut parameters for the standard and loose configurations for the Mono, Hybrid and Stereo analyses are summarized in Table 3.2.

Config		min p.e.	max MSSG	min NSB	max dir error	min prim depth
Mono	Std	60	0.7	19	0.3	-1.1
	Loose	60	0.6	15	0.3	-1.1
Hybrid	Std	60	0.9	28	0.2	-1.1
	Loose	40	0.9	13	0.2	-1.1
Combined	Std	60	0.9	32	0.2	-1.1
		60	0.6	32	0.3	-1.1
	Loose	60	0.9	16	0.2	-1.1
		60	0.6	24	0.3	-1.1

Table 3.2: Cut parameters for Mono, Hybrid and Combined analysis with H. E. S. S. Phase-II and their corresponding cut parameters for Std and Loose configurations in *Model Analysis*. The Combined profile has two set of cuts, adapted to be applied to Mono and Stereo events.

3.6.3 Source detection and background estimation

Even after the set of cuts introduced above are applied, there is still a relatively high level of background contamination. The main background consists of misclassified events, i.e. gamma-like events from hadron and electron induced showers. For source detection, it is important to have a methodology for the background estimation. The background is estimated by counting events which are reconstructed in a region or regions of the sky where no gamma-ray sources are expected. A number of approaches have been suggested as discussed below. The standard method to estimate the background is by defining the source region as ON and the background as OFF. Having a proper method for defining the OFF background is essential for good and reliable results.

The number of events attributed to a source, referred to as the number of excess events, is the difference between N_{ON} and background N_{OFF}:

$$N_{excess} = N_{ON} - \alpha N_{OFF}, \tag{3.8}$$

where α is a normalization factor that takes into account the exposure times, region sizes and the detector responses in each corresponding region. The normalization factor can be estimated using the *Reflected Region* or the *Ring Background* method [111]. This work makes use of the two methods to estimate the background.

In the *Ring Background* method, an annulus region around the source is selected to estimate the OFF background as shown in Figure 3.10b. Since the ring covers areas with different offsets from the observation position, the camera acceptance to gamma-rays has to be taken into account while calculating α. For extragalactic sources this is a straightforward calculation while for complex regions like the galactic centre requires the size of the ring to be adapted. This method allows to represent spatial distributions of the excess and the significance in two-dimensional sky maps.

The application of the *Reflected Region* requires that the observations are taken deliberately offsetting the source of interest from the center of the camera by a given angular distance, known as *"wobble"* mode. Typically the offset angles are chosen between 0.5 and 1.0 degrees, considering the instrument field of view and the broadening of the PSF at large offset angles. Multiple OFF regions n_{OFF} are taken around the camera center, with the same offset as the ON region. To avoid contamination from the source, a circular region around the ON region is excluded from the background estimation. To compensate for the excluded ON regions, *wobble* observations with alternate positive and negative right ascension (R.A.) and declination (Decl.) are taken. The value of the excluded ON region depend on the source and on the type of analysis chosen. For point like sources, the excluded value of the ON excluded region is 0.1 degrees for Stereo analysis and 0.4 degrees for Mono.

Using this method, where the ON and OFF have the same *wobble* offset allows to estimate the background during each observation. The normalization α factor in the Equation 3.8 is simply $1/n_{OFF}$. Following Equation. 17 from Li & Ma [112],

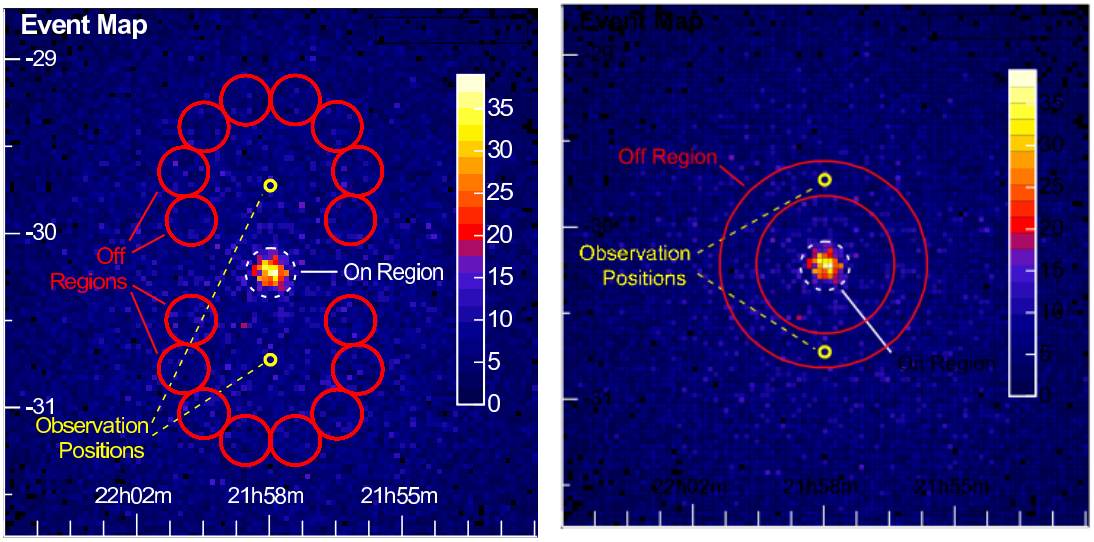

(a) (b)

Figure 3.10: Schematic of ON and OFF regions in the (a) *Reflected Region* and (b) the *Ring Background* method. Images courtesy [111].

the statistical significance of the excess is:

$$S = \sqrt{2}\left\{ \mathrm{N_{ON}} \ln\left[\frac{1+\alpha}{\alpha}\frac{\mathrm{N_{ON}}}{\mathrm{N_{ON}}+\mathrm{N_{OFF}}}\right] + \mathrm{N_{OFF}} \ln\left[(1+\alpha)\frac{\mathrm{N_{OFF}}}{\mathrm{N_{ON}}+\mathrm{N_{OFF}}}\right]\right\}^{1/2}. \tag{3.9}$$

The background subtraction also affects the energy range of the measured spectrum. The intrinsic source properties are provided by the measured spectrum, which gives insights on the acceleration power. The method used in this work to measure the energy spectrum with H. E. S. S. data is described next.

3.6.4 Spectrum

To study the high-energy emission from a given source, an accurately reconstructed gamma-ray energy is important. In astrophysics, the energy spectrum refers to the source differential flux as a function of energy. The measured energy spectrum gives information about the acceleration processes, responsible for powering particles up to very-high-energies. Telescope arrays built on the ground must determine the gamma-ray energy based on the sampled density of the Cherenkov light, which is affected by different observation conditions i.e zenith angles, offaxis angles, optical efficiency and other instrument limitations. The observational conditions like zenith angles, offaxis angles and the optical efficiency are noted as C in the following. To correct for these effects, is important to know the effective area and the angular resolution of the detector as a function of C.

The effective area $\mathcal{A}(E, C)$, is related to the detector *acceptance*, the probability to detect a particle as a function of C, impact parameter and energy. For a gamma-ray with a fixed energy, the effective area $\mathcal{A}(E, C)$ is calculated as a function of the

zenith, offaxis angle and optical efficiency by integrating the detector acceptance over impact points on the ground (transforming probability to area) and stored in multidimensional tables. Thus, depending on the different observation conditions, tables allow to interpolate in the whole parameter space. Figure 3.11b shows an example of an distribution of the effective area versus the energy and the zenith angle. In absence of statistics in the low energy range, irregularities on the tables and zero acceptance values are introduced. Such problems are avoided in the spectrum calculation by introducing an energy threshold which for a standard H. E. S. S. I analysis is typically set to 10 % of the maximum effective area.

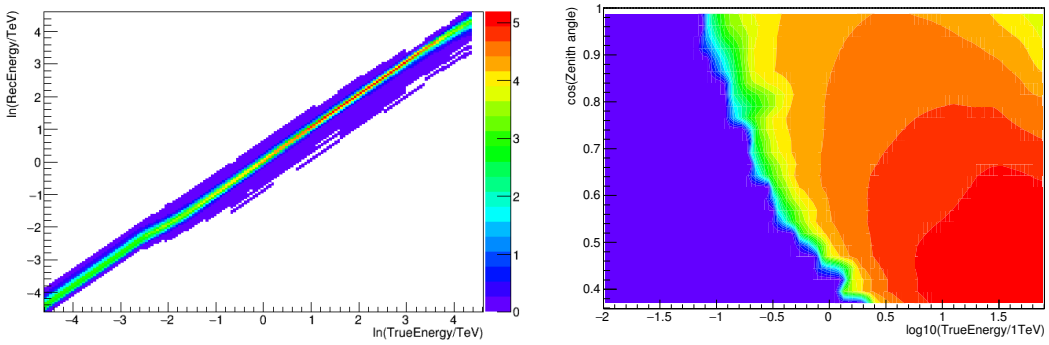

(a) (b)

Figure 3.11: (a) Example of an energy resolution table in *Model Analysis*. For a set of parameters, it gives the probability density to measure the energy E_{rec} for a given true energy E_{true}. (b) Effective area of *Model Analysis* for a given set of paramters.

The energy resolution $\mathcal{R}(E', E, C)$ is the probability density of reconstructing an event energy E′ given the true energy E. Both, the effective area and the energy resolution are calculated from simulations. Figure 3.11a shows an example of an energy resolution table in *Model Analysis*.

The expected number of events n_γ in a given energy bin $[E'_1, E'_2]$ is calculated as follows:

$$n_\gamma = \int_{\mathrm{E}'_1}^{\mathrm{E}'_2} \mathrm{d}E' \int_0^\infty \mathcal{R}(E', E, C) \times \mathcal{A}(E, C) \times \phi(E)\, \mathrm{d}E, \tag{3.10}$$

where $\phi(E)$ is the true flux of the source. For a given energy bin with n_γ gamma rays and n_h hadron events described by Poisson statistics, a likelihood minimization procedure is performed. The minimization fit determines the spectrum parameters that best describe the distribution of events. Additional information like parameter uncertainties and the covariance matrix between parameters are also determined.

The spectrum is calculated using a *"forward-folding"* method i.e. the fit is performed assuming a shape for the spectrum of the source. The spectral shapes of different sources, motivated by the *Fermi acceleration* are approximated by different

functions. The most simple spectral shape is given by a power-law function:

$$\frac{\mathrm{d}N}{\mathrm{d}E} = N_0 \left(\frac{\mathrm{E}}{\mathrm{E}_0}\right)^{-\Gamma}, \tag{3.11}$$

where N_0, E_0 and Γ are the normalization, reference energy and spectrum index. After their mathematical expressions are given, a physical interpretation is important. The simplest case of a power law spectral shape tells that the differential flux is changing (increasing or decreasing depending on the value of Γ) as a function of E in a manner that must be related to the acceleration and radiation mechanisms at place in the source.

Other spectral shapes are found to better describe the energy spectrum for other sources but the ones used on this work are presented below. In case of curvature in the measured spectrum, a log-parabola function is used:

$$\frac{\mathrm{d}N}{\mathrm{d}E} = N_0 \left(\frac{\mathrm{E}}{\mathrm{E}_0}\right)^{-\alpha-\beta\ln\frac{\mathrm{E}}{E_0}}. \tag{3.12}$$

A power law with an exponential cut-off at E_c is popular as well:

$$\frac{\mathrm{d}N}{\mathrm{d}E} = N_0 \left(\frac{\mathrm{E}}{\mathrm{E}_0}\right)^{-\Gamma} \exp(-\frac{\mathrm{E}}{\mathrm{E}_\mathrm{c}}). \tag{3.13}$$

At the analysis level, the energy threshold for the spectrum is calculated from the effective area. For H. E. S. S. I analysis, the energy threshold for each event is set to 10% of the maximum effective area. For mono analysis the threshold is set at 25% of the maximum effective area. However, these values can be changed for specific sources and different sky regions.

After the spectrum of a given astrophysical source is measured, other physical properties can be studied. The lightcurve, which provides information about the flux evolution with time, is described next.

3.6.5 Lightcurve

The term lightcurve commonly denotes the time evolution of the integrated flux in a given energy range. This is based on the principles described above and uses the best-fit spectrum values to calculate the integral flux in a given energy range, or above a given energy. The accuracy of the lightcurve is important when studying the flux evolution of variable sources like active galaxies, which are known to undergo flaring activities. The lightcurve has to be sensitive when investigating TeV flux variability for other sources like the Crab Nebula, which is found to be variable in the GeV energy range.

In the method presented here, the integral flux is determined via a likelihood minimization. For each time bin, the excess number of events is defined by Equation 3.8. The spectral index is kept fixed to the value obtained in the spectrum determination

and the integral flux is calculated in different time bins. The integral flux above 1 TeV is calculated as follows:

$$\Phi(E > 1\text{TeV}) = \int_{1\,\text{TeV}}^{\infty} \frac{\mathrm{d}N}{\mathrm{d}E}\mathrm{d}E, \tag{3.14}$$

where the spectrum shape $\mathrm{d}N/\mathrm{d}E$ varies depending on the source properties. This method is used also when performing analysis on short time bins, if there are enough statistics. The systematic errors on flux for H. E. S. S. is estimated to be 20 % [113].

Other methods have been developed, i.e. the *Transient Analysis* for variability studies. These tools are described in [114] and they are used as a cross-check for the H. E. S. S. II lightcurve presented in Chapter 6.

3.7 Multivariate Analysis

Discriminating signal events from the vast background events requires sophisticated analysis techniques. If the event is characterized by a number of independent variables, it can be categorized using a **M**ulti**V**ariate **A**nalysis (MVA). The MVA used for this analysis is implemented in the **T**oolkit for **M**ulti**V**ariate **A**nalysis (TMVA), a software distributed with ROOT [115]. TMVA includes different algorithms for MVA such as neural networks, Likelihood classifiers or Fisher discriminants which in general have a very similar working scheme.

Boosted **D**ecision **T**rees (BDT) is an MVA method commonly used in high-energy physics. Like all MVA, it combines a set of input variables to one single discriminant. The strength of the BDT is the capability of exploiting nonlinear correlations of the input variables and the high efficiency to ignore input variables with low or no separation power. The BDT algorithm adapted for the H. E. S. S. I data showed to be powerful for discriminating gamma rays from background hadronic induced showers (see [106]). In the following the basic principles of a BDT and the adaption of this method for monoscopic reconstruction of H. E. S. S. II events are described.

3.7.1 Boosted Decision Trees

BDTs provide a powerful machine learning algorithm for event classification. The decision tree is based on binary split criterion which classifies events as signal or background. The classification starts at the first node with a binary decision taken based on the most discriminating input variable (see Figure 3.12). Consequently, the classified events suffer other binary splits based on the most discriminating remaining input variables until a maximum tree depth is reached. The input variables can be ranked by discriminating power using for example the Gini index, which is based on the signal purity p after the cut ($p = N_S/N_{S+B}$). It is calculated as $p(1-p)$ and the optimal cut is found by minimizing it. The most powerful input variable is the one with the lowest Gini index. This phase space decision is sequentially repeated at each node, until each events is well positioned in a classification parameter space.

For their application as a signal-background discriminant in the H. E. S. S. analysis, the BDT is trained with Monte Carlo data. Since one single decision tree is prone to statistical fluctuations in the training sample, a forest of decision trees (boosting) is taken i.e. the classification process is repeated over many times. After each boost, misclassified events from the previous tree are multiplied with a weight α. This is called the *AdaBoost* or adaptive boost method and α is calculated as follows:

$$\alpha = \frac{1-\varepsilon}{\varepsilon}, \tag{3.15}$$

where ε is the fraction of misclassified events. The output of the BDT, ζ is calculated from the following formula:

$$\zeta(x) = \frac{1}{N_{Trees}} \sum_i \ln(\alpha_i) h_i(x), \tag{3.16}$$

where N_{Trees} is the total number trees in the forest, h_i and α_i are the classifier response and the boost weight for each tree, respectively. The classifier response h_i delivers -1 for background-like and +1 for signal-like events, hence the values of ζ are distributed between -1 and +1.

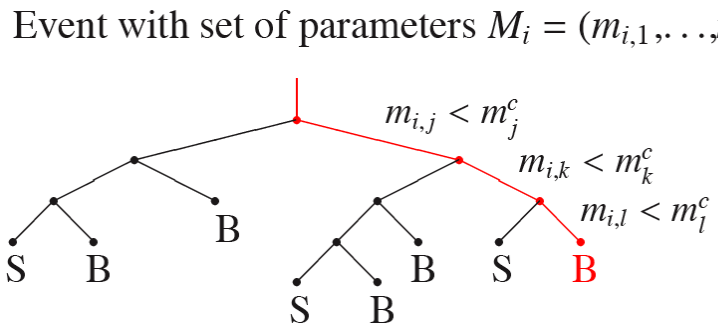

Figure 3.12: Schematic view of a decission tree where each event is characterized by a set of input varibales $M_i(m_{i,1},...)$. The event classification at each node follows a binary split criteria. Image courtesy [106].

3.7.1.1 BDT Settings

The BDT implementation in ROOT is distributed with default parameters. In general they are optimized for stable training, but they need to be understood and checked as they might cause other problems e.g. overtraining. A stable set of parameters found for the thesis work is described below:

- `NTrees`: the number of trees in the forest is 200, a compromise between separation performance and processing power. The larger this number is, the larger is the computing time needed for the classification.
- `Gini Index`: the method used for ranking the variables (see text).
- `MaxDepth`: the maximum depth of the decision trees allowed is 500.

- `nCuts`: to find the optimal cut value for each event variable, the parameter space is scanned with a step size of 100. This is to find the optimal cut in each node splitting.
- `PruneMethod`: the tree pruning is a process to eliminate the unimportant nodes. This work uses the `CostComplexity` algorithm, which compares the cost and the additional output in classification performance in case of further splitting below a certain node. The default algorithm parameters are used.

3.7.2 Monoscopic reconstruction

A multivariate analysis relying on BDTs is an alternative method that provide powerful gamma/hadron separation for H. E. S. S. data. The multivariate analysis method was tested on the H. E. S. S. I data and was implemented also in the `ParisAnalysis` framework as an additional analysis tool for the users. Observations with H. E. S. S., but also with high-energy instruments in general are prone to large systematic effects, so different reconstruction techniques are developed. Cross-checking results with two different analysis frameworks has become a mandatory procedure within H. E. S. S. Besides the `ParisAnalysis` based on *Model Analysis*, another analysis framework called HAP works with an independent calibration and event reconstruction scheme [116]. The MVA methods are widely used in the HAP framework. For the study presented in the following, the MVA with the BDT was adapted and implemented for monoscopic reconstruction in the `ParisAnalysis` framework.

The analysis of H. E. S. S. II data using solely information from CT5 is challenging due to the large systematic effects, especially at low energies. This motivated the refinement of the monoscopic identification with the BDT, planned for a later application to lower the energy threshold of the Crab Nebula, the main subject of this thesis with H. E. S. S. experiment.

After describing the BDT training procedure, the main input variables used for the signal/background event separation and the corresponding results are given.

Training of the BDT

A BDT must be trained with events of known type and classification, in this case signal and background event samples. The signal sample consists of Monte Carlo gamma events simulated with a power law spectrum with a spctral index of 3, using the latest software of `ParisAnalysis`. The generation of Monte Carlo events was done at offset angles of 0.5 degrees, zenith angles ranged between 0 and 25 degrees and azimuth angles of 180 degrees. This restriction is to limit computing time while checking the validity of the method for a given acceptance range before it is expanded to the whole dynamic range of H. E. S. S..

The background events are from the OFF regions of observations on PKS 2155-304, a distant (z=0.116) extragalactic BL Lac source continuously monitored by H. E. S. S. As an extragalactic source it has the advantage of a uniform background distribution

across the camera of the telescope and no contamination from the diffuse emission of the Galactic plane. A run selection is done to match the Monte Carlo simulations: only runs with zenith angles between 15-25 degrees and offset angles of 0.5 degrees from the camera center were used.

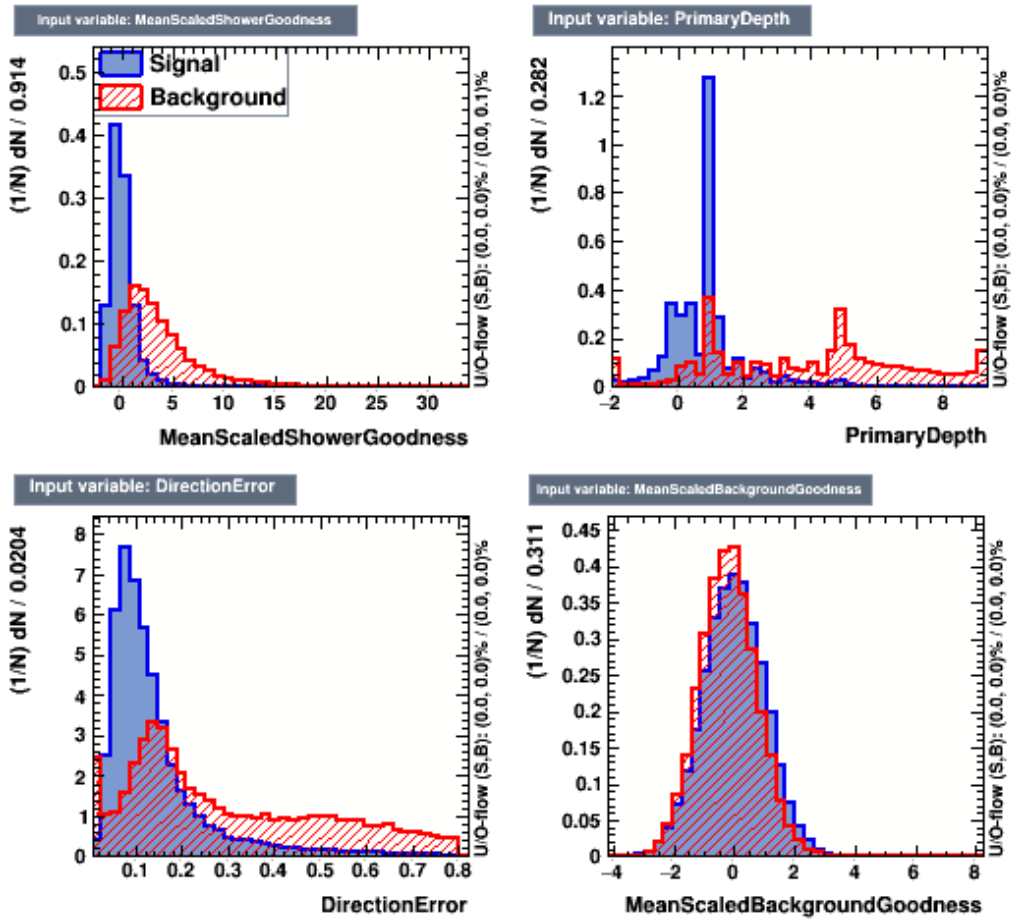

Figure 3.13: Example of input variable distributions for signal and background in the energy bin 700 GeV $< E <$ 1 TeV for zenith angles between 15-25 degrees. They reveal the variables with little to no separation power e.g. the *Mean Scaled Background Goodness* and with high separation power, e.g. the *Mean Scaled Shower Goodness.*

To avoid problematic events which cannot be well parametrized, both samples are filtered before the training. For instance, a cut on the nominal distance i.e. the distance between the center of the gravity of the reconstructed image and the camera center is applied to avoid events falling on the camera edge. These events are usually truncated and consequently not well parametrized. Possible contamination from real gamma rays from the ON region of PKS 2155-304 is mitigated by a cut on the squared angular distance between the reconstructed and true direction, with values of $\vartheta^2 > 0.3$ for signal and $\vartheta^2 < 0.1$ for background events. The input variable distributions for each training sample were checked and since some strange behavior was seen in the *Direction Error* distributions, another cut at *DirError* < 0.8 was applied for both samples.

Energy bins boundaries [GeV]	30	70	100	300	500	700	1000	
Zenith bin boundaries [degrees]	0	15	25	35	42.5	47.5	52.5	60

Table 3.3: The BDT training bins in energy and zenith.

For the training, 6 energy bins and 7 zenith bins have been constructed as in Table 3.3, resulting in a total of 42 bins. For each energy and zenith band, one BDT is created and trained with the samples introduced above. The different training bands in energy and zenith are motivated by the dependence of the Cherenkov photon density on these parameters. For the chosen samples, only 14 bins have enough events to complete the training, which is due to the zenith angles choice. To proceed with the BDT training in each bin, a minimum of signal and background 1000 events is required.

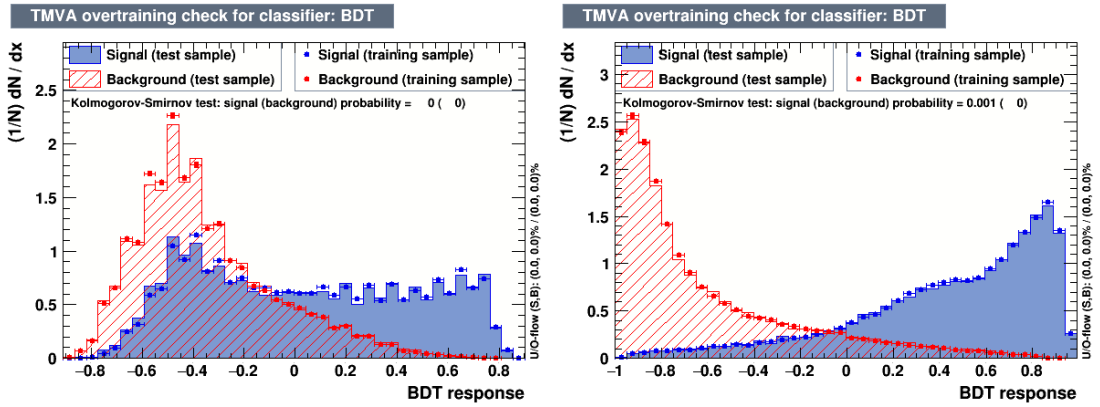

(a) Energy band 30 to 70 GeV. (b) Energy band 700 GeV to 1 TeV.

Figure 3.14: The BDT output distributions for signal (blue) and background (red) in the first zenith bin (15 - 25 degrees) in different energy bands. The overlap of signal and background in the low energy band is excepted as monoscopic observations are poor for background discrimination. At high energies the separation is better.

The list of considered input variables includes the *Mean Scaled Shower Goodness*, the *Primary Depth*, the *Mean Scaled Background Goodness*, the *NSB Likelihood* and the *Direction Error*. Figure 3.13 shows some input variable distributions, where it can be seen that the *Mean Scaled Background Goodness* has no separation power which led to its exclusion from the list of input variables. The input variables with the highest discriminating power are found with the TMVA variable ranking and correlation plots. The list of input variables kept for the training is:

- Mean Scaled Shower Goodness
- Primary Depth
- Direction Error

The selection and ranking of these variables as the most important ones is not surprising, as for example the *Mean Scaled Shower Goodness* was delibaretely con-

structed for a good separation in the *Model Analysis* framework. is the primary discrimination parameter used in *Model Analysis*, along with the other ones.

These variables complement each other to cover a wide energy range as some variables are better for the discrimination at high energies while others are better at low energies. For instance, the *DirectionError* is a better parameter at high energies.

For the training phase, 70 % of the sample was used. The rest was reserved for the application, where the performance of the BDT in each training band is benchmarked.

Figure 3.14 shows the BDT output distribution for signal and background events in both a high and low energy band for zenith angles between 15 and 25 degrees. The other training bands are not shown. Even after adding new input variables, the BDTs discrimination power does not improve and is still problematic at low energies. This is expected, as the monoscopic background separation in the energy range of 30 to 70 GeV is complicated. At highest energies, this discrimination is more powerful. Based on the BDT output, the cut on the ζ for gamma/hadron separation can be optimized depending on the physical motivation and use.

3.7.3 Discussion

A gamma-hadron separation of monoscopic events with a MVA was investigated. To perform an event separation using the BDT algorithm requires a good training sample. For the work presented here, the BDT provides a good separation at the highest energies, especially in the last band (700 GeV - 1 TeV), whereas at low energies $\mathcal{O}(10GeV)$ the signal and background BDT output is more overlapping.

The BDT was also tested on the Crab Nebula, the prime subject of this thesis work with H. E. S. S. The goal is to measure the spectrum in a wide energy range, hence make profit of the H. E. S. S. II observations to lower the energy threshold. This asks for a stable and powerful gamma-hadron separation, especially at low energies, where the separation is difficult due to the monoscopy. As the Crab Nebula can be observed only at zenith angles above 45 degrees, the separation is even more complicated. The energy threshold form H. E. S. S. I, using stereoscopy was 440 GeV on the Crab Nebula [113]. The *Model Analysis* for monoscopic reconstruction gave an energy threshold of 250 GeV (this work is presented in Chapter 6). The poor separation power of the BDT for low energies and high zenith angles excluded the possibility to use the BDT for the Crab Nebula analysis.

The BDT already used for event separation within H. E. S. S. is based on the Hillas parameters. To adapt the BDT separation power with the *Model* variables for monoscopic use would require a deep and detailed study which goes beyond the scope of this thesis.

The parameters are adapted in the `ParisAnalysis` framework for the users and are functional for further sources or tests.

3.8 Summary

The H.E.S.S. experiment in Namibia has been observing the sky in gamma rays since 2003. H. E. S. S. Phase-I consisted of four similar IACTs. The H. E. S. S. II telescope, the biggest IACT up-to-date installed in 2012 allowed H. E. S. S. to lower the energy threshold down to few tens of GeV. At present time, H. E. S. S. observes the gamma-ray sky from few tens of GeV up to hundreds of TeV. The status of the experiment and the main characteristics of the five telescopes were given. Different event identification techniques developed for IACTs were introduced. The Hillas reconstruction, traditionally used by the IACTs, naturally leades to a gamma-hadron separation based on the Hillas parameters. The *Model Analysis*, based on shower image fitting with a semi-analytical model for the discrimination is the one used in this work. The data analysis with *Model Analysis* and the corresponding variables are described. A BDT-based multivariate analysis provides another method to separate gamma/hadron events in H. E. S. S. It was adapted for monoscopic reconstruction of the H. E. S. S. II data and implemented in the ParisAnalysis framework.

Chapter 4

Characterizing the Gamma-Ray Variability of B2 1215+30

Blazars are Active Galactic Nuclei with a relativistic jet pointing close to the observer's line-of-sight, with highly relativistic particles moving in a magnetic field and emitting non-thermal radiation. This radiation, studied at all wavelengths, reveal blazars as amongst the most energetic and luminous objects in the Universe. They are known to undergo extreme, high-amplitude, variable emission at all wavelengths, with some of them undergoing flux increments at very-high-energies by a factor of almost hundred on time scales of only three minutes minutes [57]. Doppler factors greater than 100 are required to explain such extreme phenomena [57]. Observing variability of the gamma-ray flux on time scales as short as minutes is a common property of blazars [117, 118]. Multiwavelength monitoring of such events disclosed simultaneous flux increments at different energies for some blazars. This is important information to understand and characterize the emission from blazars.

B2 1215+30 is a BL Lac object located at a redshift of z = 0.13. It was listed as a gamma-ray emitter in the first *Fermi*-LAT bright catalog in 2009, where it was classified as a potential TeV emitter. It was first detected at TeV energies by the MAGIC experiment in 2011 after triggering an optical high flux state [119, 120] and was detected later by the VERITAS experiment as well [121].

We investigated the gamma-ray emission of B2 1215+30 over five decades in energy with the *Fermi*-LAT and VERITAS experiments. In collaboration with VERITAS, two gamma-ray flares detected during 2013 and 2014 at very-high-energies were studied in the energy range of *Fermi*-LAT. This work resulted in the detection of a simultaneous flare occurring in 2014 by VERITAS and *Fermi*-LAT. The results of this study, to which the author contributed, were published in [122]. Along with other multiwavelength observations, they characterize the emission from this source. The variability doubling time scale detected by the *Fermi*-LAT during the 2014 flare was less than 9.0 h. The measurement of the flaring amplitudes with *Fermi*-LAT allowed for an estimation of the Doppler factor and for setting constraints on the size of the emission region, results which were further constrained by the VERITAS flaring amplitude measurements in the very-high-energies.

To study other flares and further investigate the emission at GeV energies, all the data accumulated by *Fermi*-LAT spanning more than nine years was used. This resulted in the detection of three major flares, where the flux exceeded by a factor

of 16 the quiescent state, including the 2014 flare. Other significant flaring activities occurred between 2015 and 2017, but not as bright as the 2014 flare. These flaring activities are used to determine the variability time scale and set constraints in the size of the emission region as well. The analysis with public *Fermi*-LAT data in the energy range from 100 MeV to 500 GeV is conducted and presented in this chapter.

This chapter is organized as follows: Section 4.1 gives a short summary on the blazar B2 1215+30. Sections 4.2, 4.3 and 4.4 describe the VERITAS, *Fermi*-LAT and multiwavelength observations of the 2013 and 2014 time periods, respectively. The long-term lightcurve and the latest flaring activities of B2 1215+30 with *Fermi*-LAT are presented in Section 4.5. The summary and conclusions are given in Section 4.7.

4.1 Introduction

B2 1215+30, also known as ON 325 or 1ES 1215+303, is a BL Lac type located at a redshift of z = 0.13 [123], corresponding to a luminosity distance of $d_{\mathrm{L}} = 592\,\mathrm{Mpc}$ (for a Friedmann universe with $H_0 = 73\,\mathrm{km\ s^{-1}\ ly^{-1}}$, $\Omega_m = 0.27$ and $\Omega_\lambda = 0.73$). The 408 MHz radio source catalog of the Bologna Northern Cross telescope lists 3235 radio-sources, named after the B2 survey plus source coordinates. The appearance of B2 1215+30 in this catalog in 1970 marks its first discovery [124]. B2 1215+30 was subsequently discovered by other instruments in different energy bands resulting in its classification as a BL Lac type object. It was first discovered by *Fermi*-LAT in 2009, when it was listed among 205 other sources in the first *Fermi*-LAT bright source catalog produced with only 3 months of data [119] and it appears in all later *Fermi*-LAT catalogs with a hard spectral index [125]. As B2 1215+30 is located in the northern hemisphere, it can be seen at very-high-energies only by the VERITAS and MAGIC experiments. The first TeV emission from the source was reported in 2011 by the MAGIC telescopes, detected after triggering an optical outflow [120]. It was subsequently detected by the VERITAS experiment in 2012 with observations carried out between 2008 and 2012 [121]. MAGIC detected the source in a brighter state during 2011 observations, with integral flux $(7.7 \pm 0.9) \times 10^{-12}\,\mathrm{cm^{-2}\,s^{-1}}$ above 200 GeV, with spectral index of $\Gamma = -2.96 \pm 0.14$ [120]. VERITAS detected the source in a relatively bright state in 2011, with spectral index of power-law spectral index $\Gamma = -3.6 \pm 0.4$ and integral flux above 200 GeV of $(8.0 \pm 0.9) \times 10^{-12}\,\mathrm{cm^{-2}\,s^{-1}}$ [121]. The here-discussed observations from MAGIC and VERITAS experiments claim flux variability on time scales longer than months.

High amplitude flux variability is a distinctive characteristic of blazars. During such events, some blazars are found to exceed the flux of the Crab Nebula at very-high-energies, which is remarkable as the Crab Nebula is so much closer, and is in fact the brightest very-high-energy source. The spectral energy distribution is characterized by a double-hump structure with one peak located in the radio-to-UV/X-ray range and a second one in the X-to-gamma-ray range. The first peak is attributed to the synchrotron radiation from the relativistic electrons moving in the jet's magnetic field. The origin of the second component is still under debate, where two different scenarios of hadronic or leptonic origin exist. In the leptonic scenarios

it is commonly believed that the second component arises from electrons that suffer inverse Compton scattering with low energy photons. The origin of the low-energy photons responsible for the IC is still unclear.

B2 1215+30 is classified either as an intermediate BL Lac or high frequency peaked BL Lac (HBL) based on the position the SED synchrotron peak at $\log_{10} \nu_{\rm peak} = 15.58$ Hz [126, 127].

Simultaneous observations of B2 1215+30 with the *Fermi*-LAT and VERITAS during two very-high-energy flaring episodes detected at very-high-energies are presented in the following sections. Some of the observations of B2 1215+30 in other energy ranges are briefly described after.

4.2 VERITAS Observations

VERITAS (Very Energetic Radiation Imaging Telescope Array System) is an array of four IACTs located at the Fred Lawrence Whipple Observatory in southern Arizona [32]. VERITAS is sensitive to gamma rays in the energy range between 0.1 and 30 TeV. For these observations of B2 1215+30, data were all taken in *wobble* pointing mode [128], considering that another TeV source, 1ES 1218+304, is in the same field of view, offset 0.76° from B2 1215+30 . Standard VERITAS data processing techniques were used for the analysis, as described in [129, 130].

VERITAS observations carried out between MJD 56686 to 56802 (see Table 4.1) resulted in a detection of gamma-ray signal from B2 1215+30 with a statistical significance of 23.6σ and between MJD 56298–56424 with 8.8σ. The top panel of Figure 4.2 shows the 2013 light curve in 1-day time bins, with an average flux over the entire data set of $(6.0 \pm 1.2) \times 10^{-12}$ cm^{-2}s^{-1}. The top panel of Figure 4.3 shows the 2014 light curve in 3-day time bins, with an average flux over the entire data set of $(2.4 \pm 0.2) \times 10^{-11}$ cm^{-2}s^{-1}. With the exception of 2014 February 08, the observed nightly fluxes are comparable to previously-reported yearly-averaged values [120, 121]. On the night of MJD 56696 (2014 February 08) VERITAS measured a gamma-ray flux of $(5.0 \pm 0.1) \times 10^{-10}$cm^{-2}s^{-1}, which is more than twice that of the Crab Nebula. The source was detected with a statistical significance of 46.5σ in an exposure of 45 minutes. Given the strength of the signal, the light curve in 5-minute time bins is derived. The flux on the night of the flare was more than 60 times brighter than the average flux previously reported by MAGIC and VERITAS from this source [120, 121], making this one of the brightest flares detected in a blazar. All the errors quoted are 1-σ statistical errors.

The preliminary results of the VERITAS on the B2 1215+30 motivated the search of variability in the GeV energy range from *Fermi*-LAT. The analysis and results obtained from the *Fermi*-LAT observations, simultaneous with the two periods here discussed are given in the following.

4.3 *Fermi*-LAT Observations

Fermi-LAT is monitoring the high-energy sky in survey mode since 2008. The data accumulated by *Fermi*-LAT is publicly available, released in the form of event (PH) and spacecraft (SC) files. They contain all the event information for a given source and spacecraft pointing positions[1]. Since the launch of *Fermi*-LAT, the data is continuously updated by the LAT team using more sophisticated reconstruction techniques and IRFs. The latest reconstruction technique (Pass 8) leads to a better PSF and a substantial increase of gamma-ray acceptance, i.e. higher photon detection probability. This allowed a better reconstruction up to 500 GeV compared to the previous one (Pass 7[2]), as described in Chapter 2.

The data presented here was retrieved from the *Fermi* Science Support Center[3] (publicly available) and analyzed with Pass 8. We used all the data on B2 1215+30, accumulated by *Fermi*-LAT in survey mode to study and characterize the gamma-ray emission at energies larger than 100 MeV. The data analysis for two periods of five months in 2013 and 2014, contemporaneous with VERITAS observations are presented in the following section. It was conducted with the likelihood framework provided in the `FermiScienceTools` software package, version `v10r0p5`[4].

4.3.1 Event Selection

Two time ranges were selected from the *Fermi*-LAT data matching the VERITAS observation periods in order to perform a contemporaneous data analysis: from 2013 January 6 to 2013 May 12 and from 2014 January 1 to 2014 May 25. A circular RoI of 10 degrees, centered on the position of B2 1215+30 (R.A. = $12^{\mathrm{h}}17^{\mathrm{m}}52^{\mathrm{s}}$, decl. = $+30°07'00''1$, J2000) was selected. Only events with energies 100 MeV $< E <$ 500 GeV from the RoI were selected and analyzed. Gamma rays from the Earth's limb contaminate the sample each time the Earth enters the *Fermi*-LAT field of view. These time intervals, corresponding to a rocking angle > 52 degrees were removed. A further quality selection was applied by accepting only events with zenith angles less than 90 degrees.

Figure 4.1 shows the counts map around the position of B2 1215+30 for the 2014 data set. This region of the extragalactic sky is interesting since it is populated with bright high- and very-high-energy gamma-ray sources. All of them are BL Lac type objects and TeV emitters, except for MS 1221.8+2552 and GB6 J1159+2914 with no TeV emission detected so far. One can distinguish the BL Lac object 1ES 1218+304 (z=0.182), a bright TeV emitter located at (R.A. = $12^{\mathrm{h}}21^{\mathrm{m}}26.3^{\mathrm{s}}$, decl. = $+30°11'29''$, J2000). B2 1215+30 and 1ES 1218+304 are two nearby sources exhibit opposite brightness behaviour in the GeV and TeV energy bands. B2 1215+30 appears brighter in the GeV energy range and more faint in TeV, whereas 1ES 1218+304 exhibits the opposite behaviour [121].

[1] https://fermi.gsfc.nasa.gov/ssc/data/analysis/documentation/Cicerone/
[2] https://www.slac.stanford.edu/exp/glast/groups/canda/lat_Performance.htm
[3] http://fermi.gsfc.nasa.gov/cgi-bin/ssc/LAT/LATDataQuery.cgi
[4] http://www.fermi.gsfc.nasa.gov/

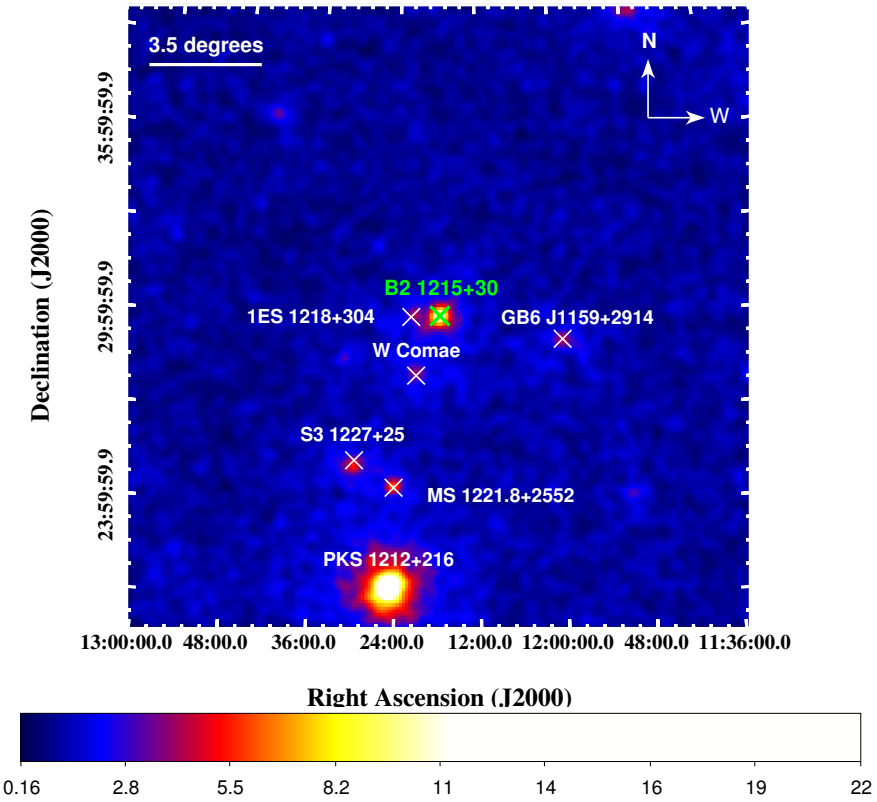

Figure 4.1: The B2 1215+30 counts map for a 20 degrees x 20 degrees RoI, chosen larger than the RoI in the analysis for illustrative reasons. The map was produced with *Fermi*-LAT 2014 data. The position of B2 1215+30 is marked with a green cross and all other bright sources are marked with white crosses. The VERITAS field of view (3.5 degrees) is shown for comparison.

4.3.2 Background Modeling and Source Detection

The likelihood framework requires a proper background model, and three background categories were further considered in the analysis. The first two are Galactic and extragalactic diffuse emission, which the *Fermi*-LAT is sensitive to [83, 131]. The Galactic diffuse model is provided in `FermiScienceTools` by a spatial and spectral template represented by a set of energy dependent maps scaled to the expected intensity. The isotropic diffuse model is a spectral template from a fit to the all-sky emission ($|b|>30°$ that includes both extragalactic diffuse gamma rays and the remaining residual (misclassified) cosmic-ray emission. The isotropic background and the Galactic diffuse emission were modeled with the `iso_source_v05` and `gll_iem_v05` templates and the recent instrument response functions (IRFs) `P7REP_SOURCE_V15`[5] from the `FermiScienceTools` were used.

[5] `http://fermi.gsfc.nasa.gov/ssc/data/analysis/user/`

The third major background are events from the other sources in the vicinity of B2 1215+30. This type of background is modeled considering all known gamma-ray sources from the third *Fermi*-LAT catalog (3FGL) up to 5° outside the RoI edges [44]. Including this 5° band outside the RoI accounts for spill-over events, caused by PSF tails from sources close to the RoI edges. The catalog lists sources detected with a significance of at least 3σ. The detection significance is determined from the likelihood difference of the background-only model and the background plus source model:

$$TS = 2\Delta\log\mathcal{L}. \tag{4.1}$$

The source significance is inferred from this test statistic: $\sigma \approx \sqrt{TS}$. Given that the 3FGL catalog was built on 4 years of data, but only half-year periods were analyzed in these *Fermi*-LAT/VERITAS studies, the sources detected with less than 5σ were treated differently with respect to sources detected above the 5σ threshold in order to avoid fit convergence problems.

To model the $> 5\sigma$ sources as good as possible in the contemporaneous data analysis, their spectral parameters were first fitted on the values from the catalog. The initial parameters for this global fit were set to the ones from the 3FGL catalog. In the subsequent modeling of the half-year time periods, only the spectral parameters were left free. The 3FGL sources below the 5σ threshold were included with all their parameters fixed to the catalog values, both in the global and half-year fits. The resulting background model for the chosen RoI consists of 50 point sources, and no extended sources.

The best-fit parameters from the global fit were used to properly model the background which is used to derive the spectrum and lightcurve. The procedure and the results are presented next.

4.3.3 Spectrum

A spectral analysis was performed on B2 1215+30 in the energy range from 0.1 to 500 GeV covering the same half-year time periods. The spectral points were produced with the standard unbinned maximum likelihood analysis in six energy bands, equally spaced on a logarithmic scale.

To initiate the fit for background model, a similar procedure as described above for the gloabl fit was followed. For sources within the RoI with $TS > 9$, the integral flux was left free, while the spectral index was fixed at the value obtained during the global fit. In each energy band, the spectrum best-fit parameters were derived using a simple power-law model:

$$\frac{\mathrm{d}N}{\mathrm{d}E} = N_0 \left(\frac{E}{E_0}\right)^{-\Gamma}, \tag{4.2}$$

where N_0 is the normalization factor at a chosen reference energy E_0, and Γ is the photon index. The best-fit power law model fit gave a spectral index of $\Gamma = 1.84 \pm 0.06$ at a normalization of $\mathrm{N_0} = (6.89 \pm 0.56) \times 10^{-12}$ $\mathrm{cm^{-2}s^{-1}MeV^{-1}}$. In

Section 4.4.3 is given the flux in each energy band as measured by *Fermi*-LAT, plotted with the other observations in the SED representation.

4.3.4 Lightcurve

To derive the lightcurve, the data were divided into time bins of three or one day duration. The spectrum of B2 1215+30 at each bin was modeled with a simple power law. For all the sources within the RoI detected with a test statistic value of $TS \geq 9$, only the integral flux was left free while the spectral index was fixed to the value obtained during the fitting procedure for the entire time range. For the other sources inside the RoI, detected with a $TS < 9$, all the parameters were fixed to the values obtained during the fitting procedure over the whole time period. Figure 4.2 shows the corresponding 2013 lightcurve. For the 2014 data set, the lightcurve is shown in Figure 4.3. The source exhibits clear variations in flux with a large flare starting on MJD 56693 (2014 February 05).

The strength of the signal allows to derive 1 day time bin lightcurve around the flaring period. For this period is derived also the spectrum, which results in a spectral index of $\Gamma = 1.7 \pm 0.09$, showing a hardening during the flare period. The decaying phase of the 1-day bin lightcurve is fitted with a function of the form $F(t) = F_0(1 + 2^{-(t-t_0)/t_{var}})$, where t_{var} is the flux halving time and t_0 is the time corresponding to the peak of the flare. From the *Fermi*-LAT flare, an upper limit on the flux halving time of $t_{var} < 9.0$ h that constrains the flare at 90 % confidence level was found. This variability time scale is seen also in other blazars. The strength of the TeV flare seen by VERITAS in the night of the flare (2014 Feb 08) allows to derive the lightcurve in 5 minute time bins. VERITAS observations on the next night (2014 Feb 09) did not show an elevated flux from B2 1215+30. This yield to a 90% c.l. limit on the flux halving time of 3.6 h.

Instrument	Energy range	Dates MJD	Live time min	Signal	Flux $\mathrm{cm^{-2}\,s^{-1}}$
VERITAS	> 0.2 TeV	56298–56424	25	8.8 σ	$6.0 \pm 1.2 \times 10^{-12}$
		56330	25	10.5 σ	$5.1 \pm 1.0 \times 10^{-11}$
		56686-56802	748	23.6 σ	$2.4 \pm 0.2 \times 10^{-11}$
		56696	45	46.5 σ	$5.0 \pm 0.1 \times 10^{-10}$
		56697	25	1.6 σ	$< 1.4 \times 10^{-11}$
Fermi-LAT	0.1–100 GeV				
		56298 - 56424		28.8 σ	$6.8 \pm 0.7 \times 10^{-8}$
		56658 - 56802		34.5 σ	$1.0 \pm 0.1 \times 10^{-7}$
		56693 - 56696		17.4 σ	$4.4 \pm 0.7 \times 10^{-7}$

Table 4.1: Summary of the VERITAS and *Fermi*-LAT results from observations of B2 1215+30 in different epochs from 2013 and 2014. The VERITAS upper limit is computed at 95% c.l. assuming a power-law spectrum with index $\Gamma = 3.0$.

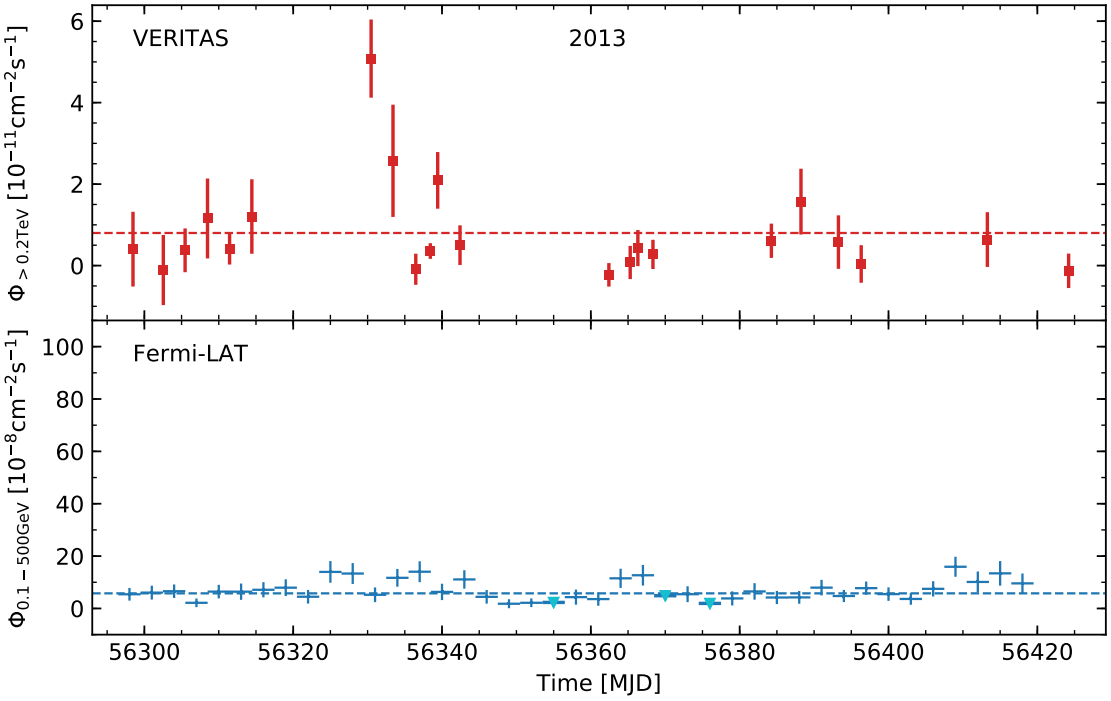

Figure 4.2: TeV and GeV lightcurves of B2 1215+30 in 2013. Fluxes are calculated in 1-day bins for VERITAS (red squares). The red dashed line shows the yearly averaged TeV flux in 2011 (8.0×10^{-12} cm^{-2} s^{-1}) [121]. The *Fermi*-LAT fluxes are calculated with 1-day integration bins (blue crosses), in the energy range 100 MeV < E < 500 GeV. The blue dashed line correspond to the average flux from the 3FGL catalog [44]. For the *Fermi*-LAT data, down-pointing triangles indicate 95 % c.l. upper limits for time bins with signal smaller than 2σ.

Multiwavelength observations of the source on X-rays, UV and Optical bands covering this flaring period are described next.

4.4 Multiwavelength observations

4.4.1 X-ray Observations

Swift was launched in 10 November 2004 by NASA with three instruments on board: a Bust Alert Telescope (BAT); an Ultraviolet/Optical Telescope (UVOT); and X-ray telescope (XRT) [133]. These instruments are designed for monitoring the sky in a wide energy range. Below are described the analysis of the data taken from these two these instruments.

***Swift*-XRT** The X-ray telescope is designed to measure X-rays in the 0.2 - 10 keV energy range [133]. An observation by *Swift* XRT Observatory was carried out one day after the VERITAS 2014-detected flare with an exposure of 1.97 ks. The

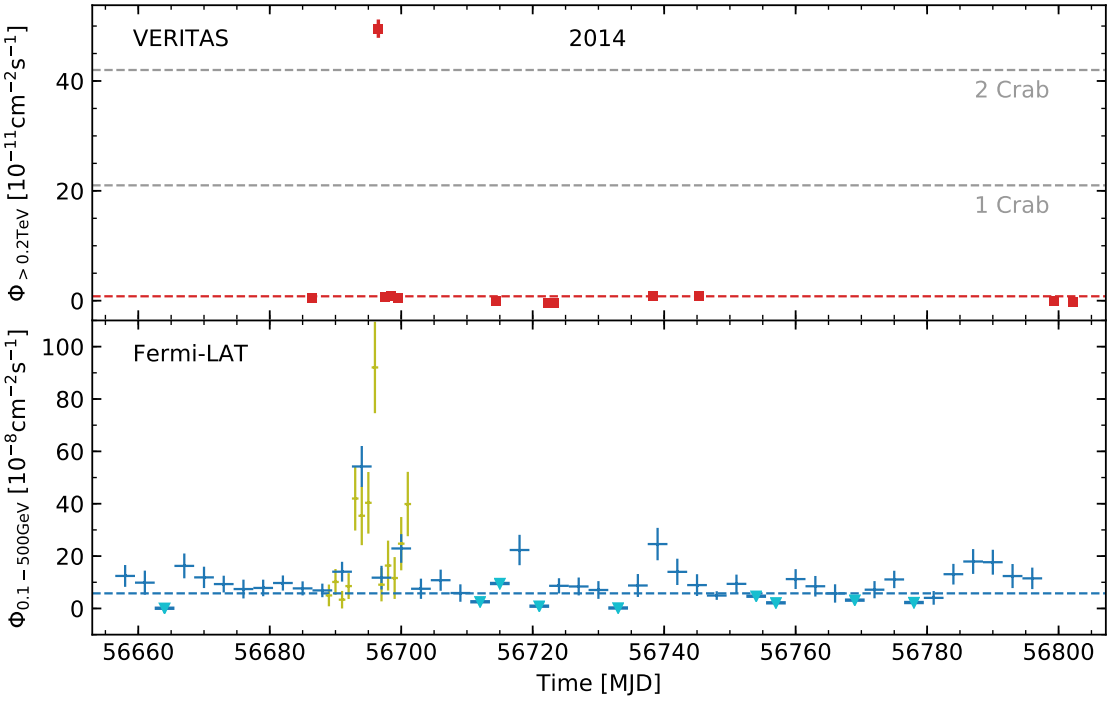

Figure 4.3: B2 1215+30 light curves for the 2014 data. In the top panel, the VERITAS integral fluxes in 1-day time bins are plotted. The red dashed line shows the yearly-averaged TeV flux in 2011 [121]. The gray dashed lines correspond to one and two Crab Nebula flux. One Crab correspond to $(2.1 \pm 0.2) \times 10^{-10}\,\mathrm{cm}^{-2}\,\mathrm{s}^{-1}$, for $E > 0.2\,\mathrm{TeV}$ [132]. Using the *Fermi*-LAT data the integral fluxes were calculated in 3-day (blue crosses). Down-pointing triangles indicate 95 % c.l. upper limits for time bins with signal smaller than 2σ. The blue dashed line correspond to the average flux from the 3FGL catalog [44]. The yellow points correspond to 1-day time bins derived around the flare period. The bright flare is seen simultaneously by the two experiments at the GeV and TeV energies on February 2014.

data were obtained in photon-counting (PC) mode and processed with `xrtpipeline` tool (HEASOFT 6.16). The source and background-extraction regions were defined as a 20 pixels ($\sim$ 4.7 arcsec) radius circle and a 40-pixel radius circle positioned near the former without overlapping, respectively. The exposure shows a stable source-count rate of $\simeq 0.3\,\mathrm{counts\,s}^{-1}$, suggesting negligible pile-up effects in photon-counting mode [134].

The spectral fitting was performed with PyXspec v1.0.4 [135] , using the dedicated Ancillary Response Functions generated by the `xrtmkarf`. The spectrum was re-binned to have at least 20 counts per bin using the `grppha`, and ignoring the channels with energy below 0.3 keV in the XRT-PC data [136]. A power law model was fitted on the data, $\mathrm{d}N/\mathrm{d}E = N_0(E/E_0)^{-\Gamma_\mathrm{X}}$. Using a hydrogen column density of $N_\mathrm{H} = 1.68 \times 10^{20}\,cm^{-2}$, the power law model fit describes good the data with a chi square test ($P(\chi^2) = 0.42$) and a photon index of $\Gamma_\mathrm{X} = 2.54 \pm 0.07$.

***Swift*-UVOT** *Swift*-UVOT is a 17 arcmin square FoV operating in the ultraviolet and optical regime [137]. The *Swift*-UVOT data were analyzed by extracting the source counts from an aperture of 5.0 arsec radius around the source. The background counts were taken from four neighboring regions with equal radius. The magnitudes were computed using the uvotsource tool (HEASOFT v6.16), corrected for extinction using E(B-V).

4.4.2 UV and Optical Observations

The optical R-band observations on B2 1215+30 were taken using two telescopes: the 35 cm Celestron telescope attached to the KVA 60 cm telescope (La Palma, Canary Islands, Spain) and the 50 cm Searchlight Observatory Network telescope (San Pedro de Atacama, Chile). The data were taken as part of the Tuorla blazar monitoring program and were analyzed by their team using a semi-analytical pipeline developed at the Tuorla Observatory [138]. From the data analysis one can conclude that there is no hint of flux variations during the period analyzed. The contemporaneous optical data described here are plotted in the SED, which is described next.

4.4.3 Spectral Energy Distribution

The spectral energy distribution, in νF_ν representation is shown in Figure 4.4. Cyan and red points show the results obtained during this work. Observations from the Tuorla and XRT taken during the flare period are shown as well. The archival data are shown in gray and they are all the data being published before the time period analyzed during this work [121]. The two-bump structure in the SED is clearly visible with the location of the synchrotron peak between UV and X-rays. The inverse Compton peak is located in the gamma-ray energy band. The 2014 period presented and analyzed here resulted in flux variability at high and very-high energies detected by *Fermi*-LAT and VERITAS respectively. The *Fermi*-LAT spectrum points, marked as red squares correspond to the 2014 period. They show a clear shift on flux compared to the previous observations reported on [121]. The SED with a leptonic model can be found here [122].

4.4.4 Size of the Emission Region

During the flare episodes an emission region emerges, whose size cannot vary on time scales shorter than the time needed to cross the region at the speed of light. For relativistic speeds the Doppler boost of the emission region has to be taken into account. If the bulk emission region moves with a Lorentz factor Γ, at an angle θ to the line of sight, the resulting Doppler factor is:

$$\delta = \frac{1}{\Gamma(1 - \beta\cos\theta)}, \tag{4.3}$$

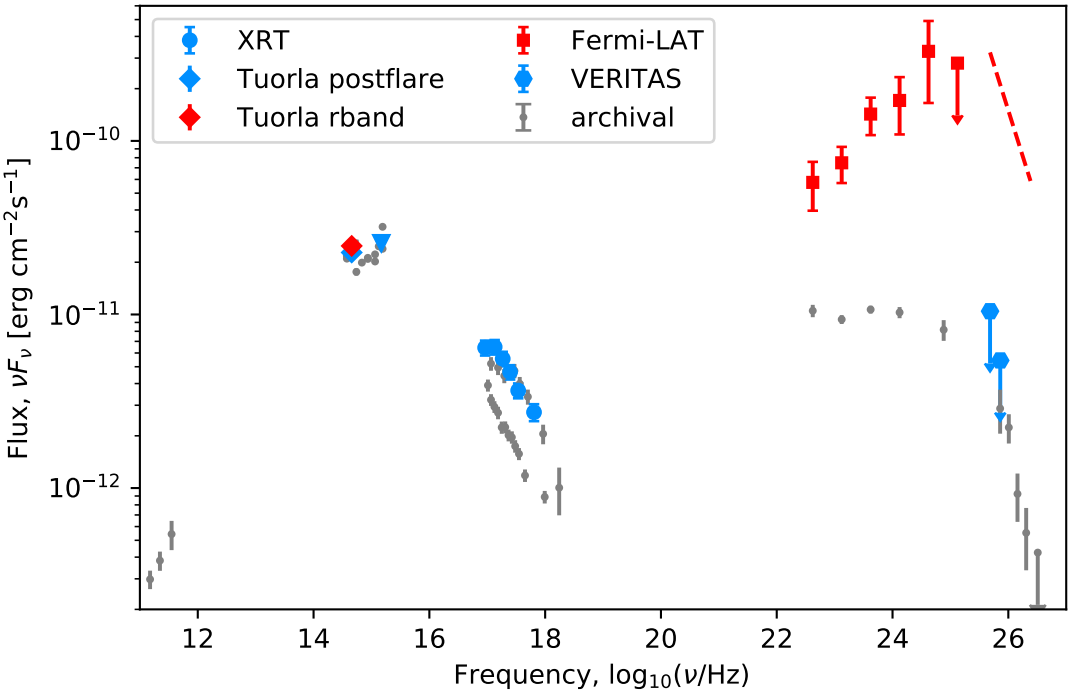

Figure 4.4: Spectral energy distribution of B2 1215+30. The cyan and red points correspond to the *Fermi*-LAT data and other observations from this work as indicated in the legend. The gray points are the archival points from [121].

with $\beta = v/c$ and $\Gamma = \frac{1}{1-\beta^2}$. For a source at a redshift z, with a variability time scale t_{var}, the source size is limited to:

$$R \leq c\, t_{var} \delta/(z+1). \tag{4.4}$$

The lightcurves derived with the VERITAS and *Fermi*-LAT show evidence for a short variability time scale. Opacity arguments for the pair production were used to set a limit on the Doppler factor of the relativistic jet, as explained below.

In the following the approach proposed by Dondi was adapted [139]. These arguments are used to explain the high luminosity produced in compact regions from the BL Lac objects. The short variability time scale and the high luminosities in gamma rays are not expected from very compact volumes with gamma rays. Photons with sufficient high energy can annihilate to produce an e^-/e^+ pair, hence energetic gamma rays will suffer from attenuation with the low-energy photons and result in softer radiation. The beamed radiation from the relativistic jet can explain the high luminosities from very compact regions and the short variability time scales.

In this calculation we assume a Friedmann universe with $H_0 = 73\,\mathrm{km\ s^{-1}\,Mpc^{-1}}$, $\Omega_m = 0.27$ and $\Omega_\lambda = 0.73$ and that the high and the low energy radiation are produced in a single region of the source. Assuming a spherical emission region, the radius of this region is constrained to be less than Equation 4.4. We assume

also that the high energy photons and the soft photons are produced in the same region.

It can be shown that the Doppler factor δ is found to be:

$$\delta \geq \left[\frac{\sigma_T d_L^2}{5hc^2} (1+z)^{2\alpha} \frac{1}{t_{var}} F_{1keV} \left(\frac{E_\gamma}{GeV} \right)^{\alpha} \right]^{\frac{1}{(4+2\alpha)}}, \tag{4.5}$$

where z is the redshift, d_L the luminosity distance (see Appendix A for the details of the calculation). The highest energy photon that resulted from 2014 *Fermi*-LAT was 73 GeV. The redshift of B2 1215+30 ($z = 0.13$) and the luminosity distance is $d_L = 614.6$Mpc are used in this calculation. To derive the X-ray photon density flux, observations from the *Swift* observatory were taken into account. As already mentioned above, these observations were taken one day after the flare at the very-high-energies. Assuming the flux does not change, these observations were used to derive the flux at 1 keV and is found that $F_{1keV} = 1.7 \mu Jy$. Using the variability time scale and X-ray spectral index of $\alpha = 2.5$ derived by *Swift* data, a limit on the beaming factor is found to be $\delta_{\rm Fermi} \geq 5.0$.

Given the simultaneous flare at GeV and TeV energies, more constraining results can be derived using the flare observations from VERITAS. The variability time scale derived from the VERITAS 5 minute lightcurve is 3.6 h and was used to calculate the Doppler factor: $\delta \geq 10$.

From the simplest leptonic emission scenario, the high-energy component of the spectral energy distribution can be produced via the synchrotron self-Compton mechanism. In the modeling of the spectral energy distribution, a self synchrotron component and external Compton were considered [122]. In an SSC scenario, the ratio between the synchrotron and inverse-Compton luminosities can be used to estimate the magnetic field. The magnetic field is constrained by following [140] and using two arguments:

(I) Non-detections by *Swift*-BAT (15-50 keV) and MAXI (4-10 keV) on the day of the TeV flare (MJD 56696) can be interpreted as a limit on the hard X-ray flux of the order of $\nu_X F_{\nu_X} \leqslant 2 \times 10^{-10} \mathrm{erg\,cm^{-2}\,s^{-1}}$. This limits the peak synchrotron luminosity to be $L_{\rm syn} \leq 10^{46} \mathrm{erg\,s^{-1}}$.

(II) Using Equation 4.5 for the Doppler factor calculation.

From these relations is found:

$$\begin{aligned} B &\simeq (1+z)\,\delta^{-3} \left(\frac{2L_{\rm syn}^2}{L_\gamma c^3 t_{\rm var}} \right)^{1/2}, \\ &\leq 1.8\,\mathrm{G} \left(L_{\rm syn} 10^{46}\,\mathrm{erg\,s^{-1}} \right) (\delta/10)^{-3}. \end{aligned} \tag{4.6}$$

A full discussion about the magnetic reconnection with the magnetic field or what might be the cause of short time scale flares in blazars are discussed more in detail here [122].

4.5 Long-Term Variability with *Fermi*-LAT

In the previous sections the analysis of two different time periods, simultaneous with the flaring activities detected by VERITAS were presented. Such events are a distinctive characteristic of BL Lac objects. To further investigate the emission from B2 1215+30 the variability at GeV energies using all the available data set from the *Fermi*-LAT was studied.

Since *Fermi*-LAT observes the whole sky every three hours, the probability to detect such events is higher compared to the ground based detectors. The LAT team has an online monitoring program which is used to send alerts to the other experiments and have multiwavelength observation of such events. Beside the brightness of the 2014 flare (16× the average flux) the *Fermi*-LAT online monitoring missed the high flux activity on B2 1215+30. Hence, a long-term lightcurve would reveal more about the activities of the source at high-energies.

All the data accumulated with the *Fermi*-LAT on B2 1215+30 was used to study the long-term variability. The lightcurve is calculated in time bins by assuming a power-law spectrum shape. Given the long-term data set, the fluxes are derived with a separate power-law spectral index fit for each year to account for any spectral variability in this time range. The flux evolution of B2 1215+30 is studied by calculating the integral flux, from 100 MeV to 500 GeV in one week time bins. The one week time bin represents a trade-off between statistics and sensitivity to such events. Figure 4.5 shows the long-term lightcurve derived from September 2008 1st to 2017 June 30 or MJD 54710-57934.

This analysis resulted in the detection of three major flares, as spectacular as the 2014 flare [141]. These events were detected during October 2008, February 2014 and April 2017 and the flux exceeded by ×16 the quiescent flux. The strength of the signal during these flaring episodes allows to derive the lightcurve down to one day time bin. The one day time bin lightcurves for the three major flares are shown in the bottom part of Figure 4.5 and the corresponding details are summarized in Table 4.2.

Fermi-LAT 0.1-500 GeV	Dates	Signal	Flux $\mathrm{cm^{-2}\,s^{-1}}$
	2008 Oct 12 – 2008 Oct 13	15.5 σ	$(9.2 \pm 0.15) \times 10^{-7}$
	2014 Feb 08 – 2014 Feb 09	12.2 σ	$(9.2 \pm 0.18) \times 10^{-7}$
	2017 Apr 12 – 2017 Apr 13	14.0 σ	$(8.0 \pm 0.15) \times 10^{-7}$

Table 4.2: Summary of the major flares of B2 1215+30 detected in nine years of *Fermi*-LAT observations. The strength of the signal and the integral flux between 0.1 and 500 GeV are given.

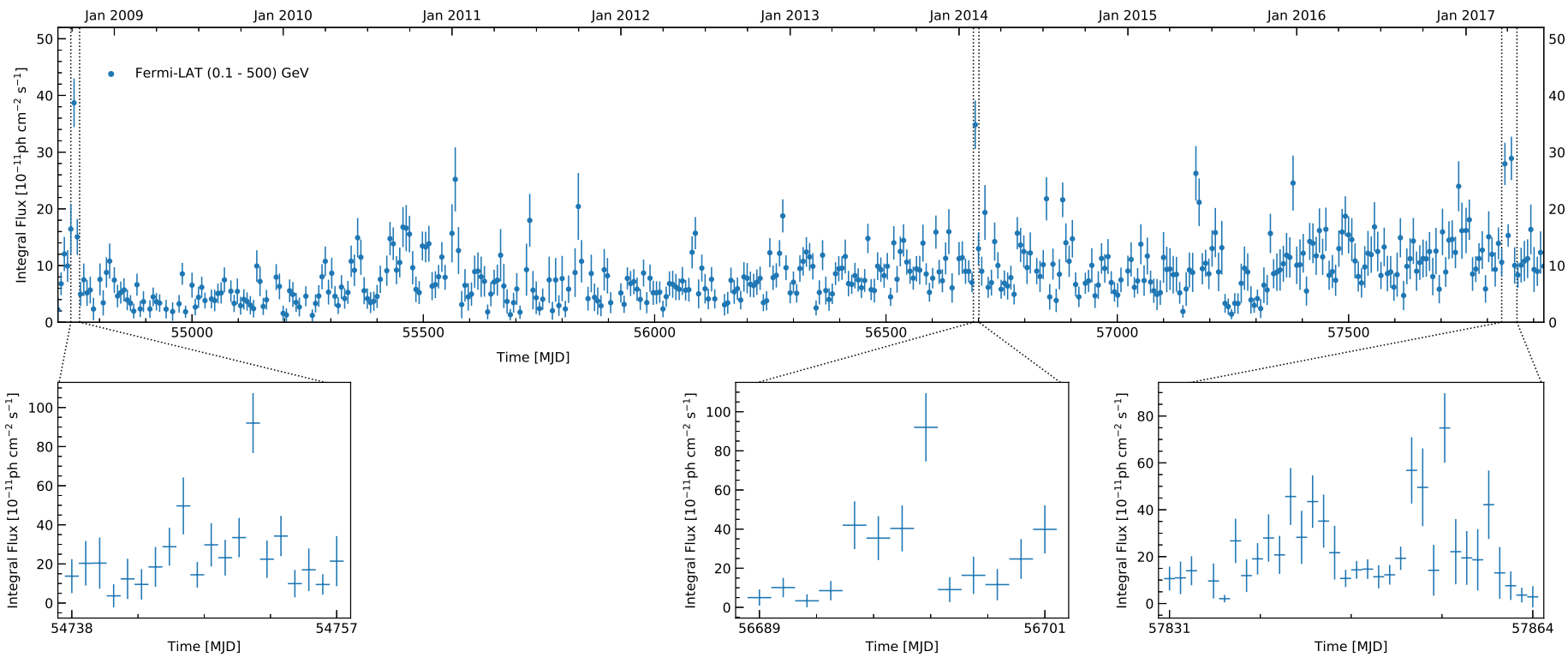

Figure 4.5: Top panel: Long-term lightcurve of B2 1215+30, from 2008 September 1st to 2017 June 30. The integral fluxes are calculated in one week time bins. The major flares, with weekly averaged flux $\Phi > 3.0 \times 10^{-07}$ cm^{-2} s^{-1} are indicated by dashed black lines. Bottom panel: lightcurve in one day time bins around the major flares detected during October 2008, February 2014 and April 2017.

From the long-term lightcurve in Figure 4.5 can be seen the increase of the flux with the time. To check the significance of this flux increase, a linear fit was performed to the data. The fluxes and the spectral indices were investigated in a year by year basics. Figure 4.6 show the yearly average fluxes and the corresponding spectral indexes. As it can be seen, the flux increases the spectral index gets harder with time.

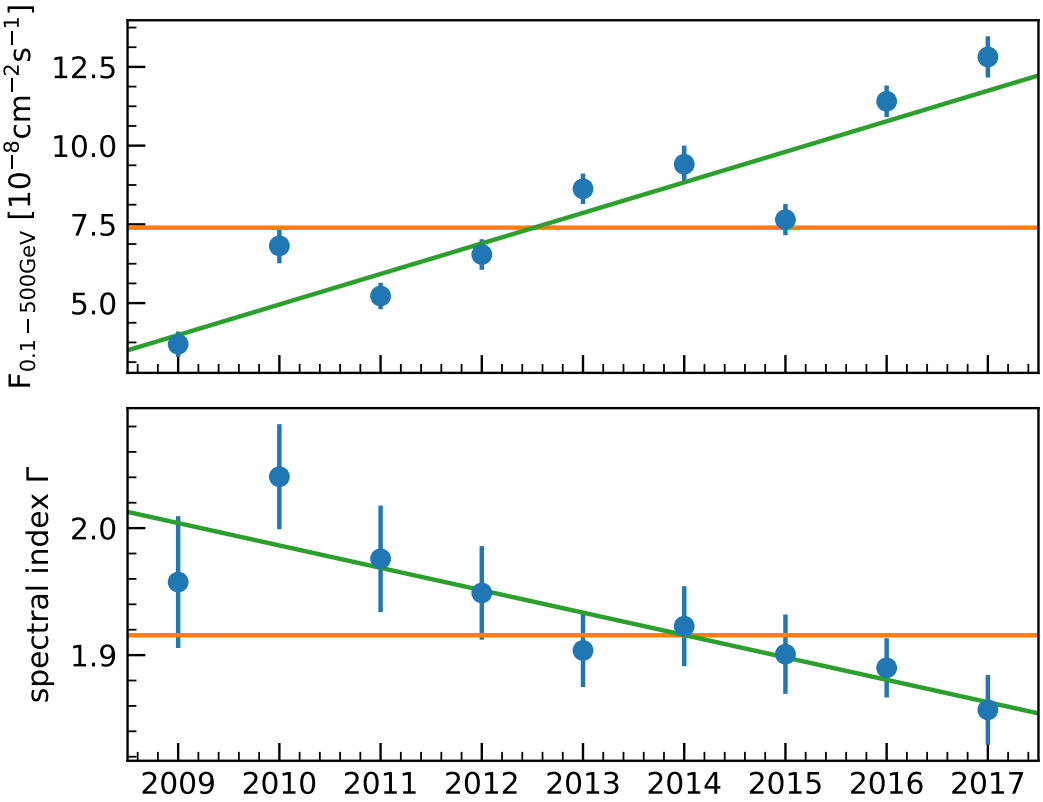

Figure 4.6: Top: The average year-by-year fluxes for B2 1215+30 from 2008 to 2017. Bottom: The corresponding spectral indices for the marked years. The orange line corresponds to a constant and the green correspond to a linear fit.

To test the significance of this correlation, each of them were fitted with constant (orange) and with a line (green). The values are summarized in Table 4.3. The linear fit agrees better with the measurements and shows a clear correlation between the flux increment with time and a hardening of the spectral index with time.

To investigate the origin the GeV flares the long-term lightcurve was studied further. If the variability is originating from random processes, the fluxes are expected to be normally distributed around the mean. This was checked by performing a Gaussian fit to the flux distribution $(\Phi_i - \bar{\Phi})/\sigma_i$, where is the Φ_i flux with error σ_i and $\bar{\Phi}$ is the mean flux weighted by the error. Figure 4.7 shows the Gaussian fit to the distribution of the data around the mean flux which is assumed to be a constant. By considering the linear increase of the flux, the distribution of the flux values around

Year	Flux [10^{-8} cm^{-2} s^{-1}]	Γ
2009	3.7	1.96
2010	6.8	2.04
2011	5.2	1.98
2012	6.5	1.95
2013	8.6	1.90
2014	9.4	1.92
2015	7.7	1.90
2016	11.4	1.90
2017	12.8	1.85
$C : \chi^2/ndf$	266.69/8	18.88/8
$L : \chi^2/ndf$	41.85/7	3.88/7

Table 4.3: Year-by-year fluxes and spectral indices of B2 1215+30, corresponding to the points presented in Figure 4.6. The fit values assuming a constant C and a linear increase for the flux and spectral index are given.

this value were also checked with a Gaussian fit (see Figure 4.7). Therefore, the high flux states during luminous flares are not likely connected to the same random processes that is dominant in the quiet state.

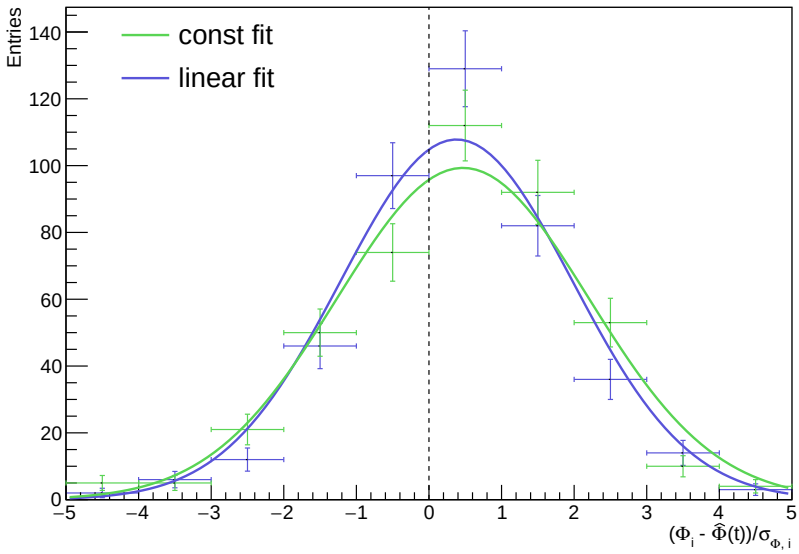

Figure 4.7: Distribution of B2 1215+30 fluxes for nine years of *Fermi*-LAT data measured in one week time bins. The distribution is fitted by a Gaussian assuming a constant flux (blue) and a linear flux (green).

In some blazars, i.e. PKS 2155-304, it was found that flares may be related to a self-amplifying, multiplicative process [142]. Unlike the random processes where the flares might originate from additive processes, the flares are result of multiplicative

processes. In this case, the fluxes are not expected to follow a normal distribution but the logarithms of the fluxes follow a normal distribution. A "log-normal" distribution of the fluxes was checked and was not compatible with a normal distribution either. The multiplicative process do not explain the flares either.

Another possible explanation would be a periodic behavior, as seen for example in another blazar PG 1553+113 [143]. Probing the B2 1215+30 lightcurve for periodic behavior a Fourier analysis was performed and is described in Section 4.6.

4.5.1 Recent flaring activities

This analysis resulted in the detection of several flux increments from 2015 to 2017, where only one flare has been reported by the *Fermi*-LAT on 2017 April 13 in the form of an Astronomer's telegram [144]. The corresponding lightcurves, in one week time bins for these years are plotted in Figure 4.8. The flux enhancements found during these years show the high-flux activities of the source. From this it can be seen an evidence of quasi-periodic behaviour. This is more evident when looking at the 2016 data (middle plot of Figure 4.8).

The flaring episodes with weekly average flux exceeding the value of $\Phi > 2.4 \times 10^{-8}\mathrm{cm}^{-2}\,\mathrm{s}^{-1}$ are summarized in Table 4.4. The highest flux states of B2 1215+30 are found to occur during 2017 March and April.

Fermi-LAT 0.1-500 GeV	Dates	Signal	Flux $\mathrm{cm}^{-2}\,\mathrm{s}^{-1}$
	2015 Jan 01 – 2015 Jan08	12.0σ	$(2.6 \pm 0.48) \times 10^{-7}$
	2015 Dec 23 – 2015 Dec 30	9.4σ	$(2.5 \pm 0.48) \times 10^{-7}$
	2016 Dec 16 – 2014 Dec 23	14.2σ	$(2.4 \pm 0.44) \times 10^{-7}$
	2017 Mar 25 – 2017 Apr 01	21.6σ	$(2.7 \pm 0.35) \times 10^{-7}$
	2017 Apr 07 – 2017 Apr 15	20.1σ	$(3.1 \pm 0.38) \times 10^{-7}$

Table 4.4: Summary of the latest flares from the B2 1215+30 detected with the *Fermi*-LAT from 2015-2017. The strength of the signal and the integral flux between 0.1 and 500 GeV are given.

These results, along with the other years are used to characterize the fractional variability and are presented next.

4.5.2 Fractional variability

To quantify the spectral variability the statistical properties of the light curves are also considered. The fractional variability F_{var} is a measure of the intrinsic variability that corrects for the noise [145]. The F_{var} is the square root of the excess variance and is calculated as follows:

$$F_{var} = \sqrt{\frac{S^2 - \langle \sigma_{err}^2 \rangle}{\langle X^2 \rangle}}, \tag{4.7}$$

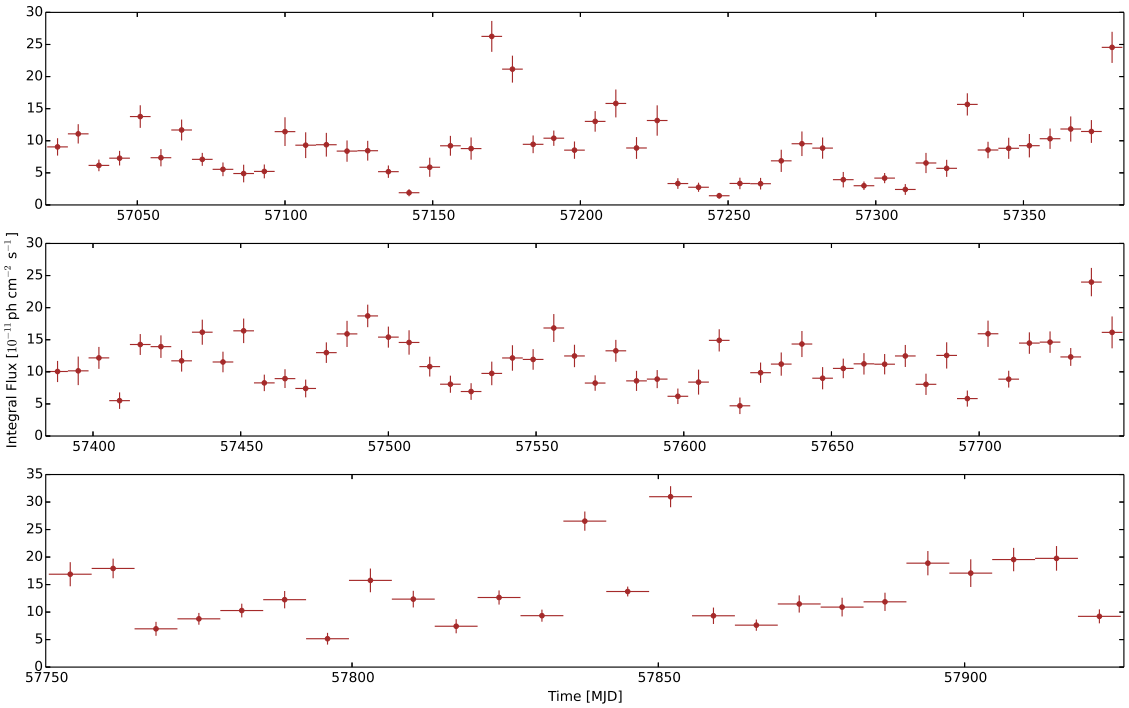

Figure 4.8: Integral flux Φ (100 MeV < E < 500 GeV) in one week time bins for all the 2015 (MJD 57023-57387) and 2016 (MJD 57388-57753) data sets in the top and middle panels. The bottom panel shows only six months of data, from 2017 January 1st to 2017 June 30 (MJD 57754-57934) in one week time bins.

where S^2 is the total variance of the lightcurve, $\langle X \rangle$ and $\langle \sigma_{err} \rangle$ are the mean flux measurements and the mean errors squared respectively. For N points, the errors on the fractional variability are propagated as follows:

$$\sigma_{F_{var}} = \frac{1}{2F_{var}} \sqrt{\frac{1}{N}} \frac{S^2}{\langle X \rangle^2} \tag{4.8}$$

For the long-term lightcurve considered only the time bins where the they have a detection of at least $TS \geq 4$ and the upper limits are excluded. The $\langle X \rangle$ is the unweighted mean flux. The F_{var}, which is a measure of the variability power of the total lightcurve was found to be 30%. This value is consistent with what was previously reported from B2 1215+30.

4.6 Periodic Behaviour

The lightcurve is further tested for quasi-periodic modulations by doing a **D**iscrete **F**ourier **T**ransform (DFT) of the long-term lightcurve, shown in Figure 4.9a.

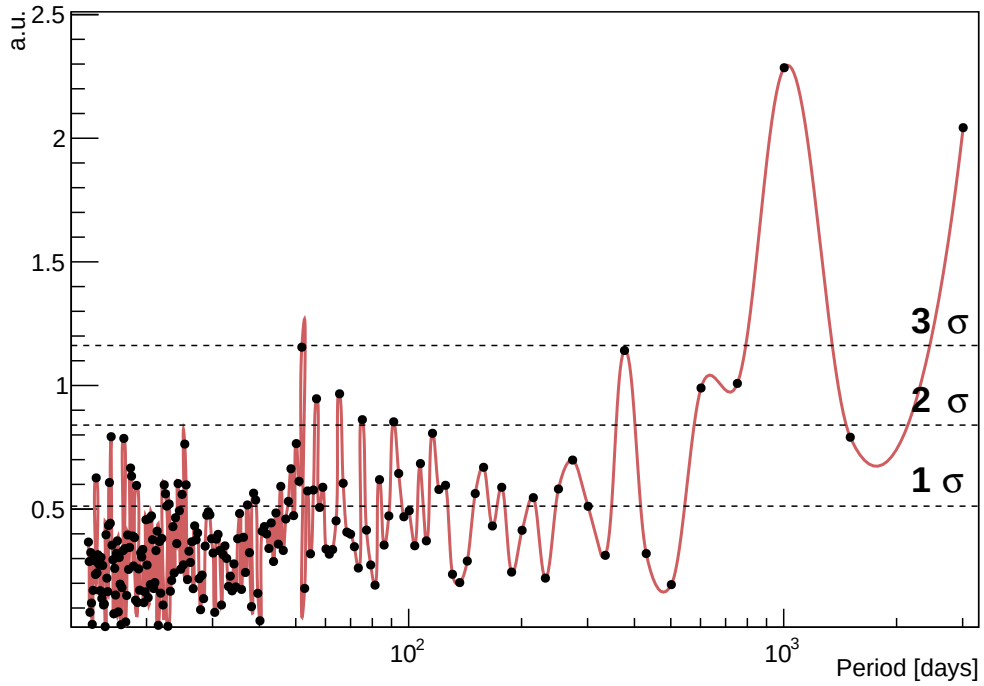

(a) Discrete Fourier transform of the long-term lightcurve.

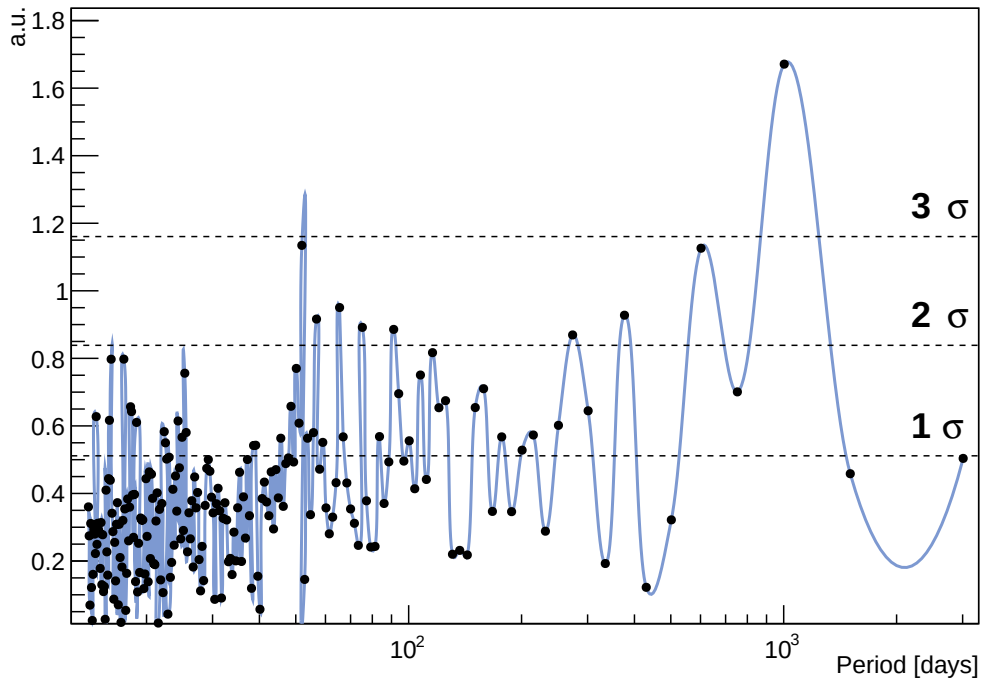

(b) Discrete Fourier transform of the long-term lightcurve linear fit subtraction.

Figure 4.9: The discrete Fourier transformed long-term lightcurve of B2 1215+30 measured with *Fermi*-LAT as a function of the period in an arbitrary unit, before and after subtracting the linear fit. The black dots are the discrete points in Fourier space, connected by a smooth curve to guide the eye. The dashed lines indicate the 1σ, 2σ and 3σ percentiles of the simulated Gaussian noise.

Gaussian noise with mean and width corresponding to the distribution of all integrated flux measurements was simulated and Fourier transformed as well, in order to enable the judgment whether an excess seen in the data at a given period is significant or not. These significance thresholds have to be interpreted carefully, as the white noise is certainly not the optimal model for blazar flux measurements in the absence of quasi-periodicity or flaring activities. However, it allows for a preliminary measure of the significance. Another possibility would be to draw toy lightcurves from the measured lightcurve by scrambling the individual bins, in order to match the null hypothesis of no quasi-periodicity.

Figure 4.9a hints periodic components with a period of about 1000 and 3000 days. As those are the longest periods accessible to the DFT, this could also be the manifestation of the seemingly liner long-term flux increase (Figure 4.3) in the Fourier transform, instead of a truly periodic component.

To account four that the lightcurve was fit by a polynomial of degree one, before applying the DFT to the lightcurve after subtracting this fit. This is shown in Figure 4.9b. The peak around 3000 days disappeared now as expected, but a significant peak acound 1000 days remains. This observation goes in the same direction as the conclusion of [118], where a approximately 1000 day quasi-periodicity was claimed for the gamma-ray blazar PG 1553+113.

Going back from the frequency to the time domain, the natural follow-up is a fit of the lightcurve with the shape expected from the DFT, which is a polynomial of degree one plus a sine:

$$\Phi(t) = At + B\sin(\frac{2\pi}{T}t - \varphi) + C. \tag{4.9}$$

The longterm lightcurve including the fit is shown in Figure 4.10. The an initial value for the period T was set to 1000 days. The fit parameters and their uncertainties are given in Table 4.5. While the DFT gave us the power density in discrete frequencies defined by the discrete measurements, the fit yields an estimate for the period including an uncertainty, which is the most striking number in Table 4.5.

To further collect evidence for this quasi-periodic component with a relatively long period, it is promising to redo the *Fermi*-LAT lightcurve of B2 1215+30 in time bins which are more adapted to lay open features in the 1000 day period-domain, for example in a 250 day time-binning.

This behaviour has been checked with Lomb-Scargle Periodogram, another independent method (this check is done by M. de Naurois). This method, was checked with and without the polynomial fit and in the case when the linear increase is subtracted, it gives a period of 1081.94 days with 3.3σ consistent with the results mentioned above.

Further checks on this behaviour, the interpretation and constraints derived from these results are a prospect for future projects.

Long-term lightcurve fit				
A	1.5	$\pm$	0.2	$\cdot 10^{-3}$
B	1.61	$\pm$	0.25	
C	-79	$\pm$	11	
T	1083	$\pm$	32	
φ	-28	$\pm$	10	

Table 4.5: The fit parameters of the long-term lightcurve fit shown in Figure 4.10.

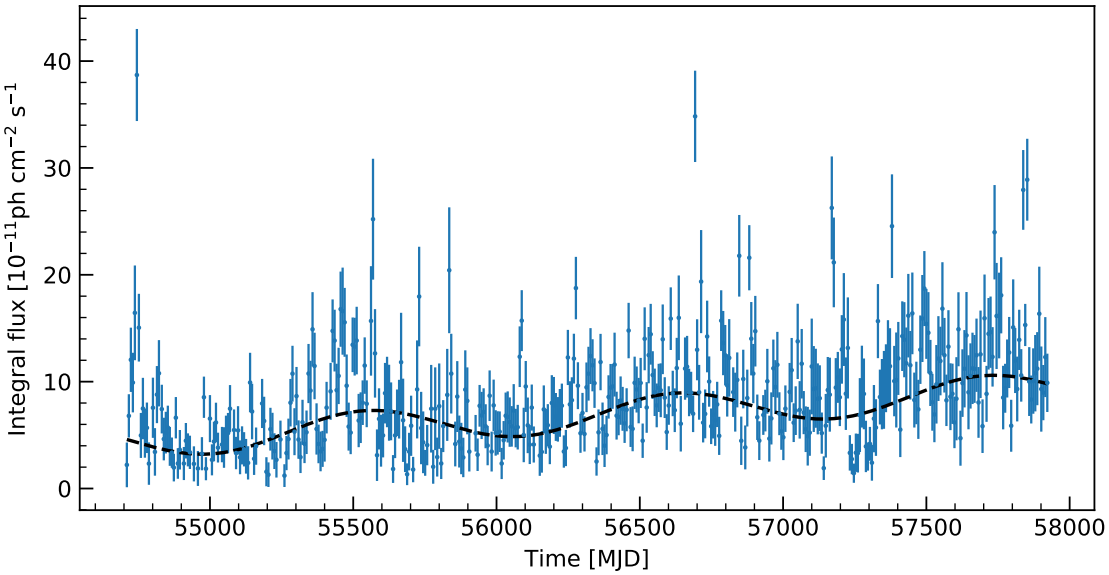

Figure 4.10: The long-term lightcurve including a fit of the form given in Equation 4.9. The fit parameters and their uncertainties are listed in Table 4.5.

4.7 Summary and Discussion

In this chapter, the gamma-ray variability of the BL Lac object was studied. For the scope of this thesis, the *Fermi*-LAT publicly available data was used.

Two periods of five months from January to May in 2013 and 2014 were analyzed using the *Fermi*-LAT data. This study was motivated by two major flares detected by the VERITAS experiment during 2013 and 2014. In collaboration with the VERITAS experiment, the gamma-ray variability of B2 1215+30 was studied over five decades in energy. VERITAS data resulted in the detection of a flare during 2013 whereas searching for counterparts in the GeV range with the *Fermi*-LAT data did not show evidence of any significant flux enhancement during this period. VERITAS and *Fermi*-LAT observed a bright gamma-ray flare from the BL Lac object B2 1215+30 on 2014 February 08, with TeV flux equivalent to 200 % of the Crab Nebula flux (a standard measure in gamma-ray astronomy). At GeV energies the flare started on 2014 February 05, whereas at TeV energies the flare was seen by VERITAS on 2014 February 08 (although the observatory did not operate on the previous nights). Quasi-simultaneous observations at other wavelengths of the

flaring period did not detect any significant flare evidence. Observations from the *Swift* X-ray telescope, taken one day after the flare were used in the estimation of the relativistic jet Doppler factor.

The variability time scale of the source during the 2014 flare was derived from the 1-day time bin *Fermi*-LAT lightcurve and was found to be $t_{\rm var} \simeq 9.0\,{\rm h}$. Such short variability timescales constrain the size of the emission regions using causality arguments. Using the opacity argument and following the calculation of [139] we derived the minimum Doppler factor $\delta \geq 5$. A more constraining limit on the relativistic Doppler factor was set by using the VERITAS flare. With the VERITAS data taken during the night of the flare an upper limit on the flux halving time of $t_{var} < 3.6$ h was found. These results were considered to set limits on the Doppler factor $\delta \geq 10$. The value reported here is in agreement with what is found in other TeV blazars.

To better understand the GeV emission picture on a large time scale, the long term variability of B2 1215+30 in the energy range 100 MeV $< E <$ 500 GeV was investigated with nine years of *Fermi*-LAT data. Several flux increment were detected. Three major flares with the same flaring amplitude as the 2014 flare were distinguished in the long-term lightcurve; in October 2008, February 2014 and April 2017. This analysis showed that the source has undergone several flaring activities after the here-discussed 2014 flare. Data from the IACT experiments, which cover the latest flares would help to better understand the gamma-ray emission and search for counterparts at TeV energies. Such investigation concerning the latest period of observations could not be studied here due to the data privacy policy of the IACT experiments and this source is outside the field of view of H. E. S. S. These flaring episodes offer the possibility to study and characterize and investigate the gamma-ray emission.

When studying the long-term gamma-ray emission from B2 1215+30, a yearly flux increase with time was found. A linear correlation between the yearly average fluxes and the spectral indexes was identified and it is under investigation. Since 2009, the flux from this source is increasing and the spectral index is getting harder showing correlation between the two. The presence of the flaring activities in the GeV energy range has been investigated to understand the origin of the variability, assuming different processes. To account for different processes, the flux and the log-flux distributions are fitted with normal distributions. The former is often associated with additive processes and the latter with multiplicative processes. The two cases are unlikely to describe the data. There is the possibility that these processes are due to quasi-periodic behavior.

A quasi-periodic study was performed using the long-term lightcurve binned in seven day time bins. The checks on the periodicity of the source, using a Discrete Fourier Transform gives a hint for a period of 1083 ± 32 days. These results were checked with a different method using a Lomb-Scargle Periodogram test, which gives a period 1081.94 days. Quasi-periodic behaviour is found in literature, which is reported in optical for some blazars and lately in the BL Lac object PG 1553+113 at GeV energies. Possible explanations can be related to a quasi-periodic process within the relativistic jet. This behaviour can also be related to geometrical effects, which might

be due to a binary black hole system or precession of the supermassive black hole [146, 147, 148, 149]. The quasi-periodic behaviour is seen in X-rays in some miqrosuars [150]. Similarities between X-ray observations of microquasars and gamma-ray observations in AGN should be investigated in the future. However, X-rays come from the accretion disk in microquasars and gamma-rays from the jet in blazars. There could be some coupling between them. This is an interesting direction for future and much longer observations of AGN. This important hint of periodicity on the BL Lac object B2 1215+30 and the physics responsible for it are going to be further investigated.

The temporal variability of B2 1215+30 has been analyzed on time scales from days to years in the GeV energy range with the *Fermi*-LAT. This study reveals B2 1215+30 as an promising gamma-ray emitting source to study and characterize the emission of this source class at high-energies and better understand the blazar picture.

Chapter 5

Crab Nebula with a decade of H. E. S. S. I observations

The first source ever detected at very-high-energies is the Crab Nebula, a pulsar wind nebula in the Galactic plane, ∼2 kpc from the Earth [14]. The Crab Nebula was created in the supernova explosion of 1054 and contains a highly magnetized rotating neutron star (Crab pulsar) which powers a wind of relativistic particles in the nebula [55]. Although is one of the best studied objects in the sky, it is an ever-surprising source.

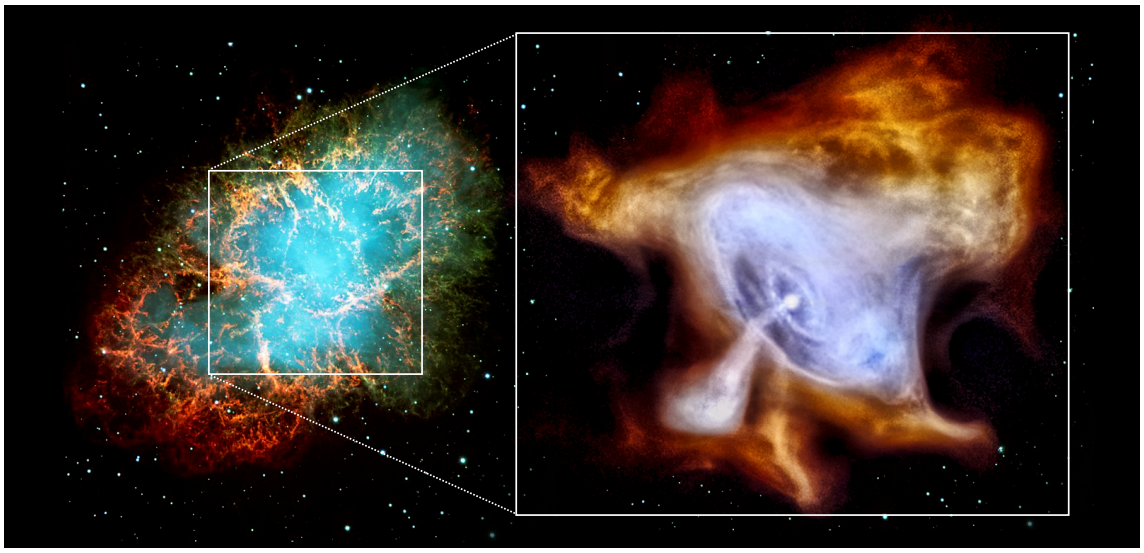

Figure 5.1: The Crab Nebula system, and the zoomed pulsar.

Since its first detection at very-high-energies by the Whipple telescope in 1989 [14], the Crab Nebula has been regularly monitored by the gamma-ray experiments. It serves as a calibration source for many imaging atmospheric Cherenkov experiments since it is very bright and no flux variations are predicted by simple SSC models, traditionally used to explain emission at the very-high-energies. And no flux variation were actually reported by the IACTs so far. Contrary, the space-borne experiments, such as *AGILE* and *Fermi*-LAT have reported on the detection of flux variations of the synchrotron component at GeV energies [151, 152], with the latest major flare at energies above 100 MeV reported by the *Fermi*-LAT in March 2013 [153]. During this flaring episode, the flux increased by a factor of 20 on time scales of only a

few hours, which come as a complete surprise as was not expected from theoretical predictions. The H. E. S. S., VERITAS and MAGIC experiments have not reported any evidence of simultaneous flux variation at very-high-energies so far [154, 155].

The unexpected flux variations detected at high-energies motivated the search for a similar behavior in the very-high-energy regime with the H. E. S. S. experiment, which has regularly monitored the Crab Nebula since the start of operation in 2003. As the Crab Nebula is in the northern hemisphere, it can be seen by the H. E. S. S. telescopes only at zenith angles larger than 45 degrees, resulting in larger systematic uncertainties. This is in contrast to the optimal observation conditions for VERITAS and MAGIC experiments, which are both in the northern hemisphere. In addition a large fraction of data is taken from September to October, the rainy season in Namibia. Another source of systematics is the presence of dust in the atmosphere from bushfires during this period. The tight visibility window on the Crab Nebula and the non-optimal atmospheric conditions increase the probability to miss such flares, which are exceptional and important events that help to understand the very-high-energy emission from this source. However, large zenith angle observations increase the effective area which, at the highest energies increases the sensitivity to the short flares in this regime.

The study presented in this chapter on the very-high-energy spectrum and variability of the Crab Nebula is based on ten years of Crab Nebula observations with the H. E. S. S. experiment. All the good quality data accumulated with the H. E. S. S. I experiment is used. To increase the sensitivity to flux variations, we correct for the atmospheric transparency, which was shown to have an effect on the flux measurements. During H. E. S. S. I observations carried out between 2003 and 2005, the energy threshold for the Crab Nebula was 440 GeV [113]. Since then the data set is greatly expanded, a 5th telescope was added to the array in 2012, lowering the energy threshold, and new reconstruction techniques have been developed. All these combined together allow to make a comprehensive study on the Crab Nebula by measuring the energy spectra in a wider energy range, study flux variations throughout the years and search for extension at very-high-energies.

When the H. E. S. S. II telescope was added to the already existing array in 2012, the Crab Nebula was one main target during the commissioning phase. The trigger of H. E. S. S. II supports mono and stereo observations. The advantages of this trigger are seen in the analysis and reconstruction results. Observations taken with CT1 to CT5 enable the reconstruction of lower energy events, bridging gamma-ray astronomy from ground and space. The observations with the H. E. S. S. II are covered in the next chapter.

In this chapter, Section 5.1 introduces the Crab Nebula with a historical overview, followed by a description of the H. E. S. S. data on the Crab Nebula in Section 5.2. The analysis results are presented in Section 5.3. The measured spectrum and variability studies are given in Sections 5.4 and 5.5 respectively. The atmospheric transparency effect on the flux measurements is described in Section 5.6. The summary and a discussion are found at the end of the chapter in Section 5.7.

5.1 Introduction

In 1054, Chinese astronomers recorded the presence of a new star above the southern horn of the Taurus constellation [156, 157]. It was visible during day time for about a month with a brightness of about six times the one of Venus and as outstanding as a full Moon [158]. This "guest star", as the Chinese astronomers called it, started to fade after 6 months. After one year it disappeared and was not seen again with the human eyes until the invention of telescopes. In 1731, John Bevis observed the nebula of this explosion with an optical telescope. The comet hunter, Charles Messier mistook this nebula for a comet and listed it as the first entry (M1) in his "Catalogue of Nebulae and Star Clusters", published in 1758 (see [159] for a review). In 1844, the nebula was named the Crab Nebula by William Parsons, third Earl of Rosse, after he discovered the filaments and drew a sketch which resembled a crab as shown in Figure 5.2a.

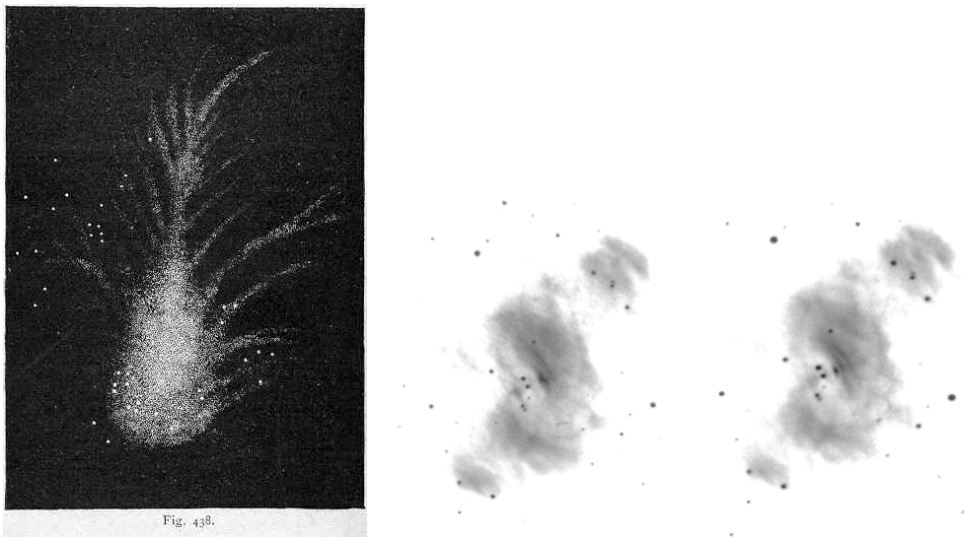

(a) (b)

Figure 5.2: (a) Lord Rosse's sketch of the Crab Nebula filaments in 1844. Image courtesy [160]. (b) Image of the Crab Nebula activity produced in 1968. Image courtesy [161].

We now understand that this "guest star" was the brilliant flash of a supernova explosion. Throughout the years, astronomers made more detailed observations and measurements. They found an expanding nebula and a central rapidly-rotating pulsar, the Crab pulsar. They combine to a system which is nowadays known as the Crab Nebula (see Figure 5.3).

The Crab Nebula is a surprisingly unusual pulsar wind nebula. The synchrotron component of the Crab Nebula extends up to the high-energies, which is found to be variable in this energy range. The emission from the pulsar remained constant during the flares, indicating that the flares are coming from the nebula. During these episodes, the synchrotron component exceeded its average luminosity up to a factor of 30. The unexpected gamma-ray flares have broadened the knowledge on

this source but also challenged the theoretical models, where complex models have to be considered to explain the observations.

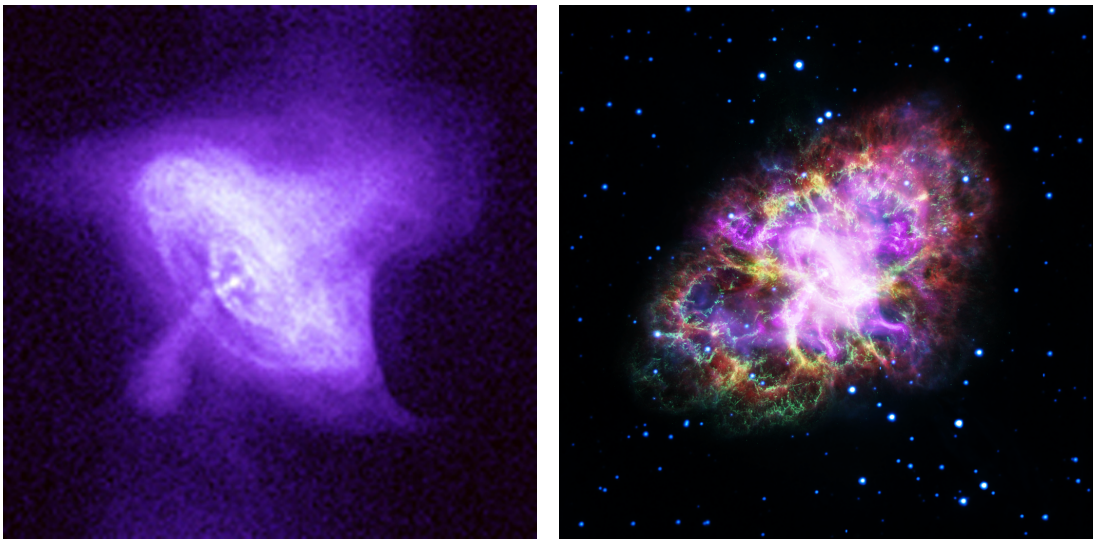

(a) (b)

Figure 5.3: (a) The Crab pulsar as seen from Chandra X-ray Observatory. (b) Composite image of the Crab Nebula from five telescopes: the Karl G. Jansky Very Large Array, the Spitzer Space Telescope, the Hubble Space Telescope, the XMM-Newton Observatory, and the Chandra X-ray Observatory. Image courtesy: NASA, ESA, NRAO/AUI/NSF and G. Dubner (University of Buenos Aires).

Another peculiarity of the Crab Nebula is the Crab pulsar and the detection of pulsed emission up to TeV energies. So far, the Crab pulsar has been detected by MAGIC [56] and VERITAS [162], but not by the H. E. S. S. experiment. The observational conditions, zenith angle and the high background make it challenging to reach the low energy threshold needed to detect the pulsar with the H. E. S. S. II. However the Crab pulsar is not on the scope of this thesis subject.

Ever since the Whipple telescope detected the first very-high-energy gamma rays from the Crab Nebula [14], the succeeding IACTs continued to monitor the Crab Nebula and measured its energy spectrum over a wide energy range. MAGIC measured the energy spectrum over three decades in energy, from 50 GeV to almost 30 TeV [155], VERITAS reported the spectrum measurement from 115 GeV to 42 TeV [154] and the H. E. S. S. I published spectrum was from 440 GeV to 40 TeV [113]. Despite all these measurements, the puzzle of the very-high-energy emission is incomplete. To better understand the picture, the Crab Nebula spectrum is investigated using all the available H. E. S. S. data.

The available H. E. S. S. I data on the Crab Nebula is described in the following.

5.2 Data Set

The first H. E. S. S. I telescope on site was built in 2002, science data taking started in 2003 with three telescopes, and the array become fully operational in 2004. The Crab Nebula was a prime target during the commissioning phase in 2003 and has been regularly observed ever since. The installation of the H. E. S. S. II telescope in 2012 allowed to access a new energy range for the study of the Crab Nebula. The observations of the Crab Nebula with H. E. S. S. I are discussed here, whereas the H. E. S. S. II observations are described in Chapter 6.

The Crab Nebula (R.A. = $05^{\mathrm{h}}34^{\mathrm{m}}31.1^{\mathrm{s}}$, decl. = $+22°00'52''$, J2000) is visible to the H. E. S. S. telescopes at zenith angles larger than 45 degrees, from September to March. Observations are possible also during August and April but only at zenith angles larger than 65 degrees. The data accumulated on the Crab Nebula during H. E. S. S. Phase-I is spread over almost ten years and was taken during different seasons, under different weather conditions and different instrument response (in particular reflectivity). For instrument response studies, a fraction of the data was taken with different observation strategies. For instance, some runs taken in *wobble-mode* have offset angles up to three degrees from the camera center. To extract meaningful results from this rich but varied dataset, a good understanding of the data and cross-checks excluding runs which might affect the reconstructed gamma-ray energy and direction are needed.

Data Set	Dates	Zenith	Offset	N runs
I	2003 – 2004	45-50	0.5	10
II	2004 – 2005	45-52	0.5	21
III	2005 – 2006	45-51	0.5	8
IV	2006 – 2007	45-55	0.5-0.8	6
V	2007 – 2008	45-48	0.5	12
VI	2008 – 2009	45-51	0.5	7
VII	2009 – 2010	45-48	0.5	22
VIII	2010 – 2011	45-50	0.7-0.8	24
IX	2011 – 2012	–	–	–
X	2012 – 2013	–	–	–
XI	2013 – 2014	45-52	0.5-0.8	39
XII	2014 – 2015	45-48	0.5	2
XIII	2015 – 2016	45-55	0.5	5

Table 5.1: Summary of Crab Nebula observations with the H. E. S. S. I telescopes.

The H. E. S. S. observations are split into runs of 28 nominal minutes duration. This is done to balance the run live time with changing observation conditions during the night i.e. pointing, night sky background or moving objects on the sky. However, different problems encountered during data taking can shorten the run duration. These problems can be external, e.g. thin clouds or shooting stars entering the field of view of the telescopes, or technical, e.g. camera voltage or DAQ problem.

This can interrupt the data taking, but the data stored before the problems can be used. Other problems which do not interrupt data taking but have to be taken into account before analysis are related to faulty drawers or dead pixels. The telescope multiplicity, zenith angles, offset angles and other parameters differ from one run to another. The response of the instrument depends strongly on these parameters. It is highly important to select good quality data after calibration; this selection is done to remove events caused by noise and reduce the systematics to improve the physics results.

Additionally, combining observations spread over a period of ten years might introduce other systematics. The aging of the optical system affect the Cherenkov light collection. The optical efficiencies of the telescopes degrade with time, yielding a lower light collection efficiency. All these parameters and their effects are checked to have more reliable scientific results and reduce systematic effects they can introduce. Table 5.1 summarizes the details from observations of the Crab Nebula with the H. E. S. S. I telescopes. The selection criteria applied to the H. E. S. S. I data is explained in the following.

5.2.1 Data Quality Selection

Before the data analysis and extraction of scientific results, a careful data selection is needed. During the calibration process (see Section 3.4), run quality parameters are stored for each observation run. The run selection was built on these parameters. This selection is done based on pre-defined standard criteria, which depend on the reconstruction technique. As described in Chapter 3, different event reconstructions are possible based on the triggered type. The trigger system of the H. E. S. S. I telescopes is discussed in detail in [163].

Parameter	Cut value
Participating telescopes	≥ 3
Broken Pixel	≤ 20 %
Trigger Rate	≥ 100 Hz
Stability Trigger Rate	≤ 4 %
Run duration	≥ 5 minutes
Relative Humidity	≤ 90 %
Radiometer Temperature	$\leq$ -20 degree
Radiometer Stability	≤ 3 degree

Table 5.2: Selection criteria applied to the H. E. S. S. I data.

For the spectrum and variability studies in this work, a custom selection was adapted. The selection of data based on the parameters given in Table 5.2 is the first step before the analysis procedure. On top of the standard data selection criteria, additional cuts were applied. A limit on the off-axis angles was set at 0.8 degrees. This is done to avoid problems in the spectrum and lightcurve calculation, caused by the non-stable effective area at large off-set angles. Also, runs with zenith an-

gles larger than 55 degrees were excluded. When including runs with larger zenith angles the effective area becomes unstable which is then reflected in the spectrum, introducing systematic effects at the energy threshold. Additionally, other checks were performed for each observation run individually. For each run, the **C**enter **o**f **G**ravity map (COG) of the participating telescopes was checked. The expected distribution over the camera is more or less homogenous. During some observation runs, faulty or non-operational drawers cause holes in the COG, biasing the final map. Therefore, this check was performed for every telescope individually. After the checks, only runs with homogeneous COG maps were kept. Figure 5.4 shows example COG maps for the CT1-4 telescopes with the faulty map for CT2, which led to the exclusion of the run.

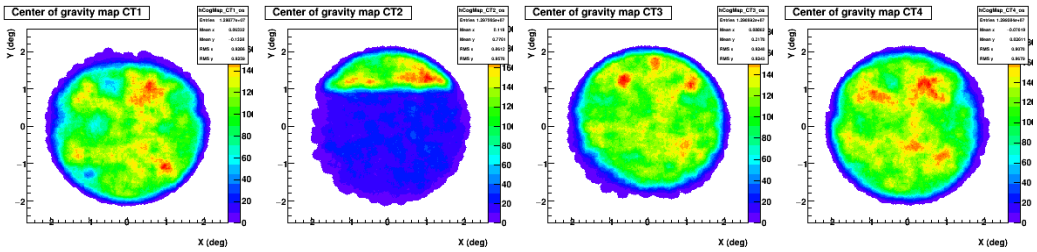

Figure 5.4: An example of a run that passed all the run selection criteria but the COG map check. The COG maps for CT1, CT2, CT3 and CT4 (left to the right) for the run number 42556 are shown. The second COG map, which correspond to CT2, is problematic and this run is excluded from the final run list.

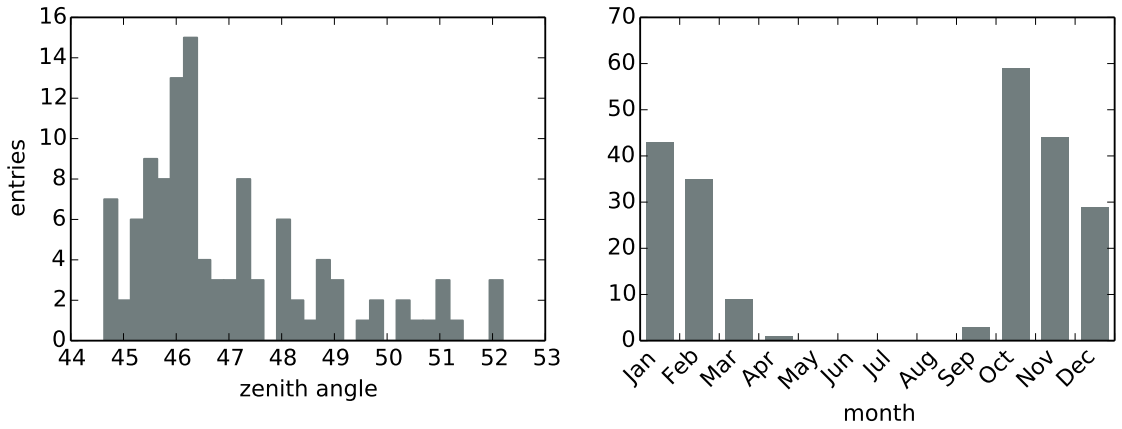

Figure 5.5: Left: Zenith angle distributions for the run list used in the analysis after applying the custom selection criteria as described in the text. Right: Observations of the Crab Nebula taken with the H. E. S. S. I telescopes, with runs distributed from 2003 to 2015. The runs presented here are obtained after applying only the standard run quality, which results in more runs than in the left plot. The majority of the runs are taken during October.

This resulted in 113 H. E. S. S. I observation runs, corresponding to an exposure of 46.6 h, taken between 2003 to 2013. Finally, six runs from 2006 passing all the previously applied run quality selection were excluded due to an incorrect pointing model. This mispointing leads to an incorrect reconstruction, and hence to incorrect results. In case of a solvable problem, correcting the pointing model for these observations could potentially make the data available again, but this can only be achieved through significant software development. The run distributions based on the month of observations for the full data set, without any selection criteria applied are shown in Figure 5.5 along with the zenith angle of the remaining good runs. The later runs (unless specified differently) are used to perform the study and results described next.

5.3 Analysis Results

The selected data was analysed with the *Model Analysis*, using the Std and Loose cuts to find the configuration which provides the best analysis results. An ON region of 0.25 degrees was defined around the source to avoid a possible spill-over into the OFF regions used for the background estimation. The background was estimated with the *Reflected Region* method (described in Section 3.6). The number of excess events and the significance are calculated from Equation 3.8 and 3.9. The distribution of ON, OFF and excess events are traditionally visualized on θ^2 histograms that represent the squared radial distribution of events. The θ^2 distributions for the here-discussed configurations are presented in Figure 5.7. The number of events n_{ON} and n_{OFF} from the chosen ON and OFF regions, together with the other analysis details are summarized in Table 5.3.

Cut config	n_{ON}	n_{OFF}	n_{excess}	S_{LiMa}	S/B	Rate [γ's/min]
Std	19929	9504	19269.6	270.7	29.2	6.9±0.05
Loose	29057	29821	26977.6	284.8	13.0	9.7±0.06

Table 5.3: Summary of H. E. S. S. I analysis results obtained from the Std and Loose cut configurations. The number of events in the ON and OFF regions n_{ON} , n_{OFF}, the number of excess events n_{excess}, significance S_{LiMa}, signal to background ratio (S/B) and the rate of gammas for each cut configuration are given.

As expected, the number of events is larger for the Loose cut configuration than for the Std cuts due in particular to a lower threshold, but this comes at the price of a lower signal to background ratio.

The Crab Nebula significance map and the significance distribution of this map are shown in Figure 5.7. As seen from Figure 5.7b, the mean and sigma for the regions of the map far from the Crab Nebula are almost 0 and 1 respectively, indicating a good background subtraction. The same check was performed for the Loose configuration and shows similar behavior.

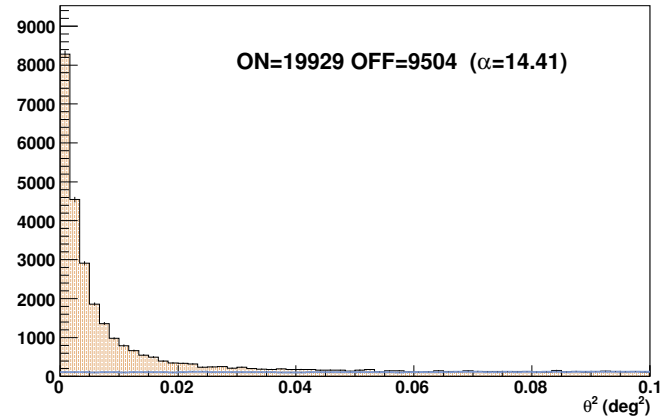

(a) Std cuts

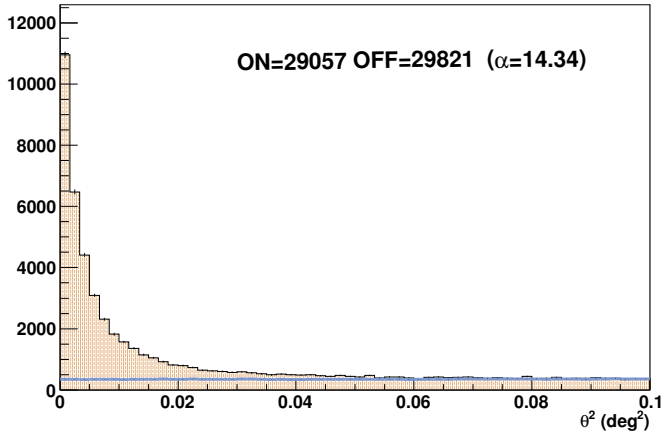

(b) Loose cuts

Figure 5.6: The θ^2 (squared angular distance) distributions for gamma-like events (filled histogram) compared with normalized θ^2 distributions of off regions (black) for the (a) Std and (b) Loose cuts. The dashed blue points correspond to the background distribution, which for the Crab Nebula is very low compared to the signal from the source.

These results are used to derive the energy spectrum of the Crab Nebula which is described next.

5.4 Differential Energy Spectrum

When reconstructing gamma-ray events, the direction and energy are the most important parameters to be measured. The energy information is used to reconstruct the spectrum of the source which gives important insights about the acceleration mechanisms of the gamma-ray source. The measured Crab Nebula spectrum, first measured by the Whipple telescope at energies above 700 GeV, has now been extended up to 50 TeV [164, 155]. In general, the spectrum of the Crab Nebula,

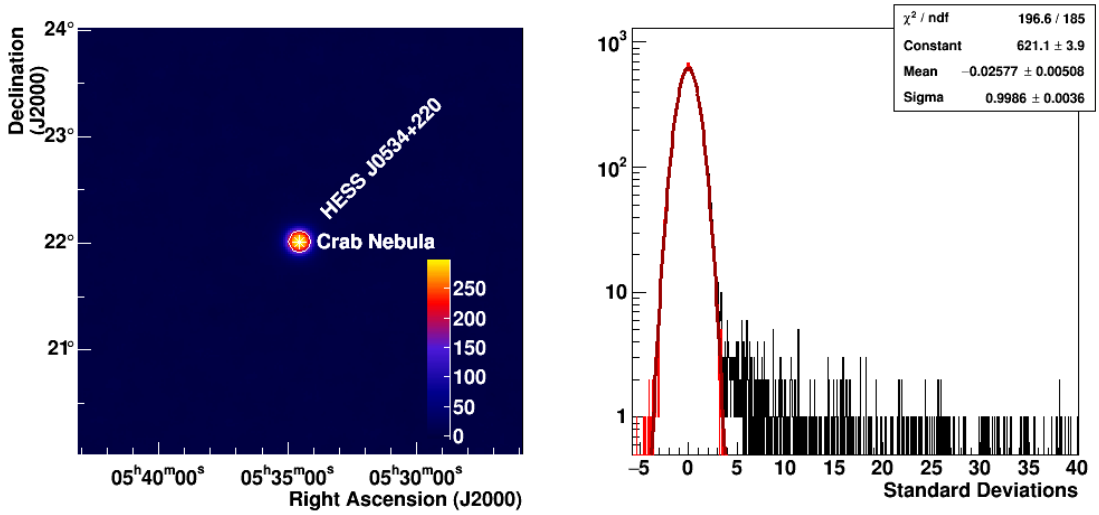

(a) Significance map. (b) Significance distribution.

Figure 5.7: (a) The significance map of the Crab Nebula using all the H. E. S. S. I data set with Std cuts. The position of the Crab Nebula is showed in the center. (b) The corresponding significance distribution of the whole map is shown in black. The distribution after excluding a circular region of 0.25 degrees around the source with a Gaussian fit is shown in red and the fit values are shown in the plot.

as measured by the IACT experiments, is compatible with a log-parabola spectral shape. The differential energy spectrum measured by the H. E. S. S. experiment in 2006 was best described by a exponential cut-off spectrum shape [113]. This measurement was performed with data from 2003 (commissioning phase with three telescopes), 2004 and 2005. Since then, the statistics have increased and more sophisticated reconstruction techniques were developed for the H. E. S. S. data. We used the extended data set to lower the energy threshold, access a new energy range and perform a precise spectrum measurement of the Crab Nebula.

The spectrum was measured using the "forward-folding" technique described in Section 3.6. To exploit a new energy range, the Std and Loose cuts were used. The energy threshold for the events passing the cuts was set to energy where the effective area is 20 % of its maximum for the corresponding observation parameters. Motivated by the previous measurements, the spectrum was fitted with three different spectral shapes: a power-law, a curved power-law[1] and a power-law with exponential cut-off. Table 5.4 gives the details of the best fit values obtained in this work and also a summary from the other IACT measurements.

[1] or log-parabola

Fit	Cuts	E_{min} TeV	E_{max} TeV	N_0 $\times 10^{-11}\mathrm{cm}^{-2}\,\mathrm{s}^{-1}\,\mathrm{TeV}^{-1}$	Γ	β	E_0 TeV	E_c TeV	χ^2/ndf
PL	Std	0.48	62.37	2.05 ± 0.12	2.66 ± 0.01	-	1.4	-	296.6/74
CPL	Std	0.48	62.37	3.26 ± 0.21	2.45 ± 0.01	0.18 ± 0.01	1.2	-	91.5/73
Exp-CutOff	Std	0.48	62.37	3.56 ± 0.35	2.38 ± 0.02	-	1.2	9.9 ± 0.57	119.5/73
PL	Loose	0.39	62.37	2.56 ± 0.13	2.61 ± 0.01	-	1.0	-	345.2/88
CPL	Loose	0.39	62.37	4.97 ± 0.28	2.40 ± 0.01	0.15 ± 0.01		-	122.2/87
Exp-CutOff	Loose	0.39	62.37	4.05 ± 0.34	2.38 ± 0.01	-	1.1	11.5 ± 0.65	148.5/87
Whipple				3.20 ± 0.17	2.49 ± 0.06				
CAT				2.20 ± 0.05	2.80 ± 0.03				
HEGRA				2.83 ± 0.04	2.62 ± 0.02				
MAGIC		0.05	30.0	3.80 ± 0.11	2.21 ± 0.02	0.24 ± 0.01	1.0	-	20.0/11
VERITAS		0.12	42.0	3.75 ± 0.03	2.47 ± 0.01	0.16 ± 0.01	1.0	-	12.9/13
H. E. S. S. I		0.44	30.5	3.76 ± 0.07	2.39 ± 0.03	-	1.0	14.3 ± 2.1	15.9/9

Table 5.4: Summary of the Crab Nebula spectrum fit parameters for Std and Loose cut configurations. The spectrum is fitted with a power-law, log-parabola and an exponential with power-law cut off. The energy range of the spectrum fit with E_{min} and E_{max}, the normalisation N_0, the reference energy E_0, the spectral index Γ, the curvature β and other parameters of the fit are summarized. Spectrum parameters from the Whipple [165], CAT [166], HEGRA [167], MAGIC [155], VERITAS [164] and H. E. S. S. I [113] experiments are shown for comparison.

After fitting the spectrum with different spectrum shapes, a statistical method is needed to conclude which is more adapted to describe the data. A likelihood-ratio test to compare two models requires them to be nested, i.e. the more complex model can be transformed into the simpler model by imposing a set of constraints on the parameters. The power-law and log-parabola are nested, and so are the power-law and exponential cut-off models, but the log-parabola and exponential-cutoff model are not. The log-parabola and the exponential-cutoff fits are compared with the reduced χ^2 of the fit. Given the fit results for these models (see Table 3.14b), the data is described best by a log-parabola spectrum:

$$\frac{\mathrm{d}N}{\mathrm{d}E} = (3.26 \pm 0.02) \times 10^{-11} \left(\frac{\mathrm{E}}{1.2\,\mathrm{TeV}} \right)^{-(2.45 \pm 0.01) - (0.18 \pm 0.01) \ln\left(\frac{\mathrm{E}}{1.2\,\mathrm{TeV}}\right)} \frac{1}{\mathrm{TeV\,cm^2\,s}}. \quad (5.1)$$

The quoted errors on the spectrum parameters are statistical uncertainties only. The spectrum corresponds to the Std cut configuration and Figure 5.8 shows the reconstructed energy spectrum of the Crab Nebula.

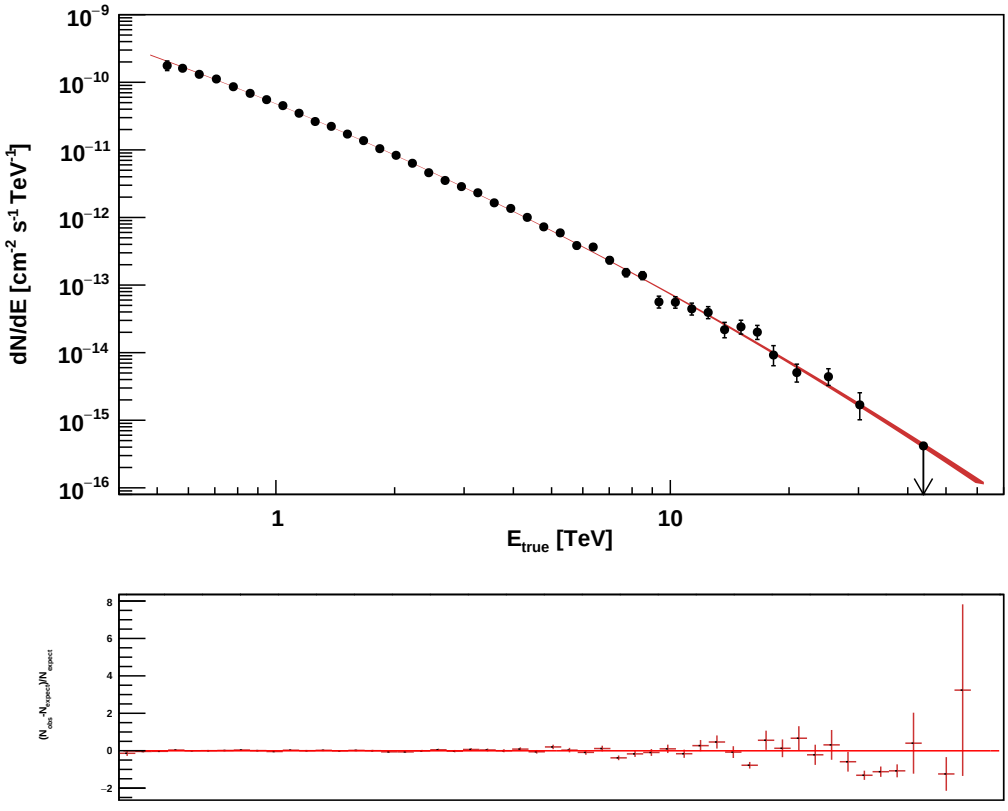

Figure 5.8: Differential energy spectrum of the Crab Nebula as measured by H. E. S. S. I from 480 GeV to 62.4 TeV. The spectrum is best described by a log-parabola spectral shape. The 1σ confidence interval of the fitted spectrum shape is plotted in solid red line. The residual plot in the form $(\mathrm{N_{obs}} - \mathrm{N_{exp}})/\mathrm{N_{exp}}$ is shown in the bottom part.

The differential energy spectrum of the Crab Nebula is measured by H. E. S. S. I in the energy range from 480 GeV to 62.4 TeV. The spectral points are shown in black and they are calculated from the difference of measured events in an energy interval N_{obs} compared to the expected events from the best-fit model, N_{exp}. The uncertainties are statistical only and a 1σ confidential band is plotted along with the points. The difference $(N_{obs} - N_{exp})/N_{exp}$ is shown in the residual plot below the spectrum. It is possible to lower the energy threshold but the systematics need to be understood and controlled. The energy threshold for this analysis is set at 20% of the maximum effective area. As the effective area depends particularly on the zenith angle and given the zenith angle range of the Crab Nebula with H. E. S. S., it is challenging to lower the energy threshold.

For the measurement of the Crab Nebula spectrum two independent analysis frameworks ParisAnalysis (PA, this work) and HAP (by J. Hahn) are involved, which is a standard procedure for cross-checking the results before publication. Since they rely on independent calibration schemes, the intersection run list is used (99 runs). This results in a more stable background control close to the energy threshold hence it allows to use the 15 % of the maximum effective area as threshold for the spectrum measurement. The spectrum is shown in Appendix B (Figure B.1) in $E^{2.5}\,\mathrm{d}N/\mathrm{d}E$ representation for a better comparison. The bottom panel of Figure B.1 shows the relative difference between the "all-world" Crab Nebula spectrum, the average spectrum defined from measurements by the published results from MAGIC and VERITAS and with the here-discussed H. E. S. S. I measurements from PA and HAP. The relative difference for each spectrum is defined as the difference $(F_i - \overline{F})/\overline{F}$, where $\overline{F}$ stands for the average "all-world" spectrum. In this thesis scope, the goal is a precise spectrum measurement and have a large data set which allows an extension at the very-high-energies is highly important. The later is of a particular importance in the variability studies which are presented next. For this reason the spectrum measurement here-discussed uses the run list from the ParisAnalysis, not the intersection run-list between the two different analysis frameworks. A discussion on the spectrum is given in Section 6.5 which includes measurements with H. E. S. S. I and H. E. S. S. II for a better over-view picture.

A detailed study of the TeV flux evolution with time is described next.

5.5 Long-Term Variability Studies

Although the Crab Nebula is considered as a standard candle in gamma-ray astronomy, several flares at energies above 100 MeV were reported from the space-borne satellites. The flares detected by the space borne satellites showed that the flux variations were coming from the end part of the synchrotron emission, followed by a hardening of the spectrum. Generally two arguments can be invoked to explain the high-energy flares. These flares can be related either with an enhancement of the parent electron population or changes in the magnetic field. If the flares are due to the variation in the electron injection, then the flare detected at the synchrotron energy one expects a flare on the inverse Compton. Hence, flaring activities at

TeV energies from the Crab Nebula are not excluded. This study profits from all H. E. S. S. observations on the Crab Nebula to investigate and search for variability in the TeV energy range. As satellites with good sensitivity i.e. AGILE and *Fermi*-LAT were launched few years after the H. E. S. S. experiment started to operate, this would give information about the early years of operation of H. E. S. S.

The lightcurve is derived with the method described in Chapter 3. The integral flux above 1 TeV is calculated on a run-by-run basis, from October 23, 2003 up to March 14, 2013, corresponding to a Modified Julian date (MJD) 52935 - 56365. Figure 5.9 shows the evolution of the integral flux with time from MJD 52935 to 56365. The plotted error bars are statistical only.

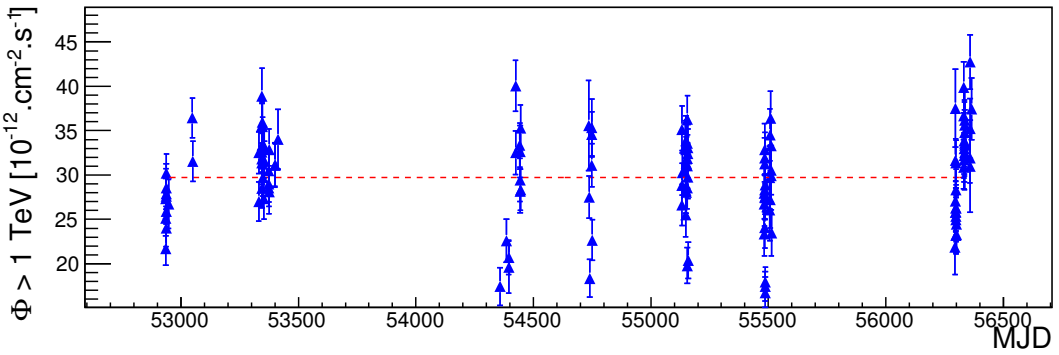

Figure 5.9: Long term lightcurve of the Crab Nebula on a run by run basis, from MJD 52935-56365. The integral flux is calculated at energies above 1 TeV are plotted along with one sigma statistical errors. The red line corresponds to the error weighted average flux.

A χ^2 test, to check if the flux is compatible with a constant C was performed. The $\chi^2/NdF = 583.2/142$ corresponds to a p-value of 0.0001, which is a low probability to obtain these measurements if the assumption of constant flux is correct. Since only statistical errors were considered, the systematic error has to be considered before making any statement about flux variations. The systematic error on the flux for H. E. S. S. measurements has been estimated to be 20 % [113].

The low fluxes of some particular runs (as seen between MJD 54500 to 55500 in Figure 5.9) were investigated. Statistical uncertainties can be introduced by instrument effects, reconstruction or external effects such as atmospheric variations. Given the spread of observations over ten years, another suspect is in the change of the optical efficiencies caused due to the degradation of mirror reflectivity. The distribution of integral fluxes with zenith angles, off-axis and optical efficiencies were checked and are scattered around the mean (see Figure 5.10). There is no evidence of apparent dependency which would introduce a bias. After all the detailed checks carried out, the presence of low fluxes was not found to be caused by known instrument or reconstruction problems. Additionally, the flux distribution with the number of excess events over the exposure time was checked and shows the expected linear increase trend as shown in Figure 5.11.

Further studies were performed to understand the origin of low flux values. To un-

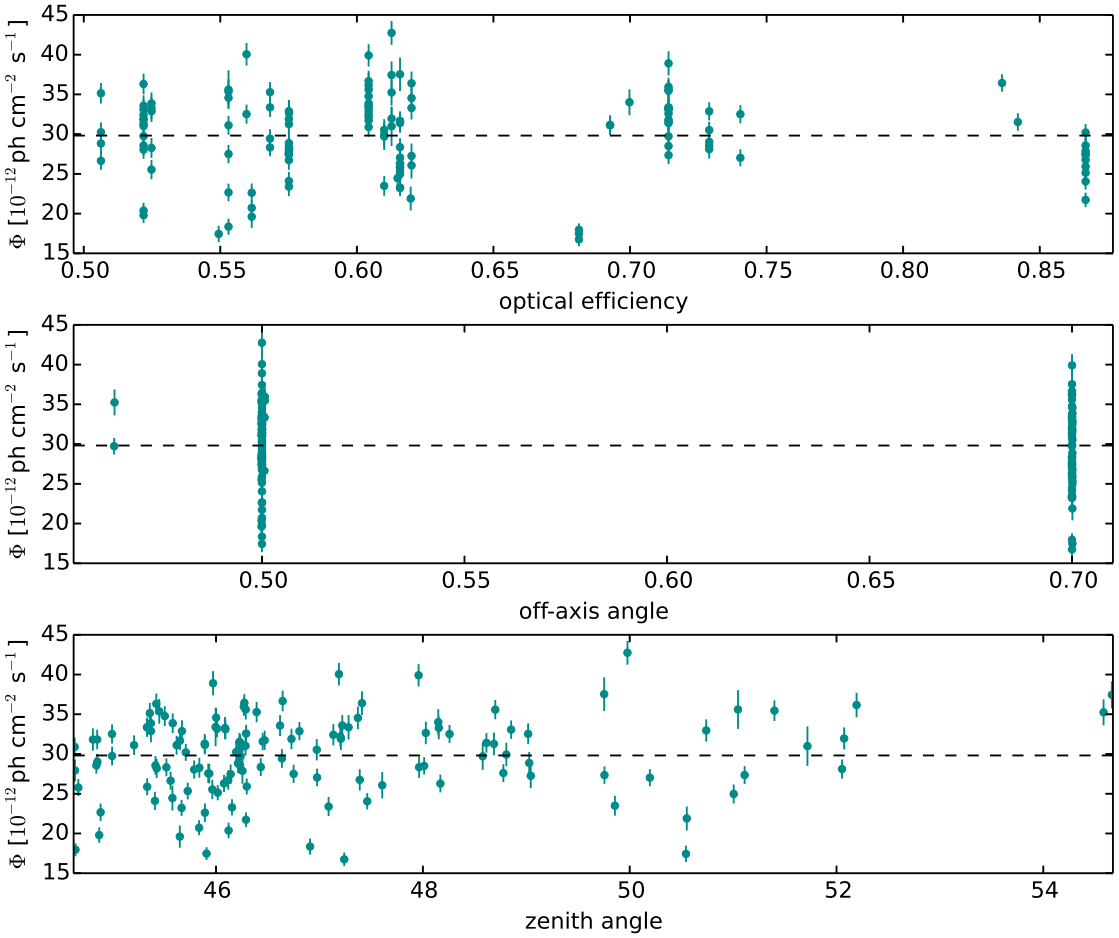

Figure 5.10: Top: Run-by-run integral flux versus optical efficiencies. Middle: Run-by-run integral flux above versus off-axis angles. Bottom: Distribution of the integral fluxes above 1 TeV with observation zenith angles. Their values are distributed around the mean, not showing any evidence of bias introduced.

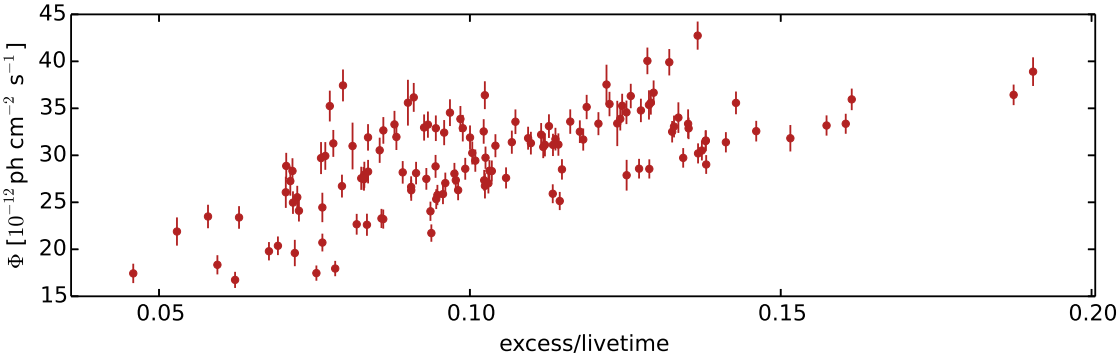

Figure 5.11: The integral flux versus excess normalized by the exposure time.

derstand and reduce the systematic effects, a possible flux attenuation due to varying atmospheric transparency has been studied. Details are given in the following.

5.6 Atmospheric Transparency Effect

The Cherenkov **T**ransparency **C**oefficient (TC) was developed to measure the atmospheric transparency and identify H. E. S. S. runs taken with non-optimal atmospheric conditions. The data analysis techniques developed for the imaging Cherenkov telescopes rely strongly on Monte Carlo simulations, which assume a particular atmospheric model. A deviation of the atmosphere from this model would introduce a systematic effect on the measured flux.

Normally, the atmospheric monitoring and aerosols is done by a LIDAR installed on H. E. S. S. site. Unfortunately, for the data set used here the LIDAR was not working. Monitoring only the trigger rate from a given source does not allow to distinguish if changes are caused by a non-optimal atmospheric quality or are instrument related. A study performed on H. E. S. S. data developed a quantity to measure the effects introduced to distinguish trigger rate changes by large-scale atmospheric absorption, namely the transparency coefficient [168]. The coefficient was first introduced and developed by R. De Los Reyes et al. in the HAP analysis framework, and was later implemented in the ParisAnalysis framework by C. Mariaud. The transparency coefficient from ParisAnalysis is used for the study presented here.

The transparency coefficient depends on the trigger rate R, the main PMT high gain over the camera g, and on the optical efficiency μ. It is calculated for each telescope from the following formula:

$$\mathrm{tc}_i = \frac{R_i^{-1.7}}{\mu_i \, g_i}, \tag{5.2}$$

and averaged over telescopes by taking into account the uncertainties:

$$\mathrm{TC} = \frac{\sum_{i=1}^{n} \frac{tc_i^2}{\mathrm{d}tc_i^2}}{\sum_{i=1}^{n} \frac{1}{\mathrm{d}tc_i^2}}, \tag{5.3}$$

where n is the number of the telescopes participating in a given run.

The presence of thin layers of clouds, dust or fume affects the transparency of the atmosphere, attenuating the Cherenkov photon density on ground level, resulting in an underestimated particle energy. Hence the quality of the atmosphere affects the outcome of the results, in particular when studying the flux variations with time. The TC values from all the Crab Nebula data set taken over more than ten years are shown in Figure 5.12. It can be seen that some runs have low TC values, some as low as 0.4. There are two strategical methods used for the study presented here. The first is to identify and reject runs taken under bad conditions and the second is to try to correct for this effect.

To study this effect on the Crab Nebula flux, all the available data was taken. For an initial study, the run selection was based on only two criteria, before performing the study with a good run-list to minimize other systematic effects. The two criteria were: broken pixels less than 15 % and a *multiplicity* of at least two telescopes. The

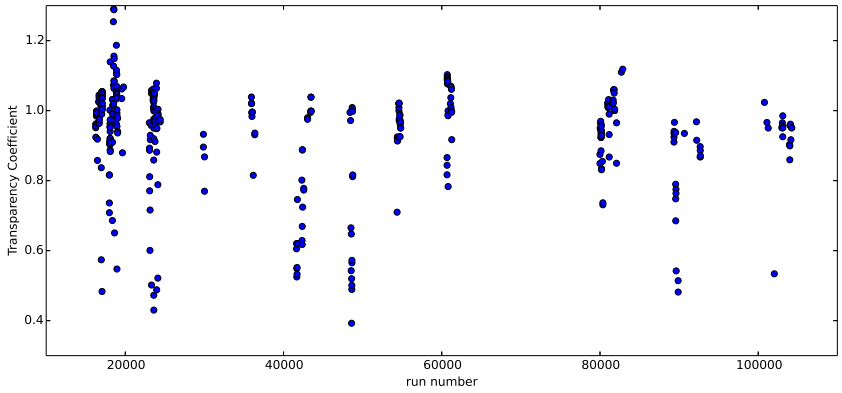

Figure 5.12: The transparency coefficient averaged over telescopes for each observation run. The data plotted here is taken on the Crab Nebula over ten years.

whole data was divided in categories based on the TC value: 80-90 %, 90-95 %, 95-100 % and 100-105 %. A separate analysis was performed on each of the sub-data sets with the Std configuration and the integral flux was calculated. Figure 5.13 shows the integral fluxes versus time for both the initial run selection and the good run list in the different TC categories. The atmosphere has a non-negligible impact on the flux attenuation for TC $\simeq 85\,\%$. To clarify, the TC value of 105 % is an artifact of the calculation method, which is based on an empirical formula. This value refers to perfect atmospheric conditions.

Based on those results, the runs for which the atmosphere had TC < 90 % are considered as not good and to investigate the residual systematic uncertainties an additional cut is introduced. Only runs that fulfill the H. E. S. S. I quality selection criteria and have TC > 90 % are considered. The results are shown in Figure 5.14. By taking into account the atmospheric coefficient to reject bad runs when studying the flux evolution with time, we reduce the systematic effects and the excess variance. With a χ^2 test (see Table 5.5), these results can be compared with the previous results, where the transparency of the atmosphere is not considered in the run selection. The value of the reduced χ^2 shows the improvement, where flux measurements are spread more uniformly spread around the mean. The improvement can also be seen in the pull distributions before and after the TC cut in Figure 5.15. In the following, possible methods to correct for this effect are discussed.

5.6.1 Correcting the Flux for Atmospheric Transparency

Introducing the transparency coefficient as a quality cut when studying the flux time evolution improves the results and reduces the excess variance on cost of statistics. Based on the Figure 5.13 the TC was introduced as a data quality cut by accepting only runs with TC > 0.9. The goal is to recover the data taken under non optimal weather conditions that we had to exclude before due to the introduced effects in the flux measurements. When performing variability studies, in particular at short

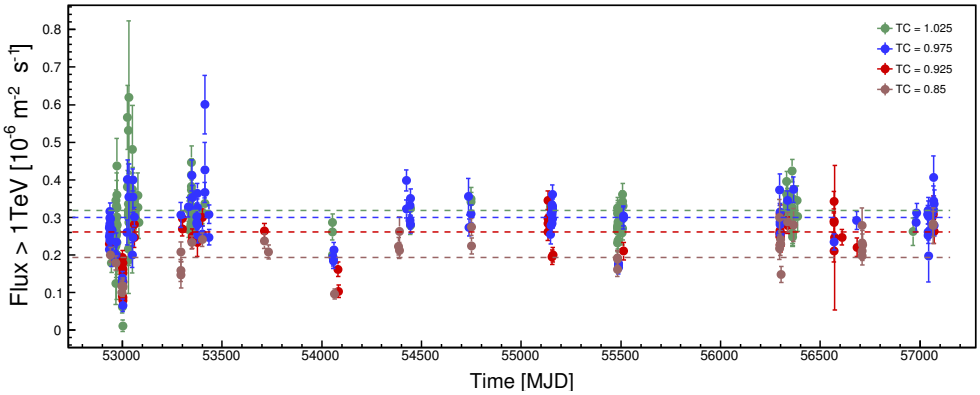

(a) Lightcurve with run selection based on broken pixels and telescope *multiplicity*.

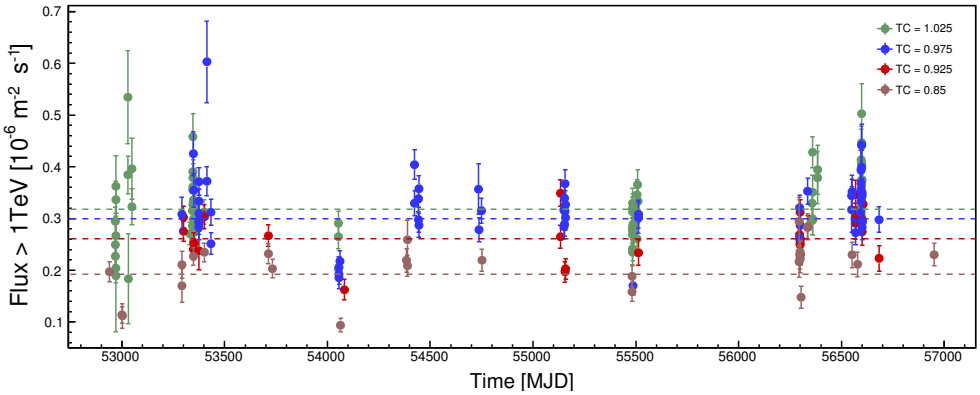

(b) Lightcurve with good quality data run-list.

Figure 5.13: Lightcurves of the Crab Nebula including the mean, with different TC categories in different colors. The categories are named after the averages of their TC ranges. The effect of the transparency on the data can be seen, and it has a bigger impact for low TC values.

time-scales, each run may contain important information. To keep the data, the possibility to correct for this effect was studied.

The attenuation of the Cherenkov light by the atmospheric quality can lead to an underestimated energy reconstruction. If E_{reco} and E_{true} are the particle reconstructed energy and the true energy, with $E_{\mathrm{true}} \propto E_{\mathrm{reco}}/\mathrm{TC}$, the differential flux is found to be:

$$\frac{\mathrm{d}N}{\mathrm{d}E_{rec}} \propto E_{reco}^{-\Gamma}\,\mathrm{TC}^{\Gamma-1}. \tag{5.4}$$

which leads to a change of the normalization with the transparency coefficient and is described by a power law function (as shown in [168]).

A first order, the correction of the flux is done assuming a linear correlation between the flux and the TC. In this case, the flux of each observation run is divided by its

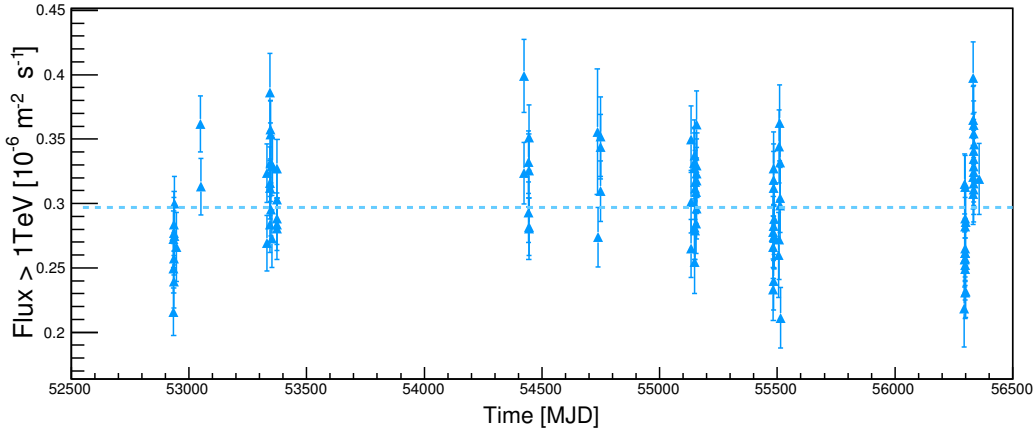

Figure 5.14: The Crab Nebula long term lightcurve on a run by run basis after removing runs with TC < 0.9. The flux errors are statistical only. The cyan dashed line correspond to the mean error weighted flux.

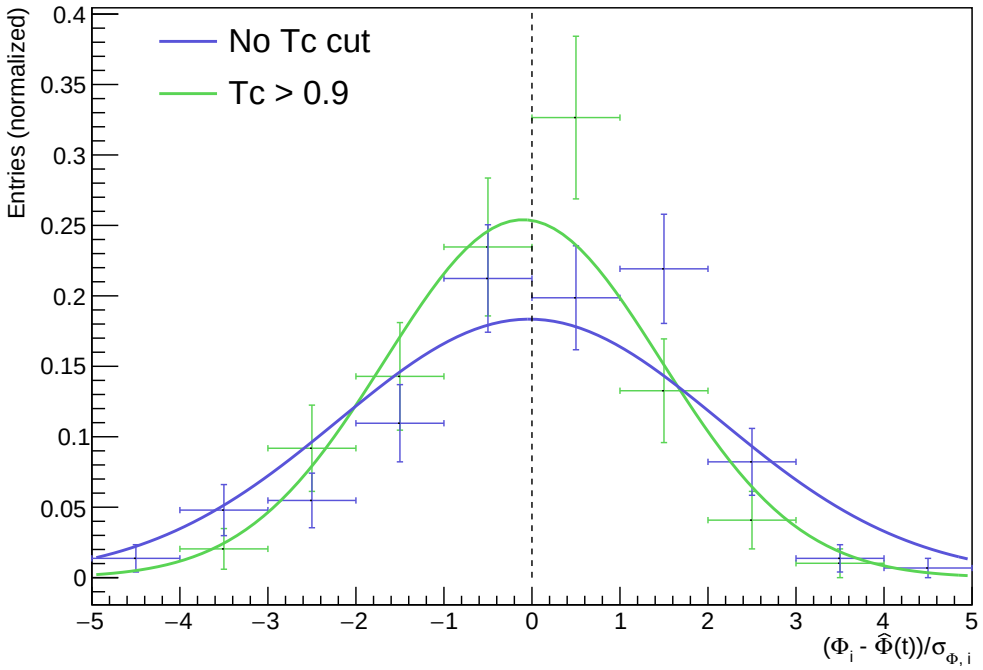

Figure 5.15: The pull distributions of the flux measurements before and after the TC cut, both normalized to unity. The pull is the flux Φ_i minus the mean flux divided by the flux error $\sigma_{\Phi,i}$. For a statistical error only, the pull distribution has width one. For the runs before the TC cut it is 2.2 and after the TC cut it is 1.6, indicating that effects introduced by the varying atmospheric quality make up a large fraction of the systematic uncertainty. The flux errors are statistically only.

corresponding TC value. The resulting lightcurve can be seen in Figure 5.16. The errors on the flux are propagated as follows:

$$\Delta F_{\text{corr.}} = \sqrt{\left(\frac{\Delta F}{F}\right)^2 + \left(\frac{\Delta \text{TC}}{\text{TC}}\right)^2} \times \frac{F}{\text{TC}} \tag{5.5}$$

Linearly accounting for the atmospheric transparency causes a shift on the flux normalization [168]. This hinted a possible nonlinear dependence of the integral flux on the transparency coefficient $F \propto \text{TC}^{\,\alpha}$, in which case the flux correction and error propagation should be done as follows:

$$F_{\text{corr.}} = \frac{F}{\text{TC}^{\,\alpha}}, \qquad \Delta F_{\text{corr.}} = \sqrt{\left(\frac{\Delta F}{F}\right)^2 + \alpha^2 \left(\frac{\Delta \text{TC}}{\text{TC}}\right)^2} \times \frac{F}{\text{TC}^{\,\alpha}} \tag{5.6}$$

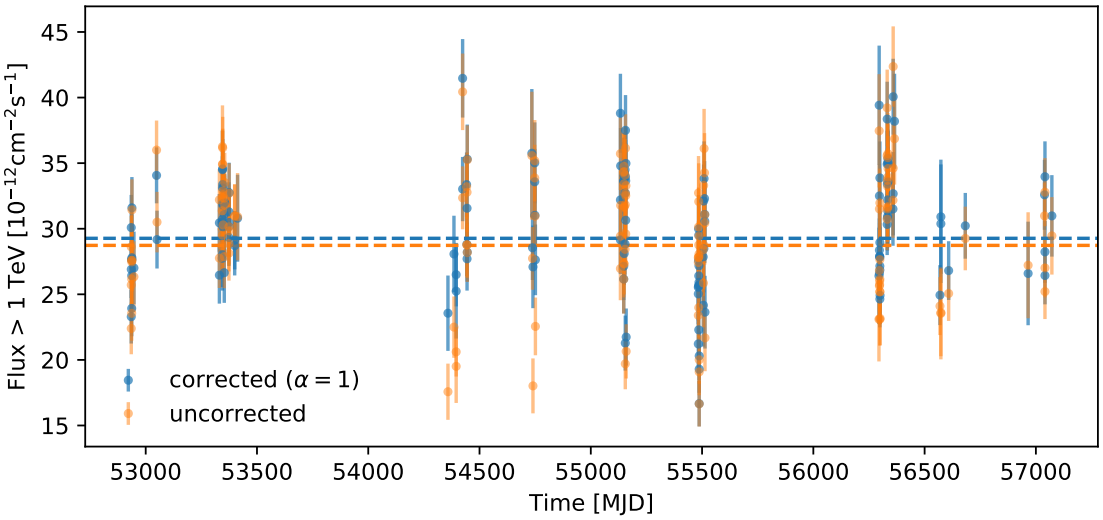

Figure 5.16: The H. E. S. S. I long term lightcurve of the Crab Nebula on a run by run basis. The orange points correspond to the lightcurve without any correction or any cut on the transparency coefficient. The blue correspond to the same data set, corrected for the transparency coefficient. The dashed lines represent the mean error weighted flux for each data set.

The projected lightcurves for the uncorrected, linearly corrected and $\alpha = 1.7$ power-law corrected flux are shown in Figure 5.17. The projections are fitted with Gaussians in an unbinned likelihood-fit. It is evident that correcting for the atmospheric transparency reduces the systematic uncertainty, as can be seen by the reduced standard deviations of the corrected flux fits. However, one can not conclude whether the linear or power-law dependence of the flux on the TC is the better model to correct the flux for the data set used here.

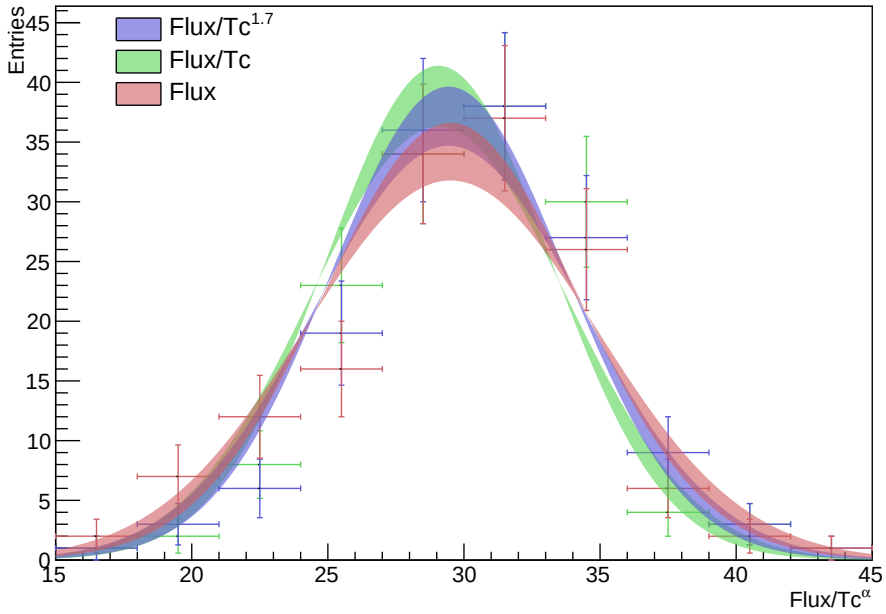

Figure 5.17: The projected lightcurve for the uncorrected flux and the TC corrected flux with power-law index of $\alpha = 1$ and $\alpha = 1.7$, including unbinned Gaussian fits. The uncertainty bands visualize the fit error on the width.

5.6.2 Systematic Flux Uncertainty

To check if the flux is compatible with a constant, a χ^2 test is commonly used. We include a systematic error in the definition of the χ^2, which is proportional to the constant flux of the source C using a proportionality constant α. This is given as follows:

$$\chi^2 = \sum_{i=data} \frac{[x_i - C]^2}{\sigma_i^2 + \alpha^2 C}. \tag{5.7}$$

If the Crab Nebula flux is really constant, this would result in $\langle \chi^2 \rangle \sim NDF$. Requiring that this condition is satisfied, the systematic error is estimated to be $\alpha = 16.1\,\%$. Such a value is acceptable for H. E. S. S. I flux measurements and it slightly improves over the systematic error of 20 % published in previous the Crab Nebula results [113], and is approximately what would be expected given the uncertainties in the Monte Carlo simulation. After being more strict in the data selection, it is possible to reduce the systematic effects on the flux measurements. This estimation is based on the assumption that the flux from the Crab Nebula is constant, but the possibility of having significant flux variations is not excluded.

Table 5.5 summarizes the results for different data sets. The data set I correspond to the lightcurve presented in Figure 5.9, where the transparency coefficient was not taken into account. Data set II is for the lightcurve with transparency coefficient cut of 0.9 (see Figure 5.14). The data sets III and IV correspond to the corrected flux assuming a linear and a power-law dependence.

Data Set	$\Phi > 1$ TeV $\times 10^{-12}$ cm $^{-2}$ s^{-1}	χ^2/ndf	nr runs	α
I	28.73 ± 0.21	583.2/142	143	16.1 %
II	29.30 ± 0.21	471.0/133	134	14.0 %
III	29.27 ± 0.21	431.6/142	143	12.6%
IV	29.29 ± 0.21	427.4/142	143	12.5 %

Table 5.5: Crab Nebula lightcurve fit parameters for data set I, II, III and IV (as defined in the text). The integral flux Φ, the fit parameters to a constant C, the number of runs and the systematic uncertainty α are given.

As shown in Table 5.5, the systematic uncertainty is lower when the flux is corrected by the TC. The two cases when the flux was corrected by a linear and a power-law dependence were further investigated and was found to be related with the TC distribution of this particular data set, which peaks at the unity.

5.6.3 Season Dependence on Flux Measurements

To account for any seasonal variation due for instance to variations of atmospheric profile another check was performed on the Crab Nebula flux. The data were divided into two categories corresponding to the observation season. Data taken from September to December and data from January to April are grouped together. The former is called the first season and the later second season. This division is done to account for seasonal changes during September to November as during this period is the rainy season in Namibia. As it was shown in Figure 5.5, the majority of the data are taken during these months. Hence, the spectrum would possibly manifest changes if there is a systematic effect due to this. The differential energy spectrum for the two seasons is shown in Figure 5.18. Taking into account 20 % systematic uncertainty (the published value from H. E. S. S.), no significant change is seen between the spectra derived for the two seasons. The fit results are summarized in Table 5.6.

Season	N_0 cm^{-2}s^{-1}TeV^{-1}	$\Phi > 1$ TeV cm^{-2}s^{-1}	Γ	β
I	$(4.8 \pm 0.05) \times 10^{-11}$	$(3.01 \pm 0.04) \times 10^{-11}$	2.42 ± 0.02	0.18 ± 0.01
II	$(4.6 \pm 0.04) \times 10^{-11}$	$(3.02 \pm 0.03) \times 10^{-11}$	2.27 ± 0.02	0.25 ± 0.01

Table 5.6: Summary on the Crab Nebula spectrum parameters for the first and the second season. The flux normalisation N_0 and the integral flux Φ values correspond to the reference energy of 1 TeV.

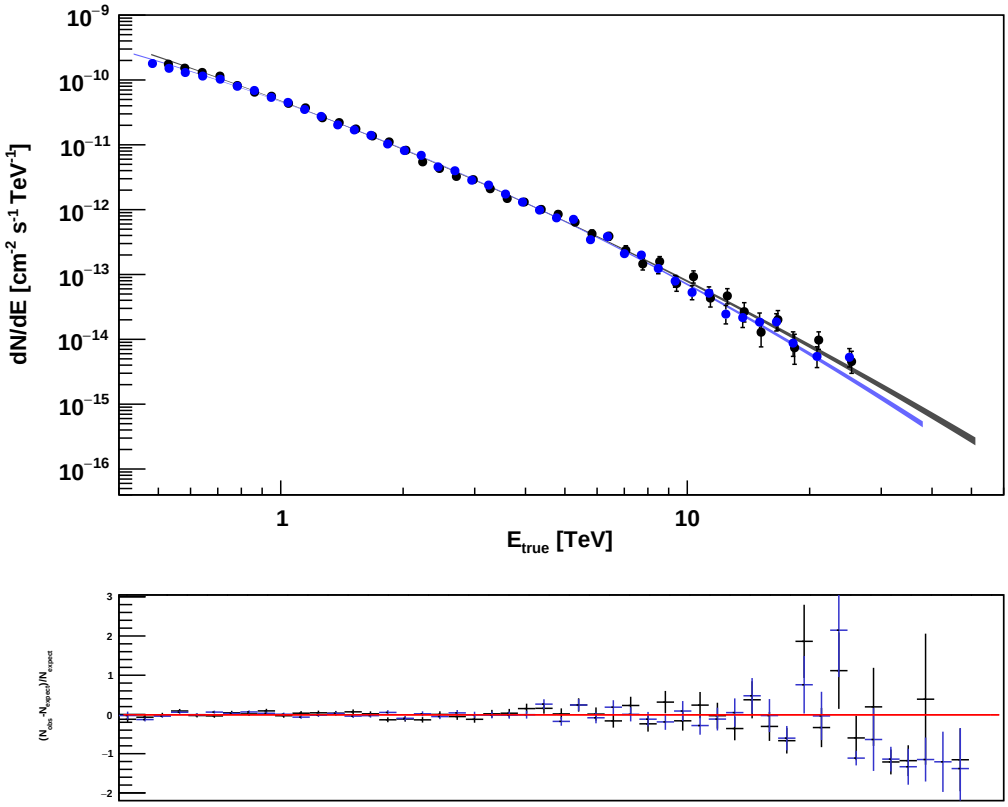

Figure 5.18: Superimposed Crab Nebula spectrum from two different seasons as described in the text. The first season is represented by the black points and the second season by the blue ones. The 1σ confidence interval of the fitted spectrum shape are plotted by solid lines. The spectra are fitted with a curved power-law spectral shape and are compatible within the estimated H. E. S. S. systematic uncertainties. The residual plot in the form $(N_{obs} - N_{exp})/N_{exp}$ are shown in the bottom part.

5.7 Discussion and Conclusions

In this chapter, the high-energy emission from the Crab Nebula was investigated with almost a decade of H. E. S. S. I observations using the newest reconstruction techniques. The differential energy spectrum and flux variability were studied on a long-term. Observing the Crab Nebula from the southern hemisphere is challenging, but not without prospects. On the one hand, the zenith angles larger than 45 degrees enhance systematic effects, in particular atmospheric effects. On the other hand the effective area is increasing with the zenith angle, allowing the H. E. S. S. I measurement to extend to very-high energies.

The spectrum of the Crab Nebula was reconstructed using the *Model Analysis*. Three models were fitted to the data: a power-law, a log-parabola and a power-law with exponential cut-off. The Crab Nebula spectrum presented here, measured

from 480 GeV to 62.4 TeV, is best described by a log-parabola spectral shape. This spectral shape has already been measured by the VERITAS and MAGIC experiments, whereas the energy spectrum published by the H. E. S. S. collaboration about a decade ago was most compatible with a power-law with exponential cut-off in the energy range from 440 GeV to 30.5 TeV. The Crab Nebula spectrum as measured by H. E. S. S. I and H. E. S. S. II are discussed and compared to measurements from other experiments in the next chapter.

Motivated by the surprising Crab Nebula flares reported by the spaceborne satellites which arise from the high-energy part of the synchrotron component, the flux variability at very-high-energies was studied with H. E. S. S. The *Fermi*-LAT instrument is suitable to study the high-energy synchrotron emission, whereas H. E. S. S. can access the high-energy part of the inverse Compton component. The origin of the flares is still not understood, but different scenarios could explain these events. If the flux variations are related to the parent population of electrons, the flux enhancements would be accompanied by flux variations in the inverse Compton component. Alternatively, if the rapid flares are due to changes on the magnetic fields, the inverse Compton flux is not expected to vary. Since the *Fermi*-LAT started operating at the end of 2008, there is no information on GeV flux variations before this time, but if the synchrotron flare has a counterpart in the TeV, investigating all H. E. S. S. data also helps to better understand the high-energy emission.

The long term variability of the Crab Nebula at energies above 1 TeV was studied from MJD 53331-56358, putting emphasis on systematic effects from varying atmospheric conditions. Introducing the atmospheric transparency coefficient in the data selection improved the results by reducing the systematic uncertainties. Given that the observation time with IACTs is already limited to the night and their field of view is small, some attempts to correct for this effect were considered so runs with bad atmospheric transparency could be kept. With a flux correction factor linear in the transparency coefficient, the systematic uncertainties on flux measurements were reduced to 12 %. This is significantly improved compared to the 20 % previously quoted by the H. E. S. S. collaboration. As it is actually the energy measurement which should scale with the transparency coefficient, another way to correct for this effect would be to correct the energy by the transparency coefficient for each event before analysis level.

This study concluded that the integral flux above 1 TeV is stable within the systematic and statistical uncertainty of H. E. S. S. on a run-by-run basis. No significant flux variations were found with stand-alone H. E. S. S. I data. The flux variability studied by H. E. S. S. I indicated stable flux from the inverse Compton component, whereas the high-energy synchrotron component is not stable. Over nine years, the *Fermi*-LAT reported on the detection of major flares in 2009, 2010, 2011, 2013 and 2016. Observations from the ground based detectors did not report evidence of simultaneous flux variation at the highest energies so far. Future observations of the Crab Nebula at high-energies and very-high-energies will reveal more about the evolution of the flux with time.

Chapter 6

Crab Nebula with H. E. S. S. Phase-II Observations

With the installation of the H. E. S. S. II telescope in 2012 on site in Namibia, the H. E. S. S. experiment entered a new phase. The current trigger schemes allow to go down to few tens of GeV for some sources and explore a wider energy range on the very-high-energy sky. We profit from this scheme to perform spectrum and variability studies of the best studied object on the sky; the Crab Nebula.

Figure 6.1: The H. E. S. S. II telescopes. Image courtesy M. Lorentz.

This chapter presents a temporal and spectral analysis of the *Fermi*-LAT and the H. E. S. S. II data and the search for correlated variability in the energy bands covered by the two experiments. A short introduction and an explanation of the employed data set are given in Section 6.1 and Section 6.2. The results of the Mono, Hybrid and Combined analyses are presented in Section 6.3. These results are used to perform the spectrum measurements given in Section 6.4. The spectral energy distribution from the H. E. S. S. I and H. E. S. S. II measurements of this work are shown in Section 6.5. The *Fermi*-LAT and H. E. S. S. II results of the October 2016 flare are described in Section 6.7 and the chapter summary is given in Section 6.8.

6.1 Introduction

The H. E. S. S. I telescope array with its large effective area is adapted for very-high-energy studies. Combined with H. E. S. S. II, the full array allows to measure the Crab Nebula spectrum over a wide energy range. This is also important to perform variability studies to trace the physical phenomena underlying the GeV flares.

Different analysis configurations are used to exploit the lower energy range and measure the spectrum of the Crab Nebula over a wide energy range, namely both monoscopic and stereoscopic reconstructions. The Crab Nebula spectrum measurement is more challenging in the low energy range. The monoscopic reconstruction of CT5 events is in general challenging due to the degraded hadron rejection. Reconstructing events with CT1 to CT5 provides a better background separation with an increased signal over background ratio at the analysis level at the expense of a higher threshold.

H. E. S. S. did not observe the brightest flare detected by *Fermi*-LAT in 2011. The other flare occurred in March 2013 and coincided with the H. E. S. S. II commissioning phase. Hence, the H. E. S. S. II runs from this flaring period can not be used to derive scientific results as the experimental setup was changed almost every night.

In March 2013, the Crab Nebula underwent the second brightest flare detected at GeV energies by the *Fermi*-LAT. The flare lasted for about two weeks and the flux increased by a factor of six relative to the average within in less than six hours. As during the other gamma-ray flares, only the synchrotron component of the nebula varied. Multiwavelength campaigns undertaken by different experiments in radio, optical and X-rays had an excellent coverage of the 2013 flaring period. A good coverage was also accomplished at the very-high-energies by the major IACT experiments pointing at the Crab Nebula. Despite the coverage of the Crab Nebula during the 2013 *Fermi*-LAT flare, there was no enhancement reported in this energy range by any experiment. The absence of other correlated flux enhancements at other wavelengths kept the origin of the Crab Nebula flares a mystery.

Other flares have been reported lately by the spaceborne experiments i.e. *Fermi*-LAT and *AGILE* [169, 170, 171]. The latest flare reported in October 2016 by the *Fermi*-LAT satellite has increased the chances to understand the origin of the gamma-ray flares by investigating it [171]. During this flaring episode, the small H. E. S. S. telescopes were in re-commissioning phase after the camera upgrade. The Crab Nebula was observed as a Target of Opportunity (ToO) with CT5 and CT1 for several nights. These observations, along with the *Fermi*-LAT public data, were used to perform the flux variability and correlation studies reported here.

6.2 Data Set

The 28 m diameter mirror telescope, installed on site in 2012 was commissioned and inaugurated during 2013. The Crab Nebula was the prime target during the commissioning phase. The observations taken during this period are not included

in the reconstruction. The observation conditions are similar to the ones described in Section 5.2 for H. E. S. S. I

After calibration, the data selection criteria depend on the observation strategy and on the scientific goal. Given the different physical trigger modes with the H. E. S. S. II telescope array, introduced in Section 3.6.2, different reconstruction methods exist to analyze the data. Each of them has its own set of selection criteria. These criteria for the monoscopic reconstruction, which demands the most careful event selection, are given below:

- source location within $0.5 - 0.7$ degrees offset from the camera center
- minimum trigger rate 1200 Hz with a stability ≤ 10 %
- minimum run duration ≥ 5 minutes
- maximum broken pixel fraction 5 %
- zenith angles $54 - 60$ degrees

Only runs with atmospheric transparency larger than 80 % were selected. Other external parameters, like the relative humidity or temperature, are similar to the ones for H. E. S. S. I. To select events for the Hybrid reconstruction (CT1-5 events), a mixture between the H. E. S. S. I and Mono selection criteria is applied.

A total of 33 runs passed the run selection and the subsequent results are derived from this data (unless specified differently). More runs pass the selection criteria for the Hybrid analysis. The choice to use the same run list is done for a better comparison between results of different analysis configurations.

6.3 Data Analysis

To fully exploit the low and high energy events, the data was analyzed with the Combined, Stereo and Mono configurations, using Std and Loose cuts. The Mono reconstruction uses exclusively the CT5 events, whereas the Stereo Hybrid reconstruction uses CT1-5 events. The Combined analysis method combines the monoscopic reconstruction at low energies and stereoscopic reconstruction at high energies, developed to cover a wider energy range.

The analysis results and the corresponding cut parameters for the hadron rejection are summarized in Table 6.1. The θ^2 cut for the Mono, Stereo and Combined were set to 0.015, 0.006 and 0.015 degree^2, respectively. The θ^2 distribution for the Mono analysis with Std cuts is shown in Figure 6.2, where the OFF events are uniformly distributed as expected. The θ^2 histograms for the other analysis configurations were also checked. Table 6.1 summarizes the Combined, Stereo and Mono analysis results. The total number of events in the source region n_{ON}, in the background region n_{OFF} and the corresponding excess are given for each configuration. For the loose cuts, it can be seen that the signal to background ratio is generally lower. This cut configuration provides a lower threshold, but weaker hadron rejection. The use of Stereo Hybrid allows to have a lower energy threshold and a better hadron rejection.

Config	Cut	n_{ON}	n_{OFF}	n_{excess}	S_{LiMa}	S/B	Rate [γ's/min]
Mono	Std	6799	4224	6319.3	131.4	13.2	7.2±0.09
	Loose	7798	5988	7106.1	133.4	10.3	8.1±0.10
Hybrid	Std	5667	2676	5495.9	147.4	32.1	6.9±0.09
	Loose	8127	4764	7775.6	165.0	22.1	9.8±0.11
Combined	Std	8953	4599	8469.2	160.2	17.5	9.6±0.11
	Loose	12147	8851	11211.6	173.9	12.0	12.7±0.13

Table 6.1: Analysis results of H. E. S. S. II Mono, Stereo and Combined with Std and Loose cut configurations. The number of events in the ON and OFF regions n_{ON} , n_{OFF}, the number of excess events n_{excess}, significance S_{LiMa}, signal to background ratio (S/B) and the rate of gammas for each cut configuration are given.

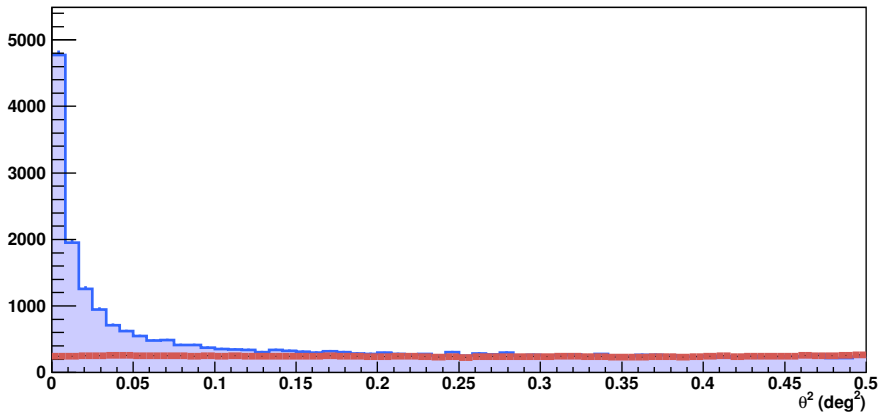

Figure 6.2: The distribution of θ^2 , the angular distance between the reconstructed direction and source position, for the Mono Std. The background from the OFF regions is shown in red.

Figure 6.3 shows the *Ring Background* significance distribution for the Std cuts in Mono, Stereo and Combined analysis. The red line corresponds to the distribution of the events with target region excluded. This is fitted with a Gaussian which gives a sigma and mean of almost zero and one respectively, indicating a good background estimation and subtraction.

The main challenge of the H. E. S. S. II data analysis is the background subtraction at low energies. Controlling the background systematics at low energies with Mono reconstruction is challenging. The stereoscopic reconstruction with events from CT1 − 5 provides a better background subtraction.

Additional consistency checks were performed, including the *acceptance* maps and distributions of the main background separation variables (*MSSG*, *Direction Error* and *Primary Depth*). The center of gravity maps for every telescope participating in a given run were also checked. These results were used for a spectrum measurement of the Crab Nebula, which is described in the following.

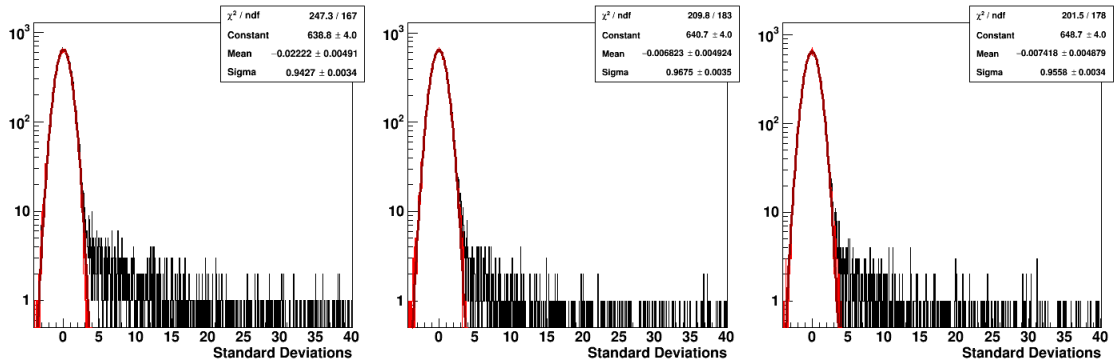

Figure 6.3: The ring background significance distributions for Mono, Hybrid and Combined analysis with Std cuts. The significance distribution of the whole map is shown in black. The distribution after excluding a circular region around the source with a Gaussian fit is shown in red. The latter includes a Gaussian fit with the fit parameters indicated.

6.4 Energy Spectrum with H. E. S. S. II

The spectrum of the Crab Nebula has been measured from H. E. S. S. II data with different H. E. S. S. II analysis configurations, with the same method as for the H. E. S. S. I spectrum measurement described in Section 3.6.4. Only the events above the safe energy threshold are used for the spectrum measurement. For the Mono spectral analysis, the energy threshold is set to 25 % of the maximum effective area, which is higher than for the H. E. S. S. I Stereo analysis due to the larger background systematic effects. For the Stereo Stereo and Combined analysis configurations, the threshold was set to 15 %.

The spectrum is fitted with a simple power-law and a log-parabola[1]. The results of the spectrum fit for Mono, Hybrid and Combined analysis are summarized in Table 6.4. The Mono analysis provides the lowest energy threshold whereas the combined analysis provides the a spectrum measurement up to 63 TeV. For all the configurations, the data is best described by the log-parabola shape.

The superimposed spectra for the Mono, Stereo and Combined analysis configurations, with Std or Loose cuts, are shown in Figure 6.4. The spectral shape of Combined and Stereo agree in the full energy range, whereas the Mono spectrum is shifted relative to them at the highest energies. This gap is seen for the Std and Loose cuts, but for Loose it is more than 20 %, which is under investigation. It could be a systematic effect related to the monoscopic reconstruction at very-high energies. At high energies, the flux uncertainties are larger due to the lack of statistics.

[1]log-parabola is also referred to as curved-power law (CPL)

Config.	Fit	Cuts	E_{thresh}	E_{min} GeV	E_{max} TeV	N_0 $\mathrm{m^{-2}\,s^{-1}\,TeV^{-1}}$	Γ	β	$\mathrm{E_0}$ TeV	χ^2/ndf
Mono	PL	Std	25 %	240	15.5	$(114.5 \pm 1.2)\,10^{-8}$	2.62 ± 0.01	-	0.65	87.5/33
	CPL	Std	25 %	240	15.5	$(238.4 \pm 2.7)\,10^{-8}$	2.45 ± 0.03	0.11 ± 0.01	0.49	50.3/32
	PL	Loose	25 %	220	15.5	$(147.8 \pm 1.4)\,10^{-8}$	2.55 ± 0.01	-	0.59	87.5/33
	CPL	Loose	25 %	220	15.5	$(334.2 \pm 3.8)\,10^{-8}$	2.38 ± 0.03	0.13 ± 0.02	0.43	50.0/32
Hybrid	PL	Std	15 %	440	41.9	$(20.4 \pm 0.2)\,10^{-8}$	2.56 ± 0.02	-	1.3	154/74
	CPL	Std	15 %	440	41.9	$(38.4 \pm 0.5)\,10^{-8}$	2.32 ± 0.03	0.19 ± 0.02	1.1	78.4/73
	CPL	Loose	15 %	320	41.9	$(70.5 \pm 0.7)\,10^{-8}$	2.34 ± 0.02	0.17 ± 0.01	0.87	79.7/75
	PL	Loose	15 %	320	41.9	$(36.3 \pm 0.3)\,10^{-8}$	2.56 ± 0.01	-	1.1	175.5/76
Combined	PL	Std	15 %	360	62.4	$(28.8 \pm 0.3)\,10^{-8}$	2.52 ± 0.01	-	1.13	213.5/81
	CPL	Std	15 %	360	62.4	$(58.5 \pm 0.6)\,10^{-8}$	2.30 ± 0.02	0.17 ± 0.01	0.87	93.2/80
	PL	Loose	15 %	290	62.4	$(46.2 \pm 0.4)\,10^{-8}$	2.50 ± 0.01	-	0.95	282.2/91
	CPL	Loose	15 %	290	62.4	$(104.4 \pm 0.9)\,10^{-8}$	2.25 ± 0.02	0.17 ± 0.01	0.7	105.2/90

Table 6.2: Summary of the Crab Nebula spectrum fit parameters derived from Mono, Hybrid and Combined using the Std and Loose cut configurations. The best fit parameters for each spectrum shape, a power-law (PL) and log-parabola (CPL) for the Std and Loose cut configurations are given. The energy threshold E_{thresh}, the spectral index Γ, curvature β, normalization N_0, reference energy E_0 and the fit parameters for each configuration are given. E_{min} and E_{max} correspond to the energy range of the fit, obtained during the spectrum fit procedure.

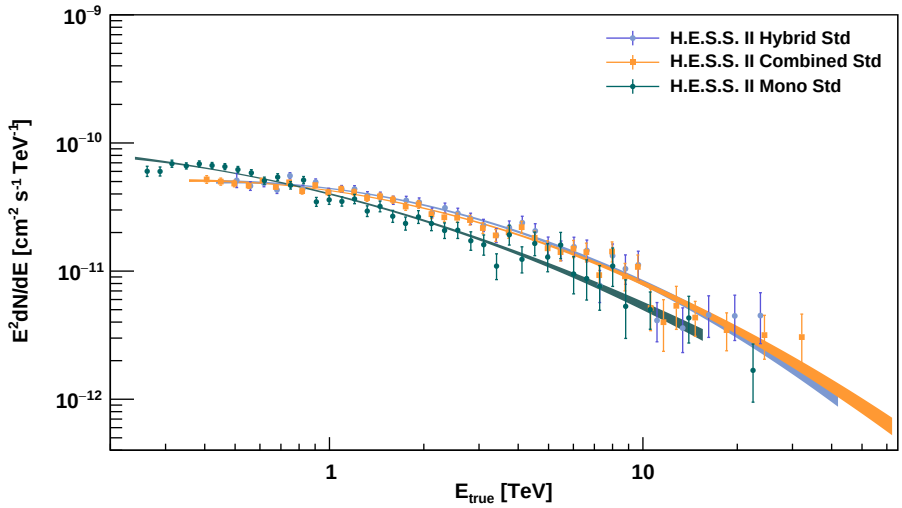

(a) Std cuts.

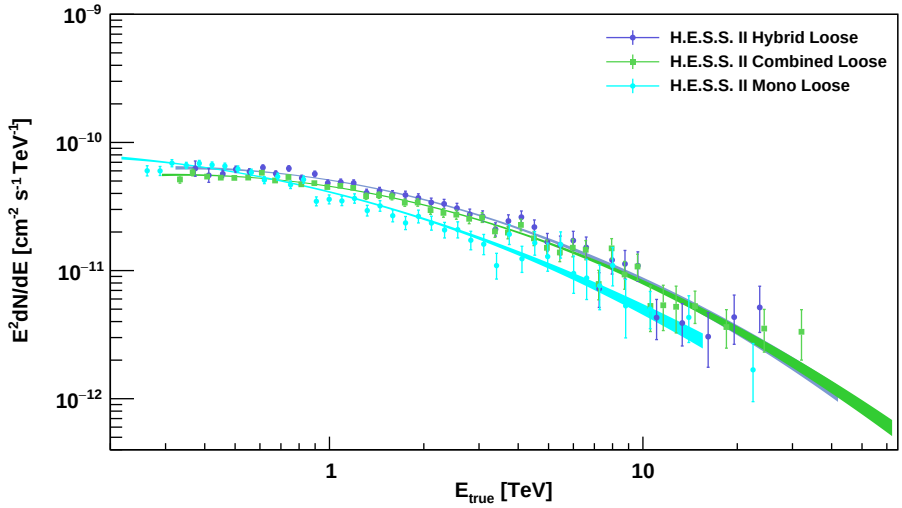

(b) Loose cuts.

Figure 6.4: The spectral energy distribution of the Crab Nebula as measured with H. E. S. S. II and fitted with log-parabola spectrum shape. The Mono, Stereo and Combined spectra are derived using the Std (a) and Loose (b) cuts. The spectrum derived with the Mono configuration (cyan) provides a lower energy threshold compared to the spectrum from the Stereo and Combined analyses, which agree well with one-another.

The Combined analysis configuration provides a lower energy threshold compared to the Hybrid. The best fit spectrum parameters for the Combined Std are:

$$\frac{\mathrm{d}N}{\mathrm{d}E} = (5.9 \pm 0.06) \times 10^{-11} \left(\frac{\mathrm{E}}{0.87\,\mathrm{TeV}} \right)^{-(2.3\pm0.02)-(0.17\pm0.01)\ln(\frac{\mathrm{E}}{0.87\,\mathrm{TeV}})} \frac{1}{\mathrm{TeV\,cm^2\,s}}. \quad (6.1)$$

These results have been-cross checked with the HAP framework, another reconstruction framework within H. E. S. S. (done by J. Hahn). The intersection run list of both analysis pipelines was used for the cross-check. Both analysis frameworks agree well on the differential flux within 20 % uncertainty. Systematic checks performed to understand the difference indicated that it's due to the flux normalization. For this scope, the spectrum measured by the two different H. E. S. S. analysis chains was compared to the "global" Crab Nebula spectrum, taken as the average spectrum of the three major IACT experiments i.e. MAGIC, VERITAS and H. E. S. S. (PA + HAP). The relative flux differences $(F_i - F_{\text{Average}})/F_i$ were calculated, where F_i stands for the H. E. S. S. measurement (this work) and $F_{Average}$ is the average spectrum obtained from H. E. S. S. (PA + HAP), MAGIC and VERITAS measurements. An example of this check is shown in Appendix B. The three instruments are taking independent measurements, during different time periods and under different observation conditions. Comparing the spectrum of different measurements from different experiments is not an easy task, since the systematics between the different experiments are not known. Systematic uncertainties are due to the different calibration and reconstruction methods of individual experiments and an absolute calibration between the experiments is difficult. In the comparison plot shown in Figure B.1, the uncertainty between the experiments is assumed to be 30%.

6.5 Spectral Energy Distribution

The measured spectrum with the H. E. S. S. II and H. E. S. S. I experiments from this work are plotted along with measurements from the other high-energy experiments in Figure 6.5 in an SED representation.

The highest energy points from the *Fermi*-LAT measurement are connecting with the low energy spectral points from the IACT experiments close to the inverse Compton peak. The first spectral points from the H. E. S. S. II Mono analysis provide a link to the *Fermi*-LAT points as a continuation of the spectrum energy distribution. The MAGIC experiment location on the Canary island allows to observe the Crab Nebula near zenith and has the best observation position to bridge the spectrum measurements from space and ground measurements. The data point from the two experiments overlay. The peak of the spectral energy distribution was estimated by MAGIC at (53±3) GeV in a joint fit with *Fermi*-LAT data [155].

The H. E. S. S. I spectrum from this work extends up to 62 TeV, making this the highest energy spectrum measurement for the Crab Nebula from all IACTs. The spectrum measured by VERITAS goes up to 42 TeV, even though they observe the Crab Nebula at zenith angles between 8-35 degrees. Nevertheless, the telescope configuration, i.e. collection area and telescope design is more suited for low energy measurements, not for the high energies [164].

The spectrum measured here is more curved than the spectrum from the other analysis framework. It is still under investigation if it's due to systematic effects or physics. A more precise measurement could be achieved with **R**un-**W**ise-**S**imulations (RWS),

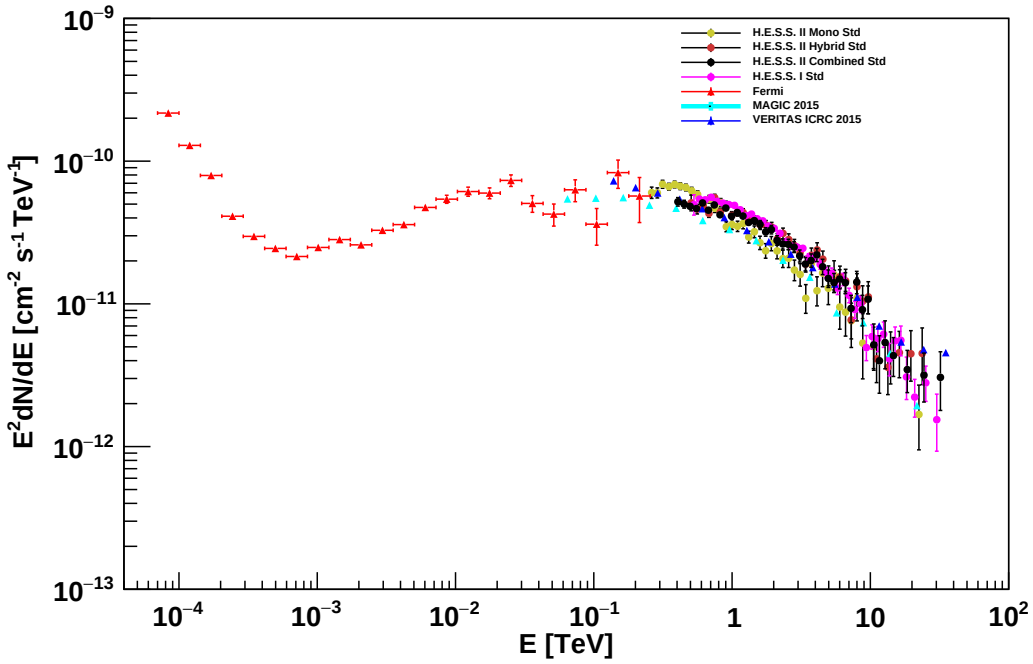

Figure 6.5: The spectral energy distribution of the Crab Nebula as measured with H. E. S. S. I and H. E. S. S. II (from this work) along with the published data points from MAGIC, VERITAS and *Fermi*-LAT experiments [172, 164, 155].

which provide simulation for each set of run observation parameters, i.e. zenith angle, optical efficiencies, azimuth, night sky background level etc. In the current scheme are classical Monte Carlo simulations which have a predefined ranges of these parameters. RWS are currently being developed for H. E. S. S.

6.6 Variability Studies

This part is dedicated to variability studies with H. E. S. S. II, strongly motivated by the puzzle on the origin of the GeV flares.

Four major flares detected by the *Fermi*-LAT are summarized in Table 6.3. During all these flares only the flux from the synchrotron component varied and the corresponding details are summarized. The flare amplitude are compared to the average quiescent synchrotron photon flux ($6.1 \pm 0.2 \times 10^{-7}\,\mathrm{cm}^{-2}\mathrm{s}^{-1}$) from [55]. The spectral energy distribution of the GeV flares reported from the AGILE and *Fermi*-LAT spaceborne satellites, obtained at the maximum flare level are plotted in Figure 6.6. As seen from the plot, during the flares the spectrum of the synchrotron component hardens with the increased flux levels. From all flares, only the most recent flare (until this thesis was written) reported by the *Fermi*-LAT during October 2016 was observed by the H. E. S. S. II telescope. Studying the emission at TeV energies and

search for correlated variability is important to understand the origin of the flares.

Fermi-LAT flares	Feb 2009	Sep 2010	Apr 2011	Mar 2013	Sep 2016
Duration [days]	16	4	9	14	30
Amplitude	x4	x6	x30	x6	x5
Variability [h]	<10	<10	<8	<6	-
H. E. S. S. II Obs.	-	-	-	-	yes

Table 6.3: The major GeV flares detected by the *Fermi*-LAT along with duration, amplitude and variability time scale. This table also indicates if the flare was observed by H. E. S. S. II. The major flares details are taken from [152, 172, 153], while the 2016 flare details are from this analysis.

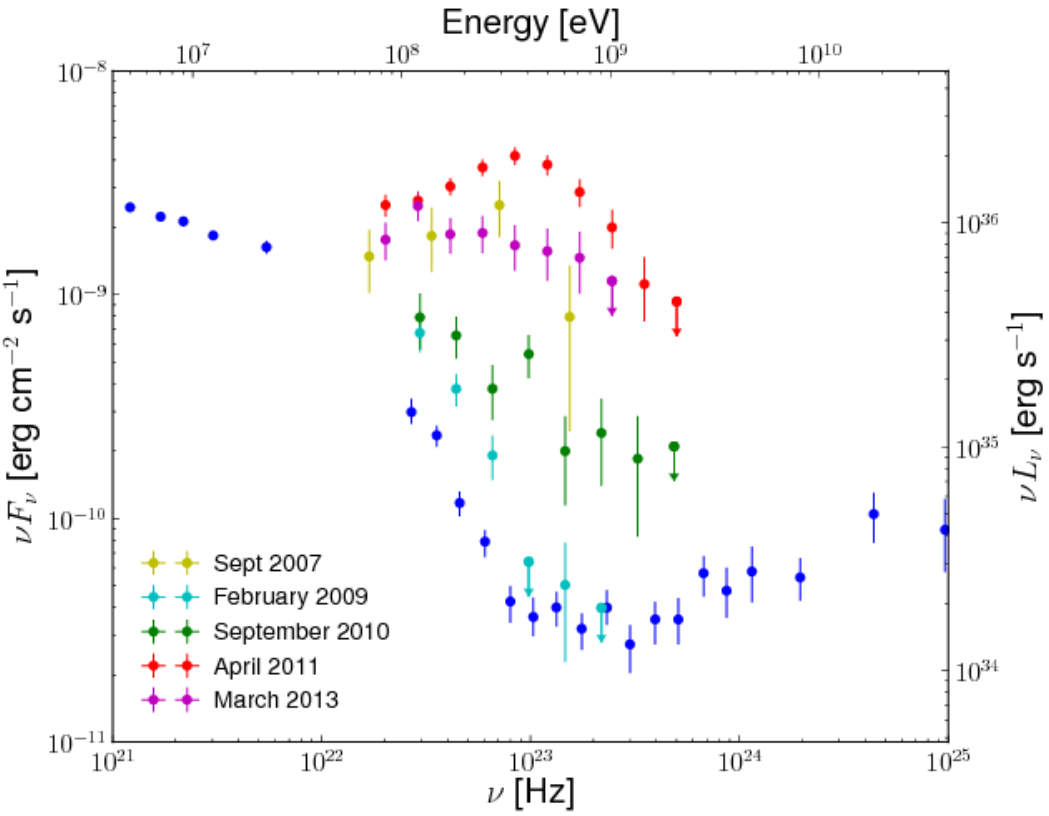

Figure 6.6: Spectral energy distribution of the Crab Nebula compiled with data from the spaceborne satellites. The spectral points correspond to the maximum flare level of the major flares detected on the Crab Nebula by *AGILE* and *Fermi*-LAT satellites. The blue data points belong to the average nebula flux values. Image courtesy [55].

The October 2016 flare with the *Fermi*-LAT and H. E. S. S. II was subject of this thesis and the analysis details are described next.

6.7 The Crab Nebula 2016 GeV Flare

The *Fermi*-LAT and *AGILE* collaborations reported on an increase of the flux from the Crab Nebula in 2016 October 03: flare alerts were posted on the Astronomer's Telegram [171, 170]. The H. E. S. S. telescopes observed the Crab Nebula during this period. The upgrade phase of the CT2-4 telescopes started in the beginning of the year, so unfortunately three telescopes were not available for observations during this flaring period. Nevertheless, one of the small telescopes (CT1) and the H. E. S. S. II telescope observed the Crab Nebula as a target of opportunity for several days.

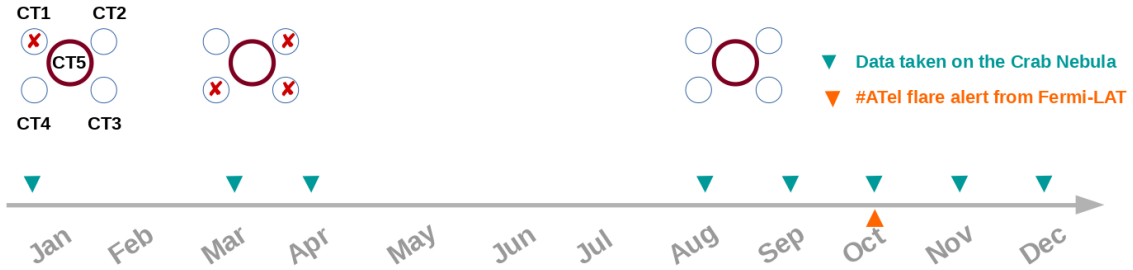

Figure 6.7: Observations of the H. E. S. S. experiment before and after the upgrade phase. The CT1 telescope was not included in observations until March, the month during which the three other H. E. S. S. telescopes entered in the upgrade phase. After August 2016, the array started to be re-commissioned with five telescopes. The months during which the H. E. S. S. experiment observed the Crab Nebula are marked with down cyan triangles and the *Fermi*-LAT flare is indicated in orange.

6.7.1 H. E. S. S. II Observations

Crab Nebula observations with H. E. S. S. II started in January 2016 and were intensified after the upgrade phase was completed, with many observation runs taken for re-commissioning purposes (see Figure 6.7). The zenith angle range during this period extended up to more than 60 degrees, making the analysis of this data challenging. From all the observation runs taken during 2016 that pass the standard quality selection criteria, 16 runs were taken at zenith angles greater than 60 degrees. These runs were excluded from the analysis. Many runs had other problems or were of too short duration, which also led to their exclusion from the final run list. Additionally, several runs with a non-optimal transparency coefficient values were not taken into account.

For the GeV flare, the only public information was the initial flare reported on the Astronomer's telegram by the *Fermi*-LAT. Other important information for the variability study with H. E. S. S. II, like the flare amplitude or duration in GeV, were not known. Therefore, an analysis on the Crab Nebula with publicly available *Fermi*-LAT data taken during this flaring period was performed; the details are given next.

6.7.2 Fermi-LAT Analysis

As the Crab Nebula analysis with the *Fermi*-LAT is more challenging compared to extragalactic sources, the analysis of the March 2013 flare were reproduced to check the credibility of the 2016 results. After having obtained consistent results with the published ones, on the 2013 flare, it was proceeded to the analysis of the 2016 flare, which is described next.

For this study, the *Fermi*-LAT publicly available data from 2016 September 01 to 2016 October 31, corresponding to MJD 57632-57692, were analyzed. All events with energies between 100 MeV and 500 GeV coming from a 15 degrees circular region of interest (RoI) of the sky centered on the position of the Crab Nebula were selected. This RoI size was chosen in order to account properly for the background contamination from nearby sources and to have an optimal normalization of the Galactic diffuse model. Considering the motion of the LAT instrument during the operation, good time intervals are selected by excluding the time when the Earth was in the field of view of the LAT. The counts map of the RoI for the here-discussed time period is shown in Figure 6.8.

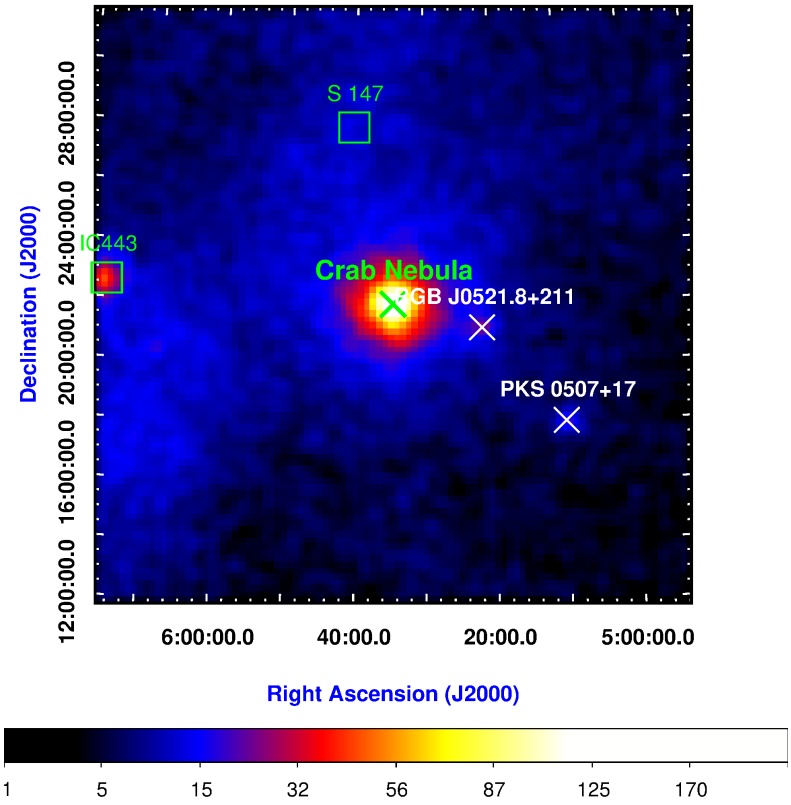

Figure 6.8: A $15° \times 15°$ RoI counts map centered on the position of the Crab Nebula. This correspond to the period of the 2016 flare and the brightness of the Crab Nebula is visible. The Crab Nebula is marked with green cross and other bright sources are marked as well. The squared symbols indicate two extended sources located within RoI.

6.7.2.1 Background Model File

In order to perform the likelihood analysis, the first step after selecting good quality data is to determine the background model for the RoI on the entire time range. For this purpose, all known gamma-ray sources from the 3FGL catalog [44], located within 20 degrees of the RoI were considered. A total of 123 point sources and 2 extended sources were found within the RoI. The extended sources, namely S 147 and IC443 were modeled by the templates provided by the 3FGL catalog. The background model also accounts for the Galactic and isotropic emission by including the two diffuse components provided by the *Fermi*-LAT collaboration (`iso_source_v05` and `gll_iem_v05`) in the model.

In the default 3FGL based background-model, the parameters of the sources detected with a significance $>5\sigma$ are left free. As the 3FGL is based on 4 years of data, the short time period analyzed in this work prohibits such significance limits. It would cause problems in the convergence of the likelihood fit due to the fact that for some sources there is not enough statistics. For this reason, only source listed with a detection significance $>12\sigma$ were left free.

In the previous analysis of the Crab Nebula (see [173, 153]), as well as in the 3FGL catalog [44], the Crab Nebula spectrum consists of three independent components. For this *Fermi*-LAT analysis therefore, the Crab Nebula emission was split into three components accounting for the pulsar, for the inverse Compton and synchrotron emission, named as J0534.5+2201i, J0534.5+2201s and 3FGL J0534.5+2201. The Crab Nebula components were modeled as point like in this analysis, given the *Fermi*-LAT resolution of 0.1° and the apparent size 0.03° of the Crab Nebula. The extension of the Crab at very-high-energies would require a dedicated study which goes beyond the scope of this work. Note that H. E. S. S. measures the spectrum well beyond the synchrotron peak and is not able to resolve the pulsar, so the composition in the three components is not considered in H. E. S. S. analyses.

6.7.2.2 Spectral Analysis

To derive the average spectrum of the Crab Nebula over the time period mentioned above, a likelihood analysis with `gtlike`[2] was performed. In the background model the components of the Crab Nebula were left free, together with the Galactic diffuse emission components, while all the other sources within 20 degrees were initialized to their 3FGL catalog values. The synchrotron component was modeled by a so-called *Power Law2*, which calculates the integrated flux in each bin:

$$\frac{\mathrm{d}N}{\mathrm{d}E} = F_{\mathrm{synch}} \frac{-\Gamma + 1}{E_{\mathrm{max}}^{-\Gamma+1} - E_{\mathrm{min}}^{-\Gamma+1}} E^{-\Gamma}. \tag{6.2}$$

The inverse Compton component is modeled by a log-parabola:

$$\frac{\mathrm{d}N}{\mathrm{d}E} = \Phi_{\mathrm{IC}} \left(\frac{E}{E_0}\right)^{-\alpha-\beta\log(E/E_0)} \tag{6.3}$$

[2] https://fermi.gsfc.nasa.gov/ssc/data/analysis/scitools/overview.html

The Crab pulsar spectrum, following [174], was parametrized by a smoothly broken power law:

$$\frac{\mathrm{d}N}{\mathrm{d}E} = \Phi_{\mathrm{pulsar}} \left(\frac{E}{100\,\mathrm{MeV}} \right)^{-p_1} \left(1 + \left(\frac{E}{E_b} \right)^{\frac{p_2 - p_1}{s}} \right)^{-s}, \tag{6.4}$$

where $p_{1,2}$ are the spectral index before and after the energy break E_b and s is the sharpness of the transition between the two slopes. The spectrum parameters of the Crab pulsar are kept fixed to their catalog values, whereas the synchrotron and the inverse Compton components were left free. From the *Fermi*-LAT observations of the previous flares, it was found a constant flux from the Crab pulsar, which is assumed also here to simplify this calculation. Checking if the Crab pulsar emission really remains constant would require the pulsar ephemeris for this period.

6.7.2.3 Temporal flux variations

To investigate the temporal flux evolution, the data was divided in 3-day time bin duration. The choice of this duration represents a trade-off between being sensitive to variability and have enough statistics in the time bins where there is no flux enhancements. In each bin, the synchrotron component was modeled as a simple power law. The only parameter left free in the short time bins is the integral flux of the Crab Nebula with the spectral index fixed to the value obtained for the complete data set. The pulsar spectrum parameters were fixed to the catalog values during the fitting procedure. The lightcurve is presented in Figure 6.10. It can be seen that the flare duration was about one month and the flux peaks at 2016 October 07. The flux points plotted in the lightcurve correspond to the synchrotron component. The average flux for the synchrotron component from MJD 57632-57692 was: $F_{\mathrm{synch}} = (2.01 \pm 0.12) \times 10^{-6}\,\mathrm{ph\,cm^2 s^{-1}}$. The flux at the amplitude peak, from MJD 57671-57674, was $F_{\mathrm{peak}} = (4.27 \pm 0.26) \times 10^{-6}\,\mathrm{ph\,cm^2 s^{-1}}$. The flux from the synchrotron component has reached a factor of five compared the quiescent flux reported before by the LAT collaboration [172].

6.7.3 H. E. S. S.-*Fermi* lightcurves

The H. E. S. S. II observations taken between September to October resulted in nine good quality runs, corresponding to an acceptance-corrected live time of 3.6 hours. For the spectral and variability studies here-discussed, the Mono analysis configuration with Std cuts were used. The spectrum of the Crab Nebula for the data taken between September and October was fitted by a curved power-law shape, that best represents the shape of the IC peak. The H. E. S. S. spectrum derived simultaneously with the *Fermi*-LAT observations is shown in Figure 6.9, superimposed the overall H. E. S. S. II spectrum and extends from 230 GeV to 10.44 TeV.

The corresponding lightcurve with integral flux above 1 TeV was calculated in run-by-run basis (28 minutes). The highest value corresponds to the 2016 October 07. The lightcurve was fitted to a constant flux and gave a reduced $\chi^2/ndf = 67.6/21$ ($P = 0.0001$). The lightcurve derived by H. E. S. S. II has an excess variance of 15%

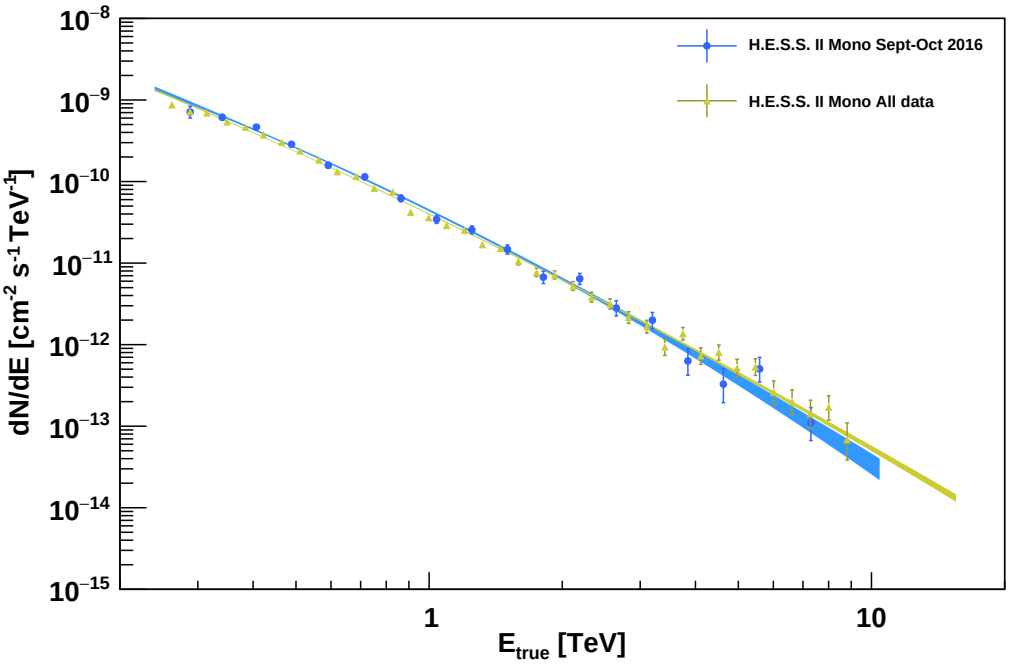

Figure 6.9: The Crab Nebula energy spectrum derived with data from September to October 2016 superimposed to the overall H. E. S. S. II Mono spectrum for comparison. The 1σ confidence interval of the fitted spectrum shape are plotted as solid lines. Both spectra are obtained from Mono Std analysis configurations and are compatible within the estimated H. E. S. S. uncertainties. The errors plotted are statistical only.

but it has to be compared to the 20% systematic uncertainty quoted by H. E. S. S. The lightcurves obtained by *Fermi*-LAT and H. E. S. S. are shown in Figure 6.10. The lightcurve points from H. E. S. S. II appear to have higher fluxes in the beginning and lower after, which could be a flare starting before at TeV energies. However, by assuming a systematic uncertainty of 15% in each run, the χ^2/ndf is reduced to 17.86/21 ($P = 0.66$). Since the error on the flux is increased, this automatically reduces the χ^2/ndf.

All the Crab Nebula flares at GeV energies, including the one presented here, are coming from the synchrotron component. To investigate the high and the low flux variations with H. E. S. S., the spectrum of the Crab Nebula was divided into two parts. The "low" energy spectrum is restricted to events with energies up to 1 TeV. Whereas the "high" energy spectrum is fitted at energies above 1 TeV. The former does not show evidence of flux variability which is characterized by an excess variance larger than 15%. The later case for the monoscopic reconstruction above 1 TeV shows the same behaviour.

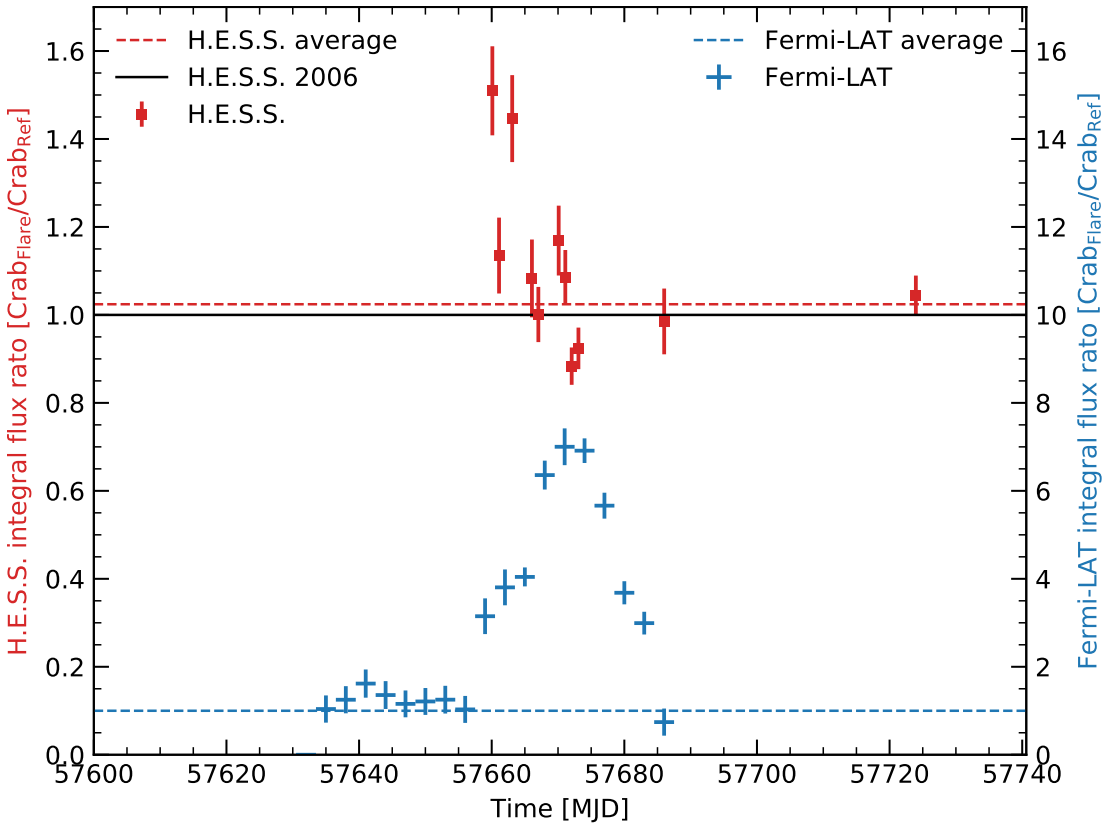

Figure 6.10: TeV and GeV lightcurves of Crab Nebula in 2016. Top: The lightcurve in a run-by-run basis measured from H. E. S. S. II from MJD 57390.94-57724.02 (red squares). The integral fluxes, calculated above 1 TeV are normalized to the average flux from the H. E. S. S. flux from 2006 publication [113]. The dashed red line correspond to the average flux for this period, whereas the black line to the average flux from 2006. In the bottom part of the plot, the Crab Nebula integral flux of the synchrotron component between 57632-57692 MJD as derived from *Fermi*-LAT data is plotted (blue crosses). The integral fluxes are calculated in 3-day time bins, from 100 MeV $<$ E $<$ 500 GeV and normalized to the published average synchrotron flux from [172]. The dashed blue line correspond to the average synchrotron flux from the previous *Fermi*-LAT measurements ($6.1 \pm 0.2 \times 10^{-7}\,\mathrm{cm}^{-2}\mathrm{s}^{-1}$).

6.8 Summary and Discussion

The installation of the H. E. S. S. II telescope in 2012 with new trigger schemes, along with the sophisticated analysis techniques developed for it, opened up the low GeV energy range to the H. E. S. S. experiment. This chapter was dedicated to observations of the Crab Nebula with H. E. S. S. Phase-II. Even though the experiment was taking data continuously during 2013, the commissioning runs were not included to derive scientific results due to the continuous changes in the camera configuration during this period.

Run	Date 2016	MJD	t_{live} h	Z_{mean} deg	N_{ON}	N_{OFF}	Excess	Sig.	$\Phi > 1\,\mathrm{TeV}$ $\times 10^{-11}\mathrm{cm}^{-2}\,\mathrm{s}^{-1}$
124790	09-29	57660.1	0.4	49.3	263	131	245.7	25.7	3.05 ± 0.22
124842	09-30	57661.1	0.4	48.4	208	126	192.3	22.4	2.32 ± 0.20
124917	10-02	57663.1	0.4	49.5	255	102	240.5	25.8	2.84 ± 2.21
125081	10-05	57666.1	0.4	51.8	183	100	170.6	21.5	2.23 ± 0.21
125124	10-06	57667.1	0.4	46.4	190	109	176.6	21.8	2.12 ± 0.18
125220	10-09	57670.1	0.4	45.8	251	130	235.0	25.5	2.35 ± 0.17
125263	10-10	57671.1	0.4	45.6	247	138	226.7	23.5	2.35 ± 0.17
125269	10-10	57671.1	0.2	49.0	127	71	117.9	17.6	1.98 ± 0.20
125333	10-12	57673.1	0.4	48.1	178	111	164.7	20.9	1.98 ± 0.18
full-set	-		3.4	48.2	1902	1018	1770	68.6	2.54 ± 0.05

Table 6.4: Analysis results for each observation run taken during September-October 2016. The run number, Modified Julian date (MJD), the live time t_{live}, mean zenith angle Z_{mean}, the number of ON (N_{ON}) and OFF (N_{OFF}) events, the excess and the significance for each run are given. The integral flux Φ above 1 TeV is also given.

The study performed on the Crab Nebula profited from the current trigger schemes which allowed to lower the energy threshold, particularly important for spectral and variability studies. All the available H. E. S. S. II Crab Nebula data taken after the commissioning is used to measure the energy spectrum down to 260 GeV. This allows H. E. S. S. to get closer to the inverse Compton peak and to the *Fermi*-LAT spectral points. The spectrum was best described by a log-parabola function, similar to the shape previously measured by the MAGIC and VERITAS experiments. In combination with the spectrum measured by H. E. S. S. I, presented in Chapter 5, this is the broadest H. E. S. S. Crab Nebula spectrum measurement so far, as it covers more than three decades in energy. All the spectra obtained from this work have been cross-checked with another analysis framework (HAP, done by J.Hahn) using the intersection run list between the two analysis frameworks. The relative differences on the differential flux are compared with the the "global" spectrum derived from all IACT measurements. In general, the spectra as measured by MAGIC, VERITAS and H. E. S. S. agree well with each other and show the curved shape around the inverse Compton peak. The relative differences of all spectrum measurements are within 30 % and the measurement from this work exhibits a higher curvature compared to the other measurements.

The flux variability at GeV energies is another peculiarity of the Crab Nebula. A flare reported by the *Fermi*-LAT via an Astronomer's Telegram made the H. E. S. S. trigger on the Crab Nebula during September and October 2016. In this chapter, the *Fermi*-LAT and H. E. S. S. II observations of this flare were also described. The analysis of the *Fermi*-LAT data revealed that the Crab Nebula flare lasted about one month in the energy range of *Fermi*-LAT. This analysis showed the flux instabilities were in the synchrotron component, whereas the inverse Compton component remained at the level of the reported constant flux, as seen in the previous flares.

The H. E. S. S. I telescopes could not observe the flare as they were in recommissioning, and commissioning runs are generally not used to derive scientific results due to the continuously changing experiment setup. Fortunately, the H. E. S. S. II telescope was operating during this period and its data was used to investigate the flux variability. With a total of 9 runs, corresponding to an exposure of 3.4 hours, the emission from the Crab Nebula simultaneous with the *Fermi*-LAT observations was studied. The flux from this period had an excess variance of 15%, which is within the H. E. S. S. uncertainty level. The energy spectrum measured by H. E. S. S. II during this time was compatible with the time-average spectrum from all H. E. S. S. II data, also within the uncertainties quoted by H. E. S. S.. There is a possibility that H. E. S. S. missed any significant flux enhancements in this period as only a few runs (3.4 h observations) were considered as good quality and were used to perform the study. The variability study from the H. E. S. S. and *Fermi*-LAT data hints a TeV flare, which starts increase before the GeV flare.

Run-wise simulations can help to reduce and control the systematic uncertainties and to conclude more about the flux variation of the Crab Nebula. Also a detailed correlation study of the flaring amplitudes between the *Fermi*-LAT and the H. E. S. S. experiments could provide more information about the flares. The 2016 flare has been partly observed with H. E. S. S. II standing alone. H. E. S. S. is now fully operational again after the successful upgrade phase, offering the opportunity to observe the Crab Nebula with the full array if any flux enhancement is reported again in the time when the Crab Nebula is visible to the H. E. S. S..

Chapter 7

Conclusions and Outlook

Energetic gamma rays from high-energy processes in the Universe are studied by space satellites and ground based detectors. The *Fermi*-LAT satellite scans the whole sky every three hours in the energy range from about 30 MeV up to more than 500 GeV since June 2008. The H. E. S. S. experiment located in the southern hemisphere in Namibia detects very-high-energy gamma rays from a few tens of GeV up to hundreds of TeV since 2003. The present generation of detectors have opened a new window to study the gamma-ray emission from the Universe.

In the work presented here, data from the *Fermi*-LAT and H. E. S. S., state-of-the-art experiments in gamma-ray astronomy, were used to perform spectral and variability studies at high-energies. The gamma-ray emission from B2 1215+30 and the Crab Nebula, two prototypical sources representing the most abundant source types at GeV and TeV energies, is studied. B2 1215+30 belongs to the blazar source class, a type of active galactic nuclei, whereas the Crab Nebula is a pulsar wind nebula located in the galactic plane.

A systematic investigation of the complete H. E. S. S. data on the Crab Nebula was performed to study in particular the flux, spectrum and variability. Standalone H. E. S. S. measurements did not result in any evidence for variability. The synchrotron emission from the Crab Nebula was found to be variable at high-energies by the space detectors. Multiwavelength observations of the Crab Nebula flare with the H. E. S. S. experiment kept the origin of this flares uncertain by not revealing any variability in the very-high-energies. New flaring activities at the GeV energy range have been detected by the *Fermi*-LAT in 2016, and the simultaneous H. E. S. S. II observations were presented here.

Blazars constitute the vast majority of sources detected at gamma-ray energies. Multiwavelength observations of blazars reveal them as variable at all wavelengths. Observations of high luminosity with rapid flux variation from small emission regions characterize blazars at very-high-energies. Their flaring activities reveal different behaviour at high-energies, offering a new opportunity to study and characterize the emission from these sources. Part of this work was dedicated to the study of the emission from one source of this class; the B2 1215+30 blazar represents an interesting case to study the high-energy emission. This work studied and characterized a large gamma-ray flare amplitude and long-term variability studies were performed. This study relied on *Fermi*-LAT publicly available data.

B2 1215+30 with almost a decade of Fermi-LAT data

One important feature of BL Lac objects is the flux variation with different amplitudes and on different time scales, in some cases down to minutes. Such events are important to characterize the high-energy emission from these objects. The flux emission from two short time periods of five months during 2013 and 2014 was investigated with *Fermi*-LAT data. The study of these two episodes was done in collaboration with the VERITAS experiment, with gamma-ray emission studied over five decades in energy. This work resulted in the detection of one major flare on 2014 February 08, simultaneously seen by *Fermi*-LAT and VERITAS.

The flux from B2 1215+30 during the 2014 TeV flare was 16 times higher than the average in the GeV range, whereas the TeV flux scaled by a remarkable factor of 60. The blazar Mrk 421 (z=0.0308) would have to exhibit a 35 Crab flare to reach the luminosity of the B2 1215+30 outburst reported here. To date, only few blazars are found to reach this brightness during flaring episodes. Around the time period of the flare, a hardening of the spectral index in the GeV energy range was measured.

These results were used to set limits on the size of the emission region and estimate a minimum Doppler factor following opacity arguments. From the strength of the GeV flare in the *Fermi*-LAT energies, a lower limit of $t_{var} < 9.0$ on the variability time scale and a minimum Doppler factor of 5 was found. The *Fermi*-LAT measurements were complemented by *Swift*-XRT data taken 24 h after the flare to estimate the synchrotron photon field density. The variability time scale of the TeV flux measured with VERITAS further constrained the results on the Doppler factor of the emission jet with a minimum Doppler factor of 10. Multiwavelength observations taken quasi-simultaneously during the 2014 flaring episode were used to model and understand the high-energy emission. Two scenarios were considered to explain the emission from the B2 1215+30: the highest part of the spectral energy distribution can be explained by the synchrotron self-Compton or external Compton models. From the SSC scenario, the ratio between the synchrotron and inverse-Compton luminosities were used to estimate the magnetic field.

Observations with the *Fermi*-LAT have opened a new window to study and monitor the gamma-ray emission of the sky objects. The long-term flux evolution of the BL Lac object B2 1215+30 was studies with almost nine years of observations. This showed other GeV flares with the flux reaching similar values as in the spectacular flare of February 2014. Three major flares, where the average flux increases by a factor of 16, were found. Studies of the long-term variability show that the yearly average flux is increasing linearly with time, correlated with a hardening of the spectral index.

Prospects

In nine years of *Fermi*-LAT data, an almost linear increase of the year-average integral flux and hardening of the spectrum was found. The evolution of the flux

was further investigated to understand the origin of the flares. The possibility of additive and multiplicative processes within the emission region were investigated by fitting the fluxes and log-fluxs by a normal distribution. Both cases do not describe the data in a satisfactory way. As the source exhibits several flux variations and high states through the years, a quasi-periodic modulation could explain the flaring activities. A discrete Fourier transform of the lightcurve hints a periodicity of of about 1083 ± 32 days. A similar periodicity has been reported only in one blazar, the PG 1553+113 [143]. The steady increase of the integrated flux on a long-term of nine years and the rich variability pattern make this blazar a promising object for future projects.

Crab Nebula with more than a decade of H. E. S. S. data

The Crab Nebula, one of the best studied objects in the sky, was the subject of this thesis work with H. E. S. S. More than ten years of observations from the H. E. S. S. experiment were used to measure the energy spectrum and perform variability studies on the Crab Nebula. The H. E. S. S. I experiment provides the best opportunities for studies at energies above 10 TeV due the large collection area. With the installation of the H. E. S. S. II telescope, there is a new possibility to exploit the lower energy range and with the increased H. E. S. S. I statistics, to expand the spectrum at even higher energies.

Crab Nebula's flux measurements are prone to systematic uncertainties for H. E. S. S. due to large zenith angle observations. This makes a spectrum measurement over a large time scale of ten years particularly challenging. The atmosphere is an electromagnetic calorimeter, which can not be calibrated with beam tests, so the reconstruction relies heavily on Monte Carlo simulations, assuming an atmospheric model. A deviation of the atmosphere from this model introduces systematic uncertainties. Observations at large zenith angles mean that the Cherenkov light traverses more atmosphere before reaching the camera, emphasizing the importance of correcting for varying atmospheric conditions. In this work, the atmospheric transparency effect on the Crab Nebula flux measurements was studied. This represents the first usage of the atmospheric transparency coefficient for large-zenith data with H. E. S. S., including also flux corrections.

The spectrum of the Crab Nebula presented here, measured with H. E. S. S. Phase-I and Phase-II, extends from 280 GeV up to 62 TeV. The increased data set was used to refine a H. E. S. S. I legacy spectrum and the H. E. S. S. II data set allows to measure the spectrum with lower energy threshold, which goes down to 280 GeV. With the monoscopic reconstruction, it is possible to measure the spectrum down to 240 GeV and get closer to the inverse Compton peak and connect with the highest points of *Fermi*-LAT. The measured spectrum is best described by a log-parabola shape, compatible with the spectral shape measured by the MAGIC and VERITAS experiments, while the spectrum previously measured by the H. E. S. S. collaboration was described best by a exponential power-law with a cut-off.

Another particularity of the Crab Nebula are flux variations of the high-energy synchrotron component. With the current scheme of H. E. S. S., it is possible to study the very-high-energy emission, taking advantage of the large collection area of H. E. S. S. II to bridge the GeV and TeV energy ranges. Among all the flares reported by the *Fermi*-LAT, only a recent flare in October 2016 was observed by H. E. S. S. II. The analysis of the *Fermi*-LAT public data reveals the GeV flare lasting for about a month. A simultaneous data analysis was conducted with H. E. S. S. II data. The faring episode was not completely covered by H. E. S. S., as the small telescopes were recommissioned after a camera upgrade. Observation carried out between the 29th of September and the 12th of October 2016 with a total of 3.4 h live time corrected by the acceptance was used for investigating the variability with H. E. S. S. II. The energy spectrum of this period was found to be compatible with the spectrum measured for all the data set within the systematic uncertainties. The evolution of the integral flux above 1 TeV during this time period gives an excess variance of 15 %. Possible flux variability in the energy range covered by H. E. S. S. are not excluded. Given the observation limitations of ground-based detectors, such flares can also be missed.

Given the puzzle on the GeV flares, part of the thesis was dedicated to hunt for TeV flares with 15 years of H. E. S. S. observations. Adding together H. E. S. S. I and H. E. S. S. II studies on the variability of the Crab Nebula, no evidence of an excess variance larger than 15% was found in a run-by-run lightcurve. This favours the scenarios that relate GeV flares with changes in the magnetic field. However, more is to be seen from future observations.

Prospects

The Crab Nebula spectrum measured from this work starts at 280 GeV and extends up to 62 TeV. The current limitations to the lower energy threshold are related to systematic effects. One possibility to reduce the systematic effects and lower the energy threshold is the use of run-wise-simulations, dedicated simulations of the observational conditions on a run-by-run basis instead of using averaged values as done in classical Monte Carlo simulations. Simulating the zenith angles, azimuth, night sky background and other observable variables for each run would decrease the systematic uncertainty. This would result in a more stable effective area and allow to lower the energy threshold even more. These simulations are still under development and not yet ready for use within the H. E. S. S. analysis framework.

The flux correction by the atmospheric transparency coefficient improves the results and reduces the excess variance. Correcting the flux by the transparency coefficient changes the normalisation of the spectrum, which a correction at the event energy level wouldn't. Hence, a more precise correction of this effect would be to correct the energy of the events before the analysis, which would increase the sensitivity. After the upgrade phase was successfully completed and H. E. S. S. become fully operational again, the possibility to detect such flares is higher. The H. E. S. S. experiment will continue to monitor the Crab Nebula in the future.

There is no future project confirmed as the *Fermi*-LAT successor as of now, but the Cherenkov Telescope Array, the future ground-based gamma-ray observatory, is currently under design and development. The two sites of CTA planned in La Palma in the northern hemisphere and Chile in the southern hemisphere offer the exclusive possibility to observe and explore a new energy range for the Crab Nebula. CTA south, planned as a large array of particularly small size telescopes, offers the opportunity to study the very-high-energy emission from the Crab Nebula. Whereas the north site, planned to operate with four large size telescopes, will allow to get closer to the inverse Compton peak. For the design of CTA, a more sophisticated atmospheric monitoring is planned.

List of Tables

1.1 Main historical instruments used in high-energy gamma-ray astronomy. Details about these instruments can be found in the reference list given here and references therein [19, 20, 25, 26, 27, 28, 29, 30, 31, 32, 33, 34]. 5

3.1 Cut parameters for the H. E. S. S. I Stereo analysis and their corresponding cut parameters for *Std* and *Loose* configurations in *Model Analysis*. 54
3.2 Cut parameters for Mono, Hybrid and Combined analysis with H. E. S. S. Phase-II and their corresponding cut parameters for Std and Loose configurations in *Model Analysis*. The Combined profile has two set of cuts, adapted to be applied to Mono and Stereo events. 54
3.3 The BDT training bins in energy and zenith. 63

4.1 Summary of the VERITAS and *Fermi*-LAT results from observations of B2 1215+30 in different epochs from 2013 and 2014. The VERITAS upper limit is computed at 95% c.l. assuming a power-law spectrum with index $\Gamma = 3.0$. 73
4.2 Summary of the major flares of B2 1215+30 detected in nine years of *Fermi*-LAT observations. The strength of the signal and the integral flux between 0.1 and 500 GeV are given. 79
4.3 Year-by-year fluxes and spectral indices of B2 1215+30, corresponding to the points presented in Figure 4.6. The fit values assuming a constant C and a linear increase for the flux and spectral index are given. 82
4.4 Summary of the latest flares from the B2 1215+30 detected with the *Fermi*-LAT from 2015-2017. The strength of the signal and the integral flux between 0.1 and 500 GeV are given. 83
4.5 The fit parameters of the long-term lightcurve fit shown in Figure 4.10. 87

5.1 Summary of Crab Nebula observations with the H. E. S. S. I telescopes. 95
5.2 Selection criteria applied to the H. E. S. S. I data. 96
5.3 Summary of H. E. S. S. I analysis results obtained from the Std and Loose cut configurations. The number of events in the ON and OFF regions $n_{\mathrm{ON}}, n_{\mathrm{OFF}}$, the number of excess events n_{excess}, significance S_{LiMa}, signal to background ratio (S/B) and the rate of gammas for each cut configuration are given. 98

5.4 Summary of the Crab Nebula spectrum fit parameters for Std and Loose cut configurations. The spectrum is fitted with a power-law, log-parabola and an exponential with power-law cut off. The energy range of the spectrum fit with E_{min} and E_{max}, the normalisation N_0, the reference energy E_0, the spectral index Γ, the curvature β and other parameters of the fit are summarized. Spectrum parameters from the Whipple [165], CAT [166], HEGRA [167], MAGIC [155], VERITAS [164] and H. E. S. S. I [113] experiments are shown for comparison. 101
5.5 Crab Nebula lightcurve fit parameters for data set I, II, III and IV (as defined in the text). The integral flux Φ, the fit parameters to a constant C, the number of runs and the systematic uncertainty α are given. 112
5.6 Summary on the Crab Nebula spectrum parameters for the first and the second season. The flux normalisation N_0 and the integral flux Φ values correspond to the reference energy of 1 TeV. 112

6.1 Analysis results of H. E. S. S. II Mono, Stereo and Combined with Std and Loose cut configurations. The number of events in the ON and OFF regions n_{ON} , n_{OFF}, the number of excess events n_{excess}, significance S_{LiMa}, signal to background ratio (S/B) and the rate of gammas for each cut configuration are given. 118
6.2 Summary of the Crab Nebula spectrum fit parameters derived from Mono, Hybrid and Combined using the Std and Loose cut configurations. The best fit parameters for each spectrum shape, a power-law (PL) and log-parabola (CPL) for the Std and Loose cut configurations are given. The energy threshold E_{thresh}, the spectral index Γ, curvature β, normalization N_0, reference energy E_0 and the fit parameters for each configuration are given. E_{min} and E_{max} correspond to the energy range of the fit, obtained during the spectrum fit procedure. . 120
6.3 The major GeV flares detected by the *Fermi*-LAT along with duration, amplitude and variability time scale. This table also indicates if the flare was observed by H. E. S. S. II. The major flares details are taken from [152, 172, 153], while the 2016 flare details are from this analysis. 124
6.4 Analysis results for each observation run taken during September-October 2016. The run number, Modified Julian date (MJD), the live time t_{live}, mean zenith angle Z_{mean}, the number of ON (N_{ON}) and OFF (N_{OFF}) events, the excess and the significance for each run are given. The integral flux Φ above 1 TeV is also given. 131

List of Figures

0.1 Images superposées du plan galactique en lumière optique et rayons gamma de très haute énergie. Les images à très haute énergie sont prises avec les télescopes H.E.S.S. en Namibie. Photographie et montage de F. Acero. VII

0.2 *En haut*: l'expérience H.E.S.S. située dans l'hémisphère sud en Namibie est composée de cinq télescopes Cherenkov. *En bas à gauche*: l'expérience MAGIC installé à La Palma. *En bas à droite*: l'expérience VERITAS, composée de quatre télescopes Cherenkov, est située dans l'hémisphère Nord, en Arizona. VIII

0.3 Le système de nébuleuse du crabe et le Crabe pulsar zoomé. X

1.1 (a) Victor Hess in one of his balloon accents. Picture taken before take-off of one of his famous flights that took place between 1911 and 1913. Image courtesy [1]. (b) Present-day spectrum of cosmic rays spanning over twelve orders of magnitude in energy as measured from several independent experiments. The majority of the spectrum follows a power-law over twelve orders of magnitude in energy with a spectral index of 2.7. The two features of the cosmic ray spectrum, known as the "knee" and "ankle" are seen around 10^{15} eV and 10^{17} eV respectively. Image courtesy [2]. 2

1.2 Schematic of Fermi acceleration in a strong shock wave. The dynamics of high-energy particles in the rest frames of the shock front, the upstream and downstream medium. *(Left)*: Rest frame of the shock front; the upstream gas is moving with velocity $v_1 = U$ and the shocked plasma with velocity $v_2 = 3/4U$. *(Middle)*: Rest frame of the upstream medium; particles from downstream are moving with velocity of $3/4U$. *(Right)*: Rest frame of the downstream medium; particles from the upstream are advancing with velocity $3/4U$. Everytime particles cross the shock, there is a gain of energy by ΔE (shown in blue and orange lines). Image courtesy [39]. 7

1.3 Hillas plot showing possible sources of proton acceleration for $E =$ 100 EeV and E=1 ZeV. The linear size R of different sources is plotted versus the magnetic field B in order to accelerate particles up to $E \sim 10^{20}\,eV$. The diagonal line correspond to the maximum reachable energy by a population of sources. Image courtesy [41]. 9

1.4 (a) The total sources detected by *Fermi*-LAT instrument in percentage, plotted together with the BL Lac and FSRQ type sources which belong to blazar source class. (b) Total sources detected in TeV show the majority belong to the BL Lac source class, a subclass of active galactic nuclei. The GeV and TeV sky is populated mainly by BL Lac type objects. Plotted with data from [45]. 13
1.5 (a) The gamma-ray excess map of the known shell-type SNR RX J1713.7-3946 as measured by H. E. S. S. Image courtesy [49]. (b) First extension measurement of the Crab Nebula at very-high-energies by H. E. S. S. Image courtesy [50]. 14
1.6 Active Galactic Nuclei unification model as described by Urry and Padovani [58]. The classification is based on the orientation of the jet with respect to the observer line-of-sight. If the observer is looking down the jet, it sees a blazar (BL Lac or FSRQ). 17
1.7 (a) Overlay of the Centaurus A galaxy with the prominent dust lanes and the emerging jet. Image courtesy: optical and radio image (VLA 6 cm), STScI/NASA. (b) The jet of the blazar 3C 279. Image courtesy: VLBA, 1.7 GHz. 17
1.8 (a) Artistic illustration of a millisecond pulsar and its companion. The pulsar is accreting material from its companion star and increasing its rotation rate. (b) Globular cluster. Images courtesy: ESA. . . 18

2.1 (a) Interaction probability in radiation length of photons as function of energy W in eV in lead material, with σ_p and σ_c the probability of pair creation and Compton scattering. Image courtesy [67]. (b) Schematic construction of EGRET, the predecessor of the *Fermi*-LAT satellite. The main parts of the detector are given to be compared to the *Fermi*-LAT. Image courtesy [68]. 22
2.2 *Fermi* spacecraft with two instruments on board: the Large Area Telescope and the Gamma-Ray Burst Monitor. Image courtesy: NASA. 23
2.3 (a) Schematic view of the *Fermi*-LAT cutaway where the three main parts of the detector are shown. (b) Cosmic gamma rays after hitting the silicon tracker get converted into an electron/positron pair. The energy released is measured in the calorimeter. Image courtesy: NASA. 25
2.4 (a) Sketch of 3D maps used to perform data analysis with the *Fermi*-LAT. The source i and other sources are marked with $j = 1, 2, 3$. (b) The counts map of B2 1215+30 for a 15° radius RoI. The known gamma-ray sources from the *Fermi* catalog are marked in green. . . . 28
2.5 Comparison of the gamma-ray acceptance map for Pass 7 and Pass 8, as indicated by the legend in the plot. Image courtesy [81]. 29
2.6 The *Fermi*-LAT full sky map in aitoff projection in Galactic coordinates. It shows the gamma-ray intensity for energies $E > 300\,\mathrm{MeV}$ produced from 48 months of observations. Image courtesy [82]. 29
2.7 All sources detected from the *Fermi*-LAT using 4 years of data. The majority of the sources detected are AGNs, whereas the PWN are the most abundant source class in the Galactic plane. Image courtesy [44]. 30

2.8 In (a) and (b) are shown the schematic view of an electromagnetic and hadronic cascade, respectively. Image courtesy [86]. 32
2.9 Schematic view of the Cherenkov light production when a charged particle moves at speeds $v > c/n$ through a medium of refractive index n. The Cherenkov light is produced at an emission angle θ. . . 34
2.10 The Cherenkov light emitted from a gamma-ray with initial energy of 1 TeV. The emission angle marked as α here changes with altitude and the superimposition of the Cherenkov light illuminates a light poll of 250 m diameter in the ground. This is seen at an observation level at 1800 m above sea level. Image courtesy [88]. 34
2.11 Cherenkov light pool of an extensive air shower induced by a photon with energy of 300 GeV (left) and by a proton with an energy of 1 TeV (right). Image courtesy [91]. 36
2.12 Illustration of the shower imaging principle in a telescope. The image shape of the shower in the telescope camera is almost elliptic and the corresponding reflection of different points of the shower into the focal plane of a camera are shown. The two main properties of gamma rays, the energy and direction are derived from the shower image on the camera. For gamma-ray induced showers, the image intensity gives information about its primary energy. Image courtesy [88]. 37
2.13 (a) The MAGIC telescopes located in La Palma. Image courtesy: Daniel Lopez/IAC. (b) An artistic image of VERITAS telescopes located in Arizona. Image courtesy UCLA [93]. 38
2.14 The differential sensitivity of CTA South and North compared to H. E. S. S., MAGIC, VERITAS and HAWC experiments. The CTA South and North, for 50 h of observations are expected to have a higher sensitivity with respect to other experiments and extend up to 100 TeV. Image courtesy [96]. 39

3.1 Picture of the H.E.S.S. telescopes in Namibia. Different trigger modes are supported by the current telescope configuration. 41
3.2 (a) A picture of CT1 camera taken during the H. E. S. S. I camera upgrade in 2015. (b) One of the camera *drawers*, a unit of 16 photomultiplier tubes. The drawers are fitted in the hexagonal structure of the camera. Image courtesy of H. E. S. S. 42
3.3 (a) The H. E. S. S. I telescopes with reflective area made of facet mirrors arranged in Davies-Cotton fashion. (b) The H. E. S. S. II telescope with refractive area made of facets arranged in parabolic fashion. Image courtesy of H. E. S. S. 43
3.4 (a) Example of a muon event on the H. E. S. S. camera. (b) The same image after cleaning and fitted by the model used for the calculation of the optical efficiency. 44
3.5 Efficiency evolution for one (CT2) of the H. E. S. S. I telescopes (blue). For each period, the calculated muon efficiency is plotted together with the mean (red) and one σ error (green). Figure courtesy [105]. . 47

3.6 Two example images of the light intensity distribution in the camera of the telescope. Left: a 1.0 TeV gamma-ray shower image, with an regular ellipse-like shape. Right: the image of a 2.6 TeV proton in the camera, with an irregular and more wide shape. Image couresy [88]. 48
3.7 Longitudinal shower development as a function of energy, measured from the first interaction point. The black and red histograms correspond to the simulated and analytical (from Equation 3.2) results respectively. Image courtesy [108]. 49
3.8 (a) Model of a 1 TeV shower started at one radiation length and falling 250 m away from the telescope. (b) Shower falling 20 m away from the telescope. Image courtesy [108]. 51
3.9 Schematic illustration of different event trigger and reconstruction types of the H. E. S. S. experiment. The top part of the figure correspond to the trigger of H. E. S. S. Phase-I which are reconstructed with Stereo. In the bottom are shown the H. E. S. S. Phase-II trigger modes. The array can trigger CT5 and CT1-4 and only CT5 and reconstruct events by using the Combined, Hybrid and Mono. 53
3.10 Schematic of ON and OFF regions in the (a) *Reflected Region* and (b) the *Ring Background* method. Images courtesy [111]. 56
3.11 (a) Example of an energy resolution table in *Model Analysis*. For a set of parameters, it gives the probability density to measure the energy E_{rec} for a given true energy E_{true}. (b) Effective area of *Model Analysis* for a given set of paramters. 57
3.12 Schematic view of a decission tree where each event is characterized by a set of input varibales $M_i(m_{i,1}, ...)$. The event classification at each node follows a binary split criteria. Image courtesy [106]. 60
3.13 Example of input variable distributions for signal and background in the energy bin $700\,\mathrm{GeV} < E < 1\,\mathrm{TeV}$ for zenith angles between 15-25 degrees. They reveal the variables with little to no separation power e.g. the *Mean Scaled Background Goodness* and with high separation power, e.g. the *Mean Scaled Shower Goodness*. 62
3.14 The BDT output distributions for signal (blue) and background (red) in the first zenith bin (15 - 25 degrees) in different energy bands. The overlap of signal and background in the low energy band is excepted as monoscopic observations are poor for background discrimination. At high energies the separation is better. 63

4.1 The B2 1215+30 counts map for a 20 degrees x 20 degrees RoI, chosen larger than the RoI in the analysis for illustrative reasons. The map was produced with *Fermi*-LAT 2014 data. The position of B2 1215+30 is marked with a green cross and all other bright sources are marked with white crosses. The VERITAS field of view (3.5 degrees) is shown for comparison. 71

4.2 TeV and GeV lightcurves of B2 1215+30 in 2013. Fluxes are calculated in 1-day bins for VERITAS (red squares). The red dashed line shows the yearly averaged TeV flux in 2011 ($8.0 \times 10^{-12}\,\mathrm{cm}^{-2}\,\mathrm{s}^{-1}$) [121]. The *Fermi*-LAT fluxes are calculated with 1-day integration bins (blue crosses), in the energy range $100\,\mathrm{MeV} < \mathrm{E} < 500\,\mathrm{GeV}$. The blue dashed line correspond to the average flux from the 3FGL catalog [44]. For the *Fermi*-LAT data, down-pointing triangles indicate 95 % c.l. upper limits for time bins with signal smaller than 2σ. 74

4.3 B2 1215+30 light curves for the 2014 data. In the top panel, the VERITAS integral fluxes in 1-day time bins are plotted. The red dashed line shows the yearly-averaged TeV flux in 2011 [121]. The gray dashed lines correspond to one and two Crab Nebula flux. One Crab correspond to $(2.1 \pm 0.2) \times 10^{-10}\,\mathrm{cm}^{-2}\,\mathrm{s}^{-1}$, for $E > 0.2\,\mathrm{TeV}$ [132]. Using the *Fermi*-LAT data the integral fluxes were calculated in 3-day (blue crosses). Down-pointing triangles indicate 95 % c.l. upper limits for time bins with signal smaller than 2σ. The blue dashed line correspond to the average flux from the 3FGL catalog [44]. The yellow points correspond to 1-day time bins derived around the flare period. The bright flare is seen simultaneously by the two experiments at the GeV and TeV energies on February 2014. 75

4.4 Spectral energy distribution of B2 1215+30. The cyan and red points correspond to the *Fermi*-LAT data and other observations from this work as indicated in the legend. The gray points are the archival points from [121]. 77

4.5 Top panel: Long-term lightcurve of B2 1215+30, from 2008 September 1st to 2017 June 30. The integral fluxes are calculated in one week time bins. The major flares, with weekly averaged flux $\Phi > 3.0 \times 10^{-07}\ \mathrm{cm}^{-2}\,\mathrm{s}^{-1}$ are indicated by dashed black lines. Bottom panel: lightcurve in one day time bins around the major flares detected during October 2008, February 2014 and April 2017. 80

4.6 Top: The average year-by-year fluxes for B2 1215+30 from 2008 to 2017. Bottom: The corresponding spectral indices for the marked years. The orange line corresponds to a constant and the green correspond to a linear fit. 81

4.7 Distribution of B2 1215+30 fluxes for nine years of *Fermi*-LAT data measured in one week time bins. The distribution is fitted by a Gaussian assuming a constant flux (blue) and a linear flux (green). 82

4.8 Integral flux Φ ($100\ \mathrm{MeV} < \mathrm{E} < 500\ \mathrm{GeV}$) in one week time bins for all the 2015 (MJD 57023-57387) and 2016 (MJD 57388-57753) data sets in the top and middle panels. The bottom panel shows only six months of data, from 2017 January 1st to 2017 June 30 (MJD 57754-57934) in one week time bins. 84

4.9 The discrete Fourier transformed long-term lightcurve of B2 1215+30 measured with *Fermi*-LAT as a function of the period in an arbitrary unit, before and after subtracting the linear fit. The black dots are the discrete points in Fourier space, connected by a smooth curve to guide the eye. The dashed lines indicate the 1σ, 2σ and 3σ percentiles of the simulated Gaussian noise. 85
4.10 The long-term lightcurve including a fit of the form given in Equation 4.9. The fit parameters and their uncertainties are listed in Table 4.5. 87

5.1 The Crab Nebula system, and the zoomed pulsar. 91
5.2 (a) Lord Rosse's sketch of the Crab Nebula filaments in 1844. Image courtesy [160]. (b) Image of the Crab Nebula activity produced in 1968. Image courtesy [161]. 93
5.3 (a) The Crab pulsar as seen from Chandra X-ray Observatory. (b) Composite image of the Crab Nebula from five telescopes: the Karl G. Jansky Very Large Array, the Spitzer Space Telescope, the Hubble Space Telescope, the XMM-Newton Observatory, and the Chandra X-ray Observatory. Image courtesy: NASA, ESA, NRAO/AUI/NSF and G. Dubner (University of Buenos Aires). 94
5.4 An example of a run that passed all the run selection criteria but the COG map check. The COG maps for CT1, CT2, CT3 and CT4 (left to the right) for the run number 42556 are shown. The second COG map, which correspond to CT2, is problematic and this run is excluded from the final run list. 97
5.5 Left: Zenith angle distributions for the run list used in the analysis after applying the custom selection criteria as described in the text. Right: Observations of the Crab Nebula taken with the H. E. S. S. I telescopes, with runs distributed from 2003 to 2015. The runs presented here are obtained after applying only the standard run quality, which results in more runs than in the left plot. The majority of the runs are taken during October. 97
5.6 The θ^2 (squared angular distance) distributions for gamma-like events (filled histogram) compared with normalized θ^2 distributions of off regions (black) for the (a) Std and (b) Loose cuts. The dashed blue points correspond to the background distribution, which for the Crab Nebula is very low compared to the signal from the source. 99
5.7 (a) The significance map of the Crab Nebula using all the H. E. S. S. I data set with Std cuts. The position of the Crab Nebula is showed in the center. (b) The corresponding significance distribution of the whole map is shown in black. The distribution after excluding a circular region of 0.25 degrees around the source with a Gaussian fit is shown in red and the fit values are shown in the plot. 100

5.8 Differential energy spectrum of the Crab Nebula as measured by H. E. S. S. I from 480 GeV to 62.4 TeV. The spectrum is best described by a log-parabola spectral shape. The 1σ confidence interval of the fitted spectrum shape is plotted in solid red line. The residual plot in the form $(N_{obs} - N_{exp})/N_{exp}$ is shown in the bottom part. . . . 102
5.9 Long term lightcurve of the Crab Nebula on a run by run basis, from MJD 52935-56365. The integral flux is calculated at energies above 1 TeV are plotted along with one sigma statistical errors. The red line corresponds to the error weighted average flux. 104
5.10 Top: Run-by-run integral flux versus optical efficiencies. Middle: Run-by-run integral flux above versus off-axis angles. Bottom: Distribution of the integral fluxes above 1 TeV with observation zenith angles. Their values are distributed around the mean, not showing any evidence of bias introduced. 105
5.11 The integral flux versus excess normalized by the exposure time. . . . 105
5.12 The transparency coefficient averaged over telescopes for each observation run. The data plotted here is taken on the Crab Nebula over ten years. 107
5.13 Lightcurves of the Crab Nebula including the mean, with different TC categories in different colors. The categories are named after the averages of their TC ranges. The effect of the transparency on the data can be seen, and it has a bigger impact for low TC values. . . . 108
5.14 The Crab Nebula long term lightcurve on a run by run basis after removing runs with TC < 0.9. The flux errors are statistical only. The cyan dashed line correspond to the mean error weighted flux. . . 109
5.15 The pull distributions of the flux measurements before and after the TC cut, both normalized to unity. The pull is the flux Φ_i minus the mean flux divided by the flux error $\sigma_{\Phi,i}$. For a statistical error only, the pull distribution has width one. For the runs before the TC cut it is 2.2 and after the TC cut it is 1.6, indicating that effects introduced by the varying atmospheric quality make up a large fraction of the systematic uncertainty. The flux errors are statistically only. 109
5.16 The H. E. S. S. I long term lightcurve of the Crab Nebula on a run by run basis. The orange points correspond to the lightcurve without any correction or any cut on the transparency coefficient. The blue correspond to the same data set, corrected for the transparency coefficient. The dashed lines represent the mean error weighted flux for each data set. 110
5.17 The projected lightcurve for the uncorrected flux and the TC corrected flux with power-law index of $\alpha = 1$ and $\alpha = 1.7$, including unbinned Gaussian fits. The uncertainty bands visualize the fit error on the width. 111

5.18 Superimposed Crab Nebula spectrum from two different seasons as described in the text. The first season is represented by the black points and the second season by the blue ones. The 1σ confidence interval of the fitted spectrum shape are plotted by solid lines. The spectra are fitted with a curved power-law spectral shape and are compatible within the estimated H. E. S. S. systematic uncertainties. The residual plot in the form $(N_{obs} - N_{exp})/N_{exp}$ are shown in the bottom part. 113

6.1 The H. E. S. S. II telescopes. Image courtesy M. Lorentz. 115
6.2 The distribution of θ^2 , the angular distance between the reconstructed direction and source position, for the Mono Std. The background from the OFF regions is shown in red. 118
6.3 The ring background significance distributions for Mono, Hybrid and Combined analysis with Std cuts. The significance distribution of the whole map is shown in black. The distribution after excluding a circular region around the source with a Gaussian fit is shown in red. The latter includes a Gaussian fit with the fit parameters indicated. . 119
6.4 The spectral energy distribution of the Crab Nebula as measured with H. E. S. S. II and fitted with log-parabola spectrum shape. The Mono, Stereo and Combined spectra are derived using the Std (a) and Loose (b) cuts. The spectrum derived with the Mono configuration (cyan) provides a lower energy threshold compared to the spectrum from the Stereo and Combined analyses, which agree well with one-another. . . 121
6.5 The spectral energy distribution of the Crab Nebula as measured with H. E. S. S. I and H. E. S. S. II (from this work) along with the published data points from MAGIC, VERITAS and *Fermi*-LAT experiments [172, 164, 155]. 123
6.6 Spectral energy distribution of the Crab Nebula compiled with data from the spaceborne satellites. The spectral points correspond to the maximum flare level of the major flares detected on the Crab Nebula by *AGILE* and *Fermi*-LAT satellites. The blue data points belong to the average nebula flux values. Image courtesy [55]. 124
6.7 Observations of the H. E. S. S. experiment before and after the upgrade phase. The CT1 telescope was not included in observations until March, the month during which the three other H. E. S. S. telescopes entered in the upgrade phase. After August 2016, the array started to be re-commissioned with five telescopes. The months during which the H. E. S. S. experiment observed the Crab Nebula are marked with down cyan triangles and the *Fermi*-LAT flare is indicated in orange. 125
6.8 A $15° \times 15°$ RoI counts map centered on the position of the Crab Nebula. This correspond to the period of the 2016 flare and the brightness of the Crab Nebula is visible. The Crab Nebula is marked with green cross and other bright sources are marked as well. The squared symbols indicate two extended sources located within RoI. . 126

6.9 The Crab Nebula energy spectrum derived with data from September to October 2016 superimposed to the overall H. E. S. S. II Mono spectrum for comparison. The 1σ confidence interval of the fitted spectrum shape are plotted as solid lines. Both spectra are obtained from Mono Std analysis configurations and are compatible within the estimated H. E. S. S. uncertainties. The errors plotted are statistical only. 129

6.10 TeV and GeV lightcurves of Crab Nebula in 2016. Top: The lightcurve in a run-by-run basis measured from H. E. S. S. II from MJD 57390.94-57724.02 (red squares). The integral fluxes, calculated above 1 TeV are normalized to the average flux from the H. E. S. S. flux from 2006 publication [113]. The dashed red line correspond to the average flux for this period, whereas the black line to the average flux from 2006. In the bottom part of the plot, the Crab Nebula integral flux of the synchrotron component between 57632-57692 MJD as derived from *Fermi*-LAT data is plotted (blue crosses). The integral fluxes are calculated in 3-day time bins, from $100\,\mathrm{MeV} < \mathrm{E} < 500\,\mathrm{GeV}$ and normalized to the published average synchrotron flux from [172]. The dashed blue line correspond to the average synchrotron flux from the previous *Fermi*-LAT measurements ($6.1 \pm 0.2 \times 10^{-7}\,\mathrm{cm}^{-2}\mathrm{s}^{-1}$). 130

B.1 The Crab Nebula spectrum and the relative difference with the "global" spectrum. The relative difference between each spectrum and the average are plotted in the bottom part of the plot. The H. E. S. S. points are derived from the intersection run list between the ParisAnalysis and HAP, two different analysis frameworks. The shadowed blue area correspond to 30% relative difference. The PA Std (green) correspond to this work and "HAP' (orange) to the other analysis framework (internal H. E. S. S. results produced by J.Hahn using HAP framework). 167

Acronyms List

ACD Anti-coincidence detector.

ADC Analog to digital convertor.

AGN Active galactic nucleus.

BDT Boosted decision trees.

BL Lac BL Lacertae.

CMB Cosmic microwave background.

COG Center of gravity map.

DAQ Data acquisition.

DFT Discrete Fourier Transform.

EAS Extensive air showers.

EBL Extragalactic background light.

FSRQ Flat spectrum radio quasar.

GMB Gamma-Ray burst monitor.

GRB Gamma-Ray burst.

HAP H.E.S.S. Analysis Package.

HBL High frequency peaked BL Lac.

IACT Imaging atmospheric Cherenkov telescope.

IBL Intermediate frequency peaked BL Lac.

IC Inverse Compton.

IRF Instrument response function.

LAT Large area telescope.

LP Log Parabola.

MJD Modified Julian date.

MSSG Mean scaled shower goodness.

MVA Multivariate analysis.

ndf Number of degrees of freedom.

NSB Night sky background.

PA Paris Analysis.

PL Power Law.

PMT Photomultiplier tube.

PSF Point-spread function.

PWN Pulsar wind nebula.

RoI Region of interest.

SED Spectral energy distribution.

SNR Supernova remnant.

SSC Synchrotron self Compton.

TC Transparency coefficient.

TMVA Toolkit for multivariate analysis.

ToO Target of opportunity.

TS Test statistics.

UV ultraviolet.

Bibliography

[1] Wikipedia. Victor Francis Hess — Wikipedia, The Free Encyclopedia. https://en.wikipedia.org/wiki/Victor_Francis_Hess, 2017. [Online; Accessed: 06-22-2017.].

[2] W. Bietenholz. The most powerful particles in the Universe: a cosmic smash. *ArXiv e-prints*, May 2013.

[3] Bertolotti Mario. *Celestial Messengers*. Springer, 2013.

[4] Nobelprize.org. The Nobel Prize in Physics 1936. http://www.nobelprize.org/nobel_prizes/physics/laureates/1936/, 2017. [Online; Accessed: 09-08-2017.].

[5] B. W. Carroll and D. A. Ostlie. *An Introduction To Modern Astrophysics*. Pearson, Addison Wesley, Weber State University, 2007.

[6] K. A. Olive and Particle Data Group. Review of Particle Physics. *Chinese Physics C*, 38(9):090001, August 2014.

[7] K. Greisen. End to the Cosmic-Ray Spectrum? *Physical Review Letters*, 16:748–750, April 1966.

[8] W. Baade and F. Zwicky. Cosmic Rays from Super-novae. *Proceedings of the National Academy of Science*, 20:259–263, May 1934.

[9] B. Edwards, J. Losty, D. H. Perkins, K. Pinkau, and J. Reynolds. Analysis of nuclear interactions of energies between 1000 and 100 000 BeV. *Philosophical Magazine*, 3:237–266, March 1958.

[10] S. Hayakawa. Propagation of the Cosmic Radiation through Intersteller Space. *Progress of Theoretical Physics*, 8:571–572, November 1952.

[11] E. M. Burbidge, G. R. Burbidge, W. A. Fowler, and F. Hoyle. Synthesis of the Elements in Stars. *Reviews of Modern Physics*, 29:547–650, 1957.

[12] J. Aublin and Pierre Auger Collaboration. Arrival directions of the highest-energy cosmic rays detected with the Pierre Auger Observatory. In *34th International Cosmic Ray Conference (ICRC2015)*, volume 34 of *International Cosmic Ray Conference*, page 310, July 2015.

[13] W. Galbraith and J. V. Jelley. Light Pulses from the Night Sky associated with Cosmic Rays. *Nature*, 171:349–350, February 1953.

[14] T.C. Weekes, M.F. Cawley, D.J. Fegan, et al. Observation of TeV gamma rays from the Crab nebula using the atmospheric Cerenkov imaging technique. *ApJ*, 342:379–395, July 1989.

[15] S. Hayakawa. High Energy Gamma-Rays from the Crab Nebula. *Progress of Theoretical Physics*, 19:219–219, February 1958.

[16] P. Morrison. On gamma-ray astronomy. *Nuovo Cimento*, 7:858–865, 1958.

[17] nasa.gov. Gamma-ray Astronomy. https://imagine.gsfc.nasa.gov/science/toolbox/gamma_ray_astronomy1.html, 2017. [Online; Accessed: 09-30-2017.].

[18] W. Kraushaar, G. W. Clark, G. Garmire, et al. Explorer XI Experiment on Cosmic Gamma Rays. *ApJ*, 141:845, April 1965.

[19] W. L. Kraushaar, G. W. Clark, G. P. Garmire, et al. High-Energy Cosmic Gamma-Ray Observations from the OSO-3 Satellite. *ApJ*, 177:341, November 1972.

[20] S. M. Derdeyn, C. H. Ehrmann, C. E. Fichtel, D. A. Kniffen, and R. W. Ross. SAS-B digitized spark chamber gamma ray telescope. *Nuclear Instruments and Methods*, 98:557–566, 1972.

[21] G. F. Bignami, G. Boella, J. J. Burger, et al. The COS-B experiment for gamma-ray astronomy. *Space Science Instrumentation*, 1:245–268, August 1975.

[22] K. T. Strong, J. L. R. Saba, B. M. Haisch, and J. T. Schmelz, editors. *The many faces of the sun : a summary of the results from NASA's Solar Maximum Mission*, 1999.

[23] F. Krennrich, C. W. Akerlof, J. H. Buckley, et al. Stereoscopic observations of gamma rays at the Whipple observatory. *Astroparticle Physics*, 8:213–221, April 1998.

[24] R. C. Hartman, D. L. Bertsch, S. D. Bloom, et al. The Third EGRET Catalog of High-Energy Gamma-Ray Sources. *ApJS*, 123:79–202, July 1999.

[25] D. J. Thompson, D. L. Bertsch, C. E. Fichtel, et al. Calibration of the Energetic Gamma-Ray Experiment Telescope (EGRET) for the Compton Gamma-Ray Observatory. *ApJS*, 86:629–656, June 1993.

[26] R. Rando and for the Fermi LAT Collaboration. Post-launch performance of the Fermi Large Area Telescope. *ArXiv e-prints*, July 2009.

[27] T. C. Weekes. a Fast Large Aperture Camera for Very High Energy Gamma-Ray Astronomy. *International Cosmic Ray Conference*, 8:34, 1981.

[28] A. Barrau, R. Bazer-Bachi, E. Beyer, et al. The CAT imaging telescope for very-high-energy gamma-ray astronomy. *Nuclear Instruments and Methods in Physics Research A*, 416:278–292, October 1998.

[29] E. Paré, B. Balauge, R. Bazer-Bachi, et al. CELESTE: an atmospheric Cherenkov telescope for high energy gamma astrophysics. *Nuclear Instruments and Methods in Physics Research A*, 490:71–89, September 2002.

[30] C. E. Covault, M. C. Chantell, Z. Conner, et al. Progress and Recent Results from the Solar Tower Atmospheric Cherenkov Effect Experiment (STACEE). In *American Astronomical Society Meeting Abstracts #194*, volume 31 of *Bulletin of the American Astronomical Society*, page 838, May 1999.

[31] E. Lorenz and The MAGIC Collaboration. Status of the 17 m MAGIC telescope. *New A Rev.*, 48:339–344, April 2004.

[32] J. Holder. VERITAS: Status and Highlights. *ICRC*, 2011.

[33] H. Anderhub, M. Backes, A. Biland, et al. Design and operation of FACT - the first G-APD Cherenkov telescope. *Journal of Instrumentation*, 8:P06008, June 2013.

[34] A. J. Smith and for the HAWC Collaboration. HAWC: Design, Operation, Reconstruction and Analysis. *ArXiv e-prints*, August 2015.

[35] E. Fermi. On the Origin of the Cosmic Radiation. *Physical Review*, 75:1169–1174, April 1949.

[36] L. O. Drury. An introduction to the theory of diffusive shock acceleration of energetic particles in tenuous plasmas. *Reports on Progress in Physics*, 46:973–1027, August 1983.

[37] L. O. Drury. Particle Acceleration in Shocks. *Ap&SS*, 233:251–260, November 1995.

[38] M. S. Longair. *High Energy Astrophysics*. February 2011.

[39] S. Funk. *A new population of very high-energy -ray sources detected with H.E.S.S. in the inner part of the Milky Way*. PhD thesis, Ruprecht-Karls-Universität Heidelberg, 2005.

[40] A. R. Bell. The acceleration of cosmic rays in shock fronts. I. *MNRAS*, 182:147–156, January 1978.

[41] F. Fraschetti. On the acceleration of ultra-high-energy cosmic rays. *Philosophical Transactions of the Royal Society of London Series A*, 366:4417–4428, December 2008.

[42] C. Patrignani et al. Review of Particle Physics. *Chin. Phys.*, C40(10):100001, 2016.

[43] E. Waxman and J. Bahcall. High energy neutrinos from astrophysical sources: An upper bound. *Phys. Rev. D*, 59(2):023002, January 1999.

[44] F. Acero, M. Ackermann, M. Ajello, et al. Fermi Large Area Telescope Third Source Catalog. *ApJS*, 218:23, June 2015.

[45] http://tevcat.uchicago.edu/. TeVCat Catalog. `http://tevcat.uchicago.edu/`, 2017. [Online; Accessed: 01-06-2017.].

[46] S. Chandrasekhar. The Maximum Mass of Ideal White Dwarfs. *ApJ*, 74:81, July 1931.

[47] W. Baade and F. Zwicky. On Super-novae. *Proceedings of the National Academy of Science*, 20:254–259, May 1934.

[48] P. Blasi. The origin of galactic cosmic rays. *A&A Rev.*, 21:70, November 2013.

[49] H. E. S. S. Collaboration, :, H. Abdalla, et al. H.E.S.S. observations of RX J1713.7-3946 with improved angular and spectral resolution; evidence for gamma-ray emission extending beyond the X-ray emitting shell. *ArXiv e-prints*, September 2016.

[50] M. Holler, D. Berge, J. Hahn, et al. Advanced search for the extension of unresolved TeV sources with H.E.S.S.: First measurement of the extension of the Crab nebula at TeV energies. *ArXiv e-prints*, July 2017.

[51] M. Ackermann, M. Ajello, A. Allafort, et al. Detection of the Characteristic Pion-Decay Signature in Supernova Remnants. *Science*, 339:807–811, February 2013.

[52] F. Aharonian, A. G. Akhperjanian, U. B. de Almeida, et al. Discovery of Gamma-Ray Emission From the Shell-Type Supernova Remnant RCW 86 With Hess. *ApJ*, 692:1500–1505, February 2009.

[53] D. H. Roberts and P. A. Sturrock. Model of Pulsar Magnetospheres. In *Bulletin of the American Astronomical Society*, volume 3 of *BAAS*, page 463, September 1971.

[54] B. M. Gaensler and P. O. Slane. The Evolution and Structure of Pulsar Wind Nebulae. *ARA&A*, 44:17–47, September 2006.

[55] R. Bühler and R. Blandford. The surprising Crab pulsar and its nebula: a review. *Reports on Progress in Physics*, 77(6):066901, June 2014.

[56] J. Albert, E. Aliu, H. Anderhub, et al. VHE γ-Ray Observation of the Crab Nebula and its Pulsar with the MAGIC Telescope. *ApJ*, 674:1037–1055, February 2008.

[57] F. Aharonian, A. G. Akhperjanian, A. R. Bazer-Bachi, et al. An Exceptional Very High Energy Gamma-Ray Flare of PKS 2155-304. *ApJ*, 664:L71–L74, August 2007.

[58] C. M. Urry and P. Padovani. Unified Schemes for Radio-Loud Active Galactic Nuclei. *PASP*, 107:803, September 1995.

[59] H. E. S. S. Collaboration, :, H. Abdalla, et al. Measurement of the EBL spectral energy distribution using the VHE gamma-ray spectra of H.E.S.S. blazars. *ArXiv e-prints*, July 2017.

[60] H. A. Kobulnicky and C. L. Fryer. A New Look at the Binary Characteristics of Massive Stars. *ApJ*, 670:747–765, November 2007.

[61] P. Bordas, H. Laffon, M. de Naurois, et al. Observations of TeV binary systems with the H.E.S.S. telescope. *ArXiv e-prints*, July 2013.

[62] H.E.S.S. Collaboration, A. Abramowski, F. Acero, et al. Search for very-high-energy γ-ray emission from Galactic globular clusters with H.E.S.S. *A&A*, 551:A26, March 2013.

[63] A. Abramowski, F. Acero, F. Aharonian, et al. H.E.S.S. Observations of the Globular Clusters NGC 6388 and M15 and Search for a Dark Matter Signal. *ApJ*, 735:12, July 2011.

[64] A. Abramowski, F. Aharonian, F. Ait Benkhali, et al. Diffuse Galactic gamma-ray emission with H.E.S.S. *Phys. Rev. D*, 90(12):122007, December 2014.

[65] F. Aharonian, A. G. Akhperjanian, U. Barres de Almeida, et al. HESS observations of γ-ray bursts in 2003-2007. *A&A*, 495:505–512, February 2009.

[66] B. Rossi. *High Energy Particles*. 1952.

[67] D. J. Thompson. Space detectors for gamma rays (100 MeV-100 GeV): From EGRET to Fermi LAT. *Comptes Rendus Physique*, 16:600–609, August 2015.

[68] J. A. Esposito, D. L. Bertsch, A. W. Chen, et al. In-Flight Calibration of EGRET on the Compton Gamma-Ray Observatory. *ApJS*, 123:203–217, July 1999.

[69] H. C. van de Hulst, A. Scheepmaker, B. N. Swanenburg, et al. Spectral Analysis of Gamma Rays with the Cos-B Satellite. The Caravane Collaboration. In F. Labuhn and R. Lust, editors, *New techniques in Space Astronomy*, volume 41 of *IAU Symposium*, page 37, 1971.

[70] A. A. Moiseev, R. C. Hartman, J. F. Ormes, et al. The anti-coincidence detector for the GLAST large area telescope. *Astroparticle Physics*, 27:339–358, June 2007.

[71] P. Gros, S. Amano, D. Attié, et al. First measurement of the polarisation asymmetry of a gamma-ray beam between 1.7 to 74 MeV with the HARPO TPC. In *Space Telescopes and Instrumentation 2016: Ultraviolet to Gamma Ray*, volume 9905 of *Proc. SPIE*, page 99052R, July 2016.

[72] C. Meegan, G. Lichti, P. N. Bhat, et al. The Fermi Gamma-ray Burst Monitor. *ApJ*, 702:791–804, September 2009.

[73] W. B. Atwood, A. A. Abdo, M. Ackermann, et al. The Large Area Telescope on the Fermi Gamma-Ray Space Telescope Mission. *ApJ*, 697:1071–1102, June 2009.

[74] W. N. Johnson, J. E. Grove, B. F. Phlips, et al. The Construction and Performance of the CsI Hodoscopic Calorimeter for the GLAST Beam Test Engineering Module. In *AAS/High Energy Astrophysics Division #5*, volume 32 of *Bulletin of the American Astronomical Society*, page 1263, October 2000.

[75] A. A. Abdo, M. Ackermann, M. Ajello, et al. The on-orbit calibration of the Fermi Large Area Telescope. *Astroparticle Physics*, 32:193–219, October 2009.

[76] S. Zimmer, L. Arrabito, T. Glanzman, et al. Extending the Fermi-LAT Data Processing Pipeline to the Grid. In *Journal of Physics Conference Series*, volume 396 of *Journal of Physics Conference Series*, page 032121, December 2012.

[77] W. Cash. Parameter estimation in astronomy through application of the likelihood ratio. *ApJ*, 228:939–947, March 1979.

[78] J. R. Mattox, D. L. Bertsch, J. Chiang, et al. The Likelihood Analysis of EGRET Data. *ApJ*, 461:396, April 1996.

[79] M. Ackermann, M. Ajello, A. Albert, et al. The Fermi Large Area Telescope on Orbit: Event Classification, Instrument Response Functions, and Calibration. *ApJS*, 203:4, November 2012.

[80] W. Atwood, A. Albert, L. Baldini, et al. Pass 8: Toward the Full Realization of the Fermi-LAT Scientific Potential. *ArXiv e-prints*, March 2013.

[81] slac.stanford.edu. LAT Performance. http://www.slac.stanford.edu/exp/glast/groups/canda/lat_Performance.htm, 2017. [Online; Accessed: 16-10-2017.].

[82] fermi.gsfc.nasa.gov. . https://fermi.gsfc.nasa.gov/ssc/, 2017. [Online; Accessed: 27-08-2017.].

[83] A. A. Abdo, M. Ackermann, M. Ajello, et al. Spectrum of the Isotropic Diffuse Gamma-Ray Emission Derived from First-Year Fermi Large Area Telescope Data. *Physical Review Letters*, 104(10):101101, March 2010.

[84] K. Bechtol and Fermi Large Area Telescope Collaboration. The intensity of isotropic diffuse emission measured with the Fermi Large Area Telescope. In *American Astronomical Society Meeting Abstracts #223*, volume 223 of *American Astronomical Society Meeting Abstracts*, page 426.08, January 2014.

[85] A. U. Abeysekara, R. Alfaro, C. Alvarez, et al. Sensitivity of the high altitude water Cherenkov detector to sources of multi-TeV gamma rays. *Astroparticle Physics*, 50:26–32, December 2013.

[86] J. Matthews. A Heitler model of extensive air showers. *Astroparticle Physics*, 22:387–397, January 2005.

[87] P. K. F. Grieder. *Extensive Air Showers: High Energy Phenomena and Astrophysical Aspects - A Tutorial, Reference Manual and Data Book*. 2010.

[88] Heinrich J. Voelk and Konrad Bernloehr. Imaging Very High Energy Gamma-Ray Telescopes. *Exper. Astron.*, 25:173–191, 2009.

[89] Nobelprize.org. The Nobel Prize in Physics 1958. https://www.nobelprize.org/nobel_prizes/physics/laureates/1958/, 2017. [Online; Accessed: 02-10-2017.].

[90] M. Doering, K. Bernloehr, G. Hermann, W. Hofmann, and H. Lampeitl. Measurement of the Cherenkov light spectrum and of the polarization with the HEGRA-IACT-system. *ArXiv Astrophysics e-prints*, July 2001.

[91] D. Berge. *Development of an Algorithm for the Shower Reconstruction with the H.E.S.S. Telescope System*. PhD thesis, Humboldt-Universität zu Berlin, 2002.

[92] HEGRA Collaboration: A. Daum. First Results on the Performance of the HEGRA IACT Array. *ArXiv Astrophysics e-prints*, April 1997.

[93] http://www.ucla.edu/. University California Los Angeles. http://www.ucla.edu/, 2017. [Online; Accessed: 10-09-2017.].

[94] T. C. Weekes, H. Badran, S. D. Biller, et al. VERITAS: the Very Energetic Radiation Imaging Telescope Array System. *Astroparticle Physics*, 17:221–243, May 2002.

[95] B. S. Acharya, M. Actis, T. Aghajani, et al. Introducing the CTA concept. *Astroparticle Physics*, 43:3–18, March 2013.

[96] https://www.cta observatory.org/. CTA Homepage. https://www.cta-observatory.org/, 2017. [Online; Accessed: 10-09-2017.].

[97] R. Cornils, S. Gillessen, I. Jung, et al. The optical system of the H.E.S.S. imaging atmospheric Cherenkov telescopes. Part II: mirror alignment and point spread function. *Astroparticle Physics*, 20:129–143, November 2003.

[98] W. T. Welford and R. Winston. *High collection nonimaging optics*. 1989.

[99] K. Bernlöhr, O. Carrol, R. Cornils, et al. The optical system of the H.E.S.S. imaging atmospheric Cherenkov telescopes. Part I: layout and components of the system. *Astroparticle Physics*, 20:111–128, November 2003.

[100] C. L. Naumann, J. Bolmont, P. Corona, et al. NECTAR: New electronics for the Cherenkov Telescope Array. In F. A. Aharonian, W. Hofmann, and F. M. Rieger, editors, *American Institute of Physics Conference Series*, volume 1505 of *American Institute of Physics Conference Series*, pages 785–788, December 2012.

[101] P. Hofverberg, R. Kankanyan, M. Panter, et al. Commissioning and initial performance of the H.E.S.S. II drive system. *ArXiv e-prints*, July 2013.

[102] A. Balzer, M. Füßling, M. Gajdus, et al. The H.E.S.S. central data acquisition system. *Astroparticle Physics*, 54:67–80, February 2014.

[103] F. Aharonian, A. G. Akhperjanian, K.-M. Aye, et al. Calibration of cameras of the H.E.S.S. detector. *Astroparticle Physics*, 22:109–125, November 2004.

[104] I. Braun. *Improving the Pointing Precision of the H.E.S.S. Experiment. PhD Thesis, Ruprecht-Karls Universität, Heidelberg.* PhD thesis, PhD thesis, Ruprecht-Karls-Universität Heidelberg, 2007.

[105] R. Chalme-Calvet, M. de Naurois, J.-P. Tavernet, and for the H. E. S. S. Collaboration. Muon efficiency of the H.E.S.S. telescope. *ArXiv e-prints*, March 2014.

[106] S. Ohm, C. van Eldik, and K. Egberts. γ/hadron separation in very-high-energy γ-ray astronomy using a multivariate analysis method. *Astroparticle Physics*, 31:383–391, June 2009.

[107] A. M. Hillas. Cerenkov light images of EAS produced by primary gamma. In F. C. Jones, editor, *International Cosmic Ray Conference*, volume 3 of *International Cosmic Ray Conference*, pages 445–448, August 1985.

[108] M. de Naurois and L. Rolland. A high performance likelihood reconstruction of γ-rays for imaging atmospheric Cherenkov telescopes. *Astroparticle Physics*, 32:231–252, December 2009.

[109] S. Le Bohec, B. Degrange, M. Punch, et al. A new analysis method for very high definition imaging atmospheric Cherenkov telescopes as applied to the CAT telescope. *Nuclear Instruments and Methods in Physics Research A*, 416:425–437, October 1998.

[110] M. P. Kertzman and G. H. Sembroski. Computer simulation methods for investigating the detection characteristics of TeV air Cherenkov telescopes. *Nuclear Instruments and Methods in Physics Research A*, 343:629–643, April 1994.

[111] D. Berge, S. Funk, and J. Hinton. Background modelling in very-high-energy γ-ray astronomy. *A&A*, 466:1219–1229, May 2007.

[112] T.-P. Li and Y.-Q. Ma. Analysis methods for results in gamma-ray astronomy. *ApJ*, 272:317–324, September 1983.

[113] F. Aharonian, A. G. Akhperjanian, A. R. Bazer-Bachi, et al. Observations of the Crab nebula with HESS. *A&A*, 457:899–915, October 2006.

[114] S. Bernhard. *The The Variable High Energy γ-Ray Sky with H.E.S.S. & Towards a Calibration Unit for CTA FlashCam*. PhD thesis, Leopold-Franzens-Universität Innsbruck Institut für Astro-und Teilchenphysik, 2017.

[115] Andreas Hoecker, Peter Speckmayer, Joerg Stelzer, et al. TMVA: Toolkit for Multivariate Data Analysis. *PoS*, ACAT:040, 2007.

[116] R. D. Parsons and J. A. Hinton. A Monte Carlo template based analysis for air-Cherenkov arrays. *Astroparticle Physics*, 56:26–34, April 2014.

[117] J. Aleksić, L. A. Antonelli, P. Antoranz, et al. MAGIC Discovery of Very High Energy Emission from the FSRQ PKS 1222+21. *ApJ*, 730:L8, March 2011.

[118] T. Arlen, T. Aune, M. Beilicke, et al. Rapid TeV Gamma-Ray Flaring of BL Lacertae. *ApJ*, 762:92, January 2013.

[119] A. A. Abdo, M. Ackermann, M. Ajello, et al. VizieR Online Data Catalog: Fermi/LAT bright gamma-ray source list (0FGL) (Abdo+, 2009). *VizieR Online Data Catalog*, 218, November 2009.

[120] J. Aleksić et al. Discovery of VHE γ-rays from the blazar 1ES 1215+303 with the MAGIC telescopes and simultaneous multi-wavelength observations. *A&A*, 2012.

[121] E. Aliu, S. Archambault, T. Arlen, et al. Long Term Observations of B2 1215+30 with VERITAS. *ApJ*, 779:92, December 2013.

[122] A. U. Abeysekara, S. Archambault, A. Archer, et al. A Luminous and Isolated Gamma-Ray Flare from the Blazar B2 1215+30. *ApJ*, 836:205, February 2017.

[123] S. Paiano, M. Landoni, R. Falomo, et al. On the Redshift of TeV BL Lac Objects. *ApJ*, 837:144, March 2017.

[124] G. Colla et al. A catalogue of 3235 radio sources at 408 MHz. *A&AS*, page 281, 1970.

[125] M. Ackermann, M. Ajello, W. B. Atwood, et al. The Third Catalog of Active Galactic Nuclei Detected by the Fermi Large Area Telescope. *ApJ*, 810:14, September 2015.

[126] E. Nieppola, M. Tornikoski, and E. Valtaoja. Spectral energy distributions of a large sample of BL Lacertae objects. *A&A*, 445:441–450, January 2006.

[127] M. Ackermann, M. Ajello, A. Allafort, et al. The Second Catalog of Active Galactic Nuclei Detected by the Fermi Large Area Telescope. *ApJ*, 743:171, December 2011.

[128] V. P. Fomin et al. New methods of atmospheric Cherenkov imaging for gamma-ray astronomy. I. The false source method. *Astroparticle Physics*, 1994.

[129] V. A. Acciari et al. Veritas Observations of a Very High Energy γ-Ray Flare From the Blazar 3C 66A. *ApJ*, 2009.

[130] S. Archambault et al. Discovery of a New TeV Gamma-Ray Source: VER J0521+211. *ApJ*, 2013.

[131] M. Ackermann, M. Ajello, A. Albert, et al. The Spectrum of Isotropic Diffuse Gamma-Ray Emission between 100 MeV and 820 GeV. *ApJ*, 799:86, January 2015.

[132] A. M. Hillas, C. W. Akerlof, S. D. Biller, et al. The Spectrum of Teravolt Gamma Rays from the Crab Nebula. *ApJ*, 503:744–759, August 1998.

[133] D. N. Burrows et al. The Swift X-Ray Telescope. *Space Sci. Rev.*, 2005.

[134] A. Moretti et al. In-flight calibration of the Swift XRT Point Spread Function. In S. S. Holt, N. Gehrels, and J. A. Nousek, editors, *Gamma-Ray Bursts in the Swift Era*, volume 836 of *American Institute of Physics Conference Series*, 2006.

[135] K. A. Arnaud. XSPEC: The First Ten Years. In *Astronomical Data Analysis Software and Systems V*, Astronomical Society of the Pacific Conference Series, 1996.

[136] R. Petre, P. J. Serlemitsos, F. E. Marshall, et al. Highlights of the BBXRT mission. In E. H. Silver and S. M. Kahn, editors, *UV and X-ray Spectroscopy of Laboratory and Astrophysical Plasmas*, 1993.

[137] P. W. A. Roming, T. E. Kennedy, K. O. Mason, et al. The Swift Ultra-Violet/Optical Telescope. *Space Sci. Rev.*, 120:95–142, October 2005.

[138] L. O. Takalo, K. Nilsson, E. Lindfors, et al. Tuorla Blazar Monitoring Program. In F. A. Aharonian, W. Hofmann, and F. Rieger, editors, *American Institute of Physics Conference Series*, volume 1085 of *American Institute of Physics Conference Series*, pages 705–707, December 2008.

[139] L. Dondi and G. Ghisellini. Gamma-ray-loud blazars and beaming. *MNRAS*, 273:583–595, April 1995.

[140] G. Ghisellini, L. Maraschi, and L. Dondi. Diagnostics of Inverse-Compton models for the γ-ray emission of 3C 279 and MKN 421. *A&AS*, 120:503–506, December 1996.

[141] Floriana Zefi. Characterizing the long-term gamma-ray variability of the BL Lac object 1ES 1215+303 with Fermi-LAT. In *35th International Cosmic Ray Conference (ICRC2017)*, volume 35 of *International Cosmic Ray Conference*, July 2017.

[142] H.E.S.S. Collaboration, H. Abdalla, A. Abramowski, et al. Characterizing the γ-ray long-term variability of PKS 2155-304 with H.E.S.S. and Fermi-LAT. *A&A*, 598:A39, February 2017.

[143] M. Ackermann, M. Ajello, A. Albert, et al. Multiwavelength Evidence for Quasi-periodic Modulation in the Gamma-Ray Blazar PG 1553+113. *ApJ*, 813:L41, November 2015.

[144] S. Ciprini and Fermi Large Area Telescope Collaboration. Fermi LAT detection of a GeV gamma-ray flare from the high-energy peaked BL Lac object 1ES 1215+303 (B2 1215+30, ON 325). *The Astronomer's Telegram*, 10270, April 2017.

[145] S. Vaughan, R. Edelson, R. S. Warwick, and P. Uttley. On characterizing the variability properties of X-ray light curves from active galaxies. *MNRAS*, 345:1271–1284, November 2003.

[146] A. Sillanpaa, S. Haarala, M. J. Valtonen, B. Sundelius, and G. G. Byrd. OJ 287 - Binary pair of supermassive black holes. *ApJ*, 325:628–634, February 1988.

[147] F. M. Rieger. On the Geometrical Origin of Periodicity in Blazar-type Sources. *ApJ*, 615:L5–L8, November 2004.

[148] M. J. Graham, S. G. Djorgovski, D. Stern, et al. A possible close supermassive black-hole binary in a quasar with optical periodicity. *Nature*, 518:74–76, February 2015.

[149] R. Fender and T. Belloni. GRS 1915+105 and the Disc-Jet Coupling in Accreting Black Hole Systems. *ARA&A*, 42:317–364, September 2004.

[150] A. Rau, J. Greiner, and M. L. McCollough. The 590 Day Long-Term Periodicity of the Microquasar GRS 1915+105. *ApJ*, 590:L37–L40, June 2003.

[151] E. Striani, M. Tavani, G. Piano, et al. The Crab Nebula Super-flare in 2011 April: Extremely Fast Particle Acceleration and Gamma-Ray Emission. *ApJ*, 741:L5, November 2011.

[152] A. A. Abdo, M. Ackermann, M. Ajello, et al. Gamma-Ray Flares from the Crab Nebula. *Science*, 331:739, February 2011.

[153] M. Mayer, R. Buehler, E. Hays, et al. Rapid Gamma-Ray Flux Variability during the 2013 March Crab Nebula Flare. *ApJ*, 775:L37, October 2013.

[154] K. Meagher and VERITAS Collaboration. Six years of VERITAS observations of the Crab Nebula. In *34th International Cosmic Ray Conference (ICRC2015)*, volume 34 of *International Cosmic Ray Conference*, page 792, July 2015.

[155] J. Aleksić, S. Ansoldi, L. A. Antonelli, et al. Measurement of the Crab Nebula spectrum over three decades in energy with the MAGIC telescopes. *Journal of High Energy Astrophysics*, 5:30–38, March 2015.

[156] D. H. Clark and F. R. Stephenson. *The historical supernovae*. 1977.

[157] J. J. L. Duyvendak. Further Data Bearing on the Identification of the Crab Nebula with the Supernova of 1054 A.D. Part I. The Ancient Oriental Chronicles. *PASP*, 54:91–94, April 1942.

[158] G. W. Collins, II, W. P. Claspy, and J. C. Martin. A Reinterpretation of Historical References to the Supernova of A.D. 1054. *PASP*, 111:871–880, July 1999.

[159] J. J. Hester. The Crab Nebula: An Astrophysical Chimera. *ARA&A*, 46:127–155, September 2008.

[160] messier.seds.org. Lord Rosse's drawings of M1, the Crab Nebula. http://www.messier.seds.org/more/m001_rosse.html, 2017. [Online; Accessed: 09-15-2017.].

[161] J. D. Scargle. *Activity in the Crab Nebula*. PhD thesis, California Institute of Technology, 1968.

[162] A. McCann. Detection of the Crab Pulsar with VERITAS above 100 GeV. *International Cosmic Ray Conference*, 7:208, 2011.

[163] S. Funk, G. Hermann, J. Hinton, et al. The trigger system of the H.E.S.S. telescope array. *Astroparticle Physics*, 22:285–296, November 2004.

[164] Kevin Meagher for the VERITAS Collaboration. Six years of VERITAS observations of the Crab Nebula. *ArXiv e-prints*, August 2015.

[165] D. Carter-Lewis, S. Biller, P. J. Boyle, et al. Spectrum of TeV Gamma rays from the Crab Nebula. *International Cosmic Ray Conference*, 3:161, 1997.

[166] J. P. Finley, S. Biller, P. J. Boyle, et al. The spectrum of TeV gamma rays from the Crab Nebula. In C. D. Dermer, M. S. Strickman, and J. D. Kurfess, editors, *Proceedings of the Fourth Compton Symposium*, volume 410 of *American Institute of Physics Conference Series*, pages 558–562, May 1997.

[167] F. Aharonian, A. Akhperjanian, M. Beilicke, et al. The Crab Nebula and Pulsar between 500 GeV and 80 TeV: Observations with the HEGRA Stereoscopic Air Cerenkov Telescopes. *ApJ*, 614:897–913, October 2004.

[168] R. de los Reyes, J. Hahn, K. Bernloehr, et al. Influence of aerosols from biomass burning on the spectral analysis of Cherenkov telescopes. *ArXiv e-prints*, September 2013.

[169] R. Buehler and S. Ciprini. Enhanced gamma-ray activity from the Crab nebula. *The Astronomer's Telegram*, 8519, January 2016.

[170] P. Munar-Adrover, F. Verrecchia, C. Pittori, et al. New episode of enhanced gamma-ray emission from the Crab Nebula detected by AGILE. *The Astronomer's Telegram*, 9617, October 2016.

[171] C. C. Cheung. Fermi-LAT confirmation of enhanced gamma-ray activity from the Crab nebula. *The Astronomer's Telegram*, 9588, October 2016.

[172] R. Buehler, J. D. Scargle, R. D. Blandford, et al. Gamma-Ray Activity in the Crab Nebula: The Exceptional Flare of 2011 April. *ApJ*, 749:26, April 2012.

[173] A. A. Abdo, M. Ackermann, M. Ajello, et al. Fermi Large Area Telescope Observations of the Crab Pulsar And Nebula. *ApJ*, 708:1254–1267, January 2010.

[174] A. A. Abdo, M. Ajello, A. Allafort, et al. The Second Fermi Large Area Telescope Catalog of Gamma-Ray Pulsars. *ApJS*, 208:17, October 2013.

Appendix A

The observed energy of the high energy photons and soft photons are:

$$E_\gamma = E_\gamma^{'}\frac{\delta}{(1+z)}; \qquad E_t = E_t^{'}\frac{\delta}{(1+z)} \tag{A.1}$$

The observed energy of the soft photons can be written as:

$$E_t = \frac{\delta^2}{(1+z)^2}\frac{(mc^2)^2}{E_\gamma}$$

By taking $\delta = 4$, $z = 0.13$, $E_t = 73.551GeV$ we estimated the observed energy of the soft photons to be $E_t = 44.485088eV$.

Following the Dondi paper [139], the monochromatic luminosity of the target photons is given:

$$L^{'} = 4\pi d_L^2 \frac{mc^2}{h}\frac{\delta^{-3}}{1+z}F\left(\frac{\delta^2 mc^2}{(1+z)^2 h\nu}\right)$$

$$L^{'} = 20\pi\tau_{\gamma\gamma}\frac{mc^3}{\sigma_T}R^{'}$$

From where we find:

$$\tau_{\gamma\gamma} = \frac{4\pi d_L^2\delta^{-3}\frac{mc^2}{h}F\left(\frac{\delta^2 mc^2}{(1+z)^2 h\nu}\right)(1+z)^{-1}}{20\pi\tau_{\gamma\gamma}\frac{mc^3}{\sigma_T}R'}$$

$$= \frac{\sigma_T d_L^2}{5}\frac{F\left(\frac{\delta^2 mc^2}{(1+z)^2 h\nu}\right)}{\delta^3 hcR^{'}(1\ +z)}$$

$$\frac{d_L^2}{\delta^3 hc(1+z)R^{'}}F\left(\frac{\delta^2 mc^2}{(1+z)^2 h\nu}\right)$$

The flux $F\left(\frac{\delta^2 mc^2}{(1+z)^2 h\nu}\right) \equiv F(E_t)$ can be presented with a power law:

$$F(E_t) = F_0\left(\frac{E_t}{E_0}\right)^{-\alpha}$$

which after can be transformed as:

$$F(E_t) = F_{1keV}\frac{(1+z)^{2\alpha}}{\delta^{2\alpha}}\left(\frac{E_\gamma}{GeV}\right)^{\alpha} \tag{A.2}$$

with F_{keV}- measured flux at 1keV. The optical depth can be written as:

$$\tau(E_\gamma^{'}) = \frac{\sigma_T}{5hc^2}(1+z)^{2\alpha}\delta^{-(4+2\alpha)}\frac{d_L^2}{t_{var}}F_{1keV}\left(\frac{E_\gamma}{GeV}\right)^{\alpha}$$

With the requirement that $\tau(E_t) < 1$ we can be obtainted a lower limit on the Doppler factor δ:

$$\delta \geq \left[\frac{\sigma_T d_L^2}{5hc^2}(1+z)^{2\alpha}\frac{1}{t_{var}}F_{1keV}\left(\frac{E_\gamma}{GeV}\right)^{\alpha}\right]^{\frac{1}{(4+2\alpha)}}$$

Appendix B

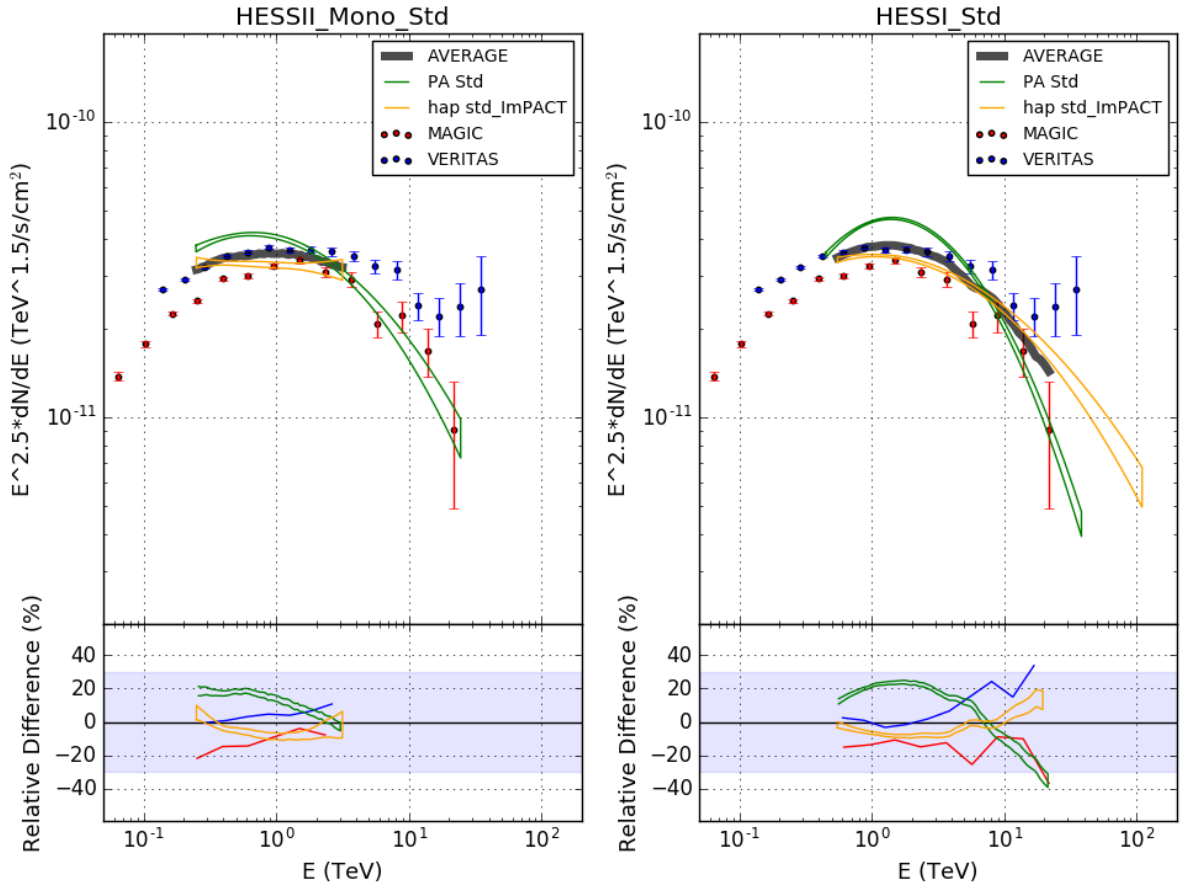

Figure B.1: The Crab Nebula spectrum and the relative difference with the "global" spectrum. The relative difference between each spectrum and the average are plotted in the bottom part of the plot. The H. E. S. S. points are derived from the intersection run list between the Paris-Analysis and HAP, two different analysis frameworks. The shadowed blue area correspond to 30% relative difference. The PA Std (green) correspond to this work and "HAP' (orange) to the other analysis framework (internal H. E. S. S. results produced by J.Hahn using HAP framework).

université PARIS-SACLAY | ÉCOLE DOCTORALE PHENIICS

Titre : Etude de la variabilité temporelle de l'émission gamma du blazar B2 1215+30 avec Fermi-LAT et de la Nèbuleuse du Crabe avec le réseau de télescopes H.E.S.S.

Mots clefs : astronomie gamma, Nébuleuse du Crabe, B2 1215+30, nébuleuse du vent pulsar, noyaux actifs de galaxies, blazars, variabilité du flux, H.E.S.S. expérience, satellite Fermi-LAT

Résumé : Les expériences actuelles en astronomie gamma sont le satellite Fermi-LAT et les expériences au sol tel que H.E.S.S., VERITAS et MAGIC. La surveillance des sources d'énergie très élevées indique une physique diversifiée. Afin d'étudier la forme la plus énergétique de ra- diation et les phénomènes les plus violents qui se déroulent dans l'Univers, l'analyse des sources individuelles est importante. Les BL Lac, un type de galaxie active, constituent la classe de source extragalactique la plus abondante détecté dans les énergies du GeV au TeV, tandis que le nébuleuses de vent de Pulsar sont la classe la plus peuplée dans le plan galactique. Ces deux types de sources ont des émissions variables de rayons gamma.

Dans cette thèse, la variabilité de l'objet BL Lac B2 1215 + 30 est étudiée avec les données du satellite Fermi-LAT. Une grande variation de flux, détectée par Fermi-LAT en février 2014, est simultanée avec un éruption très lumineux observé au TeV par l'expérience VERITAS. En collaboration avec la collaboration VERITAS, la variabilité du flux de rayons gamma a été utilisée pour établir des contraintes sur la taille de la région d'émission et sur le facteur Doppler. La variabilité à long terme, en utilisant près de neuf ans de données de Fermi-LAT de 100 MeV jusqu'à 500 GeV, a permis de détecter plusieurs flares. L'étude de la variabilité du flux indique un comportement quasi périodique avec une période de 1083 ± 32 jours.

Ensuite, la variabilité du flux de l'un des objets les plus étudié, la Nèbuleuse du Crabe, au TeV est étudiée avec dix ans d'observation de l'expérience H.E.S.S. Le spectre de la nébuleuse du crabe est mesuré de 280 GeV jusqu'à 62 TeV. Ceci est la première mesure qui s'étend à ces très hautes énergies. Considérée comme une "chandelle standard" en astronomie gamma, la nébuleuse du crabe est une source utilisée pour l'étalonnage et l'étude des instruments. L'observation de variations du flux au GeV par le satellite Fermi-LAT a par conséquent été une découverte inattendue. Ces variations de flux au GeV ont motivé la recherche de variations de flux au TeV en utilisant les données de l'expérience H.E.S.S. La position de la nébuleuse de crabe dans l'hémisphère nord et la localisation de H.E.S.S. en Namibie rendent cette enquête complexe en raison des importantes erreurs systématiques introduites par des conditions d'observation non optimales. Le travail sur la nébuleuse du crabe montre que la prise en compte de la transparence atmosphérique pour l'étude de l'évolution du flux avec le temps résulte en une réduction des effets systématiques. Aucune variation de flux n'a été observée à des énergies supérieures à 1 TeV dans les données de H.E.S.S. I. Une autre variation de flux au GeV signalée par le Fermi-LAT en octobre 2016 par télégramme astronomique, a été étudiée avec H.E.S.S. II. Cette analyse a montré que le GeV éruption a duré pendant un mois, et le flux avec H. E. S. S. a une variance excessive de 15%. Cela devrait être comparé à l'incertitude systématique de 20% fréquemment citée par H. E. S. S.

Title : Gamma-ray flux variation studies from the blazar B2 1215+30 with the Fermi-LAT and the Crab Nebula with the H. E. S. S. experiment

Keywords : gamma-ray astronomy, Crab Nebula, B2 1215+30, pulsar wind nebula, active galactic nuclei, blazar, gamma-ray flux variability, H.E.S.S. experiment, Fermi-LAT satellite

Abstract :

The current state-of-the-art experiments in gamma-ray astronomy are the Fermi-LAT in space and the ground-based H. E. S. S., VERITAS and MAGIC experiments. The monitoring of the very-high-energy gamma-ray emitting sources indicates the diverse physics taking place in astrophysical environments. To study the most energetic form of radiation and the most violent phenomena taking place in the Universe, individual source analyses are important. BL Lac objects, a subcategory of active galaxies, are the most abundant source class detected both in the GeV and TeV energies, while pulsar wind nebulae represent the most numerous identified source class in the galactic plane. Both source classes exhibit gamma-ray flux variations.

In this thesis, the gamma-ray variability of the BL Lac object B2 1215+30 is presented with Fermi-LAT data. A bright flare, with 16 times the average quiescent flux, was detected in February 2014. In collaboration with the VERITAS experiment, the gamma-ray variability was investigated over five decades in energy. This work resulted in the detection of a luminous flare, seen simultaneously in GeV and TeV energies by both instruments. These results were used to set constraints on the size of the emission region and on the Doppler factor of the relativistic jet. Additionally, the long-term variability was studied using nine years of Fermi-LAT data. This brought out new flux enhancements, which characterize the long-term lightcurve from 100 MeV up to 500 GeV. Other striking characteristics are a steady linear increase of the yearly average flux, together with a hardening of the spectral index. The investigation of the lightcurve indicates a hint of quasi-periodic behavior with a period of around 1083 ± 32 days.

This work includes spectrum and flux variability studies for the well-studied but ever-surprising Crab Nebula at TeV energies with more than a decade of H. E. S. S. observations. The spectrum measured in this work goes from 280 GeV to 62 TeV, making this the first measurement that extends to such very-high-energies. Considered as a standard candle for ground-based gamma-ray astronomy, the Crab Nebula is also used for calibration and instrument studies. The detection of GeV flares by the Fermi-LAT were unexpected and motivated the search of flux variations at TeV energies with the H. E. S. S. experiment. The position of the Crab Nebula in the northern hemisphere makes this investigation challenging due to the large systematic uncertainties introduced by the non-optimal observation conditions. This work showed that the systematic uncertainties can be reduced by taking into account the atmospheric transparency. No flux variations were found at energies above 1 TeV from the H. E. S. S. I data. A flare reported by the Fermi-LAT in October 2016 was also investigated. This analysis showed the GeV flare lasting for one month, while the flux with H. E. S. S. II had an excess variance of 15%. This should be compared to the commonly quoted 20% systematic uncertainty by H. E. S. S. experiment.

Université Paris-Saclay
Espace Technologique / Immeuble Discovery
Route de l'Orme aux Merisiers RD 128 / 91190 Saint-Aubin, France